Modelling Piezoresistive Behaviour in Finitely Deformed Elastomeric Composites

Masoud Ahmadi

James Watt School of Engineering
College of Science and Engineering
University of Glasgow

Submitted in fulfilment of the requirements for the degree of
Doctor of Philosophy

November 2024

To my dear parents,

whose unwavering love, guidance, and sacrifices
have been the compass of my life.

As educators, they nurtured my curiosity and passion for learning,
supporting me from primary school through to the completion of this PhD.

And to my beloved wife,

who entered my life later yet whose support has been
foundational during the most challenging stages of this journey.

"The Moving Finger writes; and, having writ,
Moves on: nor all thy Piety nor Wit
Shall lure it back to cancel half a Line,
Nor all thy Tears wash out a Word of it."
–Omar Khayyam

Abstract

This thesis contributes to studying the relationship between the electrical conductivity of elastomeric composites and their finite deformations. Elastomeric composites exhibit significant shifts in the orientation of their reinforcements under large deformations, altering their electrical conductivity. This piezoresistive property is exploited in applications such as wearable technology, human-machine interfaces, energy harvesting, and soft robotics. This research employs two methodologies: a computational framework for analysing mechanical behaviour under finite deformations and an analytical model to predict electrical conductivity.

A computational framework employing finite element methods is used to analyse mechanical behaviour under finite deformations, employing single-field and three-field mixed formulations. Simulations of extreme deformation numerical examples validate the developed finite element codes. A novel procedure for incorporating the plane stress condition for general hyperelastic models is introduced. The plane stress model is used for analysing elastomeric composites, where admissible boundary conditions are implemented using pixel meshing techniques, assessing fibre orientation impact. The analytical model, based on Eshelby's equivalent inclusion method, predicts electrical conductivity considering electron tunnelling and conductive network formation. This model accounts for fibre orientation and distribution, with rigorous validation against experimental data. By integrating computational and analytical approaches, this thesis offers a robust foundation for analysing piezoresistivity in elastomeric composites.

Acknowledgements

Completing this PhD has been an enriching journey, made possible by the support, guidance, and encouragement of many.

First and foremost, I extend my heartfelt thanks to my principal supervisor, Dr. Prashant Saxena. His insights and steadfast guidance were invaluable throughout this process, providing clarity and direction during the most challenging times. I am also deeply grateful to Prof. Andrew McBride for his meticulous attention to detail and significant impact on my research development. His encouragement and insightful feedback motivated me to strive for excellence. I acknowledge Prof. S. Kumar for his contributions to my supervisory team. Additionally, I owe a profound debt of gratitude to Prof. Paul Steinmann, whose influence greatly enriched my research experience. His contributions, along with the opportunity to visit his team at FAU in Germany, were pivotal.

My deepest gratitude goes to my family–my parents and brothers. Despite the distance imposed by studying abroad, their unwavering love and support have been my foundation. To my wife, who joined me in the final year of this journey, your understanding and companionship have been a sanctuary, bringing joy and balance during the demanding phases of my PhD.

I would like to thank my friend, Omid Amarloei, for his unwavering source of support and camaraderie. My colleagues and members of GCEC (Glasgow Computational Engineering Centre), who have been with me in every step of this journey, deserve a big thank you for all the stimulating discussions and for all the fun we have had during the last few years. I would especially like to acknowledge Davood Shahsavari for his valuable companionship throughout this journey. My academic journey was shaped long before this PhD, beginning with my first-grade teachers and extending to my university professors. Each has played a role in shaping my development as both a scholar and an individual.

This journey was made possible by the funding and support provided by the Engineering and Physical Sciences Research Council's (EPSRC) doctoral training fund. I am also grateful for the Jim Gatheral postgraduate travel scholarship, which enabled my visit to FAU.

While it is difficult to name everyone, I am deeply grateful to each person who has been part of this journey. Thank you all for being part of my PhD journey. Each of you has left a mark on my life and career, and I am forever grateful.

Reflections on my PhD journey

This thesis represents a substantial aspect of my PhD journey, yet it does not encapsulate the entirety of my doctoral experience. Throughout my PhD, I have undergone a transformative journey marked by significant personal and professional growth.

Professionally, I have acquired essential skills, including programming in C++, working proficiently in Linux-based environments, and mastering the utilisation of the finite element library deal.II. Moreover, I have refined my presentation and networking abilities through active participation in international conferences and courses held across the globe. Tutoring various courses, leading lab demonstrations, and assessing papers and assignments have also contributed to my teaching skills and the academic community. Regular participation in the Glasgow Computational Engineering Centre (GCEC) meetings and mentoring BSc and MSc students with their projects have been integral parts of my doctoral journey.

As a visiting researcher at FAU Erlangen–Nürnberg, I had the privilege of collaborating with the esteemed Institute of Applied Mechanics (LTM). I also actively participated in several enriching workshops and summer schools, among which stand out:

- "The finite element method using deal.II" at the International School for Advanced Studies (SISSA) and the International Centre for Theoretical Physics (ICTP) in Trieste, Italy.
- "Introduction to Uncertainty Quantification in Mechanics of Materials" at the Isaac Newton Institute for Mathematical Sciences (INI) and University of Cambridge in Cambridge, UK.

These immersive experiences have significantly shaped my academic development, expanding my horizons and expertise across diverse fields.

On a personal level, navigating a new country, immersing myself in a different language and culture, and being distanced from family and friends were pivotal experiences that contributed to my growth during this period. Furthermore, getting married during the final months of my PhD, amidst its most demanding phase, added a unique dimension to this journey and my personal life.

In summary, my PhD journey has been multifaceted, characterized by profound personal and professional development. While this thesis reflects a significant portion of that journey, it may not fully capture the entirety of my transformative experience.

Declaration

I hereby declare that the work presented in this PhD thesis is my own original research conducted at the University of Glasgow. This thesis has not been submitted previously for any degree or professional qualification at this or any other institution.

All sources of information and literature used in this thesis have been duly acknowledged and appropriately referenced. Where contributions of others are involved, every effort has been made to give credit to the respective sources.

Masoud Ahmadi

Contents

List of Tables

List of Figures

Chapter 1

Introduction

1.1 Overview of the research subject

Emerging as a modern cornerstone across various engineering fields such as mechanical, biomedical, and civil engineering, *advanced materials* shine brightly, eclipsing traditional counterparts. Engineered with tailored characteristics, these materials catalyse innovation across sectors ranging from aerospace to renewable energy and biomedicine.

As a pivotal subset, *composites* and *nanocomposites* enhance base materials by adding reinforcements to conceive novel materials with unparalleled strength, lightness, and functionality. Over the last few decades, the exploration of *nanostructures* –such as nanowires, nanoplates, nanofilms, nanorods and nanotubes– has intensified due to their outstanding physical attributes, leading to their use as reinforcing fillers in metals, polymers, ceramics and concrete.

In contrast, *soft materials*, ubiquitous in nature in the form of soft tissues such as leaves and skin, exhibit facile deformation near room temperature. Certain soft materials, including specific polymers and foams, are indispensable to applications in soft robotics and wearable sensors. While *elastomers*, a type of soft material, have ancient roots in human history, contemporary advancements have redefined them as a rapidly expanding category of modern materials. Elastomers are polymers with intrinsic *viscoelastic* properties, marked by low stiffness and high failure strain compared to other polymers (De and White, 2001; Shaw and MacKnight, 2018). These materials exhibit highly nonlinear, complex behaviour under significant deformations, encompassing both elastic and time-dependent responses. While their viscoelastic characteristics include effects like stress relaxation and energy dissipation, their large strain elastic response is frequently modelled using *hyperelasticity*, particularly useful in scenarios of rapid deformation. Although various theories, such as the rubber elasticity concept (Bergström and Boyce, 2001; Ogden, 1972, 1997) and the molecular theory of rubber elasticity (Flory, 1985), can predict the nonlinear behaviour of pure elastomers, they often struggle to accurately model more complex compositions, such as elastomeric composites (Paran et al., 2019). Elastomers often require the addition of fillers to enhance specific physical properties, addressing inherent deficiencies like mechanical strength. *Elastomeric composites* reinforced with various nanostructures, such

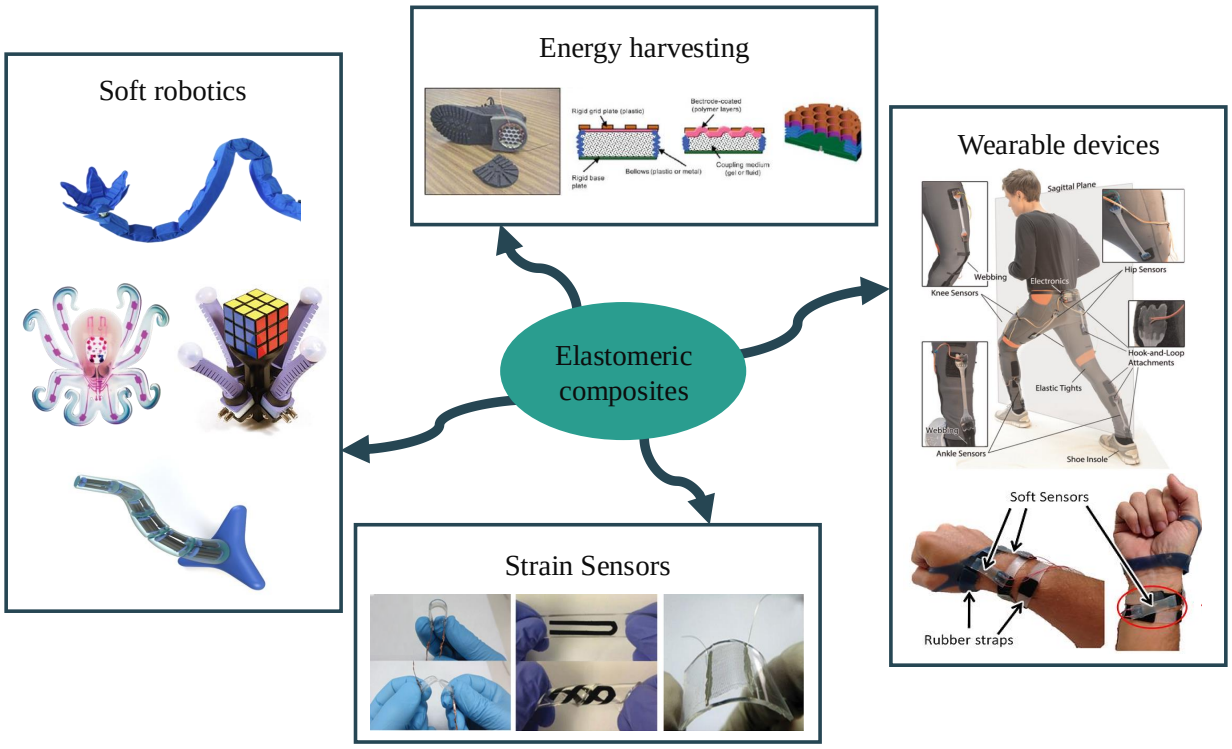

Figure 1.1: Relevant applications of elastomers and elastomeric composites: soft robotics, energy harvesting, wearable devices and strain sensors (Joo et al., 2022; Wehner et al., 2016; Harvard University, 2024; Amjadi et al., 2016).

as *carbon nanotubes* (CNTs) and *graphene nanosheets*, hold immense promise as cutting-edge, advanced materials. They have diverse practical applications across multiple industries, particularly in scenarios where piezoresistivity, flexibility, and conductivity are paramount. They enable the development of a wide range of products, including sensors, strain gauges, wearable electronics, electronic skins, and smart textiles for accurate health monitoring. Moreover, their biocompatibility and charge storage enhancement properties make them suitable for various applications, including implants and neural interfaces (Bokobza, 2023; Ariati et al., 2021; Papageorgiou et al., 2015). Figure 1.1 showcases several of these applications.

Advancing our grasp of elastomeric composites is crucial for innovation in these applications and beyond. Nonetheless, achieving this goal hinges on deepening our knowledge through research into one of the most advanced categories of materials.

1.2 Motivation and research objectives

When subjected to mechanical deformation, certain elastomeric composites with conductive fillers exhibit changes in electrical conductivity, a phenomenon known as *piezoresistive behaviour* (Taya et al., 1998; Taya, 1999). This behaviour arises from the reorientation and stretching of conductive filler networks, which disrupts or enhances pathways for electron flow within the elastomeric matrix. Understanding this electromechanical interplay is essential for advancing

next-generation wearable devices, structural health monitoring systems, cellular metamaterials, and strain sensors. Theoretical studies provide key insights while offering significant cost and time savings. As a further development of the existing knowledge, the computational and analytical models must provide accurate predictions of electrical and mechanical behaviour.

Despite significant progress, predicting the electrical conductivity of elastomeric composites remains challenging. While various models exist, many focus primarily on isotropic composites despite the typical non-uniform distribution of fillers. Elastomers typically exhibit nonlinear, nearly incompressible, and reversible behaviour under finite deformations (Ogden, 1997; Hossain et al., 2015; Saxena et al., 2013). Furthermore, the stark contrast in stiffness between the low-stiffness elastomers and high-stiffness fillers like CNTs causes these fillers to change position and orientation during large deformations, thereby altering electron pathways (Taya, 1999; Gong and Zhu, 2014; Buroni and García-Macías, 2021). Traditional models, such as those based on linear elasticity or small strain approximations (e.g., Voigt and Reuss models, Eshelby's inclusion model), often struggle to accurately represent this highly nonlinear behaviour. Developing efficient computational methods for modelling finite deformations of solids in such complex geometric domains and incompressible regimes is particularly challenging (Auricchio et al., 2013).

Accurately predicting the changes in electrical conductivity of elastomeric composites under mechanical stress remains challenging, which is critical for their functionality. Upon overviewing current research, it becomes evident that there is a crucial need for further development of comprehensive analytical and computational tools. This gap highlights the necessity for an interdisciplinary approach by integrating insights from materials science, physics, continuum mechanics, and nanotechnology. The identified gaps and challenges have led to the formulation of the following primary research questions:

1. How can computational and numerical techniques effectively simulate the highly nonlinear behaviour of elastomeric composites under finite mechanical deformation? What improvements are necessary in computational modelling?

2. How can we accurately track the changes in filler orientation and position during and after deformation in elastomeric composites? What effects do different loading conditions have on these changes?

3. How can we accurately predict the electrical conductivity of elastomeric composites, particularly in light of conductive pathways and the non-uniform distribution of fillers? Which parameters significantly affect the conductivity? Can we establish a framework to describe the piezoresistive behaviour?

Motivated by these questions, this thesis aims to develop advanced mathematical and computational frameworks to gain insights into the nonlinear piezoresistive behaviour of elastomeric composites through rigorous analyses.

Building upon the goal set forth, the principal objectives of this research are:

1. **Establish a comprehensive computational framework**: Deriving continuum mechanics formulations for the finite deformations of elastomers and creating computer codes to simulate the behaviour of elastomeric composites. This framework will focus on accurately representing the characteristics of randomly oriented fillers within the elastomeric matrix.

2. **Develop an analytical mathematical model**: Create a model to predict the electrical conductivity of filler-reinforced composites. The model will detail the complex mechanisms and parameters influencing conductivity, including the impact of the orientation and position of fillers within the composite.

3. **Lay the foundation for a piezoresistive framework:** Integrate the analytical model with the computational framework to establish a preliminary platform for investigating the piezoresistive behaviour of elastomeric composites, paving the way for future research.

Pursuing these objectives will lay the groundwork for future stochastic investigations into the effects of various parameters on piezoresistivity. This groundwork will enable data-driven and machine learning simulations, facilitating deeper exploration of elastomeric composite behaviour and fostering future innovations.

In essence, this project contributes to finding the link between the finite deformations of elastomeric nanocomposites and their electrical conductivity by analytical and computational modelling.

1.3 Research methodologies

This research employs a computational method to simulate finite deformations and an analytical method to analyse electrical conductivity. Supplementary codes and data for both methods are provided as open source.

1.3.1 Computational method

In recent decades, significant advancements in nonlinear elasticity have enabled the study of elastomers and their composites, focusing on their ability to undergo large elastic deformations with minimal energy dissipation. While analytical models provide initial insights, they often fall short of accurately capturing the complex interactions between fillers in composite materials. To bridge this gap, advanced computational tools have become essential. In modern engineering, *computational engineering* has risen to prominence due to advances in computers and technology, surpassing traditional engineering methods. This interdisciplinary approach integrates material science, continuum mechanics, mathematics, computer science, and high-performance computing (HPC), allowing for the simulation of physical behaviours that would otherwise be costly, time-consuming, or risky to experiment with physically.

Various computational methods, such as the finite element method, boundary element method, finite volume method, and variational differential quadrature method, have been widely employed to study the mechanical response of these materials under finite deformations (Dai and Song, 2014; Reese, 2002; Bijelonja et al., 2005; Sun et al., 2008; Yosibash and Priel, 2011; Ansari et al., 2021b; Pagani and Carrera, 2023). The finite element method (FEM) is a widely used tool in computational engineering, approximating solutions to boundary value problems by subdividing a complex system into smaller, simpler components, or elements, that are easier to analyse individually. This study prioritises hyperelasticity for its computational efficiency in modelling large deformations, simplifying the material model by omitting time-dependent viscoelastic effects like stress relaxation and creep. While this choice is generally suitable for rapid loading scenarios, it is noted that viscoelastic characteristics may play a role in applications involving prolonged or cyclic loads. The finite element codes are developed using deal.II, an open-source, object-oriented FEM library written in C++ that enables rapid development of modern finite element (FE) codes (Bangerth et al., 2007). The deal.II library provides advanced FE analysis capabilities with robust support for parallel computing and adaptive mesh refinement, ensuring efficient and precise simulations. Its open-source nature promotes reproducibility and ongoing research development.

Key aspects of the computational method include:

- Proposing a rigorous procedure for imposing the plane stress condition for general hyperelastic models, a topic often neglected in nonlinear elasticity.
- Using a three-field mixed formulation to address volumetric locking associated with non-plane stress models.
- Investigating representative volume elements (RVEs) with randomly dispersed fibres.
- Examining admissible boundary conditions, including affine and periodic boundary conditions, and using the pixel meshing technique.
- Integrating parallelization to optimise computational resources and speed up simulations.
- Investigating reorientation of fibres under deformation by tracking changes in their alignment and spacing.

1.3.2 Analytical method

Micromechanical theories provide a robust framework for understanding the behaviour of composite materials at micro- and nano-scales. Among these, the *equivalent inclusion method* (EIM), proposed by Eshelby (1957a), simplifies the complex problem of interactions within heterogeneous materials by treating inclusions as equivalent phases with modified properties. One of the main advantages of EIM is that the solution is limited to a system of algebraic

equations and can be applied to various material behaviours, such as elastic-plastic, viscoelastic, and creep (Taya, 2005). The concept of equivalent inclusion extends beyond mechanical characteristics, having been adapted to assess other physical properties such as thermal conductivity (Hiroshi and Minoru, 1986; Hatta and Taya, 1985, 1986; Chen and Wang, 1996) and electrical conductivity (Mora et al., 2020; Feng and Jiang, 2013; Garcia-Macias et al., 2017; Seidel and Lagoudas, 2009).

The movement of electrons between adjacent conductive fillers within a material is known as *electron hopping* or *electron tunnelling*. This phenomenon can lead to the formation of pathways for electron transport and thus impacts piezoresistive behaviour.

This study represents a rigorous analytical formulation based on EIM for computing effective electrical conductivity of nanocomposites (Hatta and Taya, 1985; Seidel and Lagoudas, 2009; Gong et al., 2013). Key aspects of the analytical method include:

- Deriving a detailed EIM formulation and providing a step-by-step explanation.
- Accounting for electron hopping and conductive networks.
- Incorporating a limit angle for filler orientation and a probability distribution function to account for non-uniform filler distribution.

1.4 Dissertation structure

This project is organized into three main phases, spread across six chapters, including this introductory chapter. The phases are outlined as follows:

(i) **Learning and preparation**: This phase entails an in-depth study of the research topic and comprehensive reviews of the relevant published research. It includes acquiring proficiency in C++ programming and gaining experience with the finite element library deal.II. This phase commenced with the initiation of the PhD program and is an ongoing process involving engagement with relevant books, papers, courses, conferences, and workshops. The knowledge and skills acquired permeate throughout all chapters of the dissertation.

(ii) **Computational framework**: The crux of this thesis revolves around this phase, which focuses on addressing the first two research questions. This phase entails the development of a nonlinear elastic model incorporating finite element formulation for both compressible and nearly incompressible hyperelastic materials. It encompasses code development, simulation execution, and exploring novel computational challenges and solutions. This central phase unfolds across three chapters: **Chapter** 2 describes the derivation of continuum mechanics formulations for hyperelastic solids and details their implementation in FEM. **Chapter** 3 discusses FEM features, 2D configurations, coding practices, and validation through challenging numerical problems. **Chapter** 4 explores the reorientation of randomly distributed fibres in RVEs, considering different distribution patterns and admissible boundary conditions.

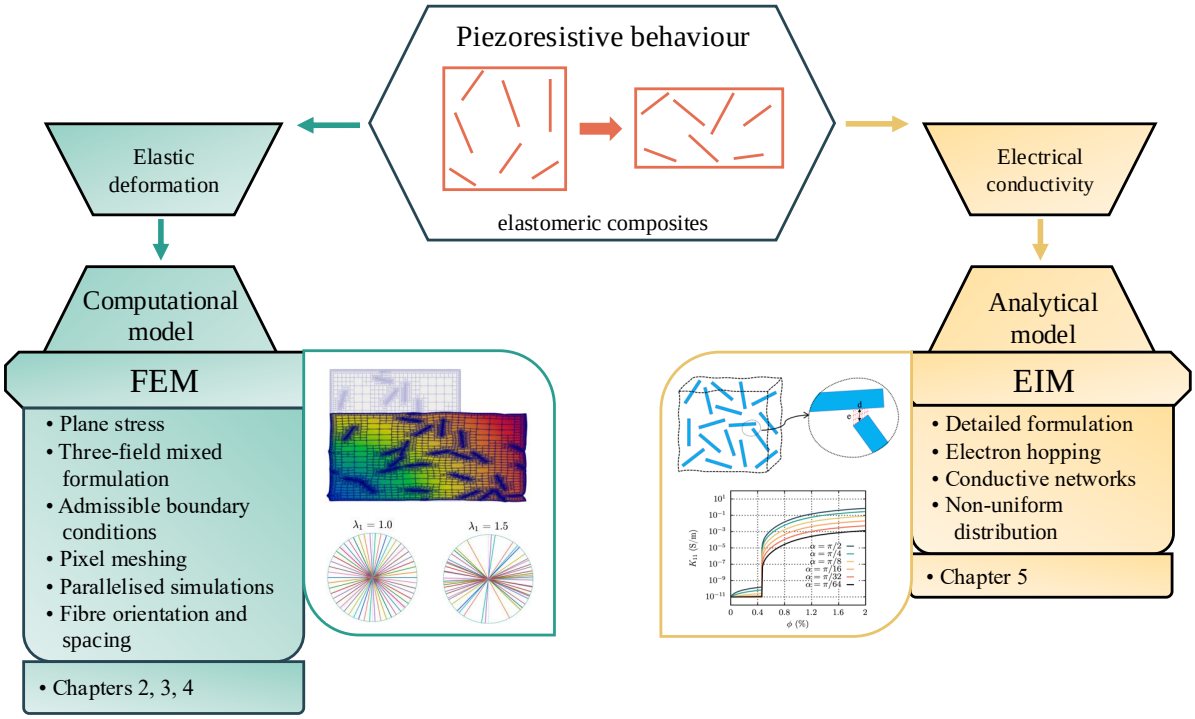

Figure 1.2: Visual representation of the structure and objectives of this study.

(iii) **Analytical framework**: Tackling the third research questions, this phase focuses on developing an analytical method for predicting the electrical conductivity of elastomeric composites. Then, the extracted data from computational simulations are applied to the analytical model to estimate the electrical conductivity of the composites under finite deformations. The methodologies and findings of this phase are presented in **Chapter** 5.

The dissertation concludes with **Chapter** 6, summarizing the significance of the research and its findings and suggesting insights for further research. Figure 1.2 provides a concise visual overview illustrating how this study is structured to address the overarching goal of this research.

1.4.1 Contemporary research practices

This thesis attempts to be a reflection of contemporary research paradigms, integrating interdisciplinary methodologies and innovative techniques to tackle complex challenges within its field of study. It aims to represent the culmination of a PhD journey, aligning with modern principles of scientific inquiry and emphasizing openness and accessibility. In alignment with the University of Glasgow's dedication to *Open Research*, this study embraces open science principles to promote transparency, foster collaboration, and accelerate scientific progress. By openly sharing all research materials –including text, codes, and publications– this thesis promotes scholarly dialogue and collective advancement in the field. By embracing modern approaches to research and inquiry, this thesis aims to make a meaningful and lasting contribution to advancing knowledge in its field.

1.5 Research outputs

This research project has produced several noteworthy outputs, including the publication of journal articles, conference presentations, and the development of open-access codes.

A significant portion of the content presented in this thesis corresponds to the material covered in these resources. This acknowledgement is made to transparently disclose the interconnectedness, ensuring that any overlap is clearly recognized as intentional and not indicative of misconduct.

The journal publications:

- Ahmadi, M., and Saxena, P. (2024), "Analytical modeling of the electrical conductivity of CNT-filled polymer nanocomposites", *Mathematics and Mechanics of Solids*. (Ahmadi and Saxena, 2024)
- Ahmadi M., McBride A., Steinmann P., and Saxena P. (2024), "Plane stress finite element modelling of arbitrary compressible hyperelastic materials". (*Under review*)

The results from Chapter 4 were in the process of being prepared for submission to a peer-reviewed journal at the time this thesis was written.

The open-access codes:

- Ahmadi, M. (2024) "madeal FE code collection". Zenodo. doi: 10.5281/zenodo.11636987. (Ahmadi, 2024)
- Ahmadi, M. and Saxena, P. (2023) "Mathematica file for article: Analytical modelling of the electrical conductivity of CNT-filled polymer nanocomposites". Zenodo. doi: 10.5281/zenodo.8114528. (Ahmadi and Saxena, 2023)

Conference presentations:

- Ahmadi M., Saxena P., and McBride A. (2023), "Electrical conductivity of CNT-reinforced composites undergoing large deformation", *UK Association for Computational Mechanics (UKACM) Conference*, Coventry, UK.
- Ahmadi M., Saxena P., and McBride A. (2023), "Computational homogenization of CNT reinforced nanocomposite undergoing large deformation considering different periodic boundary conditions", *Computational Methods in Multi-scale, Multi-uncertainty and Multi-physics Problems (CM4P)*, Porto, Portugal.
- Ahmadi M., McBride A., Saxena P., and Steinmann P. (2024), "Finite element modelling of incompressible hyperelastic materials: 2D/3D/plane-stress/plane-strain", *UK Association for Computational Mechanics (UKACM) Conference*, Durham, UK.

Chapter 2

Hyperelasticity and finite element approximation

Continuum mechanics and FEM form a robust framework for simulating mechanical deformations. This chapter details continuum mechanics formulations for hyperelastic bodies and integrates variational principles with nonlinear FEM. It covers both classical single-field and three-field mixed formulations. Readers are expected to have prior knowledge of linear algebra and tensor analysis, along with familiarity with advanced calculus concepts. For detailed expositions on the topic in continuum mechanics and FEM, consult standard references such as Ogden (1997), Holzapfel (2000), Bonet and Wood (1997), and Wriggers (2008).

2.1 Mathematical notation

Consider vectors $\mathbf{a}$ and $\mathbf{b}$, a 2nd-order tensor $\mathbf{C}$, and a scalar α. Table 2.1 shows the inner product and tensor product of the vectors in different notations. Here in this research, both direct and index notations are adapted and switched based on convenience and significance.

Table 2.1: Different mathematical notations.

Notation	Inner product	Tensor product
Direct tensor	$\alpha = \mathbf{a} \cdot \mathbf{b}$	$\mathbf{C} = \mathbf{a} \otimes \mathbf{b}$
Tensor index	$\alpha = a_i\, b_i$	$C_{ij} = a_i\, b_j$
Matrix	$\alpha = \mathbf{a}^T\, \mathbf{b}$	$\mathbf{C} = \mathbf{a}\mathbf{b}^T$

In direct notation, scalars are represented by italic letters (e.g., α), vectors and 2nd-order tensors by bold letters (e.g., $\mathbf{a}$), and 4th-order tensors by blackboard letters (e.g., $\mathbb{D}$). Einstein's summation convention is utilised for index notation, where summation over repeated indices is implied, that is

$$\sum_{i=1}^{n} a_i\, b_i = a_i\, b_i\,. \tag{2.1.1}$$

Square brackets $[\square]$ are used for grouping algebraic expressions or matrix demonstration, round

brackets ($\square$) for function argument, and double vertical bars $||\square||$ represent the Euclidean norm as $||\mathbf{a}|| = [\mathbf{a}\cdot\mathbf{a}]^{1/2}$. The dot accent $\dot{\square}$ indicates time derivatives: $\dot{\square} = \frac{\partial \square}{\partial t}$.

The double dot product between two tensors is denoted by the symbol (:), for example, $\mathbf{A} : \mathbf{B} = A_{ij}\, B_{ij}$. The nabla operator $\boldsymbol{\nabla}$ is used for the gradient and divergence of a tensor, represented as $\boldsymbol{\nabla}\mathbf{A}$ and $\boldsymbol{\nabla}\cdot\mathbf{A}$, respectively. The tensor products $\otimes$ and $\odot$ for tensors $\mathbf{A}$ and $\mathbf{B}$ are defined as $[\mathbf{A}\otimes\mathbf{B}]_{ijkl} = A_{ij}B_{kl}$, and

$$[\mathbf{A}\odot\mathbf{B}]_{ijkl} = \frac{1}{2}\left[A_{ik}B_{jl} + A_{il}B_{jk}\right]\,. \tag{2.1.2}$$

The above operator is useful for expressions such as

$$-\frac{\partial \mathbf{A}^{-1}}{\partial \mathbf{A}} = \mathbf{A}^{-1}\odot\mathbf{A}^{-1} = \frac{1}{2}\left[A^{-1}_{ik}A^{-1}_{jl} + A^{-1}_{il}A^{-1}_{jk}\right]\,. \tag{2.1.3}$$

With orthogonal basis vectors $\{\mathbf{e}_1, \mathbf{e}_2, \mathbf{e}_3\}$, the Kronecker delta $\delta_{ij} = \mathbf{e}_i\cdot\mathbf{e}_j$ and the 2nd-order identity tensor $\mathbf{I}$ are fundamental, with components $I_{ij} = \delta_{ij}$. For $\mathbf{A}$ is a 2nd-order tensor, the 4th-order symmetric identity tensor is defined as $\mathbb{I} = I_{ijkl} = \frac{1}{2}\left[\delta_{ik}\delta_{jl} + \delta_{il}\delta_{jk}\right]$, where $\mathbb{I}\colon \mathbf{A} = \mathbf{A}$.

Remark. Note the distinction $\mathbb{I} \neq \mathbf{I}\otimes\mathbf{I} = \delta_{ij}\delta_{kl}$. Different references may use varying notations, but this thesis adheres to the described conventions. For example, while some may show $\mathbf{C} = \lambda\,\mathbf{1}\otimes\mathbf{1} + 2\mu\,\mathbf{I}$, here this expression is shown by $\mathbb{C} = \lambda\,\mathbf{I}\otimes\mathbf{I} + 2\mu\,\mathbb{I}$. □

The symmetric part of a square matrix $\mathbf{A}$ is denoted by $\mathrm{sym}(\mathbf{A})$, calculated as

$$\mathrm{sym}(\mathbf{A}) = \frac{1}{2}\left[\mathbf{A} + \mathbf{A}^T\right]\,. \tag{2.1.4}$$

The deviatoric operator $\mathbb{D}$ is defined as

$$\mathbb{D} = \mathbb{I} - \frac{1}{3}\,\mathbf{I}\otimes\mathbf{I}\,. \tag{2.1.5}$$

Remarks:

(i) The notation used is not case-sensitive, permitting both lowercase and uppercase letters to denote tensors of any order.

(ii) When a second or higher-order tensor is involved in a single contraction product, the dot symbol ($\cdot$) is omitted, as is common in the literature. For example, $\mathbf{A}\cdot\mathbf{B} = \mathbf{C}$ is written as $\mathbf{AB} = \mathbf{C}$. □

These mathematical notations and definitions are fundamental to the computational model presented in this thesis, spanning the current chapter and the following two chapters.

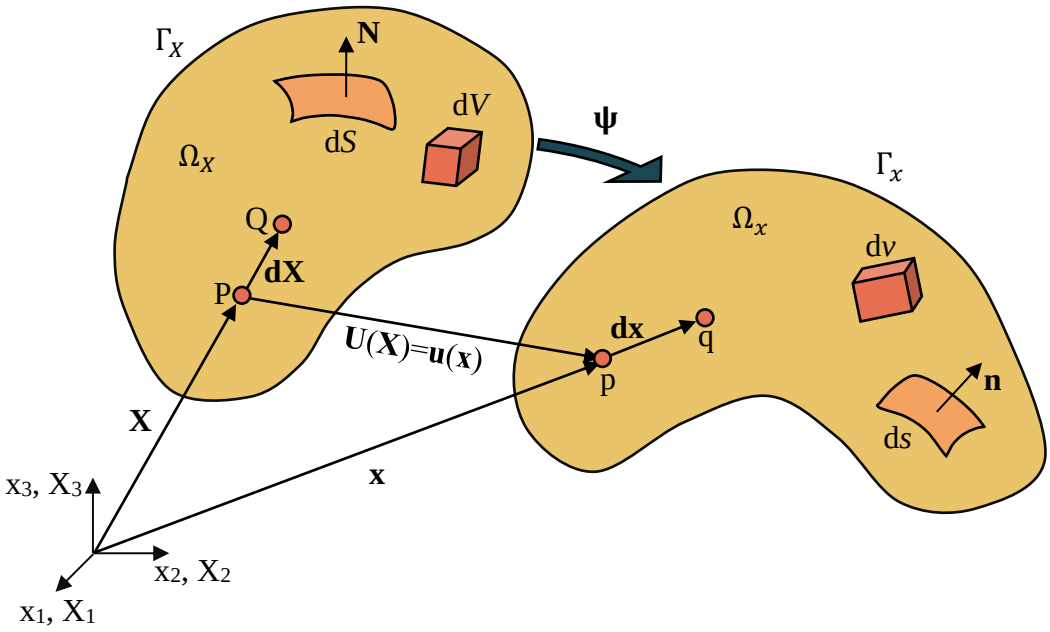

Figure 2.1: Illustration of a continuum body undergoing deformation, transitioning from its initial state described by the Lagrangian system to a deformed state described by the Eulerian system.

2.2 Mechanics of a deformed continuum body

2.2.1 Kinematics

This section reviews kinematics, which describes the deformation of a continuum body, focusing on geometric aspects without considering material properties or forces.

2.2.1.1 Deformation of a continuum body

A general body undergoing deformation from an initial (reference) state to a deformed (current) state is considered, as illustrated in Figure 2.1. The motion can be described using the Lagrangian (material) approach, based on the initial configuration, or the Eulerian (spatial) approach, based on the current configuration. The Lagrangian description of the position of an arbitrary point P in the initial configuration is denoted by $\mathbf{X} = X_I\,\mathbf{E}_I \in \Omega_X$ with material basis vectors $\mathbf{E}_I$. Upon a quasi-static deformation, the body occupies the spatial configuration Ω_x, transforming the arbitrary point to point p with position $\mathbf{x} = x_i\,\mathbf{e}_i$, with special basis vectors $\mathbf{e}_i$. Hence,

$$\mathbf{X} = X_I\,\mathbf{E}_I = \boldsymbol{\Psi}^{-1}(\mathbf{x}), \tag{2.2.1a}$$

$$\mathbf{x} = x_i\,\mathbf{e}_i = \boldsymbol{\Psi}(\mathbf{X}). \tag{2.2.1b}$$

The Lagrangian and Eulerian gradient of a tensor $(\square)$ are respectively represented by $\boldsymbol{\nabla}_X(\square) = \frac{\partial(\square)}{\partial X_I} \otimes \mathbf{E}_I$ and $\boldsymbol{\nabla}_x(\square) = \frac{\partial(\square)}{\partial x_i} \otimes \mathbf{e}_i$. A comparable notation is applied to the divergence operator. The displacement field in both descriptions $\mathbf{U}(\mathbf{X}) = \mathbf{u}(\mathbf{x})$, shown in Figure 2.1

describes the movement from point P to p. The displacement relations are expressed as

$$\mathbf{u}(\mathbf{x}) = \mathbf{x} - \mathbf{X}(\mathbf{x}), \tag{2.2.2a}$$

$$\mathbf{U}(\mathbf{X}) = \mathbf{x}(\mathbf{X}) - \mathbf{X}. \tag{2.2.2b}$$

Since $\mathbf{U}$ and $\mathbf{u}$ represent the same values, this research will use $\mathbf{u}$ to denote the displacement field, simplifying the notation. The context will clarify whether it refers to the displacement field in spatial or material coordinates.

2.2.1.2 Deformation gradient

An infinitesimal vector in the reference body $\mathbf{dX}$ deforms to $\mathbf{dx}$ in the current body. This transformation is expressed by

$$\mathbf{dx} = \frac{\partial \mathbf{x}}{\partial \mathbf{X}}\,\mathbf{dX}, \tag{2.2.3}$$

where $\partial\mathbf{x}/\partial\mathbf{X}$ is defined as the *deformation gradient*, which can be represented as

$$\mathbf{F} = \boldsymbol{\nabla}_X\,\mathbf{x} = \frac{\partial x_i}{\partial X_I}\,\mathbf{e}_i \otimes \mathbf{E}_I\,. \tag{2.2.4}$$

Using Equation (2.2.2), the above equation becomes

$$\mathbf{F} = \mathbf{I} + \frac{\partial \mathbf{u}}{\partial \mathbf{X}} = \mathbf{I} + \boldsymbol{\nabla}_X\,\mathbf{u}, \tag{2.2.5}$$

where $\partial\mathbf{u}/\partial\mathbf{X}$ is the displacement gradient. Defining J as the determinant of deformation gradient, $J = \det(\mathbf{F})$, for all materials it holds, $J > 0$, while for the incompressible materials, $J = 1$.

2.2.1.3 Deformation of surface and volume

Infinitesimal volume element before deformation $\mathrm{d}V = \mathbf{dX}_1 \cdot [\mathbf{dX}_2 \times \mathbf{dX}_3]$ transforms to $\mathrm{d}v = \mathbf{dx}_1 \cdot [\mathbf{dx}_2 \times \mathbf{dx}_3]$ as shown in Figure2.1. Using the definition of $\mathbf{F}$, one obtains

$$\mathrm{d}v = J\,\mathrm{d}V\,. \tag{2.2.6}$$

Infinitesimal areas on the boundaries of the body, with normal vector $\mathbf{N}$ for the reference body and normal vector $\mathbf{n}$ for the current body, are expressed by

$$\mathbf{N}\,\mathrm{d}S = \mathbf{dX}_1 \times \mathbf{dX}_2\,, \tag{2.2.7a}$$

$$\mathbf{n}\,\mathrm{d}s = \mathbf{dx}_1 \times \mathbf{dx}_2\,. \tag{2.2.7b}$$

One can obtain

$$\mathbf{n}\,\mathrm{d}s = J\,\mathbf{F}^{-T}\,\mathbf{N}\,\mathrm{d}S\,, \tag{2.2.8}$$

which is known as Nanson's formula (Truesdell, 1952).

2.2.1.4 Strain

Two commonly used strains are introduced here: Lagrangian and Eulerian.

Lagrangian strain. It uses the undeformed body as a reference for measurement. Writing

$$\begin{aligned} ||\mathbf{dx}||^2 - ||\mathbf{dX}||^2 &= \mathbf{dx}\cdot\mathbf{dx} - \mathbf{dX}\cdot\mathbf{dX} \\ &= \mathbf{dX}\cdot\mathbf{F}^T\mathbf{F}\,\mathbf{dX} - \mathbf{dX}\cdot\mathbf{dX} \\ &= \mathbf{dX}\cdot\left[\mathbf{F}^T\,\mathbf{F} - \mathbf{I}\right]\mathbf{dX}, \end{aligned} \tag{2.2.9}$$

the term $\mathbf{C} = \mathbf{F}^T\,\mathbf{F}$ is defined as the *right Cauchy–Green deformation* tensor. The Lagrangian –also referred to as *material* or *Green–Saint Venant*– strain is defined as

$$\mathbf{E} = \frac{1}{2}\left[\mathbf{C} - \mathbf{I}\right]. \tag{2.2.10}$$

The above expression can be written in terms of displacement gradient as

$$\mathbf{E} = \frac{1}{2}\left[\frac{\partial\mathbf{u}}{\partial\mathbf{X}} + \left(\frac{\partial\mathbf{u}}{\partial\mathbf{X}}\right)^T + \frac{\partial\mathbf{u}}{\partial\mathbf{X}}\left(\frac{\partial\mathbf{u}}{\partial\mathbf{X}}\right)^T\right] = \frac{1}{2}\left[\boldsymbol{\nabla}_X\,\mathbf{u} + (\boldsymbol{\nabla}_X\,\mathbf{u})^T + \boldsymbol{\nabla}_X\,\mathbf{u}\;\;(\boldsymbol{\nabla}_X\,\mathbf{u})^T\right]. \tag{2.2.11}$$

In a infinitesimal deformations regime, the infinitesimal strain $\boldsymbol{\varepsilon}$ is defined by

$$\boldsymbol{\varepsilon} = \frac{1}{2}\left[\boldsymbol{\nabla}_X\mathbf{u} + (\boldsymbol{\nabla}_X\,\mathbf{u})^T\right]. \tag{2.2.12}$$

Eulerian strain. It uses deformed geometry as a reference for measurement. Similarly to Lagrangian, writing

$$\begin{aligned} ||\mathbf{dx}||^2 - ||\mathbf{dX}||^2 &= \mathbf{dx}\cdot\mathbf{dx} - \mathbf{dX}\cdot\mathbf{dX} \\ &= \mathbf{dx}\cdot\mathbf{dx} - \mathbf{dx}\cdot\mathbf{F}^{-T}\mathbf{F}^{-1}\,\mathbf{dx} \\ &= \mathbf{dx}\cdot\left[\mathbf{I} - \left[\mathbf{F}\,\mathbf{F}^T\right]^{-1}\right]\mathbf{dx}, \end{aligned} \tag{2.2.13}$$

the term $\mathbf{b} = \mathbf{F}\,\mathbf{F}^T$ is defined as the *left Cauchy–Green deformation* tensor. The Eulerian –also referred to as *spatial* or *Almansi*– strain is defined as

$$\mathbf{e} = \frac{1}{2}\left[\mathbf{I} - \mathbf{b}^{-1}\right]. \tag{2.2.14}$$

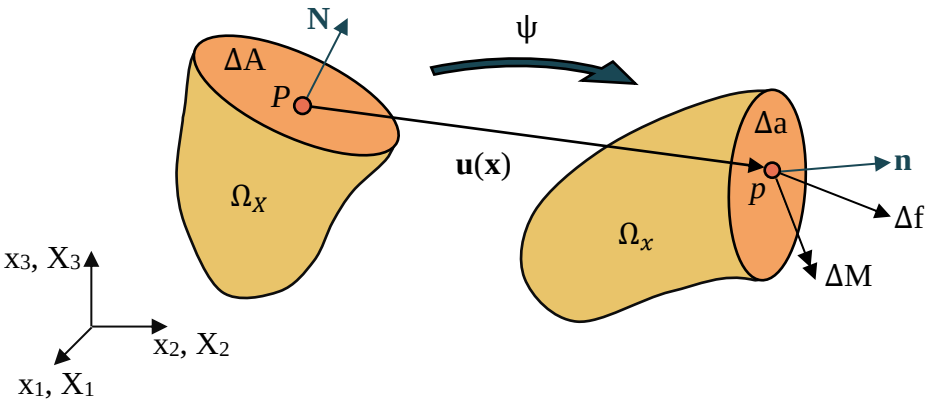

Figure 2.2: Inside a continuum body cut by a plane.

2.2.1.5 Polar decomposition

Given a non-singular deformation gradient $\mathbf{F}$, there exists a unique orthogonal tensor $\mathbf{Q}$ and unique positive-definite symmetric tensors $\mathbf{U}$ and $\mathbf{v}$ such that

$$\mathbf{F} = \mathbf{Q}\,\mathbf{U} = \mathbf{v}\,\mathbf{Q}\,, \tag{2.2.15}$$

where $\mathbf{Q}$ represents a rigid-body rotation, and $\mathbf{U}$ and $\mathbf{v}$ denote the *right* and *left stretch* tensors, respectively. The tensors $\mathbf{U}$ and $\mathbf{v}$ share the same eigenvalues (principal stretches) but possess different eigenvectors (principal axes of deformation). Expressing the right Cauchy–Green deformation tensor as $\mathbf{C} = \mathbf{F}^T\mathbf{F} = \mathbf{U}\,\mathbf{Q}^T\mathbf{Q}\,\mathbf{U} = \mathbf{U}^2$, one finds

$$\mathbf{U}^2 = \mathbf{C} \Rightarrow \mathbf{U} = \sqrt{\mathbf{C}}\,. \tag{2.2.16}$$

Similarly, one obtains $\mathbf{v}^2 = \mathbf{b}$, and since $\det(\mathbf{C}) = \det(\mathbf{b}) = J^2$, it follows that $\det(\mathbf{U}) = \det(\mathbf{v}) = J$. Thus, $\mathbf{U}$ shares the same eigenvectors with $\mathbf{C}$, and its eigenvalues are square roots of those of $\mathbf{C}$. The same relationship applies to $\mathbf{v}$ and $\mathbf{b}$. The spectral decomposition of $\mathbf{C}$ and $\mathbf{b}$ are given by

$$\mathbf{U}^2 = \mathbf{C} = \sum_{i=1}^{3} \lambda_i^2\, \mathbf{N}_i \otimes \mathbf{N}_i\,, \quad \text{and} \quad \mathbf{v}^2 = \mathbf{b} = \sum_{i=1}^{3} \lambda_i^2\, \mathbf{n}_i \otimes \mathbf{n}_i\,. \tag{2.2.17}$$

Here, λ_i denotes the principal stretches, which are the square roots of the eigenvalues of the right and left Cauchy–Green deformation tensors.

2.2.2 Stress

By metaphorically dissecting the body to reveal internal interactions, Figure 2.2 portrays a cross-section of the dissected body, showing its internal forces. In classical continuum mechanics, torque $\Delta\mathbf{M}$ is typically disregarded, while theories such as *micropolar theory* incorporate it (Eringen and Eringen, 1999). The *Cauchy traction* vector at point p in the current geometry

is expressed as

$$\mathbf{t}^{(n)} = \lim_{\Delta a \to 0} \frac{\Delta \mathbf{f}}{\Delta a} = \boldsymbol{\sigma}\mathbf{n}, \tag{2.2.18}$$

where $\boldsymbol{\sigma}$ is the *Cauchy stress*. Cauchy stress references both force and area to the current geometry, thus termed the "true" stress.

Considering the same force $\Delta\mathbf{f}$, but with differential area ΔA and unit normal $\mathbf{N}$ in the undeformed geometry,

$$\mathbf{T}^{(N)} = \lim_{\Delta A \to 0} \frac{\Delta \mathbf{f}}{\Delta A} = \mathbf{P}\mathbf{N}, \tag{2.2.19}$$

where $\mathbf{P}$ is the *Piola stress*, corresponding to what is commonly called "engineering" stress. The relationship between $\mathbf{P}$ and $\boldsymbol{\sigma}$ is given as

$$\mathbf{P} = J\boldsymbol{\sigma}\mathbf{F}^{-T}. \tag{2.2.20}$$

Unlike Cauchy stress, Piola stress $\mathbf{P}$ is not symmetric. Hence, the *Piola–Kirchhoff stress* $\mathbf{S}$ is introduced as

$$\mathbf{S} = \mathbf{F}^{-1}\mathbf{P} = J\mathbf{F}^{-1}\boldsymbol{\sigma}\mathbf{F}^{-T} = \mathbf{S}^T \quad \text{or} \quad S_{IJ} = F^{-1}_{Ii}P_{iJ} = JF^{-1}_{Ii}\sigma_{ij}F^{-1}_{jJ} = S_{JI}, \tag{2.2.21}$$

which is a symmetric tensor.

Remark. In many texts, the term "First Piola–Kirchhoff stress" is commonly used to refer to the Piola stress, whereas the term "Second Piola–Kirchhoff stress" denotes the Piola–Kirchhoff stress. □

It can be shown that the Cauchy stress is related to the Piola–Kirchhoff by

$$\boldsymbol{\sigma} = J^{-1}\,\mathbf{F}\mathbf{S}\mathbf{F}^T. \tag{2.2.22}$$

The use of the determinant in stress calculations, being dependent on deformation, is inconvenient. Hence, another stress measure called *Kirchhoff stress* is introduced as

$$\boldsymbol{\tau} = J\boldsymbol{\sigma} = \mathbf{F}\mathbf{S}\mathbf{F}^T. \tag{2.2.23}$$

Push-forward and pull-back operators. These operators are mathematical transformations to transform measures from Lagrangian to Eulerian descriptions (forward) and vice-versa (backwards). The *push-forward* operator, $\chi_*(\mathbf{A})$, transforms a tensor $\mathbf{A}$ defined in the reference configuration to the current configuration. The *pull-back* operator, $\chi_*^{-1}(\mathbf{A})$, maps tensors from the current configuration back to the reference configuration.

2.2.3 Hyperelastic materials

Constitutive relations describe the material behaviour, bridging the gap between kinematics and stresses. The deformation gradient $\mathbf{F}$ is the primary deformation measure used in *finite strain*

theory. Several models describe the elastic behaviour of solids in this context. One significant model is the *Cauchy-elastic material*, where the stress $\boldsymbol{\sigma}$ is a function of the deformation gradient $\mathbf{F}$ alone, that is,

$$\boldsymbol{\sigma} = \mathcal{G}\left(\mathbf{F}\right). \tag{2.2.24}$$

Hyperelastic or *Green-elastic* materials are conservative, ideally elastic materials, where the stress-strain relationship derives from a *strain energy density function* ψ. The computational modelling in this research primarily focuses on hyperelastic materials, assuming that the elastomers exhibit hyperelastic behaviour.

2.2.3.1 Compressible and nearly incompressible hyperelastics

Stress is derived from

$$\mathbf{S} = \frac{\partial \psi(\mathbf{E})}{\partial \mathbf{E}} = 2\,\frac{\partial \psi(\mathbf{C})}{\partial \mathbf{C}}. \tag{2.2.25}$$

Referring to the relations between $\mathbf{S}$, $\mathbf{P}$ and $\boldsymbol{\sigma}$ in Section 2.2.2, and also, relations between $\mathbf{E}$, $\mathbf{F}$ and $\mathbf{C}$ in Section 2.2.1.4, one can further derive

$$\mathbf{P} = \frac{\partial \psi}{\partial \mathbf{F}} = \mathbf{F}\,\frac{\partial \psi}{\partial \mathbf{E}} = 2\mathbf{F}\,\frac{\partial \psi}{\partial \mathbf{C}}\,, \tag{2.2.26a}$$

$$\mathbf{S} = \mathbf{F}^{-1}\,\frac{\partial \psi}{\partial \mathbf{F}} = \frac{\partial \psi}{\partial \mathbf{E}} = 2\,\frac{\partial \psi}{\partial \mathbf{C}}\,, \tag{2.2.26b}$$

and

$$\boldsymbol{\sigma} = J^{-1}\frac{\partial \psi}{\partial \mathbf{F}}\,\mathbf{F}^T = J^{-1}\,\mathbf{F}\,\frac{\partial \psi}{\partial \mathbf{E}}\,\mathbf{F}^T = 2\,J^{-1}\,\mathbf{F}\,\frac{\partial \psi}{\partial \mathbf{C}}\,\mathbf{F}^T. \tag{2.2.27}$$

Decomposition of isochoric and volumetric parts. Separating *volumetric* deformation from *isochoric* deformation enhances the numerical modelling efficiency of both compressible and nearly incompressible materials. The multiplicative decomposition of the deformation gradient is suggested as (Lubliner, 1985; Lee, 1969)

$$\mathbf{F} = J^{1/3}\,\widehat{\mathbf{F}} \Rightarrow \widehat{\mathbf{F}} = J^{-1/3}\,\mathbf{F}\,. \tag{2.2.28}$$

With $\det(\widehat{\mathbf{F}}) \equiv 1$, the volume of a body under pure $\widehat{\mathbf{F}}$ deformation is preserved. Hence, the isochoric part of the right and left Cauchy–Green deformation tensors are derived as

$$\widehat{\mathbf{C}} = \widehat{\mathbf{F}}^T\,\widehat{\mathbf{F}} = J^{-2/3}\,\mathbf{F}^T\,\mathbf{F} = J^{-2/3}\,\mathbf{C}\,, \tag{2.2.29a}$$

$$\widehat{\mathbf{b}} = \widehat{\mathbf{F}}\,\widehat{\mathbf{F}}^T = J^{-2/3}\,\mathbf{F}\,\mathbf{F}^T = J^{-2/3}\,\mathbf{b}\,. \tag{2.2.29b}$$

Upon decomposition of the deformation, strain energy function ψ for isotropic materials is decomposed into volumetric and isochoric parts represented by J and $\widehat{\mathbf{C}}$ by

$$\psi = \psi(\widehat{\mathbf{C}}, J) = \psi_{\text{iso}}(\widehat{\mathbf{C}}) + \psi_{\text{vol}}\left(J\right), \tag{2.2.30}$$

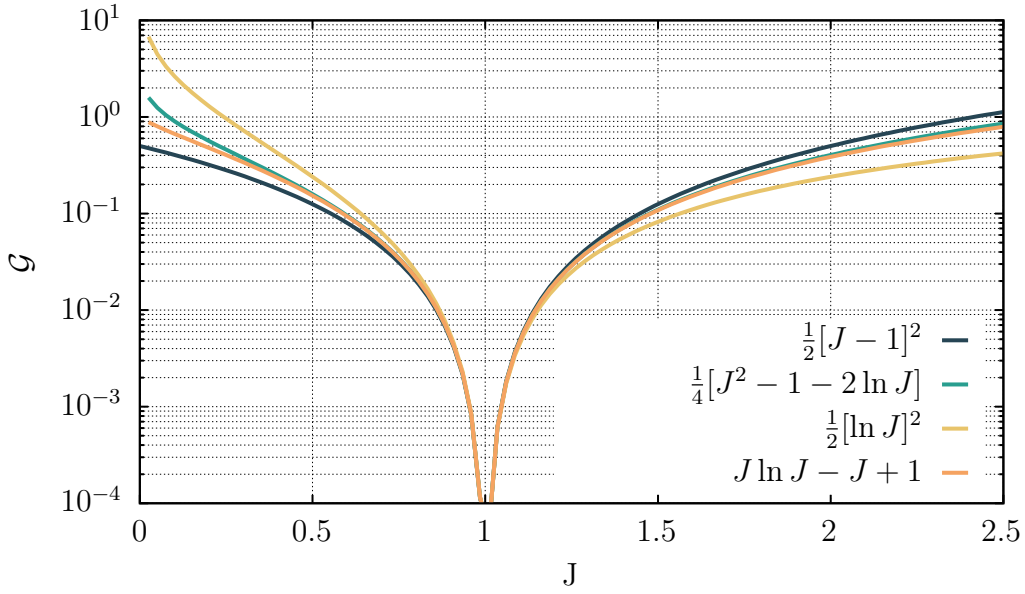

Figure 2.3: Variations of J with respect to different energy functions from Equations 2.2.32.

or based on J and $\widehat{\mathbf{b}}$ as

$$\psi = \psi(\widehat{\mathbf{b}}, J) = \psi_{\text{iso}}(\widehat{\mathbf{b}}) + \psi_{\text{vol}}(J)\,. \tag{2.2.31}$$

Denoting the first and the second *Lamé parameters* as λ and μ, the *bulk modulus*, $\kappa = \lambda + 2/3\,\mu$ is the sole material constant that appears in the volumetric part of the energy density function, i.e., $\psi_{\text{vol}}(J) = \kappa\,\mathcal{G}(J)$. The function $\mathcal{G}(J)$ must be strictly convex and fulfil the condition $\mathcal{G}(1) = 0$. Various formulations for $\mathcal{G}(J)$ have been proposed. Some examples are

$$\mathcal{G}(J) = \frac{1}{2}[J-1]^2\,, \tag{2.2.32a}$$

$$\mathcal{G}(J) = \frac{1}{4}\left[J^2 - 1 - 2\ln J\right], \tag{2.2.32b}$$

$$\mathcal{G}(J) = \frac{1}{2}[\ln J]^2\,, \tag{2.2.32c}$$

$$\mathcal{G}(J) = J\ln J - J + 1. \tag{2.2.32d}$$

These functional expressions are visualized in Figure 2.3, illustrating how each function approaches zero as $J \to 1$, suggesting similar performance of functions for incompressibility. For more discussion on these volumetric strain energy functions, interested readers are referred to (Doll and Schweizerhof, 2000; Hartmann and Neff, 2003). The decomposition of the strain energy function allows for the corresponding decomposition of stress tensors, as elaborated in Appendix A.1.

Isotropic hyaperelastics. The constitutive relation must be independent of the coordinate frame selected. Thus, the strain energy density is defined using the invariants of the strain

tensors, given by

$$\psi = \psi_C\left(\mathbf{C}\right) = \psi_{IC}\left(I_C, II_C, III_C\right) = \psi_{Ib}\left(I_b, II_b, III_b\right) = \psi_b\left(\mathbf{b}\right). \tag{2.2.33}$$

Function ψ can also be written as a function of $\mathbf{U}$ or $\mathbf{v}$, or their invariants, since $\mathbf{C} = \mathbf{U}^2$ and $\mathbf{b} = \mathbf{v}^2$, as discussed in 2.2.1.5. The invariants are calculated as

$$I_C = I_b = \mathrm{tr}\left(\mathbf{C}\right) = \lambda_1^2 + \lambda_2^2 + \lambda_3^2\,, \tag{2.2.34a}$$

$$II_C = II_b = \frac{1}{2}\left[\left[\mathrm{tr}\left(\mathbf{C}\right)\right]^2 + \mathrm{tr}\left(\mathbf{C}^2\right)\right] = \lambda_1^2\,\lambda_2^2 + \lambda_2^2\,\lambda_3^2 + \lambda_3^2\,\lambda_1^2\,, \tag{2.2.34b}$$

$$III_C = III_b = \det\left(\mathbf{C}\right) = \lambda_1^2\,\lambda_2^2\,\lambda_3^2 \;= J^2. \tag{2.2.34c}$$

Applying the chain rule, and using

$$\frac{\partial I_C}{\partial \mathbf{C}} = \mathbf{I}, \quad \frac{\partial II_C}{\partial \mathbf{C}} = I_C\,\mathbf{I} - \mathbf{C}, \quad \frac{\partial III_C}{\partial \mathbf{C}} = III_C\,\mathbf{C}^{-1}, \tag{2.2.35}$$

yields

$$\mathbf{S} = 2\,\frac{\partial \psi\left(\mathbf{C}\right)}{\partial \mathbf{C}} = 2\left[\left[\frac{\partial \psi}{\partial I_C} + I_C\,\frac{\partial \psi}{\partial II_C}\right]\mathbf{I} - \frac{\partial \psi}{\partial II_C}\,\mathbf{C} + III_C\;\frac{\partial \psi}{\partial III_C}\,\mathbf{C}^{-1}\right]. \tag{2.2.36}$$

Furthermore, the Cauchy stress tensor is derived as

$$\boldsymbol{\sigma} = 2\,J^{-1}\left[III_b\,\frac{\partial \psi}{\partial III_b}\,\mathbf{I} + \left[\frac{\partial \psi}{\partial I_b} + I_b\,\frac{\partial \psi}{\partial II_b}\right]\mathbf{b} - \frac{\partial \psi}{\partial II_b}\,\mathbf{b}^2\right] \tag{2.2.37a}$$

$$= 2\,J^{-1}\left[\left[II_b\,\frac{\partial \psi}{\partial II_b} + III_b\,\frac{\partial \psi}{\partial III_b}\right]\mathbf{I} + \frac{\partial \psi}{\partial I_b}\,\mathbf{b} - III_b\,\frac{\partial \psi}{\partial II_b}\,\mathbf{b}^{-1}\right]. \tag{2.2.37b}$$

The strain-energy function described by

$$\psi = \psi_{\mathrm{iso}}(I_{\widehat{C}}\,, II_{\widehat{C}}) + \psi_{\mathrm{vol}}(J), \tag{2.2.38}$$

can be useful for modelling compressible and nearly incompressible hyperelastic materials. The modified invariants are calculated by

$$I_{\widehat{C}} = I_{\widehat{b}} = \mathrm{tr}\left(\widehat{\mathbf{C}}\right) = \mathrm{tr}\left(\widehat{\mathbf{b}}\right), \tag{2.2.39a}$$

$$II_{\widehat{C}} = II_{\widehat{b}} = \frac{1}{2}\left[\left[\mathrm{tr}\left(\widehat{\mathbf{C}}\right)\right]^2 + \mathrm{tr}\left(\widehat{\mathbf{C}}^2\right)\right] = \frac{1}{2}\left[\left[\mathrm{tr}\left(\widehat{\mathbf{b}}\right)\right]^2 + \mathrm{tr}\left(\widehat{\mathbf{b}}^2\right)\right], \tag{2.2.39b}$$

$$III_{\widehat{C}} = III_{\widehat{b}} = \det\left(\widehat{\mathbf{C}}\right) = \det\left(\widehat{\mathbf{b}}\right) = 1\,. \tag{2.2.39c}$$

It can be shown that

$$I_{\widehat{C}} = J^{-2/3}\,I_C, \quad II_{\widehat{C}} = J^{-4/3}\,II_C\,. \tag{2.2.40}$$

2.2.3.2 Incompressible hyperelastics

Certain hyperelastic materials, preserve their volume during deformation, i.e., $J = 1$, making them favourable in various applications. For these incompressible materials, the Piola stress tensor can be expressed as

$$\mathbf{P} = \frac{\partial \psi(\mathbf{F})}{\partial \mathbf{F}} - p\mathbf{F}^{-T}\,, \tag{2.2.41}$$

and the Piola–Kirchhoff, $\mathbf{S}$ as

$$\mathbf{S} = 2\,\frac{\partial \psi(\mathbf{C})}{\partial \mathbf{C}} - p\mathbf{C}^{-1}\,, \tag{2.2.42}$$

where p can be identified as hydrostatic pressure. Numerically, a constraint, $J = 1$, must be imposed, which can lead to over stiffening of elements, which will be discussed in Section 2.4.

2.2.3.3 Hyperelastic models

Various hyperelastic models with different energy density functions are designed to characterize the elastic behaviour of different materials. For isotropic hyperelastic materials, several energy density functions can be expressed as functions of the invariants of $\mathbf{C}$ (Rivlin and Saunders, 1951):

$$\psi\left(I_C, II_C, III_C\right) = \sum_{m+n=1}^{\infty} \left[A_{mn}\left[I_C - 3\right]^m \left[II_C - 3\right]^n\right] + g(III_c). \tag{2.2.43}$$

Although infinite energy functions with innumerable parameters can be derived from the above equation, practical models are usually limited to a few parameters for convenience and experimental measurement. Among these, an overview of several popular models is provided below.

neo-Hookean.

$$\psi\left(I_C, III_C\right) = A_{10}\left[I_C - 3\right] + g(III_C). \tag{2.2.44}$$

To align with linear elastic behaviour in infinitesimal deformations, $A_{10} = \mu/2$.

Mooney–Rivlin.

$$\psi\left(I_C, II_C\right) = A_{10}\left[I_C - 3\right] + A_{01}\left[II_C - 3\right] + g(III_C). \tag{2.2.45}$$

To align with linear elasticity, the shear modulus is given by $\mu = 2\left[A_{10} + A_{01}\right]$, and setting $A_{01} = 0$ reduces this model to the neo-Hookean form as a special case.

Yeoh.

$$\psi\left(I_C\right) = A_{10}\left[I_C - 3\right] + A_{20}\left[I_C - 3\right]^2 + A_{30}\left[I_C - 3\right]^3. \tag{2.2.46}$$

Here, to align with linear elasticity, the shear modulus is given by $\mu = 2A_{10}$, and the higher order terms account for the nonlinear elasticity of the material.

Ogden.

$$\psi\left(\lambda_1, \lambda_2, \lambda_3\right) = \sum_{p=1}^{N} \frac{\mu_p}{\alpha_p} \left[\lambda_1^{\alpha_p} + \lambda_2^{\alpha_p} + \lambda_3^{\alpha_p} - 3\right]. \tag{2.2.47}$$

Here, μ is adjusted to $\mu = \frac{1}{2}\sum_{p=1}^{N} \alpha_p \mu_p$, for infinitesimal deformations compatibility. This model is based on stretch invariants rather than the full set of invariants of $\mathbf{C}$, distinguishing it from other models.

Remark. In the case of incompressibility, the principal stretches are not independent, that is, $\lambda_1\lambda_2\lambda_3 = 1$. Thus, $\lambda_3^{\alpha_p}$ can be substituted with $\lambda_1^{-\alpha_p}\lambda_2^{-\alpha_p}$ in the Ogden model. □

Modifications of the basic models improve computational efficiency for numerical modelling by incorporating the modified invariants of $\widehat{\mathbf{C}}$. For instance, the neo-Hookean model can be modified as

$$\psi(I_{\widehat{C}}, J) = A_{10}\left[I_{\widehat{C}} - 3\right] + \psi_{\text{vol}}(J)\,, \tag{2.2.48}$$

or the Mooney–Rivlin model as

$$\psi(I_{\widehat{C}}, II_{\widehat{C}}, J) = A_{10}\left[I_{\widehat{C}} - 3\right] + A_{01}\left[II_{\widehat{C}} - 3\right] + \psi_{\text{vol}}(J)\,. \tag{2.2.49}$$

These modifications aid the finite element implementation of the decoupled free energy function. This approach is followed in this research.

2.3 Variational formulation

Variational principles are used to derive the weak form of the governing equations, transforming them into an integral form. This is essential for FEM, as it allows for the handling of complex boundaries and geometries.

2.3.1 Strong form

Consider a boundary value problem where the body is subject to a traction $\overline{\mathbf{T}}$ on the Neumann boundary and a body force $\overline{\mathbf{B}}$ in the reference configuration. The whole boundary Γ_X is decomposed into Dirichlet Γ_X^u and Neumann Γ_X^t parts such that $\Gamma_X = \Gamma_X^u \cup \Gamma_X^t$ and $\Gamma_X^u \cap \Gamma_X^t = \emptyset$. The corresponding boundaries in the current configuration are denoted as Γ_x, Γ_x^u, and Γ_x^t. The aim is to find a displacement that satisfies

	Lagrangian description		Eulerian description	
Balance of the linear momentum:	$\boldsymbol{\nabla}_X \cdot \mathbf{P} + \overline{\mathbf{B}} = \mathbf{0},$	in Ω_X ;	$\boldsymbol{\nabla}_x \cdot \boldsymbol{\sigma} + \overline{\mathbf{b}} = \mathbf{0},$	in Ω_x .
Essential boundary conditions:	$\mathbf{u} = \overline{\mathbf{u}},$	on Γ_X^u ;	$\mathbf{u} = \overline{\mathbf{u}},$	on Γ_x^u .
Natural boundary conditions:	$\mathbf{P}\,\mathbf{N} = \overline{\mathbf{T}},$	on Γ_X^t ;	$\boldsymbol{\sigma}\,\mathbf{n} = \overline{\mathbf{t}},$	on Γ_x^t .

which is often called the *strong form*.

2.3.2 Weak form

By taking a scalar product with an arbitrary vector-valued function $\boldsymbol{\eta}$ (that is $\boldsymbol{\eta} = \mathbf{0}$ on Γ_x^u) on both sides of the Eulerian equilibrium equation from Section 2.3.1 and integrating over the domain,

$$\int_{\Omega_x} \boldsymbol{\eta} \cdot \left[\boldsymbol{\nabla}_x \cdot \boldsymbol{\sigma}\left(\mathbf{u}\right) + \overline{\mathbf{b}} \right] \mathrm{d}v = 0\,. \tag{2.3.1}$$

Application of *divergence theorem* yields

$$\begin{aligned} \int_{\Omega_x} \boldsymbol{\eta} \cdot \left[\boldsymbol{\nabla}_x \cdot \boldsymbol{\sigma} + \overline{\mathbf{b}} \right] \mathrm{d}v &= -\int_{\Omega_x} \boldsymbol{\nabla}_x \boldsymbol{\eta} : \boldsymbol{\sigma}\, \mathrm{d}v + \int_{\Gamma_x^u \cup \Gamma_x^t} \boldsymbol{\eta} \cdot \boldsymbol{\sigma}\, \mathbf{n}\, \mathrm{d}a + \int_{\Omega_x} \boldsymbol{\eta} \cdot \overline{\mathbf{b}}\, \mathrm{d}v \\ &= -\int_{\Omega_x} \boldsymbol{\nabla}_x \boldsymbol{\eta} : \boldsymbol{\sigma}\, \mathrm{d}v + \int_{\Gamma_x^t} \boldsymbol{\eta} \cdot \overline{\mathbf{t}}\, \mathrm{d}a + \int_{\Omega_x} \boldsymbol{\eta} \cdot \overline{\mathbf{b}}\, \mathrm{d}v = 0. \end{aligned} \tag{2.3.2}$$

Since $\boldsymbol{\eta}$ is arbitrary, it can be viewed as the virtual displacement, denoted by $\delta\mathbf{u}$; thus

$$\int_{\Omega_x} \boldsymbol{\nabla}_x\, \delta\mathbf{u} : \boldsymbol{\sigma}\, \mathrm{d}v - \int_{\Gamma_x^t} \delta\mathbf{u} \cdot \overline{\mathbf{t}}\, \mathrm{d}a - \int_{\Omega_x} \delta\mathbf{u} \cdot \overline{\mathbf{b}}\, \mathrm{d}v = 0. \tag{2.3.3}$$

Similarly, for the Lagrangian description,

$$\int_{\Omega_X} \boldsymbol{\nabla}_X\, \delta\mathbf{u} : \mathbf{P}\, \mathrm{d}V - \int_{\Gamma_X^t} \delta\mathbf{u} \cdot \overline{\mathbf{T}}\, \mathrm{d}A - \int_{\Omega_X} \delta\mathbf{u} \cdot \overline{\mathbf{B}}\, \mathrm{d}V = 0. \tag{2.3.4}$$

These two last equations are known as the *weak form* of the partial differential equation in mathematics. Note that both Eulerian and Lagrangian descriptions of the weak form are equivalent.

Principle of minimum potential energy. The system will be in equilibrium when its potential energy is minimal, aligning internal forces generated during deformation with stored energy,

$$\Pi = \Pi^{\mathrm{int}} + \Pi^{\mathrm{ext}}, \tag{2.3.5}$$

ensuring $\delta\Pi = 0$, where δ denotes the variation. Representing the set of unknowns as $\mathbf{Q}$, one can write

$$\delta\Pi\left(\mathbf{Q}; \delta\mathbf{Q}\right) = \delta\Pi^{\mathrm{int}}\left(\mathbf{Q}; \delta\mathbf{Q}\right) + \delta\Pi^{\mathrm{ext}}\left(\delta\mathbf{Q}\right) = 0. \tag{2.3.6}$$

Principle of virtual work. Applying a virtual displacement field $\delta\mathbf{u}$ results in an external virtual work that causes virtual deformation, which is stored as virtual strain energy in the system. Representing internal stored energy and external virtual work by δW_{int} and δW_{ext}, internal stored energy and external virtual work are equated as

$$\delta W_{\mathrm{int}} = \delta W_{\mathrm{ext}}\,. \tag{2.3.7}$$

Variational principles with only one field of the unknown is called *single-field variational*

principles in which displacement vector $\boldsymbol{u}$ is the only unknown field. For the single-field variational principles, δW_{int} and δW_{ext} for Eulerian description are expressed as

$$\delta W_{\text{int}}\left(\mathbf{u};\delta\mathbf{u}\right)=\int_{\Omega_x}\boldsymbol{\nabla}_x\,\delta\mathbf{u}:\boldsymbol{\sigma}\,\mathrm{d}v\,, \tag{2.3.8}$$

$$\delta W_{\text{ext}}\left(\delta\mathbf{u}\right)=\int_{\Gamma_x^t}\delta\mathbf{u}\cdot\overline{\mathbf{t}}\,\mathrm{d}a+\int_{\Omega_x}\delta\mathbf{u}\cdot\overline{\mathbf{b}}\,\mathrm{d}v\,. \tag{2.3.9}$$

Remarks. The principles of virtual work and minimum potential energy are proved to be equal for single-field variation. For instance, stating the stored strain energy as

$$\Pi^{\text{int}}=\int_{\Omega_X}\psi\left(\mathbf{F}\right)\mathrm{d}V, \tag{2.3.10}$$

and the external potential energy generated as

$$\Pi^{\text{ext}}=-\int_{\Gamma_X^t}\mathbf{u}\cdot\overline{\mathbf{T}}\,\mathrm{d}A-\int_{\Omega_X}\mathbf{u}\cdot\overline{\mathbf{B}}\,\mathrm{d}V\,, \tag{2.3.11}$$

which is the negative value of the work done by the applied load, one can express

$$\delta\Pi^{\text{int}}\left(\mathbf{u};\delta\mathbf{u}\right)=\delta W_{\text{int}}\left(\mathbf{u};\delta\mathbf{u}\right)=\int_{\Omega_X}\boldsymbol{\nabla}_X\,\delta\mathbf{u}:\mathbf{P}\,\mathrm{d}V, \tag{2.3.12a}$$

$$\delta\Pi^{\text{ext}}\left(\delta\mathbf{u}\right)=-\delta W_{\text{ext}}\left(\delta\mathbf{u}\right)=-\int_{\Gamma_X^t}\delta\mathbf{u}\cdot\overline{\mathbf{T}}\,\mathrm{d}A-\int_{\Omega_X}\delta\mathbf{u}\cdot\overline{\mathbf{B}}\,\mathrm{d}V, \tag{2.3.12b}$$

for Lagrangian description. In engineering contexts, the principle of virtual work and minimum potential energy are synonymous with the weak form. □

2.3.3 Different representations of the internal virtual work

The internal virtual work, denoted as $\mathcal{L}$, is represented by

$$\mathcal{L}:=\delta\Pi^{\text{int}}\left(\mathbf{u};\delta\mathbf{u}\right)=\int_{\Omega_x}\boldsymbol{\nabla}_x\,\delta\mathbf{u}:\boldsymbol{\sigma}\,\mathrm{d}v. \tag{2.3.13}$$

The variation of Green–Lagrange strain tensor $\mathbf{E}$ is given by

$$\delta\mathbf{E}=\frac{1}{2}\left[\left(\mathbf{F}^T\,\boldsymbol{\nabla}_X\delta\mathbf{u}\right)^T+\mathbf{F}^T\,\boldsymbol{\nabla}_X\delta\mathbf{u}\right]=\operatorname{sym}\left(\mathbf{F}^T\,\boldsymbol{\nabla}_X\delta\mathbf{u}\right). \tag{2.3.14}$$

Similarly for Eulerian strain tensor $\mathbf{e}$, one can derive $\delta\mathbf{e}=\operatorname{sym}\left(\boldsymbol{\nabla}_x\,\delta\mathbf{u}\right)$. Considering the symmetry of $\boldsymbol{\sigma}$, $\mathcal{L}$ can be expressed by

$$\mathcal{L}=\int_{\Omega_x}\boldsymbol{\nabla}_x\,\delta\mathbf{u}:\boldsymbol{\sigma}\,\mathrm{d}v=\int_{\Omega_x}\delta\mathbf{e}:\boldsymbol{\sigma}\,\mathrm{d}v. \tag{2.3.15}$$

Recalling $\boldsymbol{\tau} = J\,\boldsymbol{\sigma}$ and $\mathrm{d}v = J\,\mathrm{d}V$, one obtains

$$\mathcal{L} = \int_{\Omega_x} \boldsymbol{\nabla}_x\,\delta\mathbf{u} : \left[J^{-1}\,\boldsymbol{\tau}\right]\mathrm{d}v = \int_{\Omega_X} \boldsymbol{\nabla}_x\,\delta\mathbf{u} : \boldsymbol{\tau}\,\mathrm{d}V. \tag{2.3.16}$$

Given that $\mathbf{P}$ is not symmetric, by using $\mathbf{P} = \mathbf{FS} = \mathbf{SF}^T$, the internal virtual work in the Lagrangian description is expressed by

$$\mathcal{L} = \int_{\Omega_X} \boldsymbol{\nabla}_X\,\delta\mathbf{u} : \mathbf{P}\,\mathrm{d}V = \int_{\Omega_X} \delta\mathbf{E} : \mathbf{S}\,\mathrm{d}V. \tag{2.3.17}$$

Recalling $\mathbf{E} = 1/2\,[\mathbf{C} - \mathbf{I}]$ results in

$$\mathcal{L} = \int_{\Omega_X} \delta\mathbf{E} \colon \mathbf{S}\,\mathrm{d}V = \int_{\Omega_X} \frac{1}{2}\,\delta\mathbf{C} : \mathbf{S}\,\mathrm{d}V. \tag{2.3.18}$$

In summary, $\mathcal{L}$ across different formulations can be expressed as

$$\begin{aligned}\mathcal{L} &= \underbrace{\int_{\Omega_X} \boldsymbol{\nabla}_X\,\delta\mathbf{u} : \mathbf{P}\,\mathrm{d}V = \int_{\Omega_X} \delta\mathbf{E} : \mathbf{S}\,\mathrm{d}V = \int_{\Omega_X} \boldsymbol{\nabla}_x\,\delta\mathbf{u} : \boldsymbol{\tau}\,\mathrm{d}V}_{\text{Total Lagrangian}} \\ &= \underbrace{\int_{\Omega_x} \boldsymbol{\nabla}_x\,\delta\mathbf{u} : \boldsymbol{\sigma}\,\mathrm{d}v = \int_{\Omega_x} \delta\mathbf{e} : \boldsymbol{\sigma}\,\mathrm{d}v}_{\text{Updated Lagrangian}}.\end{aligned} \tag{2.3.19}$$

2.3.3.1 Linearization of $\mathcal{L}$

The $\mathcal{L}$ is linearized around a state of finite deformation assuming dead loads. Denoting the linearized form of an expression by Δ, the directional derivative is used so that

$$\Delta\mathcal{L} = \frac{\mathrm{d}}{\mathrm{d}h}\,\mathcal{L}\left(\mathbf{u} + h\,\Delta\mathbf{u}\right)\Big|_{h=0}. \tag{2.3.20}$$

Starting with total Lagrangian formulation, $\mathcal{L} = \int_{\Omega_X} \delta\mathbf{E} : \mathbf{S}\,\mathrm{d}V$, one can express

$$\Delta\mathcal{L} = \frac{\mathrm{d}}{\mathrm{d}h}\left[\int_{\Omega_X} \delta\mathbf{E}\left(\mathbf{u} + h\,\Delta\mathbf{u}\right) : \mathbf{S}\left(\mathbf{E}\left(\mathbf{u} + h\,\Delta\mathbf{u}\right)\right)\mathrm{d}V\right]\Big|_{h=0}. \tag{2.3.21}$$

By interchanging differentiation, integration and using the product rule, one can get

$$\Delta\mathcal{L} = \int_{\Omega_X} \left[\delta\mathbf{E} : \Delta\mathbf{S} + \mathbf{S} : \Delta\delta\mathbf{E}\right]\mathrm{d}V. \tag{2.3.22}$$

Using chain rule, for any compressible hyperelastic model, $\mathbf{S} = \frac{\partial\psi}{\partial\mathbf{E}}$, one can write

$$\Delta\mathbf{S} = \frac{\partial\mathbf{S}}{\partial\mathbf{E}} : \Delta\mathbf{E} = \frac{\partial^2\psi}{\partial\mathbf{E}\,\partial\mathbf{E}} : \Delta\mathbf{E}. \tag{2.3.23}$$

Defining incremental constitutive tensor as $\mathbb{C} = \frac{\partial^2 \psi}{\partial \mathbf{E} \, \partial \mathbf{E}}$, one can write

$$\Delta \mathbf{S} = \mathbb{C} : \Delta \mathbf{E} \,, \tag{2.3.24}$$

which is analogous to $\boldsymbol{\sigma} = \mathbb{C} : \boldsymbol{\varepsilon}$ in infinitesimal deformations. Therefore, Equation (2.3.22) becomes

$$\Delta \mathcal{L} = \int_{\Omega_X} \left[\delta \mathbf{E} : \mathbb{C} : \Delta \mathbf{E} + \mathbf{S} : \Delta \delta \mathbf{E} \right] \mathrm{d}V. \tag{2.3.25}$$

Using $\Delta \mathbf{E} = \operatorname{sym}\left(\mathbf{F}^T \left[\boldsymbol{\nabla}_X \, \Delta \mathbf{u} \right] \right)$ and $\Delta \delta \mathbf{E} = \operatorname{sym}\left(\left[\boldsymbol{\nabla}_X \, \delta \mathbf{u} \right]^T \boldsymbol{\nabla}_X \, \Delta \mathbf{u} \right)$, and also the fact that $\mathbf{S}$ is symmetric and $\mathbb{C}$ has minor symmetry, one can write

$$\Delta \mathcal{L} = \int_{\Omega_X} \left[\mathbf{F}^T \left[\boldsymbol{\nabla}_X \, \delta \mathbf{u} \right] : \mathbb{C} : \mathbf{F}^T \left[\boldsymbol{\nabla}_X \, \Delta \mathbf{u} \right] + \left[\boldsymbol{\nabla}_X \, \delta \mathbf{u} : \boldsymbol{\nabla}_X \, \Delta \mathbf{u} \right] \, \mathbf{S} \right] \mathrm{d}V. \tag{2.3.26}$$

Using $\left[\boldsymbol{\nabla}_x \, \delta \mathbf{u} \right] \mathbf{F} = \boldsymbol{\nabla}_X \, \delta \mathbf{u}$ and $\mathbb{c} = J^{-1} \, \chi_* \left(\mathbb{C} \right)$ in above, for $\mathcal{L} = \int_{\Omega_X} \boldsymbol{\nabla}_x \delta \mathbf{u} : \boldsymbol{\tau} \, \mathrm{d}V$, yields

$$\Delta \mathcal{L} = \int_{\Omega_X} \left[\boldsymbol{\nabla}_x \, \delta \mathbf{u} : J \, \mathbb{c} : \boldsymbol{\nabla}_x \, \Delta \mathbf{u} + \left[\boldsymbol{\nabla}_x \, \delta \mathbf{u} : \boldsymbol{\nabla}_x \, \Delta \mathbf{u} \right] \, \boldsymbol{\tau} \right] \mathrm{d}V. \tag{2.3.27}$$

Furthermore, one can simply derive the linearised form of $\mathcal{L} = \int_{\Omega_x} \delta \mathbf{e} : \boldsymbol{\sigma} \, \mathrm{d}v$ as

$$\Delta \mathcal{L} = \int_{\Omega_x} \left[\boldsymbol{\nabla}_x \, \delta \mathbf{u} : \mathbb{c} : \boldsymbol{\nabla}_x \, \Delta \mathbf{u} + \left[\boldsymbol{\nabla}_x \, \delta \mathbf{u} : \boldsymbol{\nabla}_x \, \Delta \mathbf{u} \right] \boldsymbol{\sigma} \right] \mathrm{d}v. \tag{2.3.28}$$

Three different forms of linearization of $\mathcal{L}$, stated by equations (2.3.26), (2.3.27) and (2.3.28) are derived, that each can be used in FEM.

Remark. Eulerian description of the elasticity tensor is related to its Lagrangian form by

$$\mathbb{c} = J^{-1} \, \chi_* \left(\mathbb{C} \right), \qquad c_{ijkl} = J^{-1} \, F_{iI} \, F_{jJ} \, F_{kK} \, F_{lL} \, C_{IJKL} \,. \quad \square \tag{2.3.29}$$

Decomposition of the incremental constitutive tensor into volumetric and isochoric contributions is also advantageous for numerical implementations. Refer to Appendix A.2 for details.

2.4 Finite element approximation

This section presents the discretisation of the variational formulation derived in the previous section using the FEM. The presentation covers both the classical single-field and the three-field mixed FE formulations. The three-field mixed formulation is especially effective for addressing challenges related to locking associated with incompressibility (Hu, 1984; Simo and Hughes, 1986; Betsch et al., 1996).

2.4.1 Infinitesimal deformations

Although the focus of this thesis is not on infinitesimal deformations, a brief overview is provided for completeness, including the implementation of the corresponding FE code.

In the infinitesimal deformations regime, there is no distinction between the initial and current configuration. Using the linearity of the gradient operator

$$\boldsymbol{\nabla}\left(\delta\mathbf{u}\right) = \delta\left(\boldsymbol{\nabla}\mathbf{u}\right) = \delta\boldsymbol{\varepsilon}\,, \tag{2.4.1}$$

the weak form for infinitesimal deformation theory is

$$\int_{\Omega} \delta\boldsymbol{\varepsilon} : \boldsymbol{\sigma}\,\mathrm{d}V = \int_{\Omega} \delta\boldsymbol{u}\cdot\overline{\mathbf{b}}\,\mathrm{d}V + \int_{\Gamma_X^t} \delta\boldsymbol{u}\cdot\overline{\mathbf{t}}\,\mathrm{d}A\,. \tag{2.4.2}$$

The constitutive equation, derived from the strain energy function for infinitesimal deformations, is

$$\psi\left(\boldsymbol{\varepsilon}\right) = \frac{1}{2}\,\boldsymbol{\varepsilon} : \mathbb{C} : \boldsymbol{\varepsilon} \Rightarrow \boldsymbol{\sigma} = \frac{\partial\psi}{\partial\boldsymbol{\varepsilon}} = \mathbb{C} : \boldsymbol{\varepsilon}\,, \tag{2.4.3}$$

with the strain-displacement relationship $\boldsymbol{\varepsilon} = \frac{1}{2}[\boldsymbol{\nabla}\mathbf{u} + (\boldsymbol{\nabla}\mathbf{u})^T]$. Hence, the weak form can be expressed as

$$\int_{\Omega} \delta\boldsymbol{\varepsilon} : \mathbb{C} : \boldsymbol{\varepsilon}\,\mathrm{d}V - \int_{\Omega} \delta\boldsymbol{u}\cdot\overline{\mathbf{b}}\,\mathrm{d}V - \int_{\Gamma_X^t} \delta\boldsymbol{u}\cdot\overline{\mathbf{t}}\,\mathrm{d}A = 0, \quad \forall\delta\boldsymbol{u} \text{ with } \delta\boldsymbol{u}\left(\Gamma_X^u\right) = \mathbf{0}\,. \tag{2.4.4}$$

Since $\mathbb{C}_{ijkl} = \mathbb{C}_{ijlk}$ has minor symmetry, one can write $\mathbb{C} : \varepsilon = \mathbb{C} : \boldsymbol{\nabla}\mathbf{u}$.

Defining the nodal variables associated with the various components of the displacement field as u^I, and introducing global vector-valued displacement shape functions $\mathbf{N}^{I,u}$, the approximations of the displacement and the associated test function using a Bubnov–Galerkin approach follow as

$$\mathbf{u} = \sum_{I=1}^{n_{\mathrm{dof}}} \mathbf{N}^{I,u}\,u^I, \quad \delta\mathbf{u} = \sum_{I=1}^{n_{\mathrm{dof}}} \mathbf{N}^{I,u}\,\delta u^I, \tag{2.4.5}$$

where n_{dof} denotes the global number of degrees of freedom. Using the arbitrariness of the test functions, the tangent stiffness matrix $\mathbf{K}$, and the right-hand side vector $\mathbf{R}$, that form the linear system of equations $\mathbf{K}\mathbf{u} = \mathbf{R}$, are obtained respectively as

$$K^{IJ} = \int_{\Omega} \boldsymbol{\nabla}\mathbf{N}^{I,u} : \mathbb{C} : \boldsymbol{\nabla}\mathbf{N}^{J,u}\,\mathrm{d}V, \tag{2.4.6a}$$

$$R^I = \int_{\Omega} \mathbf{N}^{I,u}\cdot\overline{\mathbf{b}}\,\mathrm{d}V + \int_{\Gamma_X^t} \mathbf{N}^{I,u}\cdot\overline{\mathbf{t}}\,\mathrm{d}A. \tag{2.4.6b}$$

For isotropic materials, the stiffness tensor $\mathbb{C}$ can be expressed in terms of the Lamé parameters as

$$\mathbb{C} = \lambda\,\mathbf{I}\otimes\mathbf{I} + 2\mu\,\mathbb{I}. \tag{2.4.7}$$

2.4.2 Finite deformations

In finite deformations, either the total Lagrangian approach, integrating over the reference volume V, or the updated Lagrangian approach, integrating over the current volume v, are utilised. In the following, the single-field formulation uses Equation (2.3.26), and the three-field formulation uses Equation (2.3.27) as the basis for the linearization of the internal virtual work $\mathcal{L}$.

2.4.2.1 Single-field formulation

In this classical approach, the displacement $\mathbf{u}$ is the sole primary variable. Consider a spatial discretisation of the domain into non-overlapping elements. The nodal variables associated with the displacement are interpolated using displacement global vector-valued shape functions $\mathbf{N}^{I,u}$. The fields across the domain are approximated as

$$\mathbf{u} = \sum_{I=1}^{n_{\text{dof}}} \mathbf{N}^{I,u}\, u^I, \quad \delta\mathbf{u} = \sum_{I=1}^{n_{\text{dof}}} \mathbf{N}^{I,u}\, \delta u^I, \quad \Delta\mathbf{u} = \sum_{I=1}^{n_{\text{dof}}} \mathbf{N}^{I,u}\, \Delta u^I, \tag{2.4.8}$$

where n_{dof} is the number of global degrees of freedom.

Approximating the function $\delta\Pi$ using a first-order Taylor expansion gives

$$\delta\Pi\left(\mathbf{u}^{t+1}; \delta\mathbf{u}\right) \approx \delta\Pi\left(\mathbf{u}^{t}; \delta\mathbf{u}\right) + \Delta\delta\Pi\left(\mathbf{u}^{t}; \delta\mathbf{u}, \Delta\mathbf{u}\right) = 0\,, \tag{2.4.9}$$

where $\mathbf{u}^{t+1} = \mathbf{u}^t + \Delta\mathbf{u}$ where the superscript t denotes the load step number. This equation is solved iteratively within each load step using a Newton–Raphson scheme. The second term is approximated by Equation (2.3.26), that is

$$\Delta\,\delta\Pi\left(\mathbf{u}; \delta\mathbf{u}, \Delta\mathbf{u}\right) = \int_{\Omega_X} \left[\mathbf{F}^T\left[\boldsymbol{\nabla}_X\,\delta\mathbf{u}\right] : \mathbb{C} : \mathbf{F}^T\left[\boldsymbol{\nabla}_X\,\Delta\mathbf{u}\right] + \left[\boldsymbol{\nabla}_X\delta\mathbf{u} : \boldsymbol{\nabla}_X\,\Delta\mathbf{u}\right]\mathbf{S}\right] \mathrm{d}V. \tag{2.4.10}$$

Using the arbitrariness of the test functions, the tangent stiffness matrix $\mathbf{K}$, and the right-hand side vector $\mathbf{R}$, that form the linear system of equations $\mathbf{K}\,\Delta\mathbf{u} = \mathbf{R}$, are obtained respectively as

$$K^{IJ} = \int_{\Omega_X} \mathbf{F}^T\left[\boldsymbol{\nabla}_X\,\mathbf{N}^{I,u}\right] : \mathbb{C} : \mathbf{F}^T\left[\boldsymbol{\nabla}_X\,\mathbf{N}^{J,u}\right] \mathrm{d}V + \int_{\Omega_X} \left[\boldsymbol{\nabla}_X\,\mathbf{N}^{I,u} : \boldsymbol{\nabla}_X\,\mathbf{N}^{J,u}\right]\mathbf{S}\,\mathrm{d}V, \tag{2.4.11a}$$

$$R^I = -\int_{\Omega_X} \mathbf{S} : \boldsymbol{\nabla}_X\,\mathbf{N}^{I,u}\,\mathrm{d}V + \int_{\Omega_X} \mathbf{N}^{I,u}\cdot\overline{\mathbf{B}}\,\mathrm{d}V + \int_{\Gamma^t_X} \mathbf{N}^{I,u}\cdot\overline{\mathbf{T}}\,\mathrm{d}A\,. \tag{2.4.11b}$$

2.4.2.2 Three-field mixed-formulation

For hyperelastic materials that almost preserve their volume during deformation, single-field finite element formulations often suffer from *volumetric locking*, leading to sub-optimal performance, especially in highly distorted elements (Sussman and Bathe, 1987; Wriggers, 2008).

To address locking-related issues, various solutions have been developed, including the F-bar method, enhanced assumed strain (EAS), selective reduced integration (SRI), mixed formulations and stabilization techniques (Franca et al., 1988; Maniatty et al., 2002; Reese, 2002; Sze et al., 2004; Ye et al., 2020). Among these, mixed formulations that incorporate additional primary fields such as stress or strain fields, alongside displacement, have gained widespread adoption (Simo and Armero, 1992; Weiss et al., 1996; Wriggers, 2008; Shojaei and Yavari, 2018).

Mixed formulations. These approaches improve the numerical stability of simulations by addressing incompressibility more effectively than single-field formulations. The two-field mixed formulation typically uses displacement and pressure fields as primary variables. A known issue with constant pressure interpolation in two-field variational principles is the resulting pressure oscillation. To avoid this, the three-field formulations incorporating an additional variable are introduced (Simo and Rifai, 1990; Farhat et al., 1995; Hughes, 2012).

Three-field formulations. The three-field formulation introduces the independent pressure $\widetilde{p}$ and strain variable $\widetilde{J}$ in addition to the displacement $\mathbf{u}$, expanding the set of unknowns to $\mathbf{Q} = \{\mathbf{u}, \widetilde{p}, \widetilde{J}\}$. Hence, the constraint $\widetilde{J} \to J(\mathbf{u})$ has to be fulfilled and the independent pressure follows as $\widetilde{p} \to \partial\psi_{\text{vol}}(\widetilde{J})/\partial\widetilde{J}$. The Hu–Washizu variational principle modifies the strain energy function as (Washizu, 1968)

$$\overline{\psi} = \psi_{\text{iso}}(\widehat{\mathbf{C}}(\mathbf{u})) + \psi_{\text{vol}}(\widetilde{J}) + \widetilde{p}\left[J(\mathbf{u}) - \widetilde{J}\right]. \tag{2.4.12}$$

The total potential energy for the three-field method can be expressed by

$$\Pi(\mathbf{Q}) = \Pi^{\text{int}}(\mathbf{Q}) + \Pi^{\text{ext}}(\mathbf{Q}), \tag{2.4.13}$$

where

$$\Pi^{\text{int}}(\mathbf{Q}) = \int_{\Omega_X} \overline{\psi}\,\mathrm{d}V = \int_{\Omega_X} \left[\psi_{\text{iso}} + \psi_{\text{vol}} + \widetilde{p}\left[J - \widetilde{J}\right]\right]\mathrm{d}V, \tag{2.4.14a}$$

$$\Pi^{\text{ext}}(\mathbf{Q}) = -\int_{\Omega_X} \mathbf{u}\cdot\overline{\mathbf{B}}\,\mathrm{d}V - \int_{\Gamma^t_X} \mathbf{u}\cdot\overline{\mathbf{T}}\,\mathrm{d}A. \tag{2.4.14b}$$

Using a total Lagrangian formulation, the variational formulation can be written as

$$\delta\Pi(\mathbf{Q};\delta\mathbf{Q}) = D_{\delta\mathbf{Q}}\Pi(\mathbf{Q}) \Rightarrow \begin{cases} D_{\delta\mathbf{u}}\Pi(\mathbf{Q}) = 0, \\ D_{\delta\widetilde{p}}\Pi(\mathbf{Q}) = 0, \\ D_{\delta\widetilde{J}}\Pi(\mathbf{Q}) = 0, \end{cases} \tag{2.4.15}$$

where

$$D_{\delta\mathbf{u}}\Pi\left(\mathbf{Q}\right) = \int_{\Omega_X} \boldsymbol{\nabla}_x\,\delta\mathbf{u} : \boldsymbol{\tau}\,\mathrm{d}V - \int_{\Omega_X} \delta\mathbf{u}\cdot\overline{\mathbf{B}}\,\mathrm{d}V - \int_{\Gamma^t_X} \delta\mathbf{u}\cdot\overline{\mathbf{T}}\,\mathrm{d}A\,, \tag{2.4.16a}$$

$$D_{\delta\widetilde{p}}\Pi\left(\mathbf{Q}\right) = \int_{\Omega_X} \delta\widetilde{p}\left[J(\mathbf{u}) - \widetilde{J}\right]\mathrm{d}V\,, \tag{2.4.16b}$$

$$D_{\delta\widetilde{J}}\Pi\left(\mathbf{Q}\right) = \int_{\Omega_X} \delta\widetilde{J}\left[\frac{\mathrm{d}\psi_{\mathrm{vol}}(\widetilde{J})}{\mathrm{d}\widetilde{J}} - \widetilde{p}\right]\mathrm{d}V\,. \tag{2.4.16c}$$

Using the linearized form of (2.3.27), leads to

$$\Delta\delta\Pi\left(\mathbf{Q};\delta\mathbf{Q},\Delta\mathbf{Q}\right) \Rightarrow \begin{cases} D_{\Delta\mathbf{u}}\,\delta\Pi(\mathbf{Q};\delta\mathbf{Q}) = \int_{\Omega_X}\left[\boldsymbol{\nabla}_x\,\delta\mathbf{u} : J\mathbb{c} + \boldsymbol{\nabla}_x\,\delta\mathbf{u}\cdot\boldsymbol{\tau} + \delta\widetilde{p}J\mathbf{I} : \boldsymbol{\nabla}_x\,\Delta\mathbf{u}\right]\mathrm{d}V, \\ D_{\Delta\widetilde{p}}\,\delta\Pi(\mathbf{Q};\delta\mathbf{Q}) = \int_{\Omega_X}\left[\boldsymbol{\nabla}_x\,\delta\mathbf{u} : J\mathbf{I} - \delta\widetilde{J}\Delta\widetilde{p}\right]\mathrm{d}V, \\ D_{\Delta\widetilde{J}}\,\delta\Pi(\mathbf{Q};\delta\mathbf{Q}) = \int_{\Omega_X}\left[-\delta\widetilde{p} + \delta\widetilde{J}\,\dfrac{\mathrm{d}^2\psi_{\mathrm{vol}}}{\mathrm{d}\widetilde{J}\,\mathrm{d}\widetilde{J}}\right]\Delta\widetilde{J}\,\mathrm{d}V. \end{cases} \tag{2.4.17}$$

One can further specialise the individual contributions as follows:

$$\Delta\delta\Pi\left(\mathbf{Q};\delta\mathbf{Q},\Delta\mathbf{Q}\right) \Rightarrow \begin{cases} D_{\Delta\mathbf{u}}\delta\Pi(\mathbf{Q};\delta\mathbf{Q}) \Rightarrow \begin{cases} D_{\Delta\mathbf{u}}\delta\Pi(\mathbf{Q};\Delta\mathbf{u}) = D^2_{\Delta\mathbf{u},\Delta\mathbf{u}}\,\Pi(\mathbf{Q}), \\ D_{\Delta\mathbf{u}}\delta\Pi(\mathbf{Q};\delta\widetilde{p}) = D^2_{\Delta\mathbf{u},\delta\widetilde{p}}\,\Pi(\mathbf{Q}), \\ D_{\Delta\mathbf{u}}\delta\Pi(\mathbf{Q};\delta J) = D^2_{\Delta\mathbf{u},\delta J}\,\Pi(\mathbf{Q}), \end{cases} \\ D_{\Delta\widetilde{p}}\delta\Pi(\mathbf{Q};\delta\mathbf{Q}) \Rightarrow \begin{cases} D_{\Delta\widetilde{p}}\delta\Pi(\mathbf{Q};\Delta\mathbf{u}) = D^2_{\Delta\widetilde{p},\Delta\mathbf{u}}\,\Pi(\mathbf{Q}), \\ D_{\Delta\widetilde{p}}\delta\Pi(\mathbf{Q};\delta\widetilde{p}) = D^2_{\Delta\widetilde{p},\delta\widetilde{p}}\,\Pi(\mathbf{Q}), \\ D_{\Delta\widetilde{p}}\delta\Pi(\mathbf{Q};\delta J) = D^2_{\Delta\widetilde{p},\delta J}\,\Pi(\mathbf{Q}), \end{cases} \\ D_{\Delta J}\delta\Pi(\mathbf{Q};\delta\mathbf{Q}) \Rightarrow \begin{cases} D_{\Delta J}\delta\Pi(\mathbf{Q};\Delta\mathbf{u}) = D^2_{\Delta J,\Delta\mathbf{u}}\,\Pi(\mathbf{Q}), \\ D_{\Delta J}\delta\Pi(\mathbf{Q};\delta\widetilde{p}) = D^2_{\Delta J,\delta\widetilde{p}}\,\Pi(\mathbf{Q}), \\ D_{\Delta J}\delta\Pi(\mathbf{Q};\delta J) = D^2_{\Delta J,\delta J}\,\Pi(\mathbf{Q}). \end{cases} \end{cases} \tag{2.4.18}$$

Approximating a function $\delta\Pi$ using the first-order Taylor expansion gives

$$\delta\Pi\left(\mathbf{Q}^{t+1};\delta\mathbf{Q}\right) \approx \delta\Pi\left(\mathbf{Q}^{t};\delta\mathbf{Q}\right) + \Delta\,\delta\Pi\left(\mathbf{Q}^{t};\delta\mathbf{Q},\Delta\mathbf{Q}\right) = 0\,, \tag{2.4.19}$$

or

$$D_{\delta\mathbf{u}}\,\Pi\left(\mathbf{Q}^{t+1}\right) \approx D_{\delta\mathbf{u}}\,\Pi\left(\mathbf{Q}^{t}\right) + D_{\Delta\mathbf{u}}\,\delta\Pi\left(\mathbf{Q}^{t};\delta\mathbf{Q}\right) = 0\,, \tag{2.4.20a}$$

$$D_{\delta\widetilde{p}}\,\Pi\left(\mathbf{Q}^{t+1}\right) \approx D_{\delta\widetilde{p}}\,\Pi\left(\mathbf{Q}^{t}\right) + D_{\Delta\widetilde{p}}\,\delta\Pi\left(\mathbf{Q}^{t};\delta\mathbf{Q}\right) = 0\,, \tag{2.4.20b}$$

$$D_{\delta\widetilde{J}}\,\Pi\left(\mathbf{Q}^{t+1}\right) \approx D_{\delta\widetilde{J}}\,\Pi\left(\mathbf{Q}^{t}\right) + D_{\Delta\widetilde{J}}\,\delta\Pi\left(\mathbf{Q}^{t};\delta\mathbf{Q}\right) = 0\,. \tag{2.4.20c}$$

and setting $\mathbf{Q}^{t+1} = \mathbf{Q}^{t} + \Delta\mathbf{Q}$, one can solve the system of equations iteratively employing a Newton–Raphson scheme. By taking nodal variables at global node I as $\mathbf{Q}^I = \{\mathbf{u}^I, \widetilde{p}^I, \widetilde{J}^I\}$ and

utilising the element shape functions running over the degree of freedoms, the various fields are approximated. Hence,

$$\mathbf{u} = \sum_{I \in \mathcal{I}_u} \mathbf{N}^{I,u}\, u^I, \quad \widetilde{p} = \sum_{I \in \mathcal{I}_{\widetilde{p}}} N^{I,\widetilde{p}}\, \widetilde{p}^I, \quad \widetilde{J} = \sum_{I \in \mathcal{I}_{\widetilde{J}}} N^{I,\widetilde{J}}\, \widetilde{J}^I\,. \tag{2.4.21}$$

The sets $\mathcal{I}_u$, $\mathcal{I}_{\widetilde{p}}$ and $\mathcal{I}_{\widetilde{J}}$ contain the global degrees of freedom for the corresponding variables. The components of $\delta\mathbf{Q}$ and $\Delta\mathbf{Q}$ can also be approximated by

$$\begin{aligned}
\delta\mathbf{u} &= \sum_{I \in \mathcal{I}_u} \mathbf{N}^{I,u}\, \delta u^I, \quad \delta\widetilde{p} = \sum_{I \in \mathcal{I}_{\widetilde{p}}} N^{I,\widetilde{p}}\, \delta\widetilde{p}^I, \quad \delta\widehat{J} = \sum_{I \in \mathcal{I}_{\widetilde{J}}} N^{I,\widetilde{J}}\, \delta\widetilde{J}^I, \\
\Delta\mathbf{u} &= \sum_{I \in \mathcal{I}_u} \mathbf{N}^{I,u}\, \Delta u^I, \quad \Delta\widetilde{p} = \sum_{I \in \mathcal{I}_{\widetilde{p}}} N^{I,\widetilde{p}}\, \Delta\widetilde{p}^I, \quad \Delta\widetilde{J} = \sum_{I \in \mathcal{I}_{\widetilde{J}}} N^{I,\widehat{J}}\, \Delta\widetilde{J}^I.
\end{aligned} \tag{2.4.22}$$

Then the right-hand side vector $\mathbf{R} = \left\{\mathbf{R}_u, \mathbf{R}_{\widetilde{p}}, \mathbf{R}_{\widetilde{J}}\right\}$ follows as

$$R_u^I = -\int_{\Omega_X} \boldsymbol{\tau} : \boldsymbol{\nabla}_x \mathbf{N}^{I,u}\, \mathrm{d}V + \int_{\Omega_X} \mathbf{N}^{I,u} \cdot \overline{\mathbf{B}}\, \mathrm{d}V + \int_{\Gamma_X^t} \mathbf{N}^{I,u} \cdot \overline{\mathbf{T}}\, \mathrm{d}A, \qquad \forall I \in \mathcal{I}_u\,, \tag{2.4.23a}$$

$$R_{\widetilde{p}}^I = -\int_{\Omega_X} N^{I,\widetilde{p}} \left[J - \widetilde{J}\right]\, \mathrm{d}V, \qquad \forall I \in \mathcal{I}_{\widetilde{p}}\,, \tag{2.4.23b}$$

$$R_{\widetilde{J}}^I = -\int_{\Omega_X} N^{I,\widetilde{J}} \left[\frac{\mathrm{d}\psi_{\mathrm{vol}}(\widetilde{J})}{\mathrm{d}\widetilde{J}} - \widetilde{p}\right] \mathrm{d}V, \qquad \forall I \in \mathcal{I}_{\widetilde{J}}\,. \tag{2.4.23c}$$

This forms the linear system of equations $\mathbf{K}\,\Delta\mathbf{u} = \mathbf{R}$, where the components of tangent stiffness matrix associated with the degrees of freedom $I, J \in \{\mathcal{I}_u, \mathcal{I}_{\widetilde{p}}, \mathcal{I}_{\widetilde{J}}\}$ are extracted as

$$\begin{aligned}
K_{uu}^{IJ} &= \int_{\Omega_X} \left[\boldsymbol{\nabla}_x \mathbf{N}^{I,u} : J\mathbb{c} : \boldsymbol{\nabla}_x \mathbf{N}^{J,u} + \left[\boldsymbol{\nabla}_x \mathbf{N}^{I,u} : \boldsymbol{\nabla}_x \mathbf{N}^{J,u}\right] \boldsymbol{\tau}\right]\, \mathrm{d}V, && \forall I \in \mathcal{I}_u \,\text{and}\, \forall J \in \mathcal{I}_u\,, \\
K_{u\widetilde{p}}^{IJ} &= \int_{\Omega_X} \boldsymbol{\nabla}_x \mathbf{N}^{I,u} : J\,\mathbf{I}\, N^{J,\widetilde{p}}\, \mathrm{d}V, && \forall I \in \mathcal{I}_u \,\text{and}\, \forall J \in \mathcal{I}_{\widetilde{p}}\,, \\
K_{\widetilde{p}u}^{IJ} &= \int_{\Omega_X} N^{I,\widetilde{p}}\, J\,\mathbf{I} : \boldsymbol{\nabla}_x N_k^{J,u}\, \mathrm{d}V, && \forall I \in \mathcal{I}_{\widetilde{p}} \,\text{and}\, \forall J \in \mathcal{I}_u\,, \\
K_{\widetilde{p}\widetilde{J}}^{IJ} &= \int_{\Omega_X} -N^{I,\widetilde{p}}\, N^{J,\widehat{J}}\, \mathrm{d}V, && \forall I \in \mathcal{I}_{\widetilde{p}} \,\text{and}\, \forall J \in \mathcal{I}_{\widetilde{J}}\,, \\
K_{\widetilde{J}\widetilde{p}}^{IJ} &= \int_{\Omega_X} -N^{I,\widehat{J}} N^{J,\widetilde{p}}\, \mathrm{d}V, && \forall I \in \mathcal{I}_{\widetilde{J}} \,\text{and}\, \forall J \in \mathcal{I}_{\widetilde{p}}\,, \\
K_{\widetilde{J}\widetilde{J}}^{IJ} &= \int_{\Omega_X} N^{I,\widehat{J}} \left[\frac{d^2\psi_{\mathrm{vol}}}{\mathrm{d}\widetilde{J}\,\mathrm{d}\widetilde{J}}\right] N^{J,\widehat{J}}\, \mathrm{d}V, && \forall I \in \mathcal{I}_{\widetilde{J}} \,\text{and}\, \forall J \in \mathcal{I}_{\widetilde{J}}\,,
\end{aligned} \tag{2.4.24}$$

while, $K_{u\tilde{J}}^{IJ}$, $K_{\tilde{p}\tilde{p}}^{IJ}$ and $K_{\tilde{p}\tilde{J}}^{IJ}$ are equal to zero. These matrices form the tangent matrix as

$$\mathbf{K} = \begin{bmatrix} \mathbf{K}_{uu} & \mathbf{K}_{u\tilde{p}} & \mathbf{K}_{u\tilde{J}} \\ \mathbf{K}_{\tilde{p}u} & \mathbf{K}_{\tilde{p}\tilde{p}} & \mathbf{K}_{\tilde{p}\tilde{J}} \\ \mathbf{K}_{\tilde{J}u} & \mathbf{K}_{\tilde{J}\tilde{p}} & \mathbf{K}_{\tilde{J}\tilde{J}} \end{bmatrix} = \begin{bmatrix} \mathbf{K}_{uu} & \mathbf{K}_{u\tilde{p}} & \mathbf{0} \\ \mathbf{K}_{\tilde{p}u} & \mathbf{0} & \mathbf{K}_{\tilde{p}\tilde{J}} \\ \mathbf{0} & \mathbf{K}_{\tilde{J}\tilde{p}} & \mathbf{K}_{\tilde{J}\tilde{J}} \end{bmatrix}. \tag{2.4.25}$$

Chapter 3

Finite element implementation and verification

This chapter implements the mathematical formulations from the previous chapter into FE codes across 3D, flatland, and planar models, focusing on the critical but often-overlooked plane stress approximation. The reliability of the FE framework is confirmed through benchmarking against established literature problems and further examined with various heterogeneous numerical examples. The significance of the plane stress model for simulating two-dimensional fibre-reinforced composites sets the stage for the next chapter.

3.1 Introduction

FE analysis of materials can be conducted using various 2D and 3D configurations. The planar approximations are beneficial for certain scenarios in engineering, particularly, plane stress becomes crucial where the structure is thin, such as in membranes, thin films and other surface-dominated structures such as two-dimensional composites. However, accurately modelling compressible and nearly incompressible hyperelastic materials under plane stress conditions is challenging and not well-established.

Research on FE modelling of nonlinear elasticity primarily focuses on 3D, plane strain, and flatland approaches (Shojaei and Yavari, 2019; Angoshtari et al., 2017; Auricchio et al., 2013; Brink and Stein, 1996; Chavan et al., 2007). Inspired by the novel by Abbott (1884), the term "flatland" here refers to truly two-dimensional elasticity formulations. In the flatland approach, all kinetic and kinematics quantities (stress and strain) are completely restricted to two dimensions. The flatland approach is favoured for its computational efficiency and simplicity. For instance, Auricchio et al. (2013) investigated different FEM formulations for addressing finite deformations elastic problems across both nearly incompressible and fully incompressible regimes. This analysis was conducted using 2D model problems characterized by a simple neo-Hookean constitutive law. Angoshtari et al. (2017) introduced a novel class of mixed FEM for flatland, leveraging the Hu–Washizu-type mixed formulation with independent

unknowns, including displacement, displacement gradient, and Piola stress tensor. Viebahn et al. (2018) introduced a novel mixed FEM for elasticity, validated numerically in both two and three dimensions. Their proposed method, based on the Hellinger–Reissner formulation, offered advantages such as simplicity in implementation, sparse system matrices, and efficiency in automatic mesh generation, particularly with triangular/tetrahedral structures.

In contrast, while plane stress FE analysis is well-established in linear elasticity, research on its application to nonlinear elasticity remains limited. Modelling finite deformations of hyperelastic solids under plane stress conditions poses unique challenges. For fully incompressible materials, out-of-plane deformation can be characterised entirely by in-plane components, which simplifies the modelling process. This is in contrast to the case of compressible and nearly incompressible materials, which introduces additional complexities. Nearly incompressible materials typically employ a decoupled model that separates the strain energy function into volumetric and isochoric parts (Holzapfel, 2002). In this context, the neo-Hookean model relies on the first modified invariant, $I_{\widetilde{C}}$, to account for the deformation split. While this approach improves the accuracy of modelling nearly incompressible behaviour, its implementation under plane stress condition remains unexplored in the literature due to its complexity. This study addresses this gap, highlighting the need for a more intricate mathematical formulation. In the case of compressible materials, the energy density function does not require decomposition, allowing the use of a simpler neo-Hookean model based solely on the first invariant, I_C, of the total right Cauchy–Green tensor $\mathbf{C}$. This formulation streamlines mathematical derivation for plane stress as observed in the work of Pascon (2019).

The complexity of plane stress modelling increases further when dealing with materials reinforced with fillers. Such reinforcements significantly enhance mechanical properties, but introduce complex interactions and heterogeneous behaviour (Merodio and Ogden, 2005; Miehe, 2003; Saxena et al., 2015). Betsch et al. (1996) introduced a nonlinear finite shell element formulation capable of accommodating large elastic deformations based on the three-field variational principle. They approximated the plane stress response for vanishing thickness. Steinmann et al. (1997) presented a simple efficient approach to apply arbitrary algorithmic constitutive frameworks without modifications to problems under the plane stress condition. For structural components such as thin shells, the plane stress assumption is frequently made. For example, Liu et al. (2024) investigated the inflation and finite deformations of hyperelastic thin shells, simplifying the three-dimensional constitutive equations to two dimensions using the plane stress condition coupled with an incompressibility constraint. Interest in plane stress modelling within nonlinear mechanics has experienced an uptick in recent years, albeit not to a significant extent. In a notable work, Pascon (2019) presented an FE formulation for solving hyperelastic material problems under plane stress conditions using isoparametric triangular membrane elements. Their work involved solving nonlinear equations using an iterative algorithm to determine the out-of-plane normal strain component. Their contribution has set a sturdy foundation for advancing research on the plane stress condition. A recent mathematical analysis of the plane stress problem for incompressible hyperelasticity was conducted by Horgan and Murphy

(2024) based on two formulations. The first involves prescribing a Cauchy stress field and investigating the deducible information on the stretch tensor and the deformation. The second involves prescribing a plane stress state using the Piola-Kirchhoff stress. Their study was conducted for a generic incompressible isotropic hyperelastic material, with the strain-energy density defined using two of the classical principal invariants. Nevertheless, these studies are confined to specific approaches and element types.

To address the complexity and limitations of existing studies, this chapter introduces a general framework for nonlinear FE analysis of compressible and nearly incompressible hyperelastic materials under plane stress approximation. Various two-dimensional modelling approaches are discussed, including flatland, plane strain, and plane stress models. As outlined in the previous chapter, most hyperelastic materials preserve volume during deformation, causing volumetric locking in FE simulations. Robust elements that perform well in bending-dominated scenarios and accurately handle incompressibility are essential. These elements must also resist mesh distortions common in finite deformations (Wriggers and Hueck, 1996). For non-plane stress models, the three-field mixed formulation is adopted to mitigate volumetric locking. In contrast, modelling under the plane stress condition offers another advantage: it can handle incompressibility effectively within the classic single-field formulation by allowing volume change within the plane. The development of FE codes incorporating novel numerical features to enhance computational efficiency and accuracy is presented. Key advancements include adaptive mesh refinement, and the implementation of message passing interface, which enables parallel processing, significantly reducing computation time by distributing tasks across multiple processors. These innovations are critical for handling the complex simulations required for analysing fibre-reinforced composites and elastomeric materials under finite deformations. These features are important for efficiently modelling RVEs, given their computationally expensive nature, due to the extensive number of elements involved. These FE codes are developed with a focus on accessibility and transparency, and as such, they are made open source. The FE models are tested and verified by analysing extreme nonlinear problems and their effectiveness is confirmed through benchmarking against established problems in the literature. Comparing various dimensional configurations through numerical examples, including cases involving reinforced stiff particles and fibres, further demonstrates their performance for both compressible and nearly incompressible materials.

The necessity of the plane stress model is underscored by its suitability for simulating fibre-reinforced composites in two dimensions. With insights gained in this chapter, the subsequent analysis of elastomeric composites is set for a detailed discussion in the following chapter.

3.2 Dimensional setting

This section explores the 2D and 3D configurations used in FE analysis. Selecting the appropriate dimensionality for simulations is crucial and depends on specific engineering needs and the nature of the physical phenomena.

3.2.1 Three-dimensional modelling

The most general case in FEM is 3D, which provides detailed representations of materials, enabling precise simulations. The developed FE formulations readily adapt to existing FE codes, facilitating straightforward implementations without additional modifications.

3.2.2 Two-dimensional modelling

In FE analysis for nonlinear elasticity, transitioning from 3D to simplified 2D representation brings significant benefits, such as simplified geometry and decreased computational expenses. However, the approximation error associated with this dimension reduction must be appropriately accounted for. Here, the domain is considered in $\mathbb{R}^2$, with three deformation assumptions applied: flatland, plane strain, and plane stress.

Flatland. The first and simplest method is the strict 2D assumption, where the real-world complexity is condensed into a 2D representation by assuming the existence of only two dimensions. One can adapt three-dimensional formulations to two dimensions, by simply reducing the dimensions of the mathematical model. For example, the deformation gradient tensor is simplified, where its components are given as

$$[\overline{\mathbf{F}}] = \begin{bmatrix} F_{11} & F_{12} \\ F_{21} & F_{22} \end{bmatrix}, \quad \overline{\mathbf{F}} \in \mathbb{R}^2 \otimes \mathbb{R}^2. \tag{3.2.1}$$

Henceforth, the overline indicates that the tensor is in $\mathbb{R}^2 \otimes \mathbb{R}^2$. The determinant of the flatland deformation gradient is defined by $\overline{J} = \det(\overline{\mathbf{F}})$. Although this simplification may not capture all the complexities of real-world phenomena, it is widely used in literature for its simplicity and computational efficiency. Here, a two-dimensional neo-Hookean model for hyperelastic modelling is given by

$$\psi = \frac{\mu}{2}\left[I_{\widehat{\overline{C}}} - 2\right] + \kappa\, \mathcal{G}(\overline{J}\,). \tag{3.2.2}$$

Planar assumptions. Geometry is envisioned as having two dimensions within a plane, with an additional out-of-plane dimension. This framework includes two main settings: plane strain and plane stress. In plane stress setting, the out-of-plane stress is assumed to be negligible and suitable for thin plates. Conversely, plane strain is applicable to significantly thicker plates or those confined between rigid boundaries, assuming minimal out-of-plane strain. Although the geometry for planar assumptions in FE analysis is 2D, these problems can be considered quasi-3D due to the plate thickness. The planar modelling simplifies the deformation gradient tensor, $\mathbf{F}$, into

$$[\mathbf{F}] = \begin{bmatrix} F_{11} & F_{12} & 0 \\ F_{21} & F_{22} & 0 \\ 0 & 0 & F_{33} \end{bmatrix}, \tag{3.2.3}$$

which consequently simplifies the right Cauchy–Green deformation tensor as

$$[\mathbf{C}] = \begin{bmatrix} C_{11} & C_{12} & 0 \\ C_{12} & C_{22} & 0 \\ 0 & 0 & C_{33} \end{bmatrix} = \begin{bmatrix} F_{11}^2 + F_{21}^2 & F_{11}F_{12} + F_{21}F_{22} & 0 \\ F_{11}F_{12} + F_{21}F_{22} & F_{12}^2 + F_{22}^2 & 0 \\ 0 & 0 & F_{33}^2 \end{bmatrix}. \tag{3.2.4}$$

This yields $J = \det(\mathbf{F}) = F_{33}\,[F_{11}\,F_{22} - F_{12}\,F_{21}]$. The out-of-plane component F_{33} is unknown and needs to be determined based on the underlying assumptions. The next two sections discuss this matter.

3.2.3 Plane strain

For a plane strain case in which the deformation along the X_3 coordinate is constrained, the component F_{33} in (3.2.3) is given as $C_{33} = F_{33}^2 = 1$. Consequently, the tensor $\mathbf{E}$ is given in matrix form by

$$[\mathbf{E}] = \begin{bmatrix} E_{11} & E_{12} & 0 \\ E_{21} & E_{22} & 0 \\ 0 & 0 & 0 \end{bmatrix}. \tag{3.2.5}$$

This formulation can be easily integrated into the FE code for 3D analysis, with subsequent reduction to 2D for final computations.

3.2.4 Plane stress

Unlike the plane strain assumption, evaluating the value of F_{33} for the plane stress setting is not trivial. To calculate $C_{33} = F_{33}^2$, one must apply the plane stress condition, which sets the out-of-plane stress component, S_{33}, to zero.

For ease of mathematical calculations, the right Cauchy–Green tensor $\mathbf{C} \in \mathbb{R}^3 \otimes \mathbb{R}^3$ is decomposed into in-plane and out-of-plane components as

$$\mathbf{C} = \mathbf{C}_{\parallel} + \mathbf{C}_{\perp}, \tag{3.2.6}$$

where these components are defined by

$$[\mathbf{C}_{\parallel}] = \begin{bmatrix} \overline{\mathbf{C}} & \mathbf{0} \\ \mathbf{0} & 0 \end{bmatrix}, \quad [\mathbf{C}_{\perp}] = \begin{bmatrix} \overline{\mathbf{0}} & \mathbf{0} \\ \mathbf{0} & C_{33} \end{bmatrix}, \quad \overline{\mathbf{C}}, \overline{\mathbf{0}} \in \mathbb{R}^2 \otimes \mathbb{R}^2, \quad C_{33} \in \mathbb{R}\,. \tag{3.2.7}$$

This decomposition separates the tensor into the reduced tensor $\overline{\mathbf{C}}$ and the scalar C_{33}. A similar decomposition of $\mathbf{S} \in \mathbb{R}^3 \otimes \mathbb{R}^3$, gives

$$\mathbf{S} = \mathbf{S}_{\parallel} + \mathbf{S}_{\perp}, \tag{3.2.8}$$

where

$$[\mathbf{S}_{\parallel}] = \begin{bmatrix} \overline{\mathbf{S}} & \mathbf{0} \\ \mathbf{0} & 0 \end{bmatrix}, \quad [\mathbf{S}_{\perp}] = \begin{bmatrix} \overline{\mathbf{0}} & \mathbf{0} \\ \mathbf{0} & S_{33} \end{bmatrix}, \quad \overline{\mathbf{S}} \in \mathbb{R}^2 \otimes \mathbb{R}^2, \quad S_{33} \in \mathbb{R}\,. \tag{3.2.9}$$

The value of C_{33} as a function of $\overline{\mathbf{C}}$ needs to be calculated at every quadrature point within each finite element. To do so, the nonlinear equation $S_{33} = 0$ is solved using a Newton–Raphson scheme such that

$$S_{33}\big(\overline{\mathbf{C}}, C_{33}\big)\big|_{\overline{\mathbf{C}}} + \left.\frac{\partial S_{33}\big(\overline{\mathbf{C}}, C_{33}\big)}{\partial C_{33}}\right|_{\overline{\mathbf{C}}} \mathrm{d}C_{33} = 0, \tag{3.2.10}$$

which iteratively updates the solution as

$$C_{33} \leftarrow C_{33} + \mathrm{d}C_{33}, \tag{3.2.11}$$

until convergence is achieved, resulting in the solution $\acute{C}_{33}(\overline{\mathbf{C}})$.

The next step is to update the incremental constitutive tensor to account for the plane stress approximation. The in-plane tensor $\overline{\mathbb{C}} \in \mathbb{R}^2 \otimes \mathbb{R}^2 \otimes \mathbb{R}^2 \otimes \mathbb{R}^2$, is given by

$$\overline{\mathbb{C}} = 2\,\frac{\partial \overline{\mathbf{S}}}{\partial \overline{\mathbf{C}}} = 2\left[\left.\frac{\partial \overline{\mathbf{S}}}{\partial \overline{\mathbf{C}}}\right|_{\acute{C}_{33}} + \left.\frac{\partial \overline{\mathbf{S}}}{\partial \acute{C}_{33}}\right|_{\overline{\mathbf{C}}} \otimes \frac{\partial \acute{C}_{33}}{\partial \overline{\mathbf{C}}}\right]. \tag{3.2.12}$$

To explicitly calculate the expressions in (3.2.12) one needs to know the dependence of the Piola–Kirchhoff stress tensor on the right Cauchy–Green deformation tensor.

Neo-Hookean model (*decoupled*). The expression for $\mathbf{S}$ is obtained from Equation (A.1.1), which naturally depends on the choice of the strain energy density function. In the subsequent, the following neo-Hookean strain energy density function is used for the sake of demonstration:

$$\psi = \psi_{\mathrm{iso}}(I_{\widehat{C}}) + \psi_{\mathrm{vol}}(J) = \frac{\mu}{2}\left[I_{\widehat{C}} - 3\right] + \kappa\,\mathcal{G}(J)\,. \tag{3.2.13}$$

The expression for $\mathbf{S}$ reads

$$\mathbf{S} = 2\,\frac{\partial \psi\,(\mathbf{C})}{\partial \mathbf{C}} = 2\left[\left[\frac{\mu}{2}\,J^{-2/3}\right]\mathbf{I} + J^2\,\left[\kappa\left[\frac{\partial\,\mathcal{G}}{\partial J^2}\right] - \frac{\mu}{6}\,I_C\,J^{-8/3}\right]\,\mathbf{C}^{-1}\right]. \tag{3.2.14}$$

Choosing, $\mathcal{G} = \left[J^2 - 1 - 2\ln J\right]/4$, one can further specialize the expression as

$$\mathbf{S}(\mathbf{C}) = \mu\,J^{-2/3}\,\mathbf{I} + \underbrace{\left[\frac{\kappa}{2}\left[J^2 - 1\right] - \frac{\mu}{3}\,I_C\,J^{-2/3}\right]}_{\gamma = \gamma(\mathbf{C})}\,\mathbf{C}^{-1}. \tag{3.2.15}$$

Based on the decomposition in Equation (3.2.6), one obtains

$$\mathbf{S}(\overline{\mathbf{C}}, C_{33}) = \mu\,J^{-2/3}(\overline{\mathbf{C}}, C_{33})\,\mathbf{I} + \gamma(\overline{\mathbf{C}}, C_{33})\;\mathbf{C}^{-1}(\overline{\mathbf{C}}, C_{33}). \tag{3.2.16}$$

Given that $[\mathbf{C}^{-1}]_{33} = 1/C_{33}$, an application of the plane stress assumption $S_{33} = 0$ results in

$$S_{33}(\overline{\mathbf{C}}, \acute{C}_{33}) = \mu\,J^{-2/3}(\overline{\mathbf{C}}, \acute{C}_{33}) + \gamma(\overline{\mathbf{C}}, \acute{C}_{33})\,\frac{1}{\acute{C}_{33}} = 0, \tag{3.2.17}$$

so that by substituting $\gamma = -\mu\,\acute{C}_{33}\,J^{-2/3}$ into (3.2.15), an expression for the Piola–Kirchhoff stress tensor specialised to plane stress is derived as

$$\mathbf{S}(\overline{\mathbf{C}}, \acute{C}_{33}) = \mu\,J^{-2/3}\left[\mathbf{I} - \acute{C}_{33}\,\mathbf{C}^{-1}\right]. \tag{3.2.18}$$

The in-plane stress tensor $\overline{\mathbf{S}}$ follows as

$$\overline{\mathbf{S}}(\overline{\mathbf{C}}, \acute{C}_{33}) = \mu\,J^{-2/3}\left[\overline{\mathbf{I}} - \acute{C}_{33}\,\overline{\mathbf{C}}^{-1}\right]. \tag{3.2.19}$$

Using the expression for $\overline{\mathbf{S}}$ in Equation (3.2.19), the first two expressions in Equation (3.2.12) are calculated as

$$\left.\frac{\partial\overline{\mathbf{S}}}{\partial\overline{\mathbf{C}}}\right|_{\acute{C}_{33}} = \acute{C}_{33}\,\mu\,J^{-2/3}\,\overline{\mathbf{C}}^{-1}\odot\overline{\mathbf{C}}^{-1} - \frac{2}{3}\,\mu\,J^{-5/3}\left[\overline{\mathbf{I}} - \acute{C}_{33}\,\overline{\mathbf{C}}^{-1}\right]\otimes\frac{\partial J}{\partial\overline{\mathbf{C}}}, \tag{3.2.20a}$$

$$\left.\frac{\partial\overline{\mathbf{S}}}{\partial\acute{C}_{33}}\right|_{\overline{\mathbf{C}}} = -\mu\,J^{-2/3}\,\overline{\mathbf{C}}^{-1} - \frac{2}{3}\,\mu\,J^{-5/3}\left[\overline{\mathbf{I}} - \acute{C}_{33}\,\overline{\mathbf{C}}^{-1}\right]\frac{\partial J}{\partial\acute{C}_{33}}, \tag{3.2.20b}$$

where using $J^2 = \acute{C}_{33}\det(\overline{\mathbf{C}})$ results in

$$\frac{\partial J}{\partial\overline{\mathbf{C}}} = \frac{1}{2}\,J^{-1}\,\acute{C}_{33}\,\overline{\mathbf{C}}^{-1}\det(\overline{\mathbf{C}}), \quad \text{and} \quad \frac{\partial J}{\partial\acute{C}_{33}} = \frac{1}{2}\,J^{-1}\det(\overline{\mathbf{C}}). \tag{3.2.21}$$

The third expression in Equation (3.2.12), $\partial\acute{C}_{33}/\partial\overline{\mathbf{C}}$, can be calculated by ensuring that $S_{33}(\overline{\mathbf{C}}, \acute{C}_{33})$ remains zero for all possible displacements under consideration. Hence

$$\frac{\mathrm{d}S_{33}}{\mathrm{d}\overline{\mathbf{C}}} = \mu\frac{\mathrm{d}J^{-2/3}}{\mathrm{d}\overline{\mathbf{C}}} + \acute{C}_{33}^{-1}\frac{\mathrm{d}\,\gamma}{\mathrm{d}\overline{\mathbf{C}}} + \gamma\frac{\mathrm{d}\acute{C}_{33}^{-1}}{\mathrm{d}\overline{\mathbf{C}}} = \overline{\mathbf{0}} \tag{3.2.22a}$$

$$= \mu\left[\left.\frac{\partial J^{-2/3}}{\partial\overline{\mathbf{C}}}\right|_{\acute{C}_{33}} + \left.\frac{\partial J^{-2/3}}{\partial\acute{C}_{33}}\right|_{\overline{\mathbf{C}}}\frac{\partial\acute{C}_{33}}{\partial\overline{\mathbf{C}}}\right] + \acute{C}_{33}^{-1}\left[\left.\frac{\partial\,\gamma}{\partial\overline{\mathbf{C}}}\right|_{\acute{C}_{33}} + \left.\frac{\partial\gamma}{\partial\acute{C}_{33}}\right|_{\overline{\mathbf{C}}}\frac{\partial\acute{C}_{33}}{\partial\overline{\mathbf{C}}}\right] + \gamma\frac{\partial\acute{C}_{33}^{-1}}{\partial\overline{\mathbf{C}}} = \overline{\mathbf{0}} \tag{3.2.22b}$$

$$= \underbrace{\mu\left.\frac{\partial J^{-2/3}}{\partial\overline{\mathbf{C}}}\right|_{\acute{C}_{33}} + \acute{C}_{33}^{-1}\left.\frac{\partial\,\gamma}{\partial\overline{\mathbf{C}}}\right|_{\acute{C}_{33}}}_{\beta} + \underbrace{\left[\mu\left.\frac{\partial J^{-2/3}}{\partial\acute{C}_{33}}\right|_{\overline{\mathbf{C}}} + \acute{C}_{33}^{-1}\left.\frac{\partial\gamma}{\partial\acute{C}_{33}}\right|_{\overline{\mathbf{C}}} - \gamma\,\acute{C}_{33}^{-2}\right]}_{\frac{\partial S_{33}}{\partial\acute{C}_{33}}\Big|_{\overline{\mathbf{C}}}}\frac{\partial\acute{C}_{33}}{\partial\overline{\mathbf{C}}} = \overline{\mathbf{0}} \tag{3.2.22c}$$

$$\Rightarrow \frac{\partial\acute{C}_{33}}{\partial\overline{\mathbf{C}}} = -\beta\left[\left.\frac{\partial S_{33}}{\partial\acute{C}_{33}}\right|_{\overline{\mathbf{C}}}\right]^{-1}. \tag{3.2.22d}$$

where for term β,

$$\left.\frac{\partial J^{-2/3}}{\partial \overline{\mathbf{C}}}\right|_{\acute{C}_{33}} = \frac{-2}{3}\, J^{-5/3}\, \overline{\mathbf{C}}^{-1} \det(\overline{\mathbf{C}}) \tag{3.2.23a}$$

$$\left.\frac{\partial \gamma}{\partial \overline{\mathbf{C}}}\right|_{\acute{C}_{33}} = \frac{\kappa}{2}\, \acute{C}_{33}\, \overline{\mathbf{C}}^{-1} \det(\overline{\mathbf{C}}) - \frac{\mu}{3}\left[J^{-2/3}\, \overline{\mathbf{I}} + I_C\, \frac{\partial J^{-2/3}}{\partial \overline{\mathbf{C}}}\right] \tag{3.2.23b}$$

and

$$\frac{\partial \gamma}{\partial \acute{C}_{33}} = \frac{\kappa}{2} \det(\overline{\mathbf{C}}) - \frac{\mu}{3}\left[I_C\, \frac{\partial J^{-2/3}}{\partial \acute{C}_{33}} + J^{-2/3}\right]. \tag{3.2.24}$$

By evaluating $\acute{C}_{33}$ by solving the nonlinear Equation (3.2.17) using a Newton–Raphson approach and updating the Piola–Kirchhoff stress and incremental constitutive tensors from equations (3.2.19) and (3.2.12), a robust approach is established to implement the plane stress condition for the compressible and nearly incompressible case in the FE scheme. The presented approach is general and can be easily extended to accommodate other forms of energy density functions.

Remark. Differentiation with respect to Equation (3.2.16) yields a 4th-order incremental elasticity tensor $\mathbb{C} \in \mathbb{R}^3 \otimes \mathbb{R}^3 \otimes \mathbb{R}^3 \otimes \mathbb{R}^3$ for plane stress, that exhibits slow convergence for incompressible materials, deviating from the expected quadratic rate. Although this method has been employed in some studies in the literature, the observed inconsistency suggests a potential methodological flaw. For further details, please refer to Appendix B. □

Alternative neo-Hookean model. A neo-Hookean material model that depends on the first invariant (I_C) of the total right Cauchy–Green tensor $\mathbf{C}$, is briefly discussed herein. This model requires a simpler mathematical derivation than the presented decoupled model that depends on $I_{\widehat{C}}$. The strain energy density function is given by

$$\psi = \frac{\mu}{2}\left[I_C - 3 - 2\ln J\right] + \frac{\kappa}{2}\left[J-1\right]^2. \tag{3.2.25}$$

The expression for $\mathbf{S}$ is

$$\mathbf{S}(\mathbf{C}) = 2\,\frac{\partial \psi\,(\mathbf{C})}{\partial \mathbf{C}} = \mu\left[\mathbf{I} - \mathbf{C}^{-1}\right] + \underbrace{\kappa\, J\,[J-1]}_{\alpha=\alpha(\mathbf{C})}\, \mathbf{C}^{-1}. \tag{3.2.26}$$

The plane stress assumption ($S_{33} = 0$) leads to a calculation of $\acute{C}_{33}$. Consequently, the Piola–Kirchhoff stress is expressed as

$$\mathbf{S} = \mu\left[\mathbf{I} - \acute{C}_{33}\, \mathbf{C}^{-1}\right], \tag{3.2.27}$$

and the in-plane stress $\overline{\mathbf{S}}$ as

$$\overline{\mathbf{S}} = \mu\left[\overline{\mathbf{I}} - \acute{C}_{33}\, \overline{\mathbf{C}}^{-1}\right]. \tag{3.2.28}$$

Thus, the first two expressions in Equation (3.2.12) are calculated as

$$\left.\frac{\partial \overline{\mathbf{S}}}{\partial \overline{\mathbf{C}}}\right|_{\acute{C}_{33}} = \acute{C}_{33}\,\mu\,\overline{\mathbf{C}}^{-1} \odot \overline{\mathbf{C}}^{-1} \qquad \text{and} \qquad \left.\frac{\partial \overline{\mathbf{S}}}{\partial \acute{C}_{33}}\right|_{\overline{\mathbf{C}}} = -\mu\,\overline{\mathbf{C}}^{-1}. \tag{3.2.29}$$

Finally, the third term in Equation (3.2.12), $\partial \acute{C}_{33}/\partial \overline{\mathbf{C}}$, is derived by enforcing the condition $S_{33}(\overline{\mathbf{C}}, \acute{C}_{33})$ remains zero for all displacement variations. This leads to

$$\frac{\mathrm{d}S_{33}}{\mathrm{d}\overline{\mathbf{C}}} = \acute{C}_{33}^{-1}\,\frac{\mathrm{d}\alpha}{\mathrm{d}\overline{\mathbf{C}}} + [\alpha - \mu]\,\frac{\mathrm{d}\acute{C}_{33}^{-1}}{\mathrm{d}\overline{\mathbf{C}}} = \overline{\mathbf{0}}. \tag{3.2.30}$$

Applying the chain rule and simplifying, one obtains

$$\frac{\partial \acute{C}_{33}}{\partial \overline{\mathbf{C}}} = -\acute{C}_{33}^{-1}\,\frac{\partial \alpha}{\partial \overline{\mathbf{C}}}\left[\left.\frac{\partial S_{33}}{\partial \acute{C}_{33}}\right|_{\overline{\mathbf{C}}}\right]^{-1}, \tag{3.2.31}$$

where

$$\frac{\partial \alpha}{\partial \overline{\mathbf{C}}} = \kappa\,\acute{C}_{33}\,\overline{\mathbf{C}}^{-1}\,\det\overline{\mathbf{C}}\left[1 - \frac{1}{2}J^{-1}\right]. \tag{3.2.32}$$

This alternative neo-Hookean model provides a more straightforward formulation compared to the previously presented decoupled model, which has a similar structure to that used by Pascon (2019). However, the decoupled model is preferred for modelling nearly incompressible materials (Holzapfel, 2000), and it is thus utilised in this study.

3.3 Finite element implementation

Customized coding for FEM offers significant benefits by granting practitioners flexibility and control, thus enabling the optimization of designs and exploration of complex phenomena. However, developing FE codes from scratch can be resource-intensive and time-consuming.

Open-source FEM libraries provide an efficient alternative, offering pre-built functionalities that save considerable development time, thereby eliminating the need to develop codes from scratch. These libraries are cost-effective and come with the advantage of community support, where users can benefit from shared knowledge and collective troubleshooting.

3.3.1 The deal.II library

In this project, FE codes in C++ are developed based on deal.II (version 9.2) (Arndt et al., 2020), a robust object-oriented class library designed for modern FE code development. Deal.II supports adaptive mesh refinement, parallel computing, and integration with other libraries, enhancing the efficiency and accuracy of tackling complex engineering challenges.

A key feature of deal.II is its ability to handle both 2D and 3D problems simultaneously, allowing code to be written without specific concern for space dimension, run-time, or memory consumption (Bangerth et al., 2007). The library supports parallel computations on distributed

memory clusters, which is essential for managing large-scale simulations with extensive elements and degrees of freedom.

3.3.1.1 Parallelization

Due to the computationally demanding nature of FE simulations of RVEs in this study, efforts are made to optimize simulations through innovative numerical and computational methods. To accelerate the computations, the FE codes leverage parallel computing with multiple processors using distributed memory.

The message passing interface (MPI) is a standardized and portable message-passing standard designed to operate efficiently on parallel computing architectures (Gropp et al., 1996). It facilitates communication and coordination among multiple processors, enabling the execution of complex computational tasks at significantly reduced times. By utilising parallel processing, MPI significantly speeds up computations and reduces overall simulation times. Within this framework, not only global matrices and vectors are divided among processors, but the mesh itself is distributed –each processor holds only a portion of the elements and degrees of freedom, with no single processor having full knowledge of the entire mesh, matrix, or solution.

The FE codes harness the power of MPI in conjunction with two parallel linear algebra libraries, Trilinos and PETSc, enabling sophisticated parallel computations across multiple machines (Heroux et al., 2005; Balay et al., 2019).

3.3.1.2 Mesh adaptivity

The adaptive mesh refinement feature provided by the deal.II library is invaluable for handling the intricate geometries inherent in RVEs. This capability allows for the adjustment of mesh resolution in critical regions, thereby enhancing accuracy while optimizing computational resources. The library efficiently manages hanging nodes, which are a common occurrence in non-uniformly refined meshes, ensuring continuity and accuracy across the entire mesh (Šolín et al., 2008). This adaptability is particularly efficient for handling the complexities in FE modelling of RVEs, and facilitating large-scale simulations.

3.3.2 The madeal code collection

Leveraging the capabilities of the deal.II library, the FE codes developed for this study are compiled into a package named "*madeal*". This package forms a comprehensive suite of open-source codes, which is hosted on GitHub for accessibility and collaboration (Ahmadi, 2024). The *madeal* package includes implementations for both single-field and three-field mixed formulations, catering to various computational needs. The logo of *madeal* is shown in Figure 3.1.

The codes within *madeal* are designed to handle simulations in 3D, flatland, plane strain, and plane stress settings. In plane stress simulations, the single-field formulation is employed for both compressible and nearly incompressible materials. For other settings, the formulation

choice depends on material compressibility: single-field for compressible materials and three-field for nearly incompressible materials.

In the single-field formulation, for interpolation of the field $\mathbf{u}$, Q_n is used by `FE_Q` [1] class in deal.II. The Q_n class is a series of shape functions defined on a quadrilateral (or hexahedral in 3D) mesh, using polynomials of degree n in each coordinate direction to interpolate field variables. For the three-field formulation, $\mathbf{u}$, $\widetilde{p}$, and $\widetilde{J}$ are interpolated with a combination of $Q_n \times DGP_{n-1} \times DGP_{n-1}$. The DGQ, short for discontinuous Galerkin quadrature, uses discontinuous piecewise polynomial functions to approximate field variables, which allows for flexible mesh handling and integration over complex geometries. In deal.II, the class that uses DGP is the `FE_DGP` [2]. For the single-field formulation, all three linearized forms of $\mathcal{L}$ in equations (2.3.26), (2.3.27) and (2.3.28) are implemented in the code, allowing for easy switching between them.

The main features of the *madeal* package are listed:

- **Elastic deformations**: Analysis of infinitesimal and finite deformations of hyperelastic materials.
- **Incompressibility**: Handles nearly incompressible materials using mixed three-field formulations when necessary.
- **Plane stress approximation**: Facilitates nonlinear FEM under plane stress conditions.
- **Canonical boundary conditions**: Implements both affine and periodic boundary conditions. 2D RVE generation: utilises pixel meshing technique to generate 2D RVEs.
- **Benchmarking**: Includes several examples to validate and benchmark the models.
- **Advanced solver options**: Support for various solvers and preconditioners, including iterative solvers and direct solvers.
- **Easy usage**: Modifying the input files allows users to easily change boundary conditions, material properties, and other simulation parameters.

Brief instructions for installing, using, and testing *madeal* package are detailed in Appendix C. This includes step-by-step guidance on setup, execution, and troubleshooting.

3.4 Numerical examples

Numerical examples are presented in this section to evaluate the performance of the developed formulations and codes. This includes a comparative analysis of different 2D and 3D configurations to assess their respective advantages and limitations. The evaluation encompasses

[1] https://www.dealii.org/9.2.0/doxygen/deal.II/classFE__Q.html
[2] https://www.dealii.org/9.2.0/doxygen/deal.II/classFE__DGP.html

Figure 3.1: The logo of *madeal* code collection, version 1.0.

various examples using single-field and three-field formulations for both compressible and nearly incompressible materials.

For all examples, the neo-Hookean material model with the decoupled free energy function (3.2.13) and (2.2.32b) is selected. The number of load increments is set to 10, unless otherwise stated. Quadrilateral elements are utilised for meshing 2D geometries, while hexahedral elements are employed for meshing 3D geometries. The stress values depicted in contour plots are averaged element stresses. The effective *von Mises stress* σ_{eff} in these contour plots, is given by

$$\sigma_{\text{eff}} = \sqrt{\frac{3}{2}\,\boldsymbol{\sigma}_{\text{dev}} : \boldsymbol{\sigma}_{\text{dev}}}\,, \quad \text{where,} \quad \boldsymbol{\sigma}_{\text{dev}} = \boldsymbol{\sigma} - \frac{1}{dim}\,\text{tr}(\boldsymbol{\sigma})\,\mathbf{I}, \tag{3.4.1}$$

where *dim* is the dimension of the problem which is 3 for 3D and planar assumptions and 2 for flatland. For the sake of brevity, the flatland model is henceforth referred to as *2D* in the various figures presented in this section. Since it is more convenient to represent material incompressibility using the Poisson's ratio ν, the material properties are expressed in terms of ν and the shear modulus μ, where the Poisson's ratio can be obtained as $\nu = \frac{3\kappa - 2\mu}{2[3\kappa + \mu]}$.

3.4.1 Model verification

To verify the accuracy of the developed models, three benchmark problems from the literature are examined: Cook's cantilever, the inhomogeneous compression problem, and a curved beam. The results are compared with prior studies to verify the accuracy of the present models.

3.4.1.1 Cook's cantilever

The first example is a well-known problem in nonlinear elasticity, the bending of a tapered beam known as the Cook's cantilever (Cook, 1977). Despite the dominance of bending, there is a significant amount of shear deformation. Figure 3.2 depicts the geometry of a Cook's cantilever under a traction f at the right boundary from a 2D perspective. The thickness of the cantilever is $t = 1\,\text{mm}$. The properties of the material for the neo-Hookean model (3.2.13) are a shear modulus of $\mu = 80.1938\,\text{MPa}$, and Poisson's ratio of $\nu = 0.4999$, chosen in accordance with (Simo and Armero, 1992; Betsch et al., 1996; Wriggers and Hueck, 1996; Reese, 2002; Sze et al.,

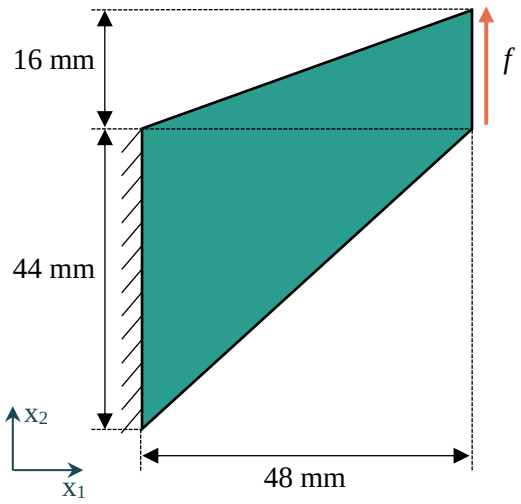

Figure 3.2: The Cook's cantilever under loading f.

Table 3.1: Vertical displacements u_2 (mm) of the right top point of Cook's cantilever.

Applied f (N/mm^2)	Mesh size	2D		plane strain		plane stress		3D*	
		$p_o = 1$	$p_o = 2$	$p_o = 1$	$p_o = 2$	$p_o = 1$	$p_o = 2$	$p_o = 1$	$p_o = 2$
24	2×2	13.91	18.45	13.77	18.29	14.42	19.26	15.47	19.85
	4×4	16.69	18.20	16.65	18.17	17.85	19.75	18.40	19.89
	8×8	17.70	18.20	17.68	18.18	19.24	19.88	19.47	19.93
	16×16	18.00	18.20	17.99	18.19	19.71	19.93	19.79	19.95
	32×32	18.11	18.21	18.10	18.20	19.87	19.95	19.89	19.96
	64×64	18.15	18.22	18.15	18.21	19.93	19.97	19.93	19.96
40	2×2	19.56	24.27	19.67	24.16	21.23	25.17	21.73	25.78
	4×4	22.40	24.20	22.46	24.17	24.18	25.78	24.42	26.01
	8×8	23.54	24.23	23.55	24.22	25.29	25.98	25.50	26.10
	16×16	23.93	24.25	23.93	24.25	25.75	26.07	25.88	26.15
	32×32	24.08	24.28	24.10	24.27	25.96	26.13	26.02	26.17
	64×64	24.16	24.31	24.16	24.30	26.06	26.16	26.09	26.18

*The mesh size for 3D models incorporates one element thickness in the x_3 direction.

2004; Angoshtari et al., 2017; Pascon, 2019). The value of $\nu \approx 0.5$ indicates that the material is nearly incompressible. The geometry is uniformly meshed into a grid of size $n \times n$, where n takes values from the set $\{2, 4, 8, 16, 32, 64\}$ representing the number of elements per edge. The 3D models are meshed with the same mesh size with one element thickness, and in this case, the mesh size is denoted as $n \times n \times 1$.

The vertical displacements u_2 of the cantilever tip (located at the top right corner point) calculated for the traction values $f = 24\,\mathrm{N/mm^2}$ and $f = 40\,\mathrm{N/mm^2}$ is given in Table 3.1. This table compares different FE models with linear ($p_o = 1$) and quadratic ($p_o = 2$) elements, as well as different mesh sizes. The results indicate that the 2D and plane strain models are nearly identical when the mesh is refined. These two models are verified when compared to the results found in (Reese, 2002; Angoshtari et al., 2017; Dhas et al., 2022). The vertical displacements of the tip of the Cook's cantilever for $f = 24\,\mathrm{N/mm^2}$ is reported $u_2 = 18.05\,\mathrm{mm}$ by Reese (2002), $u_2 = 18.2\,\mathrm{mm}$ by Angoshtari et al. (2017) and $u_2 = 18.1\,\mathrm{mm}$ by Dhas et al. (2022) for the finest

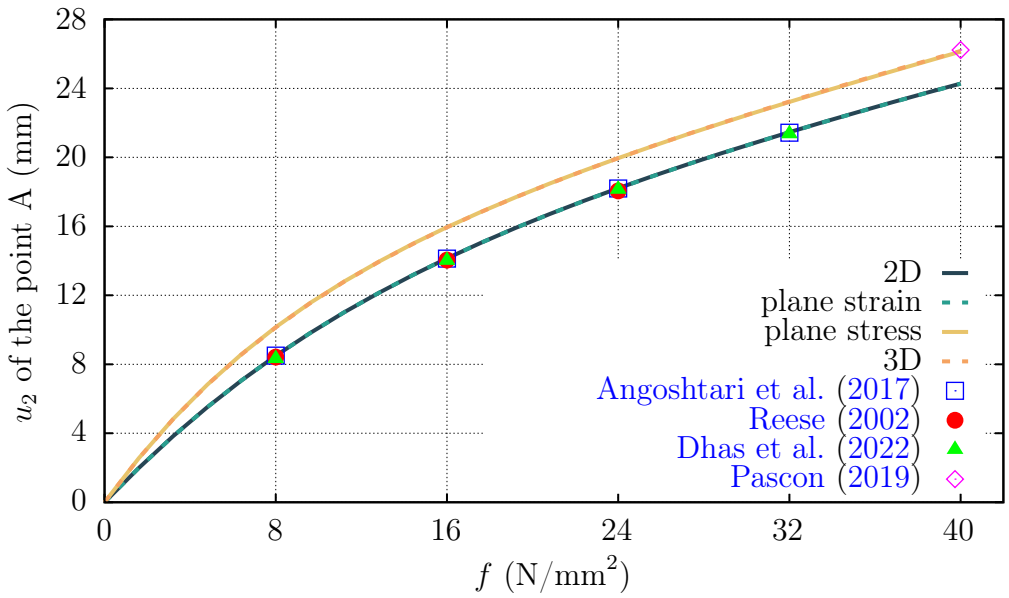

Figure 3.3: Vertical displacements of the tip of Cook's cantilever versus applying traction f.

mesh used in their works. They utilised either the plane strain or the 2D approach. The results exhibit good agreement compared to the 2D and plane strain models for the finest mesh.

Pascon (2019) uses a plane stress approximation with identical material properties and the traction force of $f = 40\,\mathrm{N/mm^2}$. They obtained displacements at the tip as $u_1 = -28.12\,\mathrm{mm}$ and $u_2 = 26.22\,\mathrm{mm}$ for their finest mesh. In the present work finest mesh, with a grid size of 64×64 and $p_o = 2$, yields displacements of the tip ($u_1 = -28.04\,\mathrm{mm}$ and $u_2 = 26.16\,\mathrm{mm}$), showing good agreement with a difference of less than 0.3% compared to their results. The results from the plane stress and 3D models align closely affirming that the plane stress assumption provides a more realistic approximation for thin structures like Cook's cantilever. Vertical displacements for the plane stress and 3D cases are notably higher than those for the plane strain and 2D models, with a percentage difference of approximately 8% at the maximum load. Furthermore, results for higher-order elements converge more rapidly, with this effect being more pronounced than that of mesh size.

Remark. It should be noted that the 3D model is unconstrained in the x_3 direction, allowing free movement. However, if the displacement of the cantilever is fixed in the x_3 direction so that it is trapped between two walls, the results will align more closely with the 2D and plane strain cases. For instance, when the above Cook's cantilever is constrained in the x_3 direction, using the most refined mesh ($64 \times 64 \times 1$) with $p_o = 2$, the vertical displacements of the tip for the 3D model when applying $f = 24\,\mathrm{N/mm^2}$ is calculated as $u_2 = 18.21\,\mathrm{mm}$, which is closer to the plane strain case than the plane stress one. □

To further demonstrate the verification of the present results, the vertical displacements of the tip of the cantilever versus the applied traction f is depicted in Figure 3.3. It is noted that the results from other research articles correspond to the finest mesh used in those studies. This graph highlights the nonlinear relationship between the applied load and the displacement

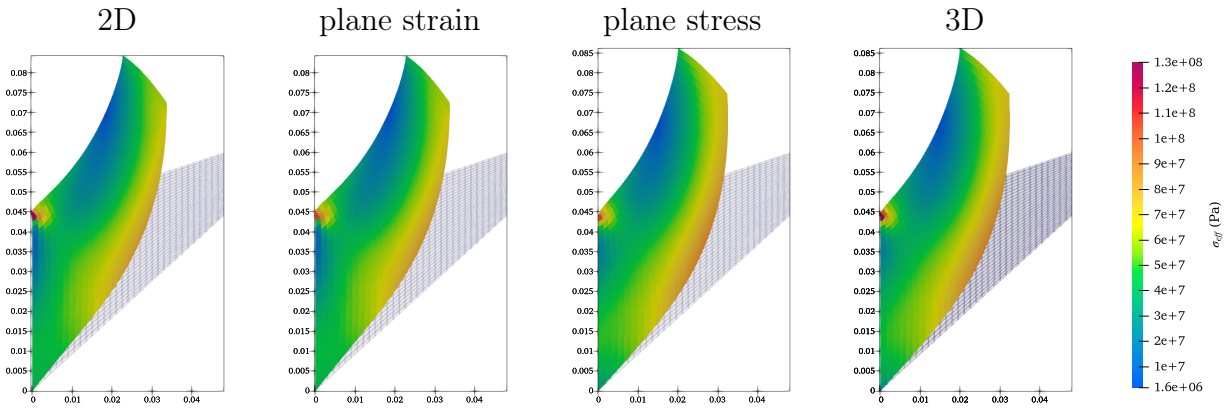

Figure 3.4: The deformed Cook's cantilever with 32×32 mesh size, $p_o = 2$ for different models under $f = 40\,\mathrm{N/mm^2}$.

of the tip.

Remark. It is noted that some of the references that the present results were compared against used a slightly different version of the volumetric energy density function, such as the ones shown in Equations (2.2.32). However, despite this variation, the differences observed in the results are negligible since the material is nearly incompressible ($\nu = 0.4999$). □

Figure 3.4 shows the deformed Cook's cantilever with 32×32 mesh size, $p_o = 2$ and $f = 40\,\mathrm{N/mm^2}$ for different configurations. The first element from the top left corner is critical in this problem since it undergoes a significant distortion. As seen from the contours, this element is more distorted in 2D, plane strain and 3D models than in the plane stress model.

Figure 3.5 illustrates the impact of the thickness (t) of the cantilever on the vertical displacements of the structure tip for $f = [24\,t]\,\mathrm{N/mm^2}$. As the thickness increases, the results from the 3D models diverge further from the plane stress bound and approach those of the 2D/plane strain models, as anticipated. This highlights the importance of careful selection of modelling approaches, considering the nature of the problem under analysis.

Table 3.2: Normalised runtimes for different FE simulations with linear and quadratic elements.

Mesh size	2D		plane strain		plane stress		3D	
	$p_o = 1$	$p_o = 2$	$p_o = 1$	$p_o = 2$	$p_o = 1$	$p_o = 2$	$p_o = 1$	$p_o = 2$
4×4	1×10^{-4}	3×10^{-4}	1×10^{-4}	4×10^{-4}	1×10^{-4}	3×10^{-4}	6×10^{-4}	0.01
8×8	2×10^{-4}	1×10^{-3}	2×10^{-4}	2×10^{-3}	2×10^{-4}	1×10^{-3}	2×10^{-3}	0.05
16×16	8×10^{-4}	6×10^{-3}	9×10^{-4}	7×10^{-3}	7×10^{-4}	4×10^{-3}	0.01	0.2
32×32	4×10^{-3}	0.03	5×10^{-3}	0.03	3×10^{-3}	0.02	0.06	1

Table 3.2 presents the computational runtimes for different models. The values are normalised with respect to the runtime of the 3D model with a mesh size of 32×32 and $p_o = 2$. The number of elements for the finest mesh, 32×32, is 1024 for all four models, while the number of nodes are 14594, 14594, 8450, and 46217, and the total number of degrees of freedom are 7297, 7297, 4225, and 15405, for the 2D, plane strain, plane stress, and 3D models with $p_o = 2$, respectively. To provide a clearer demonstration, the computational cost of the

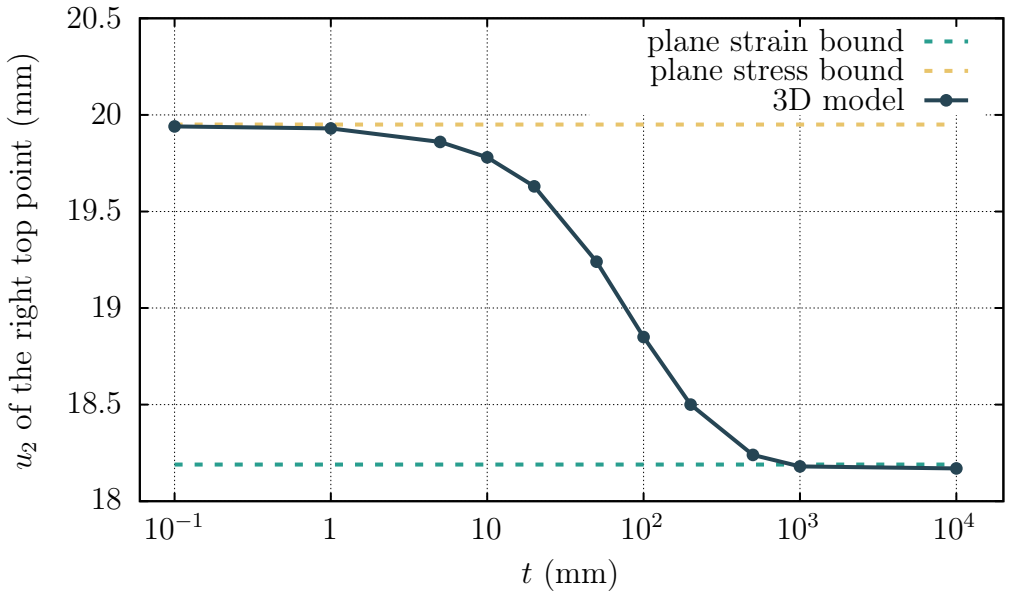

Figure 3.5: The effect of the thickness of the Cook's cantilever on the vertical displacements of the tip.

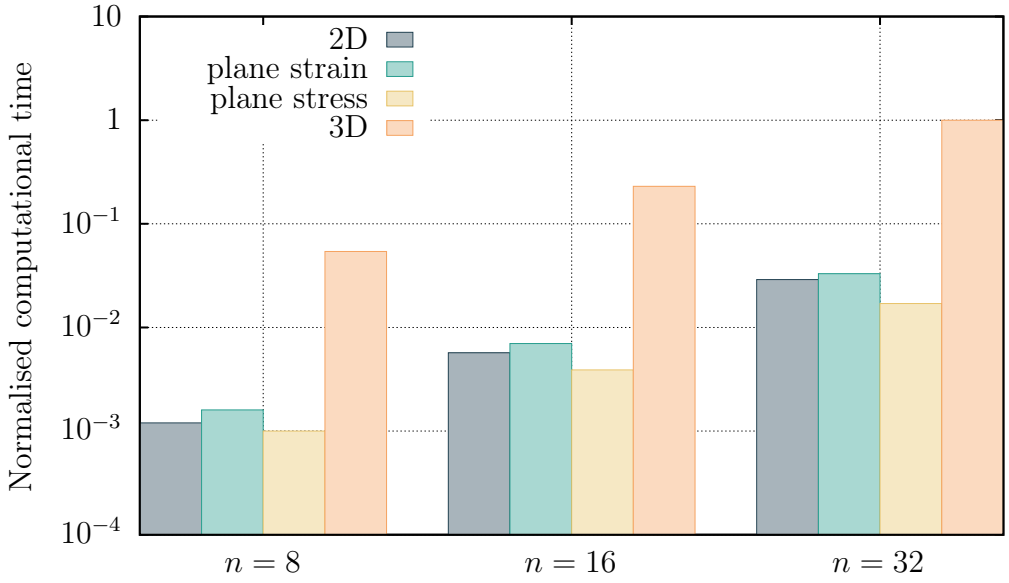

Figure 3.6: Normalised computational cost of the different FE models.

different models with different mesh sizes is illustrated in Figure 3.6. The following trend is observed:

$$t_{\text{3D}} \gg t_{\text{plane strain}} > t_{\text{2D}} > t_{\text{plane stress}} \,. \tag{3.4.2}$$

Although the classic single-field model for plane stress requires additional Newton–Raphson iterations to determine C_{33}, its computational time is lower than that of the plane strain and 2D mixed-formulation models due to fewer degrees of freedom. The planar and 2D models exhibit considerably lower runtimes compared to the 3D model. For instance, with the finest mesh and $p_o = 2$, the runtime for the 3D model is approximately 50 times longer than that of the plane stress model. Given the close results between the 3D and plane stress models and the significant difference in runtime, using a 2D model is preferable when applicable.

3.4.1.2 Inhomogeneously compressed block

The second example explores the problem of a nonlinear elastic block undergoing inhomogeneous compression, also known as the "punch problem". Figure 3.7 illustrates the geometry, loading, and boundary conditions. The bottom surface is fixed in the x_2 direction but can freely move in the x_1 direction. It is also noted that the top surface of the block is constrained in the x_1 direction. For the 3D model, the back and front surfaces are constrained in the x_3 direction, simulating a scenario where the block is confined between two rigid walls. The material properties are the same as those of the previous example. To leverage problem symmetry, the FE analysis only considers half of the geometry by dividing the block into two halves, each measuring 10 mm × 10 mm × 10 mm.

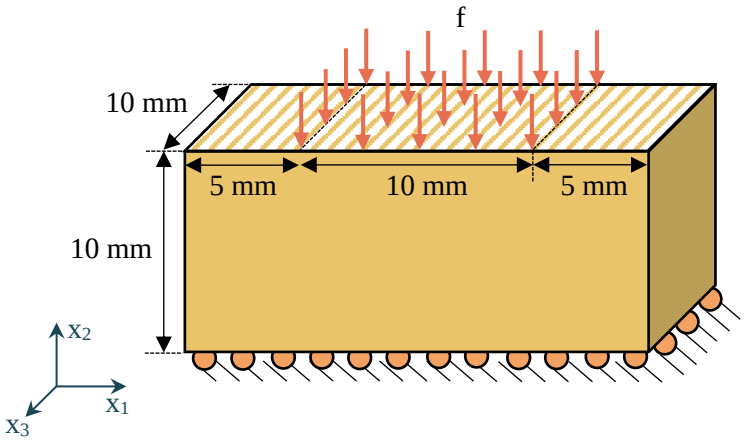

Figure 3.7: The block under inhomogeneous compression; the top surface is constrained in x_1 direction.

The geometries are uniformly meshed, that is, $n \times n$ ($n \times n \times n$ for 3D), where n is the number of elements per each edge and $n \in \{2, 4, 8, 16, 32\}$. Defining the maximum compression of the block as the percentage of the maximum vertical displacements of a node relative to its maximum achievable displacement, Figure 3.8 illustrates the maximum compression across different models, considering various mesh sizes and polynomial degrees of the elements. The

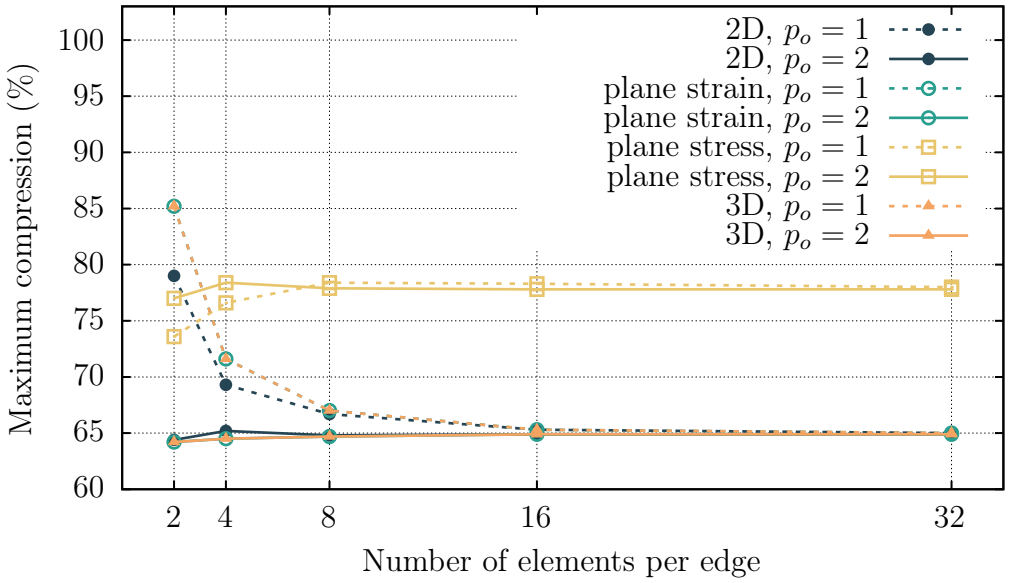

Figure 3.8: Maximum compression of the block for different mesh sizes and applied traction of $f = 6000\,\mathrm{N/mm^2}$.

centre of the block naturally experiences the maximum compression, a trivial observation in such symmetrical deformations. It is evident that increasing the number of elements leads to convergence in results for all models. By $n = 16$, the results appear to be converged across all different models. Moreover, models utilising quadratic elements exhibit faster convergence than those with linear elements; even a model with $n = 2$ and quadratic elements demonstrates high accuracy. Given that the block is confined between two walls, restricting movement in the x_3 direction, the 3D model is expected to converge to the plane strain model, which indeed occurs. Interestingly, the block under plane stress condition experiences approximately $\sim 20\%$ higher compression than other models.

Figure 3.9 depicts the maximum compression of the block versus the applied traction f. The compression demonstrates nonlinear behaviour across the range of applied traction. The recurring trend persists; the plane stress model demonstrates higher compression relative to all other models, a distinction notably apparent even at lower loads. This graph also validates the 3D, 2D, and plane strain models by comparing our results against those from previous studies (Angoshtari et al., 2017; Reese, 2002; Dhas et al., 2022), demonstrating good agreement. These studies utilised either a 2D model or a plane strain model.

To validate the results of the plane stress model, a traction of $f = 12000\,\mathrm{N/mm^2}$ is applied, following the study by Pascon (2019). The maximum compression under this traction is measured as 86.7%, closely matching the approximately 87% compression reported by Pascon (2019) at the centre. The compressed block with $n = 16$ and $p_o = 2$ is illustrated in Figure 3.10, demonstrating the capability of the formulation to model extreme deformations.

Given the near-identical results between the 2D and plane strain models in these examples, it is opted to present only the plane strain model in subsequent analyses. This similarity is

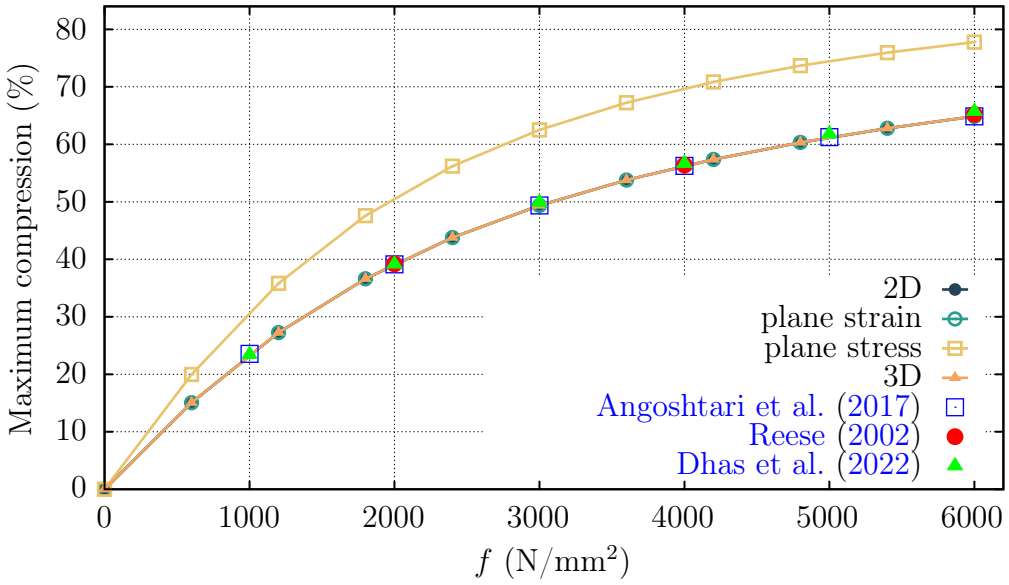

Figure 3.9: Maximum compression of the block versus applying traction f.

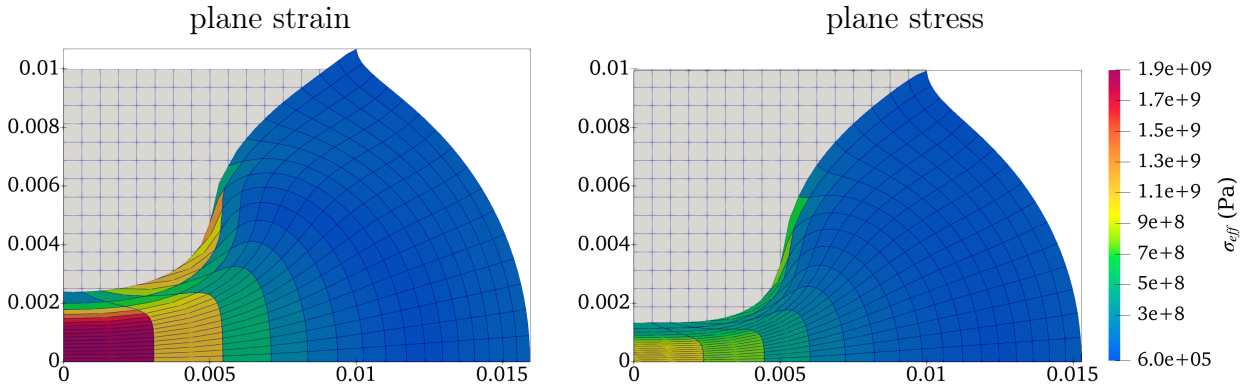

Figure 3.10: Compressed block with applied traction of $f = 12000\,\mathrm{N/mm^2}$ under planar conditions.

expected for simpler hyperelastic models, like the neo-Hookean model, where strain energy primarily depends on the first invariant, $I_{\widehat{C}}$, effectively capturing in-plane deformations in both cases. However, it is important to note that this congruence may not hold for more complex hyperelastic models, such as the Yeoh or Fung formulations (Chagnon et al., 2015; Fung, 2013). These models include higher-order terms and additional strain invariants that introduce dependencies on out-of-plane components. For these models, plane strain typically provides a more accurate representation than 2D formulations, particularly in scenarios involving large deformations or multiaxial stresses.

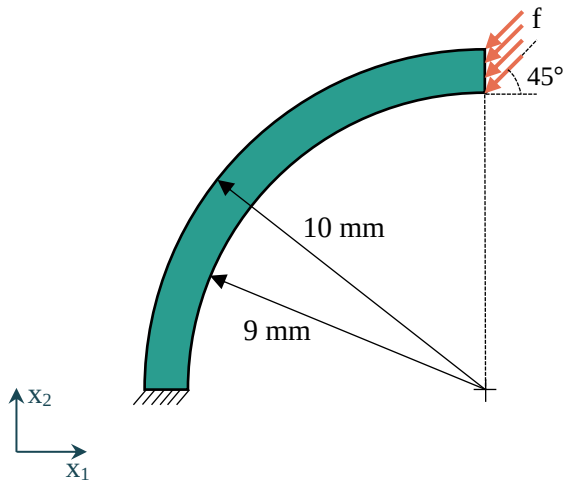

Figure 3.11: A curved beam under traction f.

3.4.1.3 Curved beam

The first two examples were performed on nearly incompressible materials. This example verifies the validity of FE codes for compressible hyperelastic materials.

Consider a curved beam of thickness $t = 1\,\text{mm}$ subjected to boundary conditions and traction f as depicted in Figure 3.11. The material is compressible, characterized by a shear modulus $\mu = 80.1938\,\text{MPa}$, and Poisson's ratio $\nu = 0.2271$, chosen in accordance with Nguyen et al. (2021). This problem utilises a 9×127 mesh and 25 load steps. Figure 3.12 illustrates the nonlinear relationship between the traction f and displacement magnitude $||\mathbf{u}||$ at the top corner point of the right edge. It compares the present results with those in Nguyen et al. (2021), where a 2D model was utilised. The analysis considers plane strain and plane stress conditions for both compressible and nearly incompressible materials. For the nearly incompressible case, the same shear modulus but Poisson's ratio of $\nu = 0.4999$ is considered. The present model for compressible materials with plane strain condition shows good agreement with the referenced work. Furthermore, it is observed that while there is little difference between plane strain and plane stress results for compressible materials, a significant distinction exists in nearly incompressible models, indicating pronounced sensitivity to incompressibility. This difference is further highlighted by the deformed shapes depicted in Figure 3.12. These contours are plotted for $f = \{0, 2, 3, 5\}\,\text{N/mm}^2$.

3.4.2 Inhomogeneous problems

After the verification of the FE models, further examples featuring inhomogeneities are introduced to assess the performance of the FE framework in simulating extreme nonlinear behaviour of inhomogeneous structures. Both compressible and nearly incompressible materials are analysed for the subsequent examples. The volumetric average stress in these examples is calculated

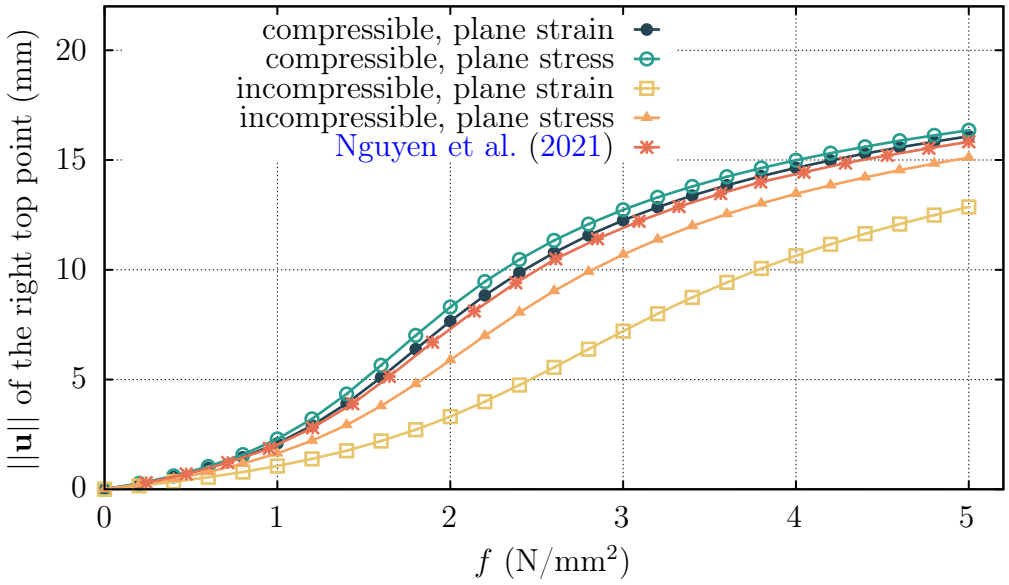

Figure 3.12: Displacement magnitude of the top right point of the curved beam versus applying traction f. The result by Nguyen et al. (2021) is for compressible material in 2D.

as

$$\widetilde{\sigma} = \frac{1}{v}\int_{\Omega_x} \sigma \, \mathrm{d}v, \tag{3.4.3}$$

for each stress component. Sufficiently refined meshes are utilised to discretise the geometry, ensuring the convergence of results.

3.4.2.1 Plate with a hole

In this example, the stretching of a square plate with a central hole is explored, a scenario frequently encountered in structural mechanics and engineering. Figure 3.14 schematically illustrates the geometry, loading, and boundary conditions for this example. The hole occupies 40% of the area of the plate in the reference configuration. The left end is fixed and the right end is displaced to a length twice that of the plate. The shear modulus remains consistent with those used in previous examples, while the value of Poisson's ratio is adjusted to $\nu = 0.3$ for the compressible case.

Figure 3.15 illustrates the stretched plate with a central hole, showcasing results obtained under plane strain and plane stress conditions for the nearly incompressible material (a) and the compressible material (b). While the deformed plates appear similar, subtle differences highlight distinctions between the two models. Specifically, plane stress cases exhibit a larger in-plane area, indicating the presence of out-of-plane displacement. These discrepancies are more conspicuous in the compressible material. Notably, the in-plane area remains unchanged for the nearly incompressible model under plane strain conditions.

Figure 3.16 plots the volumetric average Cauchy stresses for both nearly incompressible and compressible materials under plane strain and plane stress conditions. The graph includes the

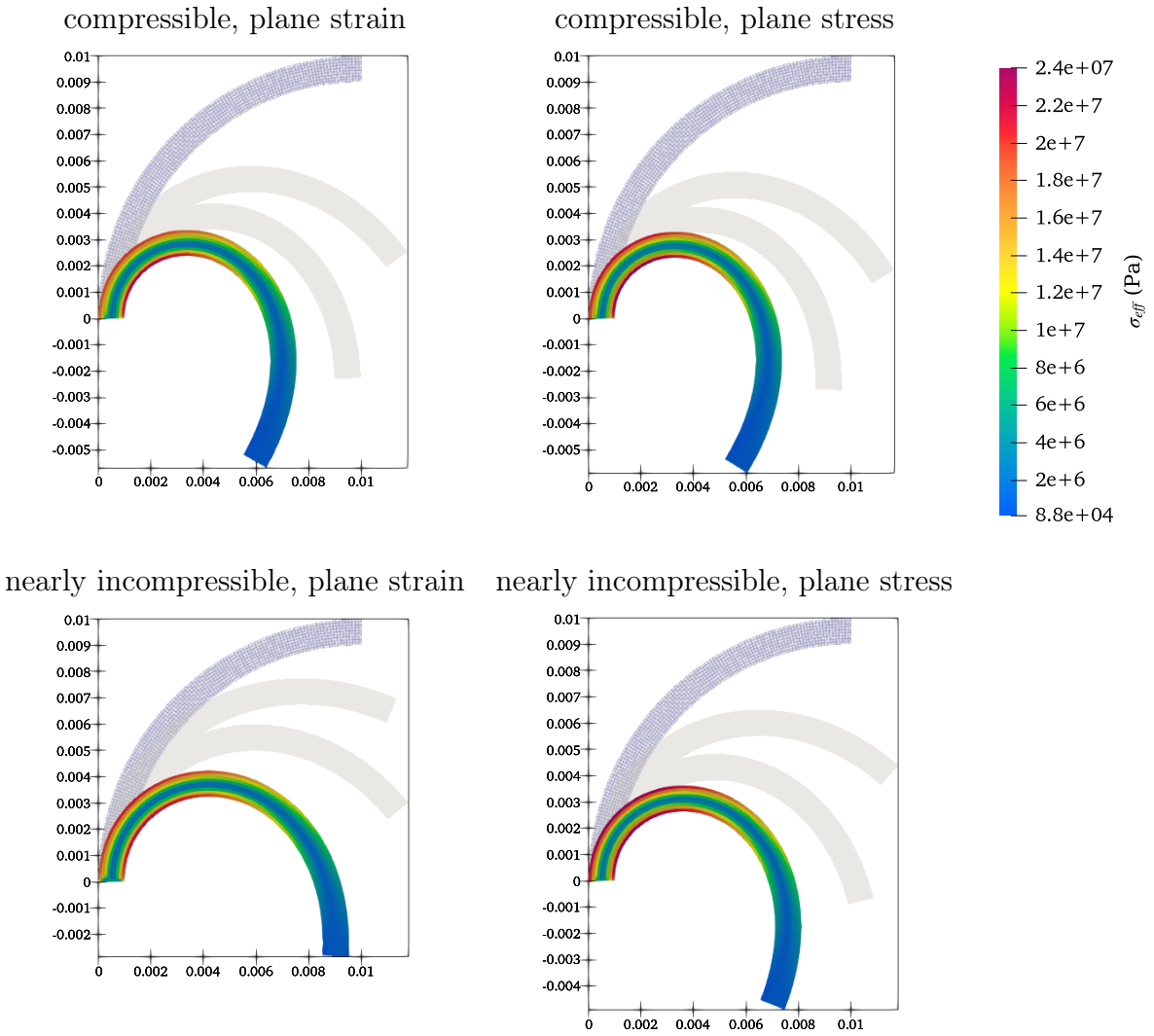

Figure 3.13: The deformed curved beams for $f = \{0, 2, 3, 5\}$ N/mm^2. The shaded beams represent the corresponding configurations for each force value.

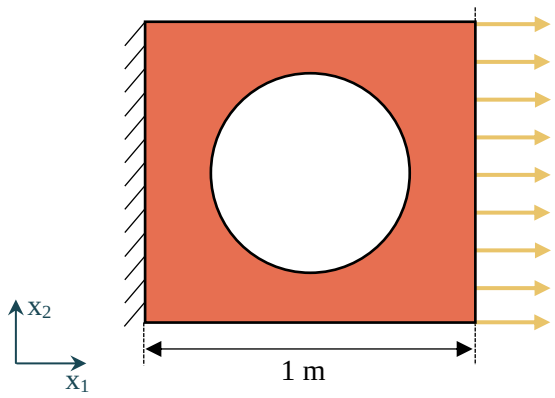

Figure 3.14: A plate with a central hole under stretching.

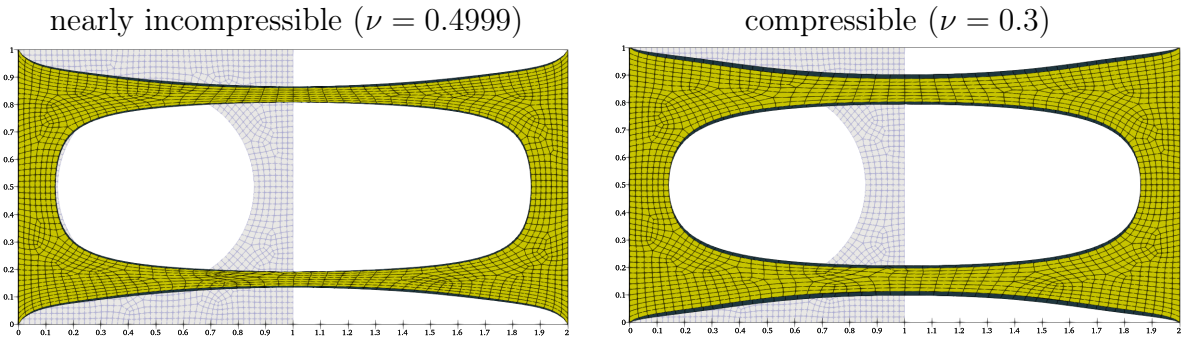

Figure 3.15: The stretched plate with a hole for plane strain (dark colour) and plane stress (bright colour) assumptions.

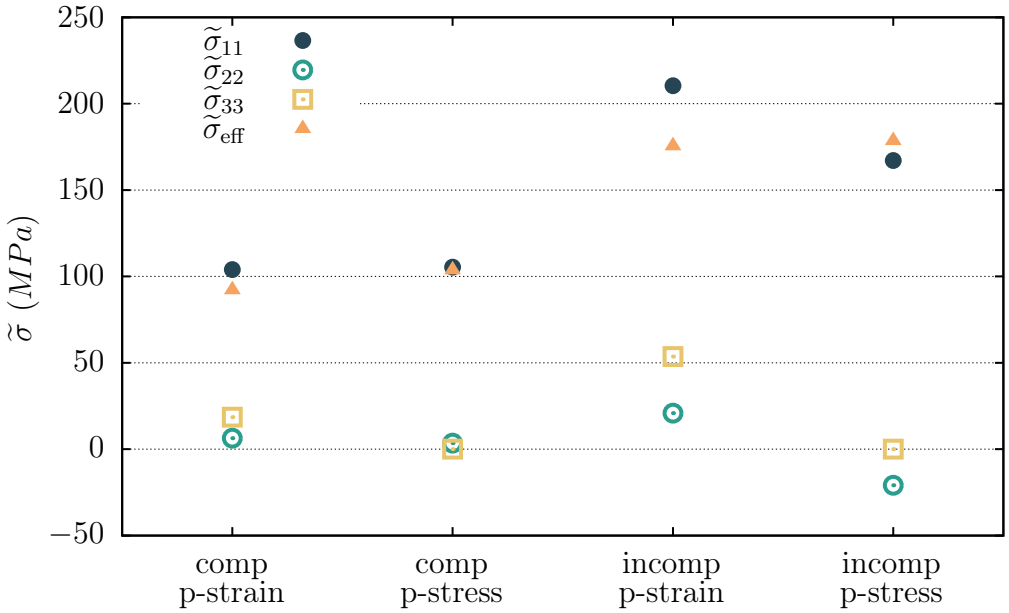

Figure 3.16: Comparison of volumetric average stress of plate with a hole between plane strain and plane stress models for stretch $\lambda = 2$.

three normal components and the effective von Mises stress at the maximum stretch, $\lambda = 2$. The average stress component along the loading direction, $\widetilde{\sigma}_{11}$, shows similar values for both plane strain and plane stress models in compressible materials. However, for nearly incompressible materials, $\widetilde{\sigma}_{11}$ is noticeably higher in the plane strain model compared to the plane stress model. The $\widetilde{\sigma}_{22}$ component is significantly smaller than $\widetilde{\sigma}_{11}$ across all models. In compressible materials, $\widetilde{\sigma}_{22}$ of the plane strain model surpasses that of the plane stress model. For nearly incompressible materials, $\widetilde{\sigma}_{22}$ remains positive in the plane strain model, while it becomes negative in the plane stress model. As expected, the $\widetilde{\sigma}_{33}$ component is zero for the plane stress models. However, for nearly incompressible materials in the plane strain model, $\widetilde{\sigma}_{33}$ exceeds more than twice the value observed in the compressible case. The effective von Mises stress, $\widetilde{\sigma}_{\text{eff}}$, shows remarkable consistency between the plane strain and plane stress models for nearly incompressible materials, with both values surpassing their compressible counterparts. In compressible materials, the plane stress model slightly outpaces the plane strain model in terms of $\widetilde{\sigma}_{\text{eff}}$. Overall, stress levels in nearly incompressible materials are notably higher than in

compressible materials. This difference arises due to the constraint on volume change in nearly incompressible materials, leading to a greater resistance to deformation. Consequently, the stresses required to achieve the same level of deformation are considerably higher in structures made of nearly incompressible materials compared to their compressible counterparts.

In order to analyse the difference in deformation under plane stress and plane strain conditions, the normalised displacement difference, ζ is defined as

$$\zeta = \frac{1}{n_{\text{nod}}} \sum_{i=1}^{n_{\text{nod}}} ||\boldsymbol{u}_s^i - \boldsymbol{u}_n^i|| \,, \tag{3.4.4}$$

where $\boldsymbol{u}_s^i$ and $\boldsymbol{u}_n^i$ represent the displacement vectors of the ith node in the plane stress and plane strain models, respectively. The variation of ζ for compressible and nearly incompressible materials is compared in Figure 3.17. Looking at the trends, it is observed that the ζ values for the compressible material are consistently higher compared to the nearly incompressible material across all stretch values. While for the compressible material, ζ exhibits a relatively linear increase with stretch, the trend for the nearly incompressible material appears nonlinear.

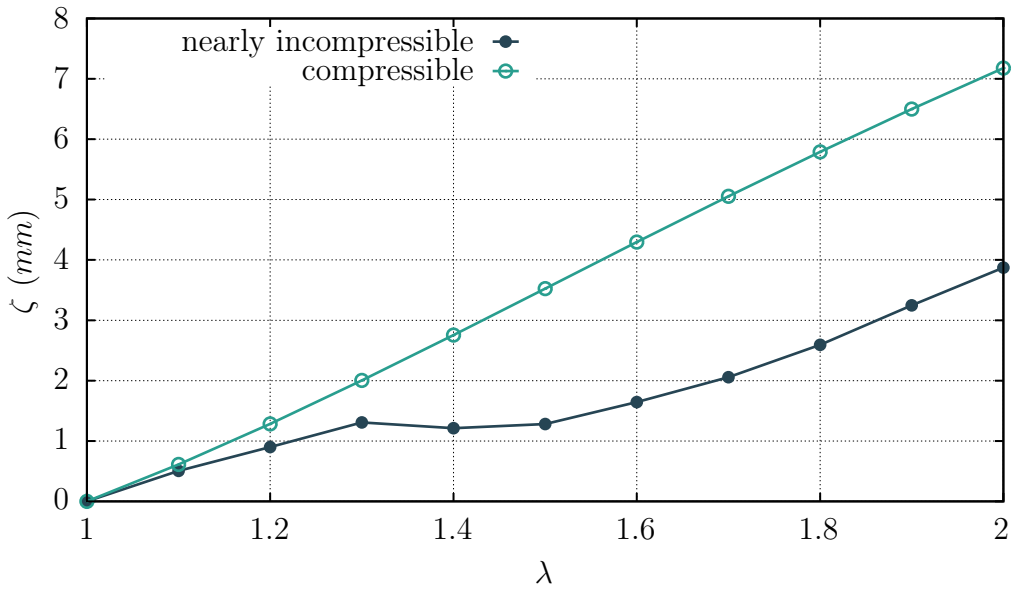

Figure 3.17: Variation of the normalised displacement difference, ζ for a plate with a central hole under stretching.

3.4.2.2 Plate with several particles

Moving on to the next example, the stretching of a square plate containing several circular particles schematically shown in Figure 3.18 is investigated. The left end is fixed, and the right end is displaced to a length twice that of the plate. Ten particles that are stiffer than the matrix are randomly positioned within the matrix material. The particles possess a shear modulus of $\mu_p = 50\,\text{MPa}$ and a Poisson's ratio of $\nu_p = 0.3$. The matrix material is characterized by a shear modulus of $\mu_m = 1\,\text{MPa}$ and a Poisson's ratio of $\nu_m = 0.4999$ for the nearly

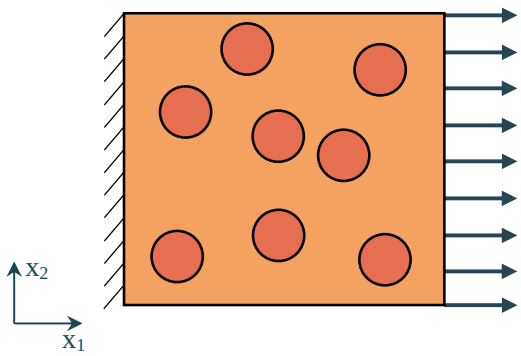

Figure 3.18: Loading and boundary conditions of the plate reinforced with particles.

incompressible case or $\nu_m = 0.3$ for the compressible case. The volume fraction of the particles is fixed at 25% of the total volume of the plate in the reference configuration. Figure 3.19 visualizes the deformed plates reinforced by circular particles under plane strain and plane stress conditions for compressible and nearly incompressible materials. The contour bars illustrate the distribution of von Mises stress values. The results indicate that compressible plates exhibit less deformation perpendicular to the stretch direction compared to the nearly incompressible ones. This discrepancy arises due to the compressible nature of the material, which allows for more volumetric changes. Additionally, the circular particles mostly remain undeformed due to their higher stiffness than the matrix material. For both materials, plane stress deformation perpendicular to the stretch direction is less pronounced, primarily because the plane strain assumption restricts out-of-plane deformation, leading to more constrained behaviour in this direction. Moreover, the plots underscore that the positions of the particles alter differently in plane strain and plane stress models post-deformation.

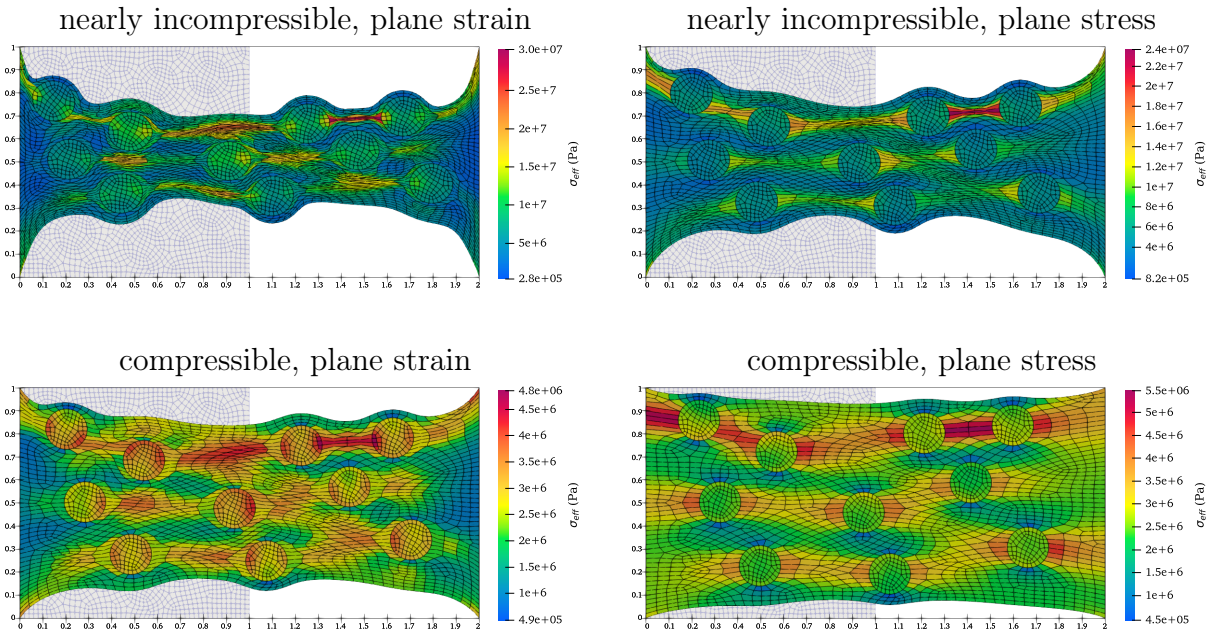

Figure 3.19: The compressible ($\nu = 0.3$) and nearly incompressible ($\nu = 0.4999$) stretched plate with several particles for plane strain and plane stress models.

Figure 3.20 illustrates the volumetric average Cauchy stress versus stretch. The plot showcases the three normal stress components along with the effective von Mises stress. Figure 3.21 illustrates the volumetric average Cauchy stress variation within the plate containing multiple particles under both plane strain and plane stress conditions. Analysing the graphs, it is observed that the nearly incompressible plates visibly experience higher stresses compared to the compressible plates, reflecting the influence of material compressibility on stress distribution. This disparity is particularly notable in the σ_{22} and σ_{33} components. Moreover, the stress components in the plane stress model are generally lower compared to the plane strain model.

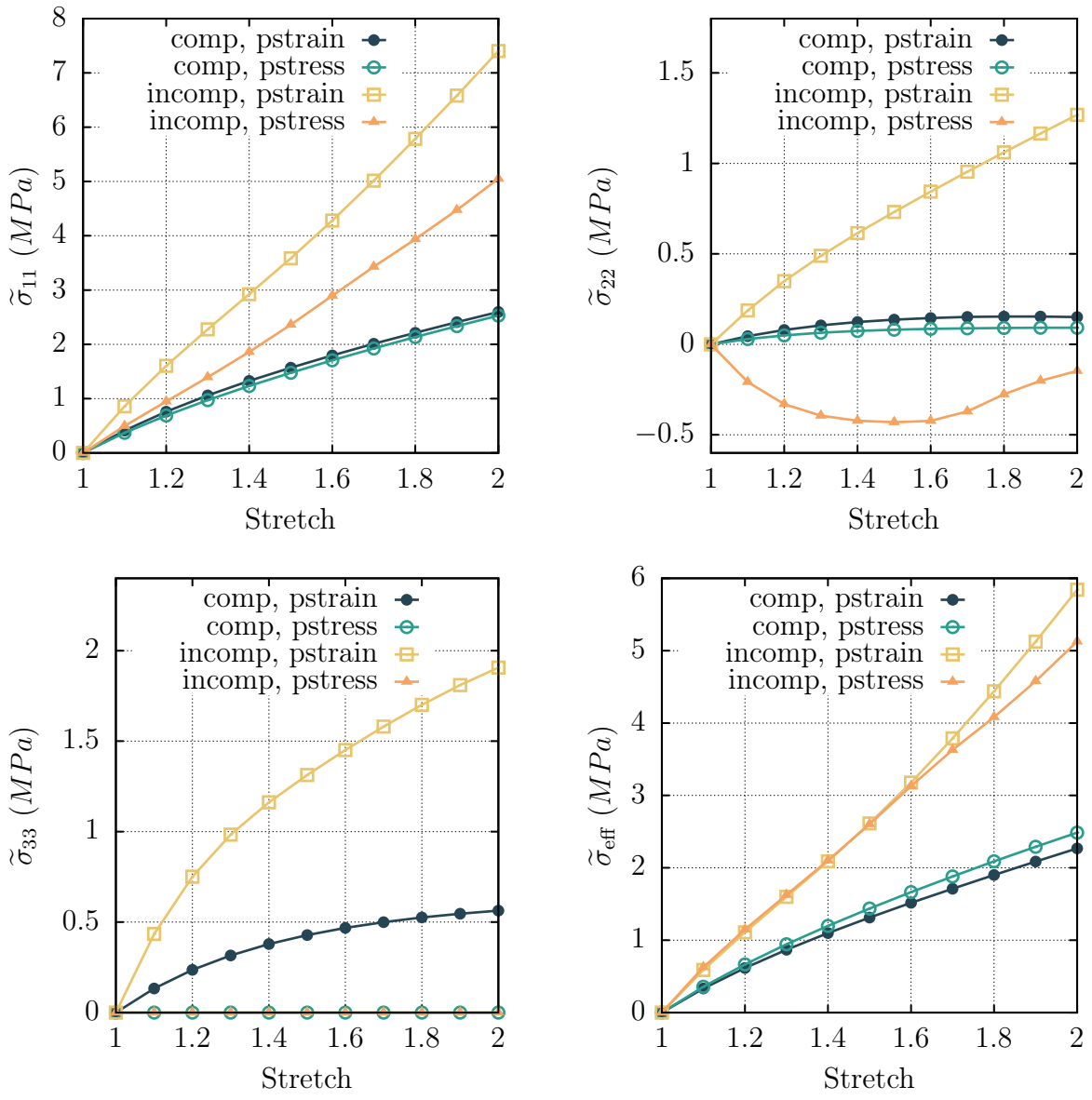

Figure 3.20: Comparison of volumetric average stress of plate with several particles for $\widetilde{\sigma}_{11}$, $\widetilde{\sigma}_{22}$, $\widetilde{\sigma}_{33}$, and $\widetilde{\sigma}_{\text{eff}}$.

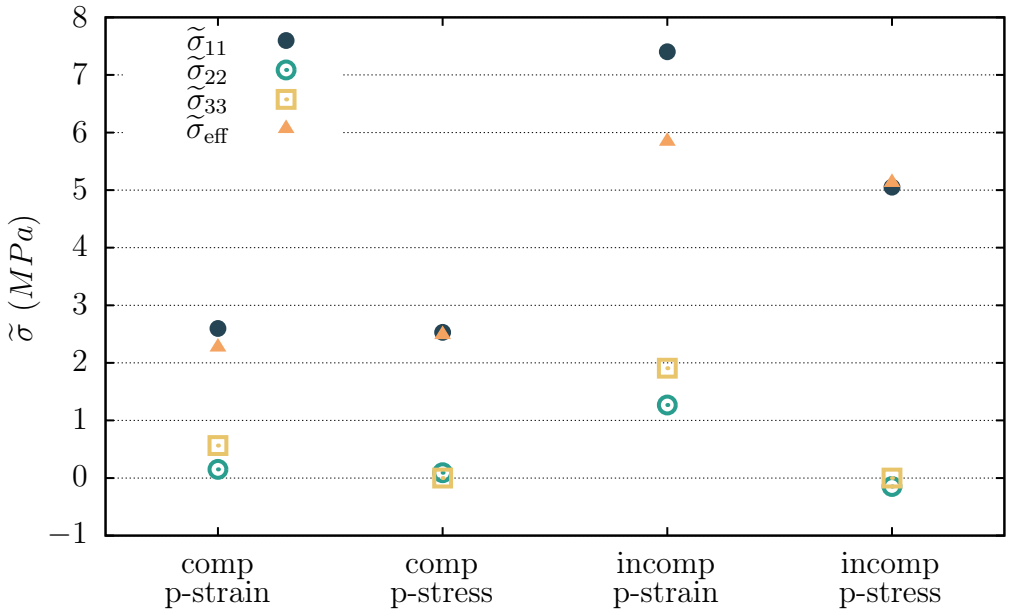

Figure 3.21: Comparison of volumetric average stress of a plate with several particles between plane strain and plane stress models for stretch $\lambda = 2$.

3.4.2.3 Plate with short fibres

In the final example, the stretching of a square plate containing short fibres, a scenario commonly encountered in composite materials and reinforced structures (Ahmadi et al., 2017; Gao et al., 2019), is investigated. A total of 25 rectangular fibres are distributed throughout a plate, with the volume fraction of the fibres set at 3%. The fibres are randomly dispersed in terms of both position and angle within the plate. The aspect ratio of the fibres, defined as the ratio of length to diameter, is chosen as $(l/d) = 10$, where l represents the length and d denotes the diameter of the fibres. The matrix material properties remain consistent with the previous example: $\mu_m = 1\,\text{MPa}$ and $\nu = 0.4999$ for the nearly incompressible case, or $\nu_m = 0.3$ for the compressible case. The fibres have a shear modulus of $\mu_f = 50\,\text{MPa}$ and a Poisson's ratio of $\nu_f = 0.3$. Applying consistent boundary conditions and stretching procedures as employed in two prior examples, the deformed plates under plane strain and plane stress conditions for both compressible and nearly incompressible materials are analysed. Figure 3.22 depicts the volumetric average Cauchy stress components and effective von Mises stress under both plane strain and plane stress conditions. Upon analysis, trends similar to those observed in the previous example become apparent, with the stress components in the plane stress model generally exhibiting lower values compared to the plane strain model.

Furthermore, Figure 3.23 presents contour plots illustrating the von Mises stress distribution within the plate, where the presence of embedded fibres profoundly influences stress patterns. The contour plots convey insights similar to those in the previous example, yet with a notable distinction. Unlike the circular particles, the fibres undergo considerable bending and twisting, deviating from their initial shapes. This behaviour arises from the elongated shape of fibres, contrasting with the uniform shape of circles despite both having equivalent stiffness. The

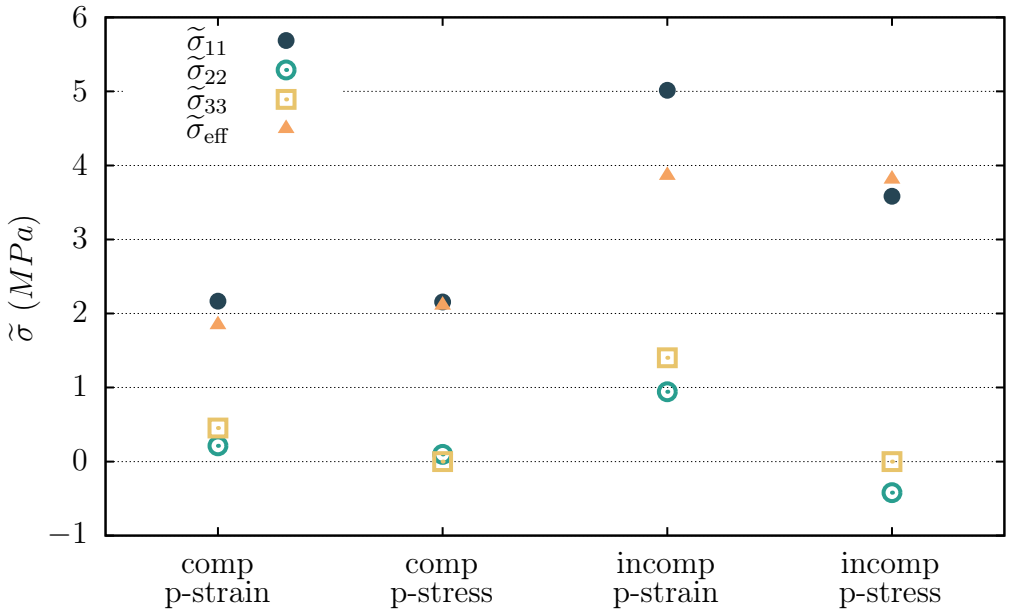

Figure 3.22: Comparison of volumetric average stress of a plate with short fibres between plane strain and plane stress models for stretch $\lambda = 2$.

bending and twisting of fibres are more pronounced in the case of incompressible materials, primarily due to the matrix undergoing significantly more necking. This emphasizes the critical importance of such discrepancies between plane stress and plane strain models in applications where precise particle positioning significantly influences overall performance. Moreover, it can be seen that the fibres aligned with the loading direction exhibit higher stress levels compared to those not aligned with the loading direction.

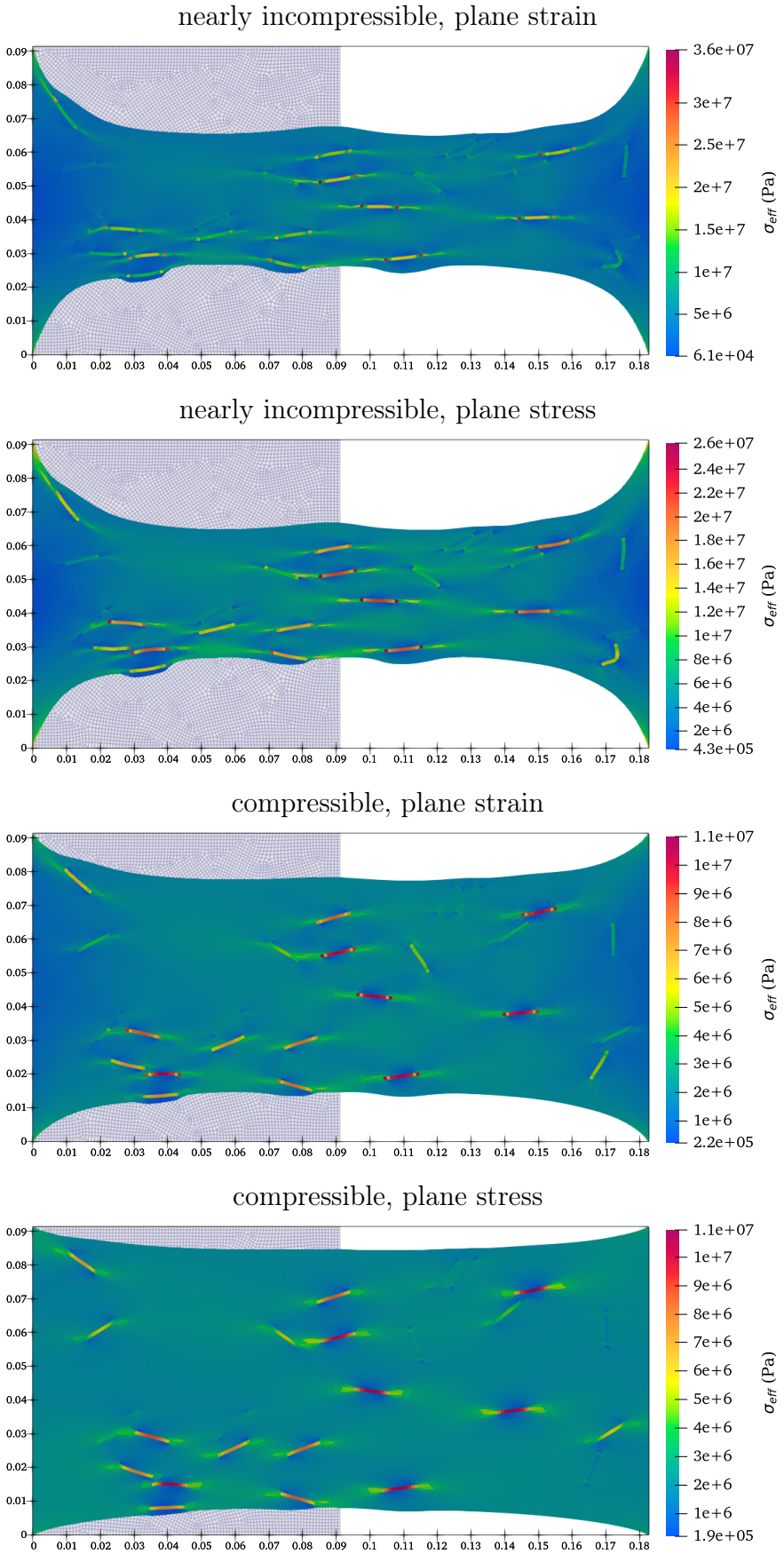

Figure 3.23: The compressible ($\nu = 0.3$) and nearly incompressible ($\nu = 0.4999$) stretched plate with short fibres for plane strain and plane stress models.

Chapter 4

Computational modelling of microstructural deformation

Under finite deformations, elastomeric composite properties change due to fibre repositioning and reorientation. In this chapter, the finite element framework established in the previous chapters is further developed to investigate the finite deformations of fibre-reinforced composites with periodic microstructures. To this end, 2D RVEs are generated by randomly dispersing fibres in a polymer matrix. Two types of admissible boundary conditions are examined. Pixel meshing techniques are introduced which facilitate FE modelling of RVEs with the admissible boundary conditions.

A comprehensive numerical analysis assesses the impact of various parameters, such as loading condition, distribution patterns and number of dispersed fibres, on the mechanical behaviour of the composites. Choosing an appropriate RVE configuration along with imposing proper boundary conditions to analyse RVEs under finite deformations, while considering accuracy, efficiency, and convenience, is a key challenge addressed in this chapter. This analysis underpins subsequent further investigation into piezoresistive behaviour.

4.1 Fibre-reinforced RVEs

Composite materials exhibit distinct microstructures at certain length scales, significantly influencing their macroscopic behaviour. Computational micromechanics adopts a state-of-the-art method that focuses on a small yet comprehensive structural region known as an RVE. The RVE can be defined as the smallest unit of a material that encapsulates all critical microstructural features. Initially, models typically included a single particle within an RVE (Joshi et al., 2012; Ahmadi et al., 2019c; Liu and Chen, 2003; Chen and Liu, 2004). However, to more accurately represent the complex interactions between particles and to enhance the fidelity of simulations, recent research has shifted towards multi-particle RVEs. These multi-particle models feature several inclusions arranged in various distribution patterns, such as aligned or random, thereby providing a more comprehensive understanding of composite material behaviour under different

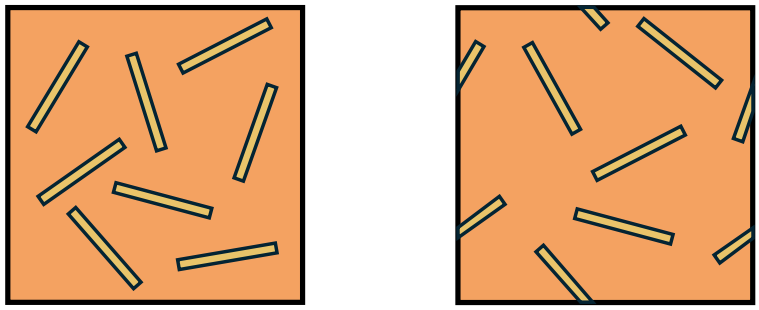

(a) (b)

Figure 4.1: 2D RVEs of fibre-reinforced composites: (a) whole fibres embedded within the RVE, and (b) fibres cutting boundaries, creating periodic patterns.

conditions (Duong et al., 2008; Zhang and Yi, 2008; Pal and Kumar, 2016; Ahmadi et al., 2017, 2019b; Javid and Biglari, 2020; Matos et al., 2019). An ideal RVE is large enough to encompass essential microstructural information but remains considerably smaller than the overall structure, minimally affecting macroscopic gradients (Bargmann et al., 2018).

In this study, the RVE serves as a conceptual tool for analysing fibre reorientation and spacing changes under deformation. The approach employs a generalised 2D structure with randomly dispersed fibres in various orientations within a polymer matrix, without consideration of specific length scales. Equal thickness is assumed for both fibres and matrix; while this differs from real-world applications, accurately capturing these variations would require either 3D modelling or approximating it as 2D plane stress with varying thickness that ignores the wrap-around matrix. The fibres are modelled as rectangular shapes to approximate the geometry of fillers such as CNTs and short carbon fibres. While these fillers are cylindrical in nature, the rectangular approximation is reasonable for a 2D geometry and simplifies the modelling process. This abstraction, free from specific physical dimensions or thickness variations, provides useful insights into fibre reorientation within the composite.

4.1.1 Fibre distribution

Two types of RVE configurations are considered: fully embedded and cut-fibre, as schematically illustrated in Figure 4.1. The first RVE embeds each fibre entirely within the matrix, avoiding any intersection with the boundaries. The second type allows fibres to intersect a boundary, with the remainder of the fibre re-entering from the opposite side, forming a periodic pattern. This periodic arrangement enables the simulation of inhomogeneous materials, effectively modelling them as if they were infinitely extended (Michel et al., 1999).

Both configurations are widely used in the literature and produce repetitive RVE patterns (Watanabe, 2002; Sukiman et al., 2017; Ahmadi et al., 2019a,d). Cut-fibre configuration, while representing more realistic microstructures, introduces complexities in meshing due to the need for matched nodes on opposite faces to enforce periodic boundary conditions.

4.1.1.1 Algorithm for generating RVE

An algorithm has been developed to distribute fibres within a square-shaped matrix by random position and direction, ensuring that the fibres do not overlap. For the cut-fibre configuration, fibres extending beyond the matrix are truncated and translated to maintain a cut-fibre RVE across the matrix boundaries. The flowchart in Figure 4.2 depicts a simplified form of this algorithm.

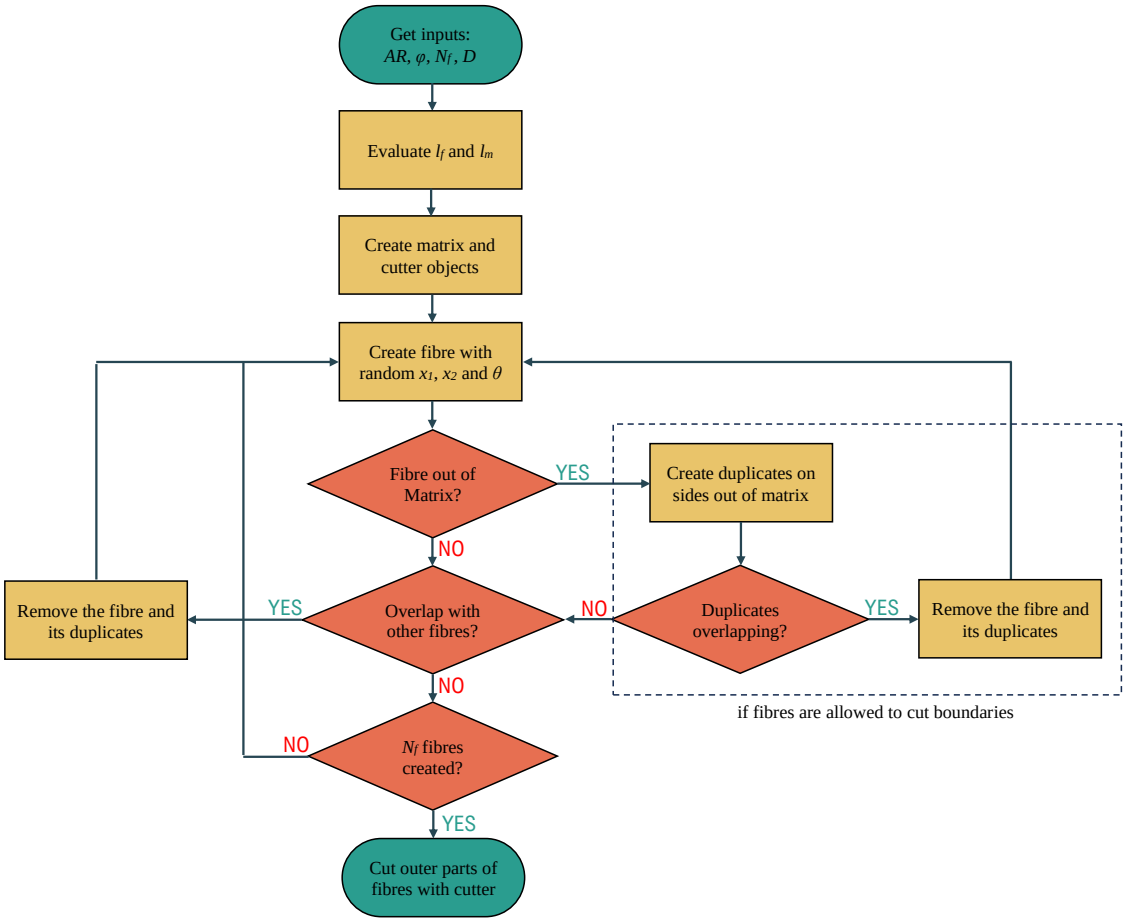

Figure 4.2: The flowchart of the algorithm used to generate randomly dispersed fibre-reinforced RVEs.

The algorithm requires as input aspect ratio $AR = l_f/D$, volume fraction ϕ, number of dispersed fibres N_f, and fibre diameter D, where l_f denotes the length of the fibres. Using these parameters, the algorithm evaluates the matrix and fibre lengths. Fibres are created sequentially with a random position and angle. If a fibre overlaps with others, it is regenerated. For cut-fibre configuration, duplicates are added on the opposite side to preserve periodic boundary conditions for fibres crossing the matrix boundary. Once the desired number of fibres is reached, the algorithm discards the parts of the fibres outside the matrix. For fully

embedded configuration, generating RVEs with all fibres inside becomes more challenging and time-consuming, particularly as the volume fraction and aspect ratio increase.

4.2 Computational homogenization

Computational homogenization has been developed to study the overall macroscopic behaviour of complex materials (Geers et al., 2010; Terada et al., 2000; Saeb et al., 2016; Le et al., 2015). The primary objective of computational homogenization is to translate microscopic heterogeneities into effective macroscopic properties by averaging microscopic heterogeneities to predict the effective behaviour of the material at a larger scale. This method considers a homogenized macro-continuum, which integrates a representative microstructure characterizing an RVE of a composite, in this case. It is assumed that all details of the microstructure can be described, possibly statistically. The macroscopic response of the material is then derived from the averaged microscopic properties. In computational homogenization, the known macroscopic deformation gradient $\widetilde{\mathbf{F}}$ is applied to the microstructure, and its response computed. The tilde indicates the averaged quantity over the volume.

Based on the average strain and stress theorems, the macroscopic deformation gradient and the macroscopic Piola stress are defined as the volume averages of their microscopic counterparts –for more details, see (Saeb et al., 2016)– as

$$\widetilde{\mathbf{F}} = \frac{1}{V}\int_{\Omega_X} \mathbf{F}\,\mathrm{d}V = \frac{1}{V}\int_{\Gamma_X} \boldsymbol{\Psi}\otimes\mathbf{N}\,\mathrm{d}A\,, \tag{4.2.1}$$

$$\widetilde{\mathbf{P}} = \frac{1}{V}\int_{\Omega_X} \mathbf{P}\,\mathrm{d}V = \frac{1}{V}\int_{\Gamma_X} \mathbf{T}\otimes\mathbf{X}\,\mathrm{d}A\,, \tag{4.2.2}$$

as shown in Figure 4.3, where the mapping $\boldsymbol{\Psi}$ and traction $\mathbf{T}$ were defined in Chapter 2. The deformation of this microstructure is linked to the local deformation at a specific point of the macro-continuum.

Hill–Mandel condition. The Hill–Mandel condition, also known as the *macro-homogeneity condition*, asserts that the virtual work done by a macroscopic stress on a macroscopic virtual deformation gradient is equal to the average virtual work done by a microscopic stress on a microscopic virtual deformation gradient (Hill, 1963). This condition establishes relationships between microscopic and macroscopic quantities, facilitating a transition from the micro to the macro scale. The Hill–Mandel condition is expressed mathematically as

$$\widetilde{\mathbf{P}} : \delta\widetilde{\mathbf{F}} - \frac{1}{V}\int_{\Omega_X} \mathbf{P} : \delta\mathbf{F}\,\mathrm{d}V = 0\,. \tag{4.2.3}$$

To satisfy the Hill–Mandel condition and therefore to accurately model the mechanical response of RVEs, appropriate boundary conditions must be applied. With the application of Hill's

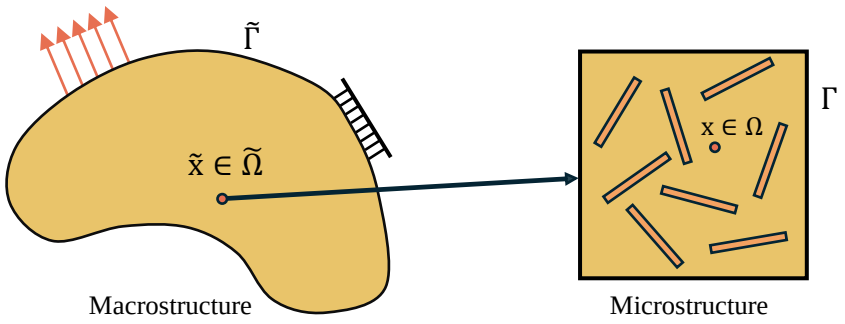

Figure 4.3: Loaded macrostructure with pointwise microstructure.

lemma, the Hill–Mandel condition is transformed into a surface integral by

$$\widetilde{\mathbf{P}} : \delta\widetilde{\mathbf{F}} - \frac{1}{V}\int_{\Omega_X} \mathbf{P} : \delta\mathbf{F}\,\mathrm{d}V = \int_{\tilde{\Gamma}_X} \left[\delta\boldsymbol{\Psi} - \delta\widetilde{\mathbf{F}}\,\mathbf{X}\right] \cdot \left[\mathbf{T} - \widetilde{\mathbf{P}}\,\mathbf{N}\right] \mathrm{d}A\,. \tag{4.2.4}$$

4.2.1 Admissible boundary conditions

Several boundary conditions can be applied to satisfy the Hill–Mandel condition. In this study, two admissible boundary conditions are discussed: affine and periodic boundary conditions. Figure 4.4 schematically illustrates an RVE with both boundary conditions applied.

Affine boundary conditions (ABCs). ABCs, also known as *kinematically uniform* BCs or *linear displacement* BCs, impose a linearly varying displacement field on the RVE boundaries. This type of boundary condition is particularly useful for simulating uniform strain states within the RVE. The displacement at any boundary point $\mathbf{X}$ on Γ_X is given by

$$\mathbf{u} = \left[\widetilde{\mathbf{F}} - \mathbf{I}\right] \mathbf{X}, \quad \forall \mathbf{X} \in \Gamma_X. \tag{4.2.5}$$

Periodic boundary conditions (PBCs). PBCs ensure that deformation and stress states are consistent across the RVE boundaries as if the RVE were part of an infinite periodic array. The boundary Γ_X is divided into matching parts $\Gamma_X = \Gamma_X^+ \cup \Gamma_X^-$, with corresponding material points $\mathbf{X}^+$ and $\mathbf{X}^-$, where "positive" and "negative" denote the paired nodes on opposite sides of the RVE. The PBCs are applied as follows

$$\mathbf{u}\left(\mathbf{X}^+\right) - \mathbf{u}\left(\mathbf{X}^-\right) = \left[\widetilde{\mathbf{F}} - \mathbf{I}\right] \left[\mathbf{X}^+ - \mathbf{X}^-\right]. \tag{4.2.6}$$

Remark. Another widely used admissible BCs in the literature is the *constant traction* BCs. The solution of the associated microscopic boundary-value problem often encounters issues with singularity, which are thoroughly discussed by Javili et al. (2017). □

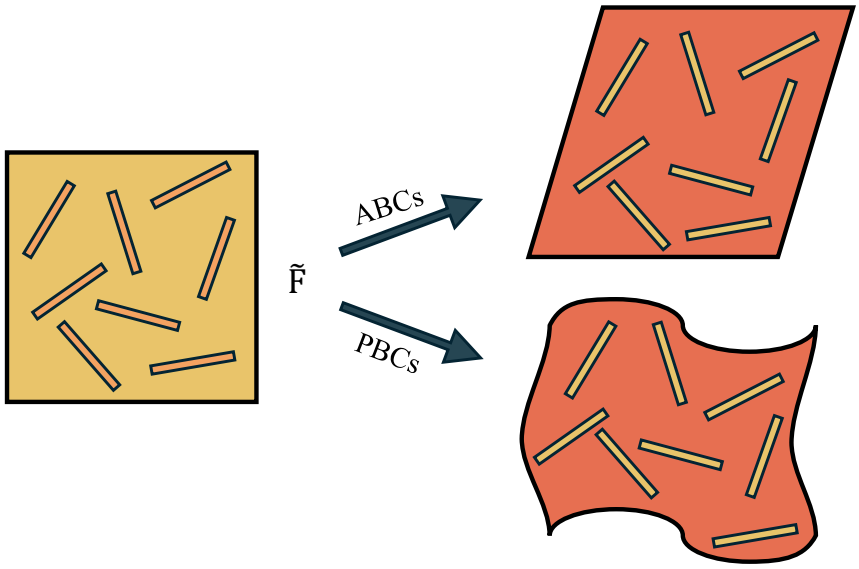

Figure 4.4: Affine and periodic boundary conditions.

4.2.2 Pixel meshing technique

As discussed in Section 4.1.1, this study examines two RVE configuration approaches: one where fibres intersect the boundaries and another where fibres are fully embedded within the matrix. To effectively apply PBCs requiring paired nodes, RVEs in 2D must be meshed such that nodes on opposite sides share the same x_2 coordinate on the left and right, and the same x_1 coordinate on the top and bottom. Meshing RVEs with boundary-crossing fibres presents challenges. A solution to these challenges is the *pixel* meshing technique –or *voxel* meshing in 3D. Due to their inherently regular and repetitive structure, pixel meshes naturally exhibit a periodic mesh topology (Bendsøe and Kikuchi, 1988). The regularity and predictability of pixel meshes ensure that the boundaries on opposite sides of the mesh can be matched and connected without complications, facilitating the implementation of PBCs (Kanit et al., 2003; Schneider et al., 2017; Watanabe and Yamanaka, 2019). Alternatives like *approximate periodic boundary conditions* along with kinematic uniform stress vectors or displacement boundary conditions are also discussed in the literature (Xia et al., 2003; Schneider et al., 2017).

The pixel technique starts with the entire geometry and incrementally refines the RVE with the aid of hanging nodes until the mesh is sufficiently refined. The refinement rules are straightforward: a cell is refined if it contains any part of a fibre or is at the boundary. Figure 4.5 illustrates a single-fibre RVE, used for demonstration purposes, that has been meshed using this technique. The green "X" marks indicate elements that require additional refinement. The meshing for this example is shown for three steps of refinement, $n = 3$, where n stands for the number of refinement steps.

The fibre distribution algorithm discussed in Section 4.1.1.1, integrated with the pixel meshing technique, is implemented in C++ to efficiently generate 2D RVEs for use with the deal.II codes. The code for generating RVEs using the pixel meshing technique is encapsulated in a namespace called "RVE" within the *madeal* code package (Ahmadi, 2024), making it easy to

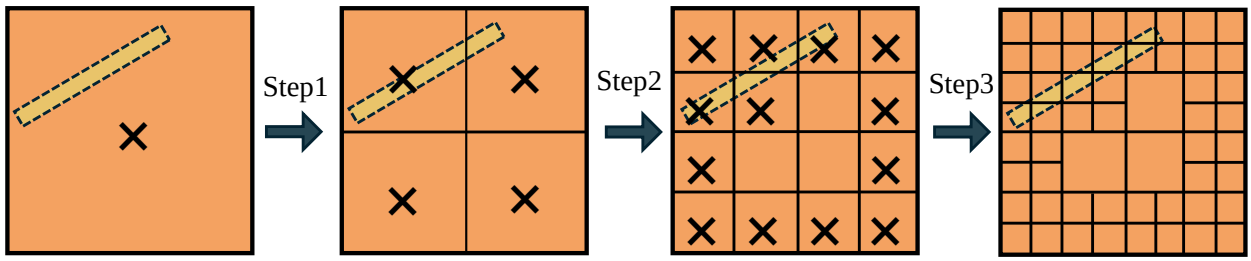

Figure 4.5: Refinement of an RVE with single fibre in three steps.

use. The code also incorporates admissible boundary conditions to ensure compatibility with various computational setups. Please refer to Appendix C.2 for a detailed implementation guide.

Volume fraction error. Each element in the FE model corresponds to either a fibre or matrix material property. In the pixel meshing technique, the refinement process continues until a distinct separation between these materials at the fibre boundaries is achieved. When the pixels are not sufficiently small, the real volume fraction ϕ_r can deviate from the desired volume fraction ϕ. A practical refinement criterion involves ensuring that the difference between the real volume fraction of fibres ϕ_r and the nominal volume fraction ϕ calculated by the pixel technique falls below a predefined threshold. The error metric used to quantify this difference is defined as

$$e_\phi = \frac{|\phi - \phi_r|}{\phi}. \tag{4.2.7}$$

Figure 4.6 illustrates an RVE generated with $\phi = 2\%$ and 10 fibres with $AR = 10$ dispersed in a matrix for different refinement levels n and the corresponding real volume fraction ϕ_r and volume fraction error e_ϕ. It visually depicts how the refinement process enhances the mesh resolution, thereby improving the accuracy of representing the fibre boundaries within the RVE.

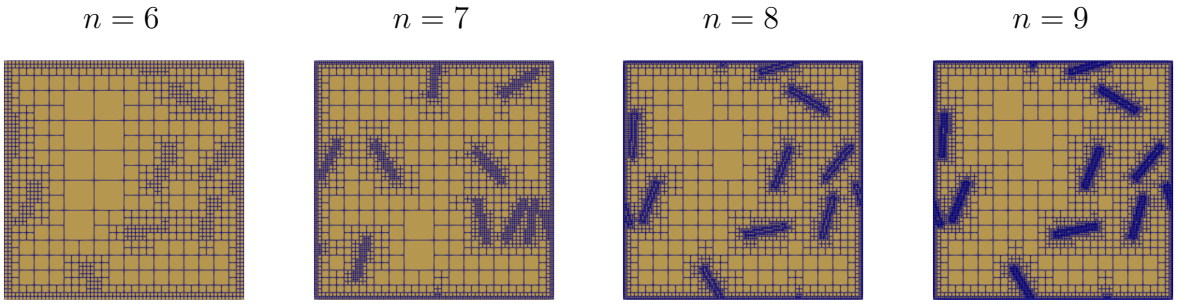

Figure 4.6: RVEs generated for different refinement levels n.

The impact of increasing the number of refinement steps n on the error metric is now analysed for varying aspect ratios, volume fractions, and numbers of dispersed fibres. Figures 4.7,

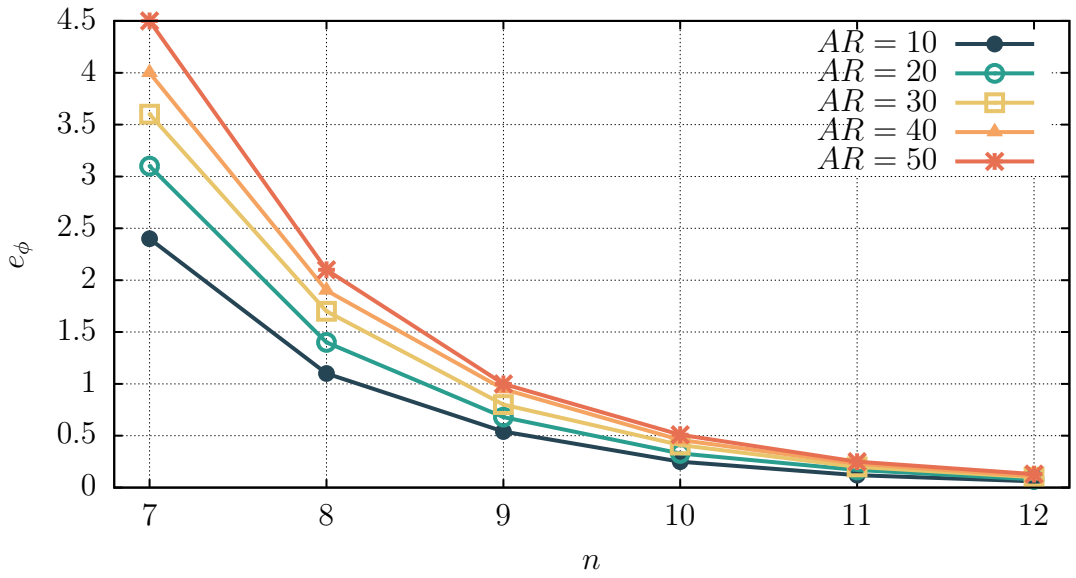

Figure 4.7: Effect of increasing n on the error for different aspect ratios AR.

4.8, and 4.9 demonstrate these effects while keeping other parameters constant (e.g., $AR = 50$, $\phi = 1\%$, $N_f = 50$). Figure 4.7 indicates that higher aspect ratios require more refinement steps to achieve a sufficiently small error. Figure 4.8 demonstrates that RVEs with lower fibre content require more refinement for accurate representation. Figure 4.9 demonstrates that a higher number of dispersed fibres, which increases the randomness within the RVE, also requires additional refinement steps to minimize errors related to the volume fraction. These findings underscore the necessity of sufficient mesh refinement to ensure the accuracy of pixelated RVEs. However, it is important to note that increasing refinement rapidly increases the number of elements and nodes, consequently impacting computation time.

4.3 Numerical setting

The numerical analysis of RVEs is conducted to investigate how various parameters influence the mechanical behaviour of fibre-reinforced composites. Specifically, the study focuses on the change in the orientation and spacing of fibres and the effect of different BCs on the mechanical response. For the simulations, the fibres are assumed to have properties similar to those of CNTs, with Young's modulus of $E_f = 1\,\text{TPa}$ and Poisson's ratio of $\nu = 0.28$ based on typical reported values (Salvetat et al., 1999; Miyagawa et al., 2005; Ansari et al., 2021a; Kashyap and Patil, 2008). Elastomers such as Polyurethane (PU), Nitrile Butadiene Rubber (NBR), Styrene-Butadiene Rubber (SBR), Thermoplastic Elastomers (TPE) and Silicone Rubber (PDMS - Polydimethylsiloxane) typically exhibit a wide range of Young's moduli, depending on their specific formulation and processing conditions. While Young's moduli can vary, values are often found within the range of $\sim 1 - 10\,\text{MPa}$ for many common elastomeric materials (Ginzburg et al., 2007; Girun et al., 2007; Wisse et al., 2006; Lötters et al., 1997). For the purposes of this study, a representative value of $E_m = 5\,\text{MPa}$ is chosen for the simulations. Considering

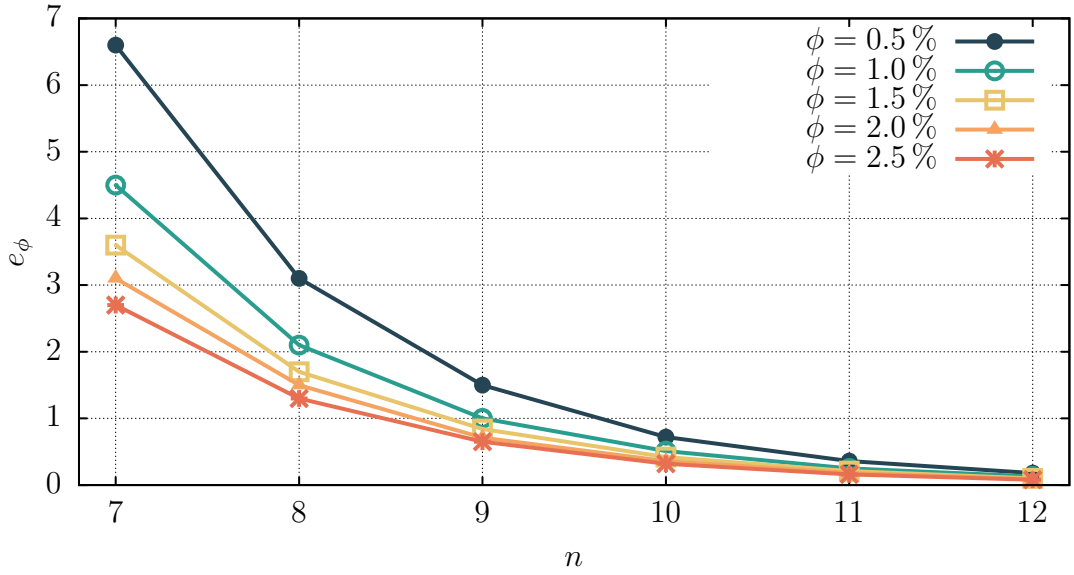

Figure 4.8: Effect of increasing n on the error considering different volume fractions ϕ.

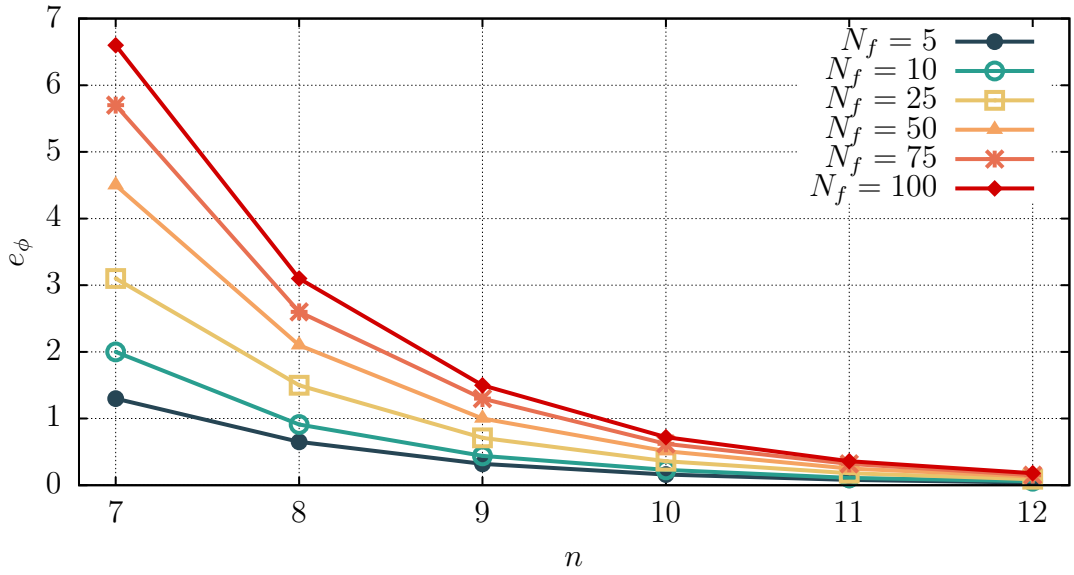

Figure 4.9: Effect of increasing n on the error considering the number of dispersed fibres N_f.

their nearly incompressible behaviour, the Poisson's ratio of the matrix materials is assumed to be $\nu = 0.4999$. Since 2D RVEs represent a cross-section of the composite, the plane stress assumption is utilised instead of plane strain. This choice is appropriate for modelling fibre-reinforced materials in 2D scenarios. Hence, to represent general uniaxial or biaxial stretching scenarios, the macroscopic applied deformation gradient in the plane is specified as

$$\left[\widetilde{\mathbf{F}}\right] = \begin{bmatrix} \lambda_1 & 0 \\ 0 & \lambda_2 \end{bmatrix}. \tag{4.3.1}$$

The component $\widetilde{F}_{33}$ does not need to be explicitly defined; it is computed automatically based on the plane stress assumption.

Given the complexity and number of parameters, default values are set for certain parameters while others are varied. These default properties are $\phi = 1\,\%$, $AR = 50$ and $n = 12$. The aspect ratio of CNTs can vary widely depending on their specific type (single-walled or multi-walled), length, and diameter. Typical aspect ratios range from about 10 to several thousand. It is important to note that the precise aspect ratio chosen for simulations may affect the overall mechanical response of the composite. For this study, an aspect ratio of $AR = 50$ is chosen as a balance between accuracy and feasibility, considering the limitations of the modelling.

4.3.1 Model verification

This section focuses on identifying an efficient distribution pattern with a sufficient number of fibres and the appropriate combination of RVE configuration and BCs. The aim is to determine the most suitable conditions for simulating RVEs.

4.3.1.1 Distribution pattern

This study suggests a uniform orientation pattern for the dispersion of fibres. Unlike the commonly used random angle distribution, fibres are assumed to be uniformly oriented by their angles. This pattern facilitates tracking the position and alignment of fibres, which is crucial since the composite properties can change with fibre alignment. Instead of using a random angle, the uniform orientation pattern uses a uniform distribution of angles. Distributing N_f fibres in the range of $\{-\pi/2, \pi/2\}$, the angle of the i-th fibre is calculated as

$$\theta_i = \theta_0 + \frac{[i-1]\pi}{N_f} - \frac{\pi}{2}, \quad \text{for}\, i = \{1 : N_f\}\,, \tag{4.3.2}$$

where $\theta_0 \in \{0, \pi/N_f\}$ is a random angle generated for each sample to maintain distribution randomness. Applying $\lambda_1 = 1.25$ and $\lambda_2 = 1/\lambda_1$, Figure 4.10 shows a boxplot (whisker plot), illustrating the volumetric average of von Mises stress for different numbers of fibres with random and uniform orientation patterns. For each number of fibres and distribution pattern, 10 random samples are analysed. The plot is based on a five-number summary: minimum, first

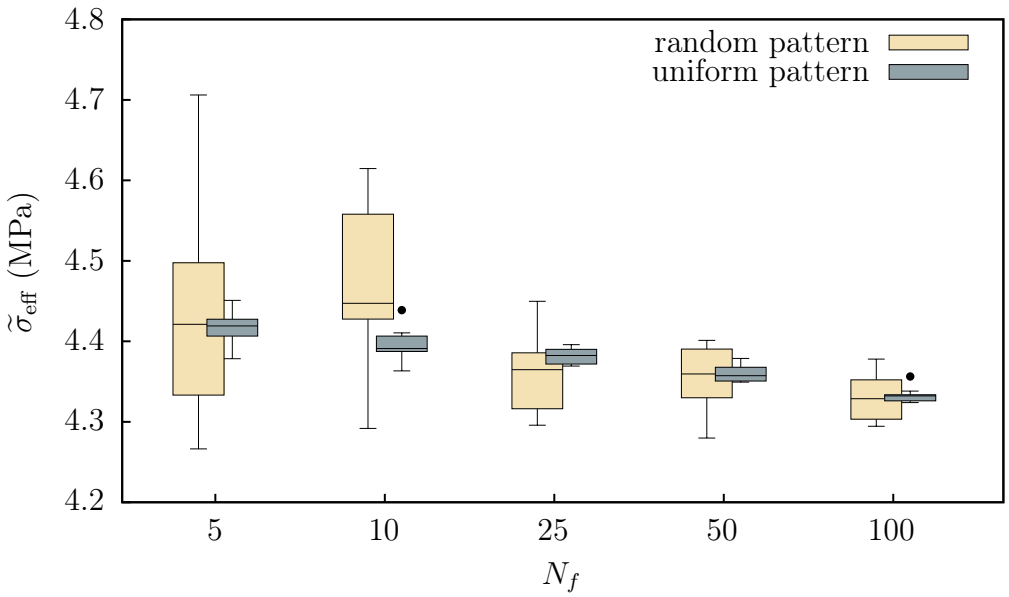

Figure 4.10: The volumetric average of von Mises stress for different numbers of fibres considering random and uniform orientation patterns.

quartile (Q1), median, third quartile (Q3), and maximum. It provides a visual representation of the central tendency, dispersion, and skewness of the data. The rectangular box spans from Q1 to Q3, representing the interquartile range (IQR), with a line inside indicating the median (Q2). Whiskers extend from the box to the smallest and largest values within 1.5 times the IQR from the quartiles, while values beyond the whiskers are plotted individually as outliers. The minimum and maximum values within the whiskers are also indicated.

As the number of distributed fibres increases, the boxes for $\widetilde{\sigma}_{\text{eff}}$ become narrower, indicating more consistent results. While the random orientation pattern requires more fibres to converge, the uniform orientation pattern converges faster. Even with a small number of fibres, the uniform orientation pattern provides more consistent results. This suggests that the uniform orientation pattern may offer acceptable results with less number of samples compared to the random orientation pattern. Therefore, the uniform orientation pattern will be used for the remainder of the study. The number of fibres is set to 25, which is considered as a reasonable trade-off between accuracy and computational cost.

4.3.1.2 BCs and RVE configuration

Selecting the most appropriate BCs and RVE configuration can be challenging. The study evaluates four combinations of BCs and configurations to consider: ABCs with cut-fibre, ABCs with fully embedded, PBCs with cut-fibre, and PBCs with fully embedded. Figure 4.11 displays the deformed RVEs at $\lambda_1 = 1.5$ and $\lambda_2 = 1/\lambda_1$ for different combinations of BCs and configurations for a random sample.

Figure 4.12 shows the volumetric average of various stress components and the von Mises stress for different combinations of BCs and configurations. These results are based on the average values calculated from 5 samples for each combination. The results indicate that ABCs

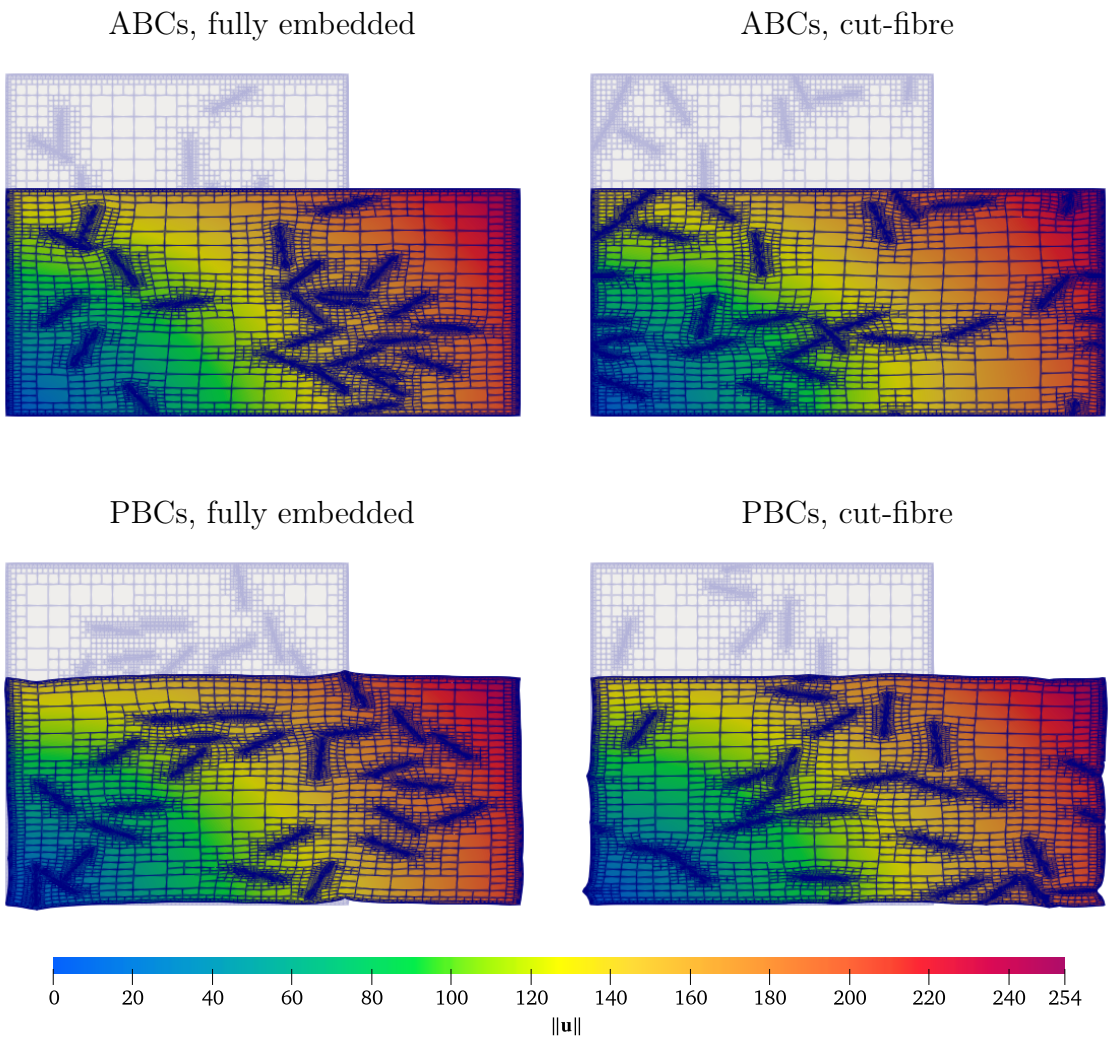

Figure 4.11: The deformed RVEs at $\lambda_1 = 1.5$ for different combinations of BCs and configurations.

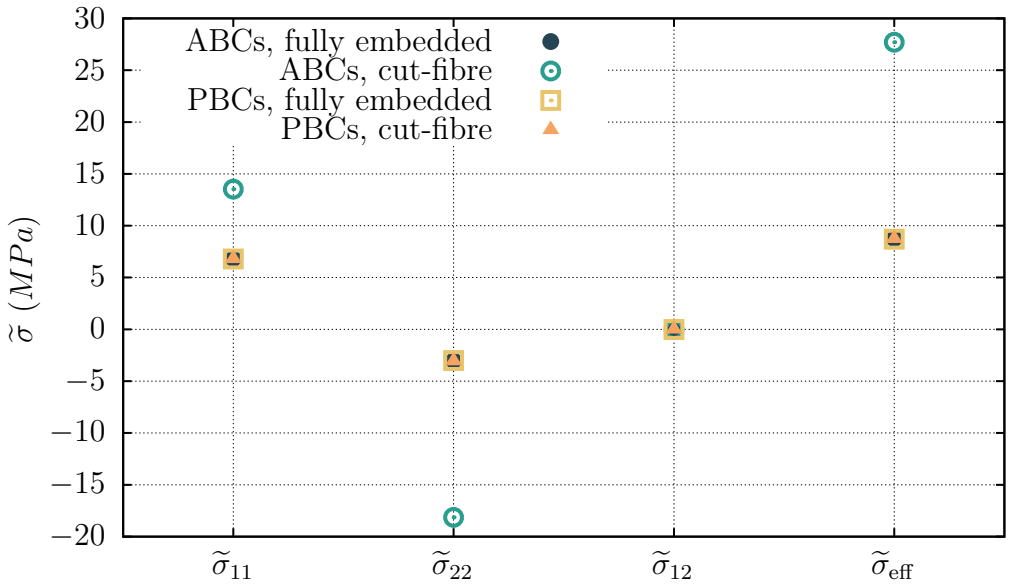

Figure 4.12: The volumetric average of various stress components and the von Mises stress for different combinations of BCs and RVE configurations.

with cut-fibre deviate significantly from other combinations. This deviation occurs because ABCs impose stricter constraints on the boundaries where the fibres are cut. Therefore, ABCs are not suitable for cut-fibre configuration where fibres intersect the boundaries. Conversely, PBCs are less constrained at the boundaries, making them more suitable for cut-fibre configuration. Given the more realistic nature of cut-fibre configuration, PBCs with cut-fibre RVE are selected for the remainder of this study.

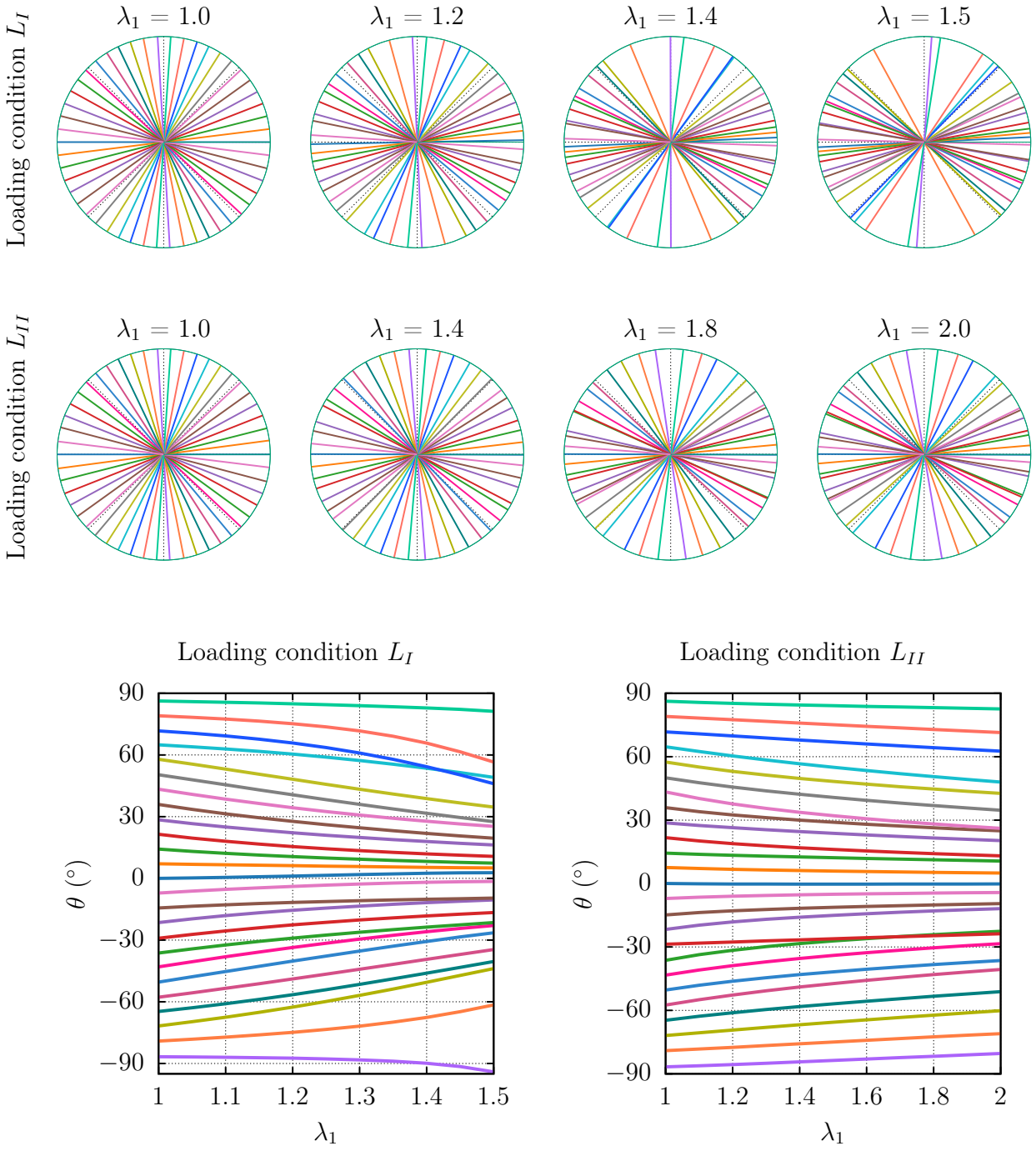

Figure 4.13: Orientation changes of fibres for different values of λ_1 under L_I (applying λ_1 while $\lambda_2 = 1/\lambda_1$) and L_{II} (applying λ_1 while $\lambda_2 = 1$) for a randomly selected sample.

4.4 Orientation and spacing

This section examines the reorientation of fibres under deformation by tracking changes in their alignment and spacing. These characteristics are essential for understanding how deformation influences the behaviour of composite materials, providing key inputs for the analysis in the next chapter, where their impact on electrical conductivity is explored. Two different loading conditions are considered: the first (L_I) applies λ_1 while constraining $\lambda_2 = 1/\lambda_1$, and the second (L_{II}) changes λ_1 while fixing $\lambda_2 = 1$.

4.4.1 Orientation change

This section investigates how the orientation of fibres changes when the composite undergoes finite deformations. Python scripts were developed to obtain the coordinates of the endpoints of each fibre and calculate the angle the fibre makes with respect to the x_1 axis. The angles are calculated within the range of $[-\pi/2, \pi/2]$. Special care was taken to ensure accurate angle calculation for each fibre, considering the periodic cut-fibre configuration. For simplicity and better demonstration of tracking orientation changes, the initial angle θ_0 for uniform distribution is set to zero.

Figure 4.13 illustrates the angles of each fibre for different values of applied λ_1 for a randomly selected sample under L_I and L_{II} loading conditions. For a better demonstration, corresponding circular representations of fibres for different values of applied λ_1 are also illustrated. As λ_1 increases, the angles of the fibres tend to align more towards the x_1 direction. Interestingly, fibres initially perpendicular to the x_1 axis tend to retain their orientation. The change in fibre orientation is nonlinear and depends on both the position and initial orientation of the fibres. More pronounced changes in fibre angles are observed under L_I loading compared to L_{II}.

The orientation of fibres is confined to a smaller range as the applied λ_1 increases, except for a few fibres that are perpendicular or nearly perpendicular to the x_1 axis. Therefore, by neglecting the outliers it can be assumed that the fibres are distributed within a range of $[-\alpha, \alpha]$, where α is a function of applied λ_1. For example, for $\lambda_1 = 1.5$ in these samples, $\alpha \approx 60$ degrees.

4.4.1.1 Limit angle

One of the scalar parameters that can be used to measure the alignment of fibres is the limit angle α. Defined as the maximum fibre orientation angle θ within the range $|\theta| < \alpha$ and $\alpha \in [0, \pi/2]$, it provides a measure of the degree of alignment under applied deformation. Figure 4.14 depicts the variation of the maximum angle α with increasing λ_1 for five randomly selected samples under both L_I and L_{II} loading conditions. The calculation of α for the current computational model follows these steps:

(i) Compute the mean of the absolute angle values.

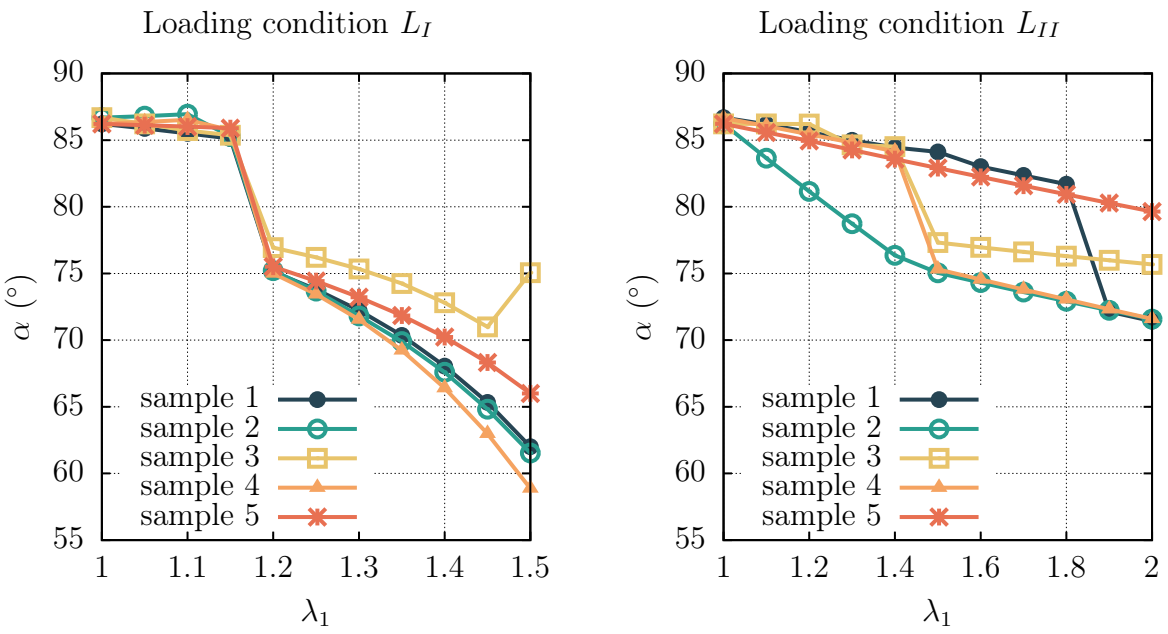

Figure 4.14: The maximum angle α for 5 randomly selected samples under L_I (λ_1 while $\lambda_2 = 1/\lambda_1$) and L_{II} (λ_1 while $\lambda_2 = 1$).

(ii) Filter angles that are less than a threshold of $\pi/4$ from the mean value.

(iii) Identify the maximum value from the filtered angles as α.

The results indicate a more pronounced decrease in α for L_I compared to L_{II}. Linear interpolation of the mean values of 10 samples for each loading condition yields the following estimations:

$$\alpha = -49.19\,\lambda_1 + 137.7 \quad \text{for } L_I, \qquad \alpha = -12.96\,\lambda_1 + 99.59 \quad \text{for } L_{II}. \tag{4.4.1}$$

Here, α is measured in degrees. These relationships are utilised in the subsequent chapter to determine the piezoresistivity of the composites.

4.4.1.2 Order parameter

Another metric that can be used to quantify the orientation of fibres is the order parameter S, which measures the degree of alignment in fibre orientations (De Gennes and Prost, 1993). The order parameter ranges from -1 (perfect alignment in x_2 direction) to 1 (perfect alignment in x_1 direction), with 0 indicating random orientation, and is defined by

$$S = \frac{1}{N_f} \sum_{i=1}^{N_f} \left[2\cos^2(\theta_i) - 1\right]. \tag{4.4.2}$$

Figure 4.15 illustrates the variation in S with applied λ_1 for five randomly selected samples under both L_I and L_{II} loading conditions. It is observed that S increases from 0 for the fully

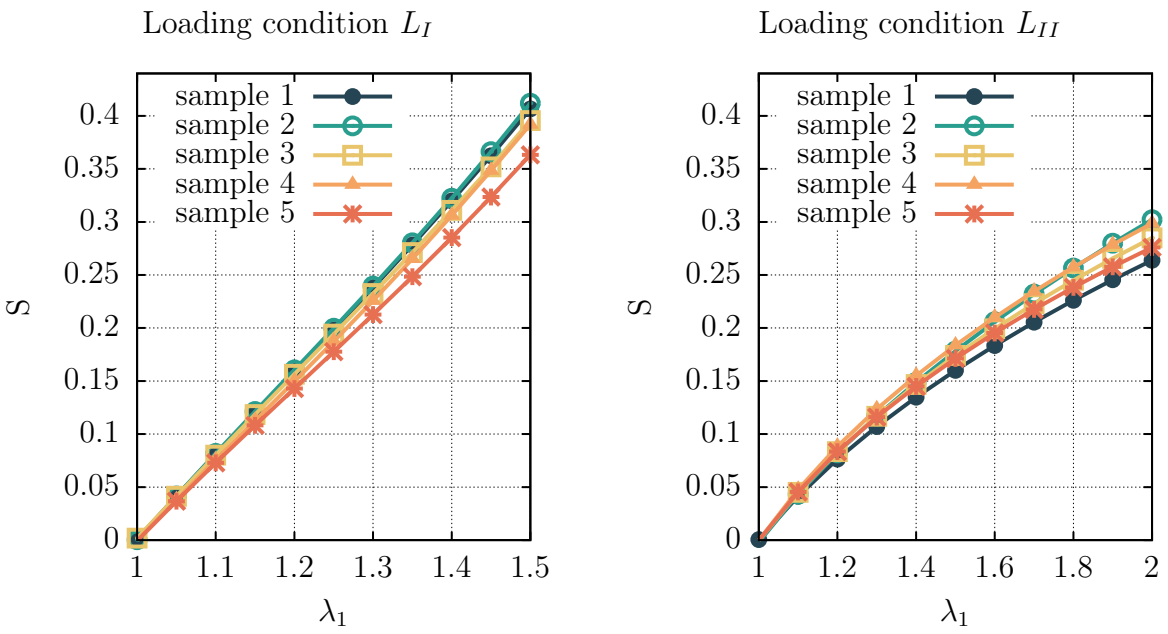

Figure 4.15: The order parameter S for 5 randomly selected samples under L_I (λ_1 while $\lambda_2 = 1/\lambda_1$) and L_{II} (λ_1 while $\lambda_2 = 1$).

uniform distribution at the initial state as the deformation is applied.

The results show that S exhibits a nearly linear trend under L_I, while displaying a nonlinear trend under L_{II}. Additionally, the changes in orientation, as indicated by S, are more significant for L_I than for L_{II}.

4.4.1.3 Probability density function

Further insights into fibre orientation are obtained by analysing the probability density function of fibre angles using kernel density estimation (KDE). KDE is a non-parametric technique to estimate the probability density function of a random variable, providing a smooth approximation of the data distribution (Chen, 2017). Unlike histograms, KDE offers a continuous, smoothed density estimate that is useful for visualizing the distribution of fibre orientations.

The KDE in this study employs a Gaussian kernel function, with the bandwidth parameter determining the level of smoothing applied to the density estimate. A smaller bandwidth yields a more detailed, jagged KDE, whereas a larger bandwidth results in a smoother KDE. Scott's rule (Scott, 2009) is used to select an appropriate bandwidth, balancing bias and variance. Scott's rule calculates the bandwidth as $h = 1.06\,\sigma m^{-1/5}$, where σ is the standard deviation of the data and m is the number of data points. This rule helps achieve an optimal balance between capturing detail and minimizing noise in the KDE, leading to a more accurate and visually interpretable density estimate.

Normalisation of the KDE ensures that the area under the density curve over the interval $[0, \pi/2]$ equals $\pi/2$, facilitating direct comparison with the theoretical distribution function $\xi = \pi/a \, \exp(-b\,\theta^2)$, used in the next chapter, where a and b are constants. The normalisation

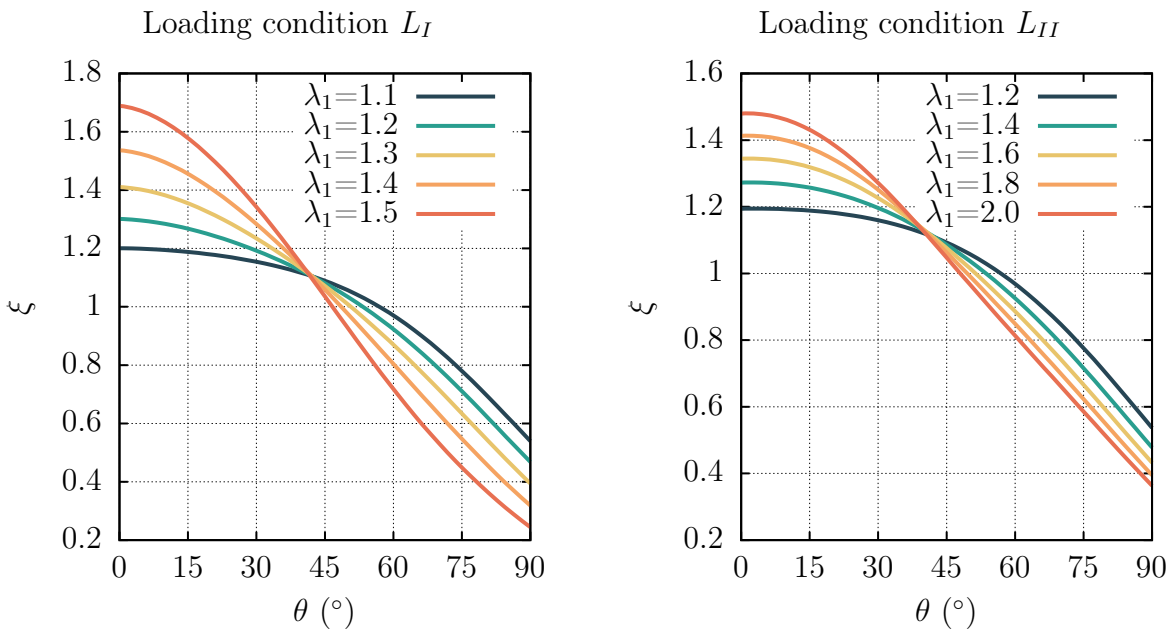

Figure 4.16: KDE for the angles of fibres for a random sample under L_I (λ_1 while $\lambda_2 = 1/\lambda_1$) and L_{II} (λ_1 while $\lambda_2 = 1$).

constant is computed by integrating the KDE over the specified interval and adjusting the KDE values accordingly.

Figure 4.16 presents the KDE plots for fibre angles at various λ_1 values for a representative sample. Each line represents the density function of fibre angles at a specific λ_1, smoothed using the Gaussian kernel. This visualization reveals how the distribution of fibre orientations evolves with deformation. As λ_1 increases, the KDE becomes more concentrated around the x_1 axis, indicating that fibres align increasingly with the direction of deformation. The plot demonstrates a shift and spread in fibre angles due to the applied mechanical forces.

Additionally, the theoretical distribution function $\xi = \pi/a \exp(-b\,\theta^2)$ is superimposed on the KDE plots to assess the alignment of the model with empirical data. Parameters a and b are obtained by fitting the normalised KDE for each λ_1, and these parameters are recorded and analysed to understand changes in fibre orientation distributions under deformation. The close fit between the KDE and the theoretical model suggests the latter accurately captures the underlying changes in fibre orientations due to deformation.

Average values of a and b for 10 samples at each λ_1 are computed for both loadings. Linear interpolation provides the following relations:

$$a = -1.543\,\lambda_1 + 4.137, \qquad b = 1.201\,\lambda_1 - 1.010 \quad \text{for } L_I \tag{4.4.3}$$

$$a = -0.560\,\lambda_1 + 3.134, \qquad b = 0.383\,\lambda_1 - 0.146 \quad \text{for } L_{II} \tag{4.4.4}$$

These relationships are utilised with the exponential probability density function in the subsequent chapter to determine the piezoresistivity of composites.

Overall, the analysis reveals that fibre orientation becomes more aligned along the x_1 axis

under applied deformation, with more pronounced effects under L_I loading. These insights into fibre reorientation are crucial for understanding the mechanical behaviour and piezoresistive properties of the composites.

4.4.2 Average minimum distance

The minimum distance between fibres is a critical parameter that will be utilised in the next chapter to demonstrate its impact on electrical conductivity. To calculate the minimum distance between two fibres in a 2D plane during deformation, the positions of the fibre endpoints are extracted using a custom Python script. The calculation considers both the direct distances between fibre endpoints and the perpendicular distances from each endpoint to the line segment defined by the opposite fibre.

The algorithm is as follows. First, the Euclidean distances between all pairs of endpoints across the fibres are computed. Next, the perpendicular distances from each endpoint of one fibre to the infinite line defined by the other fibre are calculated. If the projection of the point onto the line segment falls within the bounds of the fibre, this distance is considered; otherwise, the distance from the point to the nearest endpoint of the fibre is used. The smallest of these values is considered the minimum distance between the two fibres. To account for the periodic nature of RVEs, the minimum distance between randomly oriented fibres must consider the wrapping of the space. This involves calculating distances not only in the original domain but also in its periodic images. For each fibre, periodic images are created by shifting its positions by the domain size in all directions. For each pair of fibres, the minimum distance is computed by considering all periodic images.

The average minimum distance, $\overline{d}_m$, for each load step is computed. Figure 4.17 shows the normalised average minimum distances between fibres, $\overline{d}_m$, over deformation for both L_I and L_{II} loading conditions, considering five random samples. The value of $\overline{d}_m$ is normalised based on the initial value before deformation. It is observed that $\overline{d}_m$ for L_I does not exhibit a consistent trend with deformation; in some samples, it increases, while in others, it decreases. Averaging these samples suggests no significant change in the average minimum distance. However, for L_{II}, $\overline{d}_m$ increases with deformation. By linear interpolation, the relationship for L_{II} is given by:

$$\overline{d}_m = 0.619\,\lambda_1 + 0.409\,. \tag{4.4.5}$$

4.4.3 Analytical calculation for fully affine deformation

In order to provide a comparative baseline for the computational model, an analytical solution for fully affine deformation is presented. This approach calculates the evolution of fibre orientation and spacing under idealised conditions, where the entire 2D composite undergoes affine deformation, assuming no distinction in material properties between fibres and matrix,

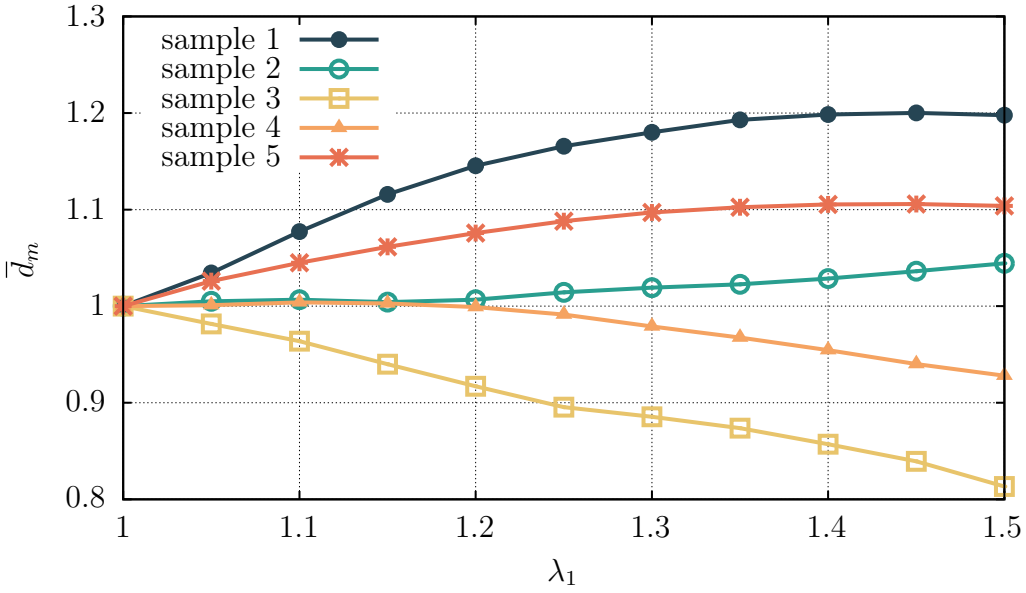

(a)

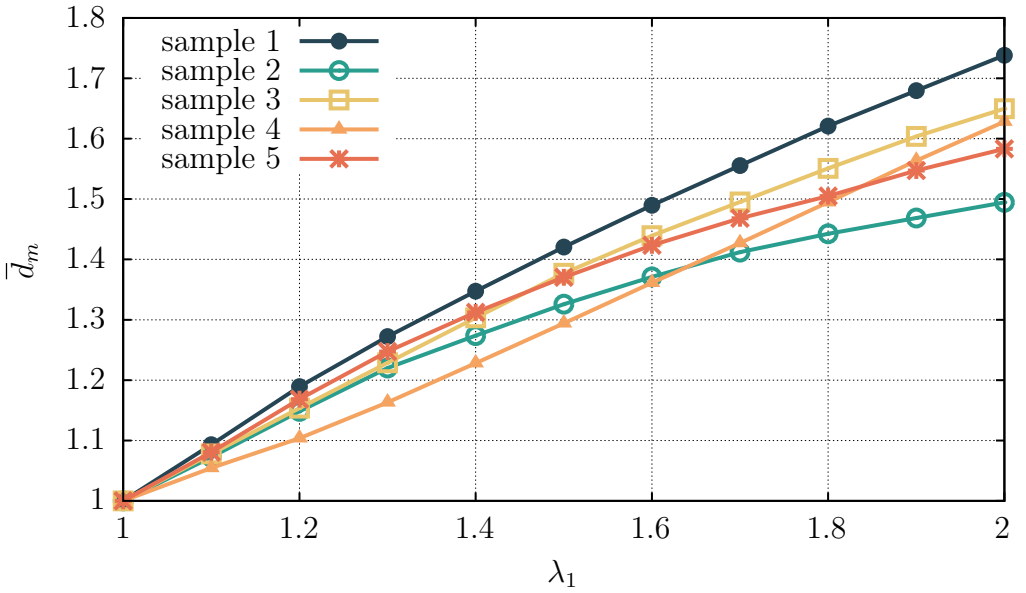

(b)

Figure 4.17: Normalised average minimum distances between fibres $\overline{d}_m$ over deformation for (a) L_I and (b) L_{II}.

resulting in isotropic deformation. The deformation mapping is expressed as

$$\mathbf{u} = \left[\widetilde{\mathbf{F}} - \mathbf{I}\right] \mathbf{X}, \quad \forall \mathbf{X} \in \Omega_X. \tag{4.4.6}$$

In this framework, both the fibres and the matrix deform identically, following the same kinematic pathways without material mismatch. This simplified model provides a reference for understanding the more complex behaviours observed in the computational model, specifically in comparison to the results obtained using PBCs with the cut-fibre RVE.

4.4.3.1 Orientation calculation

To investigate changes in fibre orientation under fully affine deformation, the initial fibre orientation is represented by the unit vector $\mathbf{d}_0 = \cos\theta_0\,\mathbf{e}_1 + \sin\theta_0\,\mathbf{e}_2$. Upon deformation, the fibre orientation vector transforms as $\mathbf{d} = \widetilde{\mathbf{F}}\,\mathbf{d}_0$. The post-deformation fibre orientation angle θ is then calculated by

$$\theta = \tan^{-1}\left(\frac{\lambda_2 \sin\theta_0}{\lambda_1 \cos\theta_0}\right). \tag{4.4.7}$$

This calculation is carried out for a uniformly distributed set of 1000 initial fibre orientations to capture a broad spectrum of possible configurations. Figure 4.18 compares the computed limit angle α and order parameter S between the analytical affine deformation solution and the computational model for loading conditions L_I and L_{II}. For the computational model, the limit angle α is derived through linear interpolation using Equation (4.4.1), and the order parameter S is averaged over 10 random samples.

The slight mismatch at $\lambda = 1$ arises because the analytical solution assumes an ideal initial configuration, while the computational model uses a discrete distribution of 25 fibres, leading to minor deviations. The results demonstrate that, under loading condition L_I, the analytical model and computational model exhibit good agreement for the order parameter S, indicating similar alignment trends. However, discrepancies arise in other cases, particularly with the limit angle α. These differences can primarily be attributed to the absence of fibre-matrix interaction effects in the analytical solution. In the computational approach, fibre stiffness prevents significant length changes, which introduces a stabilising effect not present in the analytical model.

4.4.3.2 Average distance calculation

To further compare the computational and analytical approaches, the average normalised fibre separation is calculated under the assumption of fully affine deformation. Consider two arbitrary points initially separated by a distance d_0 with an initial vector $\mathbf{d}_0$, forming an angle θ with the x_1 axis. After affine deformation, the length of the deformed vector $\mathbf{d}$ becomes

$$\|\mathbf{d}\| = d_0 \sqrt{\lambda_1^2 \cos^2\theta + \lambda_2^2 \sin^2\theta}. \tag{4.4.8}$$

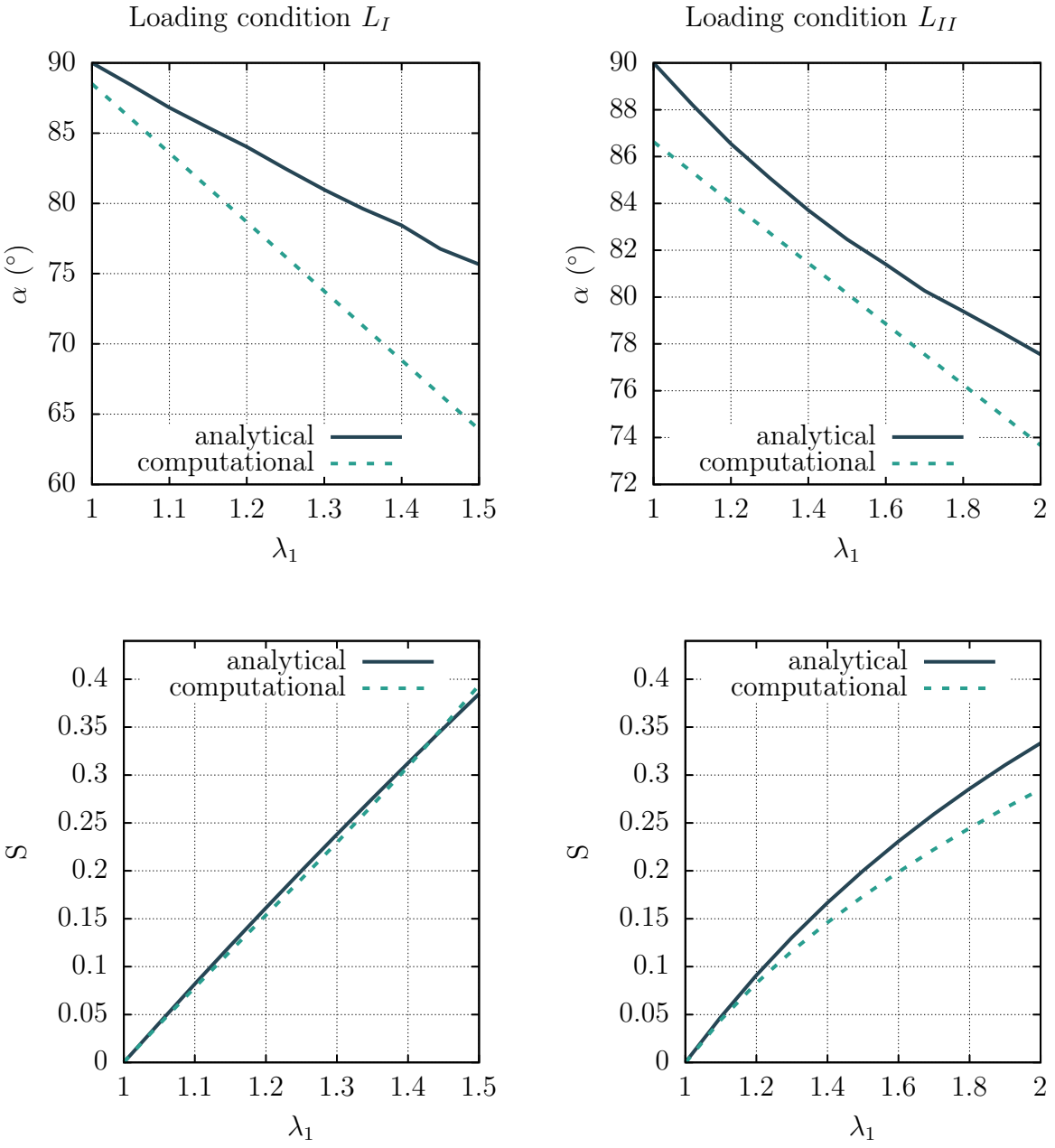

Figure 4.18: Comparing the limit angle α and order parameter S between the computational model and the analytical calculation for L_I and L_{II} loading conditions.

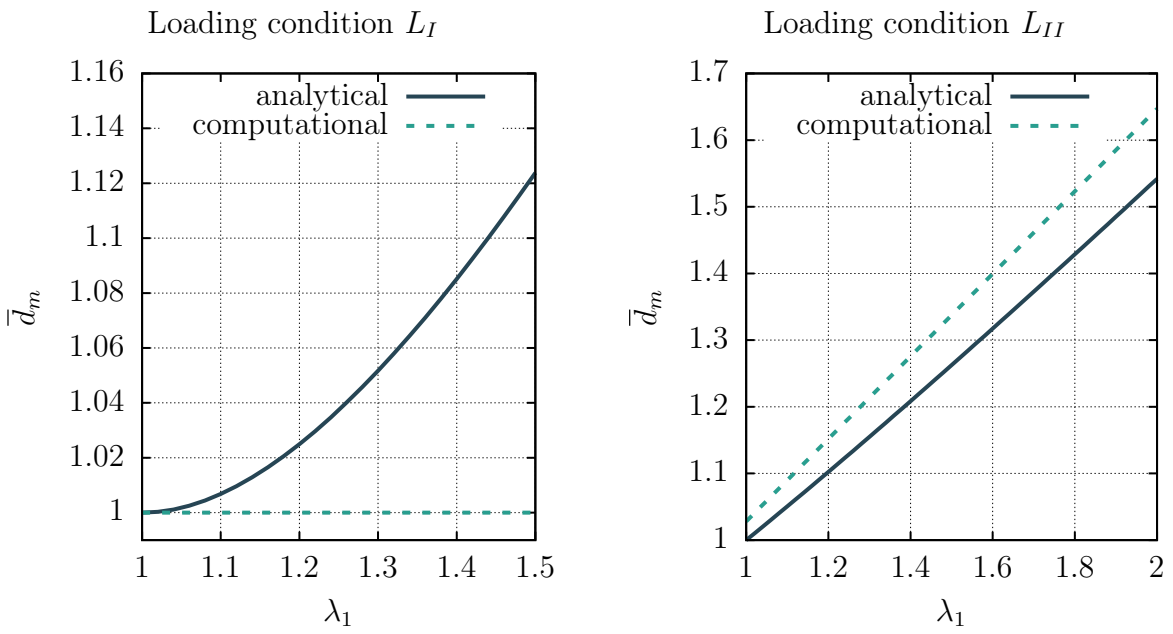

Figure 4.19: Comparing the normalised average distances between fibres $\overline{d}_m$ from the computational model and the analytical calculation for L_I and L_{II}.

The normalised change in separation $d_m = \|\mathbf{d}\|/d_0$, representing the relative change in fibre separation, is computed as

$$d_m = \sqrt{\lambda_1^2 \cos^2\theta + \lambda_2^2 \sin^2\theta}. \tag{4.4.9}$$

The average normalised distance, $\overline{d}_m$, is obtained by integrating over all directions θ from 0 to 2π and normalising by the angle interval, yielding

$$\overline{d}_m = \frac{1}{2\pi}\int_0^{2\pi} \sqrt{\lambda_1^2 \cos^2\theta + \lambda_2^2 \sin^2\theta}\, d\theta. \tag{4.4.10}$$

Figure 4.19 compares the average normalised distance between fibres, $\overline{d}_m$, predicted by the affine deformation analytical model with that from the computational model under both loading conditions. For the L_I case, the computational model assumes no change in distance between fibres, whereas for L_{II}, the normalised distance is based on the linear interpolation from Equation (4.4.5). The results show differences between the two approaches. In the computational model, fibres, being considerably stiffer than the surrounding matrix, exhibit minimal elongation, maintaining their original length under deformation. In contrast, the analytical model, assuming fully affine deformation, does not account for these material stiffness contrasts, leading to differences in deformation behaviour between the two approaches. Additionally, the computational model uses plane stress conditions, whereas the analytical model is a simplified 2D representation. These comparisons highlight the necessity of computational modelling for accurately capturing the behaviour of elastomeric composites, while the affine deformation model provides useful preliminary insights.

In the next chapter, the relationships derived by the computational model in Sections 4.4.1

and 4.4.2 are used to analyse the piezoresistive behaviour of composites under finite deformations. By understanding the changes in fibre orientation, limit angles, and minimum distances, one can predict the evolution of the electrical properties of composite with deformation.

Chapter 5

Analytical modelling of electrical conductivity

After establishing a computational framework for mechanical deformation, this chapter focuses on developing a rigorous mathematical model to estimate electrical conductivity. The foundation of this analysis is based on Eshelby's classical equivalent inclusion method (EIM), initially presented to evaluate intrinsic conductivity. The alignment of inclusions within the composites is described using both the limit angle of inclusion orientation and the probability distribution function, which together provide a cohesive measure of orientation. This model is extended to incorporate electron hopping and conductive networks of inclusions. These are critical mechanisms for electron transport in CNT/polymer composites, chosen as a representative example. The accuracy of the model is verified by comparing its predictions to several experimental results. Finally, the analytical model is integrated with the computational model to demonstrate how the developed framework can be employed to study the piezoresistive behaviour of elastomeric composites.

5.1 Introduction

Since their discovery in 1991, CNTs have significantly impacted material science due to their superior mechanical, thermal, and electrical properties. These properties drive the development of CNT-reinforced composites, promising advanced lightweight materials with diverse applications. The analytical micromechanics theories such as the rule of mixture (Liu, 1997; Dong, 2008; Fakirov, 2007), Eshelby's equivalent inclusion method (Withers et al., 1989; Eshelby, 1957b,a), Halpin–Tsai (Halpin, 1969; Affdl and Kardos, 1976; Kalaitzidou et al., 2007; Goyal et al., 2008), Lewis–Nielsen (Kostagiannakopoulou et al., 2016; Molnár et al., 2000) and Mori–Tanaka (Mori and Tanaka, 1973; Tan et al., 2005; Ferrari, 1991) have been widely used in many studies to evaluate the overall physical properties of composite materials with reasonable accuracy.

Developed by Eshelby (1957a), one of the most popular theories is the EIM. This theory

shows that the elastic fields inside an ellipsoidal inhomogeneity can be assumed to be uniform if the ellipsoidal inclusion is perfectly bonded to an infinitely extended matrix with a uniform load applied at infinity. One of the main advantages of EIM is that the solution is limited to a system of algebraic equations and it can be applied to the different behaviour of materials such as elastic-plastic, viscoelastic, and creep (Taya, 2005). The EIM was extended by Dunn and Taya (1993) for the problems with the coupled electro-elastic behaviour of piezoelectric composites based on the rigorous electro-elastic solution of an ellipsoidal inclusion in an infinite piezoelectric medium. The method in steady-state heat conduction was extended further for the randomly oriented particle composites with uncoupled thermal and electromagnetic behaviour by Hatta and Taya (1985, 1986). Chen and Wang (1996) proposed an analytical model based on the Mori–Tanaka mean field theory and the EIM to evaluate the thermal conductivity of the composite materials. They developed a new distribution function called Kacir's single-parameter exponential function to model the inclusion orientation. Seidel and Lagoudas (2006) used Mori–Tanaka, self-consistent, and composite cylinders micromechanical models in conjunction with the Eshelby method to analyse the elastic behaviour of nanocomposites reinforced by CNTs. They also considered the effects of interphase regions.

The electrical conductivity of most polymeric insulators can be drastically enhanced by adding a small volume fraction ($\sim 1\%$) of conductive nanostructures. Several analytical models were developed to analyse the electrical conductivity of CNT-reinforced composites. In another work by Seidel and Lagoudas (2009), a micromechanical model based on the Mori–Tanaka approach and EIM was proposed to investigate the effects of electron hopping by considering conductive interphase layers around particles. Their results showed that the thickness of the electrical tunnelling interphase layer relative to the CNT radius gives a distinct percolation concentration in which the well-dispersed CNTs are in close vicinity and electrical tunnelling easily happens. A simple analytical model was presented by Deng and Zheng (2008) to predict the electrical conductivity of CNT-reinforced composites considering the effects of the percolation, conductive networks, conductivity anisotropy and waviness of CNT inclusions. Their results revealed that the waviness of CNTs has an important influence in evaluating electrical conductivity. Feng and Jiang (2013) developed a hybrid analytical model to evaluate the electrical properties of CNT-reinforced polymers by incorporating electron hopping and conductive networks. An interphase layer surrounding the CNT was used to capture the nanoscale effect of electrical tunnelling based on the electron hopping theory. They illustrated that electron hopping and conductive networks contribute to the electrical conductivity, while the conductive networks effect is dominant above the percolation threshold. Garcia-Macias et al. (2017) developed a micromechanics model which can take into account the non-straightness by a helical waviness model and non-uniform dispersion of CNTs by a two-parameter agglomeration approach for evaluating the effective electrical conductivity of cement-based composites. A micromechanical model based on the Eshelby–Mori–Tanaka approach was conducted by Mora et al. (2020) to evaluate the electrical conductivity of polymer nanocomposites with agglomeration and segregation of CNT particles. Their model is able to predict the effect of segregation

on the electrical conductivity of nanocomposites. Tang et al. (2021) presented a simple analytical model to estimate the percolation threshold and electrical conductivity of CNT-reinforced composites by considering the effects of waviness, dispersion, volume fraction and size of particles.

Although the EIM was a popular choice in recent years in the literature to predict the electrical conductivity of composites, a lack of detailed derivation of the formulation is sensible. Therefore, the need for deriving EIM formulation and providing a detailed step-by-step explanation is felt. Moreover, these analytical models are heavily sensitive to their input parameters and the literature has generally shown a tendency to overlook in-depth discussions regarding this issue, with only a few articles addressing the sensitivity of analytical models to these parameters. Furthermore, in the realm of inclusion-based materials, non-uniform distributions of inclusions are often encountered, influenced by factors such as the manufacturing process or deformation due to large strain. Additionally, specific applications may call for deliberate manipulation of inclusion distribution to enhance material performance and achieve optimal designs using fewer resources. Goh et al. (2019) emphasized the benefits of directed alignment techniques in achieving enhanced device functionality. The impact of non-uniform distributions on electrical conductivity has not been extensively discussed in the literature.

Addressing these gaps, this chapter presents a rigorous analytical formulation to investigate the overall electrical conductivity of polymer composites to unravel the underlying mathematical principles governing electrical conductivity.

5.2 Equivalent inclusion method

This section summarises the equivalent inclusion method for calculating the effective electrical or thermal conductivity of two-phase composites (Eshelby, 1957a; Lai, 1977; Takao et al., 1982; Hatta and Taya, 1985, 1986). No electron hopping between inclusions is assumed in this section. The inclusions can be modelled with or without an interphase coating with a different conductivity (Yan et al., 2007; Feng and Jiang, 2013). First, the method is applied to a matrix with a single ellipsoidal inclusion and then extended to a matrix with numerous randomly distributed inclusions.

5.2.1 Overall electrical conductivity of two-phase composites

In general, the overall electrical conductivity of any two-phase composite, K_{ij} , can be estimated by volumetric average electric current density $\widetilde{J_i}$, and electric field of composite $\widetilde{E_i}$, using Ohm's law as

$$\widetilde{J_i} = K_{ij}\,\widetilde{E_j}\,, \tag{5.2.1}$$

where the tilde denotes the volumetric average of the respective quantities. The whole domain of composite represented by Ω, can be divided by the domain of matrix Ω^m and the domain of particles Ω^p such that $\Omega^m \cup \Omega^p = \Omega$, and $\Omega^m \cap \Omega^p = \emptyset$. By decomposing the average quantities

$\widetilde{J_i}$ and $\widetilde{E_i}$ into a matrix phase and a particle phase, they can be written as

$$\widetilde{J_i} = \frac{1}{V}\left[\int_{\Omega^m} J_i \,\mathrm{d}V + \int_{\Omega^p} J_i \,\mathrm{d}V\right], \tag{5.2.2a}$$

$$\widetilde{E_i} = \frac{1}{V}\left[\int_{\Omega^m} E_i \,\mathrm{d}V + \int_{\Omega^p} E_i \,\mathrm{d}V\right]. \tag{5.2.2b}$$

Ohm's law in each phase is given as

$$J_i = K^m \,\delta_{ij}\, E_j \quad \text{in } \Omega^m, \qquad J_i = K^p_{ij}\, E_j \quad \text{in } \Omega^p, \tag{5.2.3}$$

where $K^p_{ij} = \mathrm{diag}\,(K^p_{11}, K^p_{22}, K^p_{33})$ is the anisotropic electrical conductivity of particle, K^m is the electrical conductivity of the isotropic matrix. Equation (5.2.3) can be integrated over the respective domains to give

$$\int_{\Omega^m} J_i \,\mathrm{d}V = K^m \,\delta_{ij} \int_{\Omega^m} E_j \,\mathrm{d}V, \tag{5.2.4a}$$

$$\int_{\Omega^p} J_i \,\mathrm{d}V = K^p_{ij} \int_{\Omega^p} E_j \,\mathrm{d}V. \tag{5.2.4b}$$

By calculating $\widetilde{J_i}$ from equations (5.2.2a), (5.2.4a) and (5.2.4b), Equation (5.2.1) yields

$$K_{ij}\,\widetilde{E_j} = \frac{1}{V}\left[K^m \int_{\Omega^m} E_i \,\mathrm{d}V + K^p_{ij} \int_{\Omega^p} E_j \,\mathrm{d}V\right]. \tag{5.2.5}$$

By substituting $\int_{\Omega^m} E_i \,\mathrm{d}V$ from (5.2.2b), the above equation gives the overall electrical conductivity as

$$K_{ij}\,\widetilde{E_j} = K^m\,\widetilde{E_i} + \frac{1}{V}\left[K^p_{ij} - K^m\,\delta_{ij}\right] \int_{\Omega^p} E_j \,\mathrm{d}V. \tag{5.2.6}$$

Hence, in order to estimate K_{ij}, one needs to evaluate $\widetilde{E_i}$ and $\int_{\Omega^p} E_i \,\mathrm{d}V$ in (5.2.6).

5.2.2 Matrix with a single ellipsoidal inclusion

Consider a single ellipsoidal inclusion embedded in an infinite matrix while the constant electric current density J^0_i is applied at the far field as shown in Figure 5.1(a). By decomposing the electric field in the composite as $E_i = E^0_i + E^d_i$, Ohm's law inside the inclusion domain holds

$$J_i = K^p_{ij}\, E_j = K^p_{ij}\,[E^0_j + E^d_j] \quad \text{in } \Omega^p, \tag{5.2.7}$$

where E^d_i is the disturbed electric field due to the existence of inhomogeneity Ω^p, and E^0_i is the uniform electric field due to the current density J^0_i in the absence of the inclusion, that is,

$$J^0_i = K^m\, E^0_i \quad \text{in } \Omega. \tag{5.2.8}$$

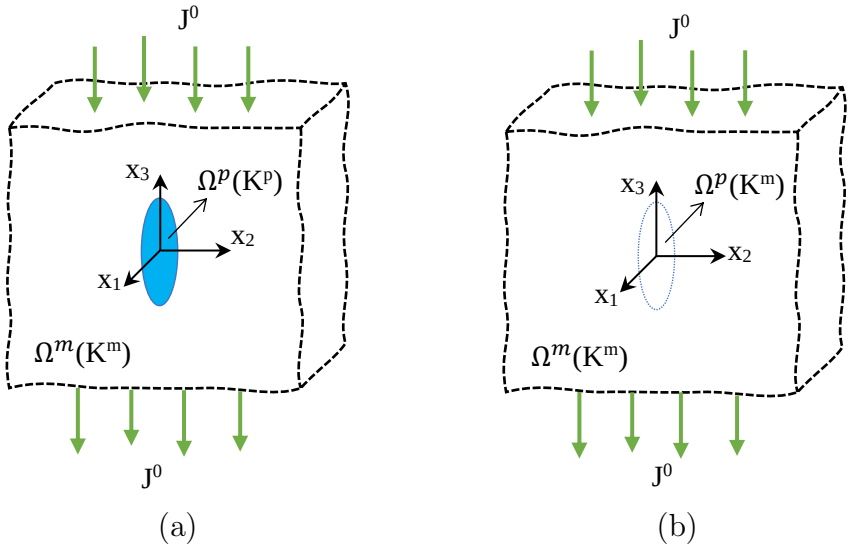

Figure 5.1: (a) A single ellipsoidal inclusion embedded in an infinite matrix, and (b) the equivalent inclusion inducing transformation electric field.

As shown in Figure 5.1(b), consider an imaginary subdomain Ω^p called an inclusion which undergoes transformation electric field but its electrical conductivity is equal to the electrical conductivity of the matrix. It can be shown that the EIM captures the disturbance of the applied electric current density by an eigenflux field generated by inclusion with a proper transformation electric field (Lai, 1977; Hatta and Taya, 1986). Based on this method, the disturbed current density inside the matrix and inclusion domains are expressed as

$$J_i - J_i^0 = K^m\, E_i^d \qquad \text{in } \Omega^m, \tag{5.2.9a}$$

$$J_i - J_i^0 = K^m \left[E_i^d - E_i^*\right] \quad \text{in } \Omega^p. \tag{5.2.9b}$$

Here, E_i^* represents the transformation electric field due to the uniformly distributed electric field. The resultant electric current density in the inclusion is given by the sum of equations (5.2.8) and (5.2.9b) as

$$J_i = K^m \left[E_i^0 + E_i^d - E_i^*\right] \quad \text{in } \Omega^p. \tag{5.2.10}$$

Upon comparing equations (5.2.7) and (5.2.10), one obtains

$$K^m \left[E_i^0 + E_i^d - E_i^*\right] = K_{ij}^p \left[E_j^0 + E_j^d\right] \quad \text{in } \Omega^p. \tag{5.2.11}$$

The above equation expresses a relation between the real composite and the equivalent inclusion. The 2nd-order tensor S_{ij}, analogous to the Eshelby tensor, relates E_i^d, and E_i^* inside the inclusion domain as

$$E_i^d = S_{ij}\, E_j^* \quad \text{in } \Omega^p. \tag{5.2.12}$$

This tensor depends solely on the geometry of the ellipsoidal inclusion.

Components of S_{ij} for different geometries. For an ellipsoidal inclusion with principal radii of a_{11}, a_{22} and a_{33}, the domain is bounded by

$$\left[\frac{x_1}{a_{11}}\right]^2 + \left[\frac{x_2}{a_{22}}\right]^2 + \left[\frac{x_3}{a_{33}}\right]^2 = 1. \tag{5.2.13}$$

Defining the partial differentiation operator $\partial_i \square = \partial \square / \partial x_i$, the tensor S_{ij} for this inclusion can be determined as (Hatta and Taya, 1985)

$$S_{ij} = \left[\frac{a_{11}\, a_{22}\, a_{33}}{4}\right] \partial_i \left(\partial_j \left(\int_0^\infty \left[\frac{x_1^2}{a_{11}^2 + s} + \frac{x_2^2}{a_{22}^2 + s} + \frac{x_3^2}{a_{33}^2 + s} \right] \frac{1}{\Delta(s)}\, \mathrm{d}s \right) \right), \tag{5.2.14}$$

where $\Delta(s) = \sqrt{[a_{11}^2 + s][a_{22}^2 + s][a_{33}^2 + s]}$. Differentiating from the above equation one obtains

$$S_{ii} = \left[\frac{a_{11}\, a_{22}\, a_{33}}{2}\right] \int_0^\infty \left[\frac{\mathrm{d}s}{[a_{11}^2 + s]\, \Delta(s)} + \frac{\mathrm{d}s}{[a_{22}^2 + s]\, \Delta(s)} + \frac{\mathrm{d}s}{[a_{33}^2 + s]\, \Delta(s)} \right]. \tag{5.2.15}$$

In the following, the components of tensor S_{ij} are listed for some specific geometries.

- Sphere: $a_{11} = a_{22} = a_{33}$

$$S_{11} = S_{22} = S_{33} = 1/3. \tag{5.2.16}$$

- Prolate ellipsoid: $a_{11} = a_{22} < a_{33}$

$$\begin{aligned} S_{11} = S_{22} &= \frac{a_{11}^2\, a_{33}}{2\sqrt{[a_{33}^2 - a_{11}^2]^3}} \left[(a_{33}/a_{11}) \sqrt{a_{33}^2/a_{11}^2 - 1} - \cosh^{-1}(a_{33}/a_{11}) \right], \\ S_{33} &= 1 - 2S_{11}. \end{aligned} \tag{5.2.17}$$

- Oblate ellipsoid: $a_{11} = a_{22} > a_{33}$

$$\begin{aligned} S_{11} = S_{22} &= \frac{a_{11}^2\, a_{33}}{2\sqrt{[a_{11}^2 - a_{33}^2]^3}} \left[\cos^{-1}(a_{33}/a_{11}) - (a_{33}/a_{11}) \sqrt{1 - a_{33}^2/a_{11}^2} \right], \\ S_{33} &= 1 - 2S_{11}. \end{aligned} \tag{5.2.18}$$

- Penny-shaped: $a_{11} = a_{22} \gg a_{33}$

$$S_{11} = S_{22} = \frac{\pi a_{33}}{4a_{11}},\ S_{33} = 1 - \frac{\pi a_{33}}{2a_{11}}. \tag{5.2.19}$$

- Elliptic cylinder: $a_{11}, a_{22} \ll a_{33} \to \infty$

$$S_{11} = \frac{a_{22}}{a_{11} + a_{22}},\ S_{22} = \frac{a_{11}}{a_{11} + a_{22}},\ S_{33} = 0. \tag{5.2.20}$$

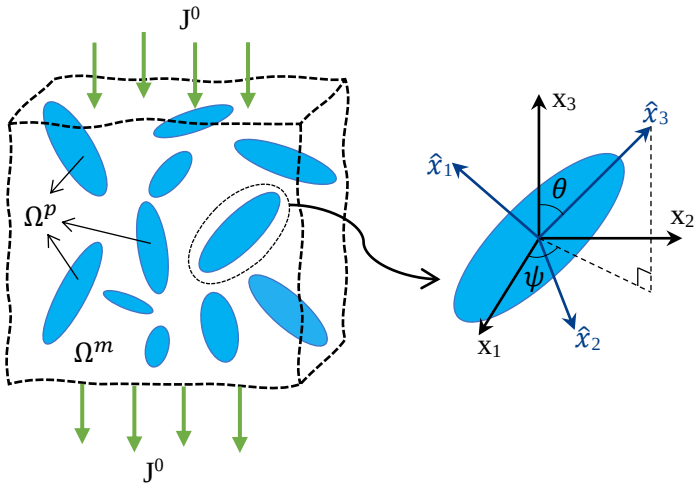

Figure 5.2: Numerous ellipsoidal inclusions embedded in an infinite matrix.

5.2.3 Matrix with numerous ellipsoidal inclusions

The approach presented in Section 5.2.2 for a single ellipsoidal inclusion can be extended for an infinite matrix with numerous ellipsoidal inclusions, as shown in Figure 5.2. In this case, the interactions between the inclusions should also be taken into account. Here, the total electric field E_i is decomposed into three parts as

$$E_i = E_i^0 + E_i^d + E_i^n \quad \text{in } \Omega, \tag{5.2.21}$$

where E_i^n is the disturbance of the electric field in the matrix due to conductive networks of inclusions and is defined as

$$E_i^n = \frac{1}{V_{\Omega^m}} \int_{\Omega^m} \left[E_i - E_i^0\right] \, \mathrm{d}V. \tag{5.2.22}$$

With a similar approach to the EIM for a single ellipsoid presented in the previous section, equations (5.2.9b) and (5.2.11) can be rewritten for composites with numerous ellipsoidal inclusions as

$$J_i - J_i^0 = K^m \left[E_i^d + E_i^n - E_i^*\right] \quad \text{in } \Omega^p, \tag{5.2.23}$$

and

$$K^m \left[E_i^0 + E_i^d + E_i^n - E_i^*\right] = K_{ij}^p \left[E_j^0 + E_j^d + E_j^n\right] \quad \text{in } \Omega^p. \tag{5.2.24}$$

By defining $|\square|$ that specify the outer boundary of $\square$, and integrating over the entire domain Ω, the electric current density $J_i - J_i^0$ vanishes using Gauss' divergence theorem as (Hatta and Taya, 1986):

$$\begin{aligned} \int_\Omega [J_i - J_i^0] \, \mathrm{d}V &= \int_\Omega [J_j - J_j^0] \, \delta_{ij} \, \mathrm{d}V = \int_\Omega [J_j - J_j^0] \, \partial_j x_i \, \mathrm{d}V \\ &= \int_{|\Omega|} [J_j - J_j^0] \, n_j \, x_i \, \mathrm{d}V - \int_\Omega \partial_j [J_j - J_j^0] \, x_i \, \mathrm{d}V = 0, \end{aligned} \tag{5.2.25}$$

since $(J_j - J_j^0)\, n_j = 0$ on $|\Omega|$ and $\partial_j (J_j - J_j^0) = 0$ in Ω. Hence, by integrating over the entire domain of the composite, Equation (5.2.23) becomes

$$\int_\Omega E_i^n \, \mathrm{d}V = \int_\Omega \left[E_i^* - E_i^d \right] \, \mathrm{d}V, \tag{5.2.26}$$

that results in

$$E_i^n = \frac{1}{V} \int_{\Omega^p} \left[E_i^* - E_i^d \right] \, \mathrm{d}V. \tag{5.2.27}$$

Thus, recalling Equation (5.2.21), the volumetric average of the total electric field is given as

$$\widetilde{E_i} = \frac{1}{V} \int_\Omega E_i \, \mathrm{d}V = E_i^0 + \frac{1}{V} \int_\Omega [E_i^n + E_i^d] \, \mathrm{d}V. \tag{5.2.28}$$

Making use of equations (5.2.23) and (5.2.25), one obtains

$$\widetilde{E_i} = \frac{1}{V} \int_\Omega E_i \, \mathrm{d}V = E_i^0 + \frac{1}{V} \int_\Omega [E_i^n + E_i^d - E_i^*] \, \mathrm{d}V + \frac{1}{V} \int_{\Omega^p} E_i^* \, \mathrm{d}V, \tag{5.2.29}$$

in which $\int_\Omega E_i^* \, \mathrm{d}V$ was added and subtracted. The second term on the right-hand side of Equation (5.2.29) is the disturbance of the electric current density $J_i - J_i^0$ when integrated over the entire domain Ω, which is equal to zero. Hence,

$$\widetilde{E_i} = E_i^0 + \frac{1}{V} \int_{\Omega^p} E_i^* \, \mathrm{d}V. \tag{5.2.30}$$

The electric field when integrated over the inclusions can be written as

$$\int_{\Omega^p} E_i \, \mathrm{d}V = K^m \left[K^m \, \delta_{ij} - K_{ij}^p \right]^{-1} \int_{\Omega^p} E_j^* \, \mathrm{d}V \, . \tag{5.2.31}$$

Hence, using $\widetilde{E_i}$ from Equation (5.2.30) and $\int_{\Omega^p} E_i \, \mathrm{d}V$ from Equation (5.2.31), the non-zero components of overall electrical conductivity K_{ij} in (5.2.6) can be estimated as

$$K_{11} = K_{22} = K^m \left[1 - \frac{\int_{\Omega^p} E_1^* \, \mathrm{d}V}{V \, E_1^0 + \int_{\Omega^p} E_1^* \, \mathrm{d}V} \right] , \tag{5.2.32a}$$

$$K_{33} = K^m \left[1 - \frac{\int_{\Omega^p} E_3^* \, \mathrm{d}V}{V \, E_3^0 + \int_{\Omega^p} E_3^* \, \mathrm{d}V} \right] . \tag{5.2.32b}$$

Next, one needs to determine $\int_{\Omega^p} E_i^* \, \mathrm{d}V$ in the above expression based on the distribution of inclusions.

5.2.4 Composites with randomly distributed inclusions

In order to evaluate the overall electrical conductivity of a composite reinforced by randomly distributed inclusions, one needs to determine $\int_{\Omega^p} E_i^* \, \mathrm{d}V$. The model used by Takao et al. (1982) for the composite reinforced by randomly distributed inclusions is used in this study.

The orientation of every inclusion is described by Euler angles θ and ψ as shown in Figure 5.2. Using the local coordinates $\{\widehat{x}_1, \widehat{x}_2, \widehat{x}_3\}$, where the $\widehat{x}_3$ axis is set to coincide with the inclusion axis, the EIM from Equation (5.2.24) for a representative inclusion yields

$$K^m \left[\widehat{E}_i^0 + \widehat{E}_i^d + \widehat{E}_i^n - \widehat{E}_i^*\right] = K_{ij}^p \left[\widehat{E}_j^0 + \widehat{E}_j^d + \widehat{E}_j^n\right] \quad \text{in } \Omega^p \tag{5.2.33}$$

and

$$\widehat{E}_i^d = S_{ij}\, \widehat{E}_j^* \quad \text{in } \Omega^p, \tag{5.2.34}$$

where the hat accent refers to the local coordinate system on representative inclusion. Equations (5.2.33) and (5.2.34) can be held for every inclusion distributed in the matrix. From equations (5.2.33) and (5.2.34), one can obtain

$$[K^m\, \delta_{ij} - K_{ij}^p]\, [\widehat{E}_j^0 + \widehat{E}_j^n] = [K_{ij}^p - K^m\, \delta_{ij}]\, S_{jk}\, \widehat{E}_k^* + K^m\, \widehat{E}_i^* \quad \text{in } \Omega^p\,. \tag{5.2.35}$$

Upon introduction of 2nd-order tensors A_{ij} and B_{ij},

$$A_{ij} = [K_{ik}^p - K^m \delta_{ik}]\, S_{kj} + K^m\, \delta_{ij}\,, \tag{5.2.36a}$$

$$B_{ij} = A_{ik}^{-1}\, [K^m \delta_{kj} - K_{kj}^p]\,, \tag{5.2.36b}$$

the value of $\widehat{E}_i^*$ in Equation (5.2.35) can be stated in a more compact way as

$$\widehat{E}_i^* = B_{ij}\, [\widehat{E}_j^0 + \widehat{E}_j^n]\,. \tag{5.2.37}$$

From equations (5.2.34) and (5.2.37), one can eliminate $\widehat{E}_i^*$ and obtain

$$\widehat{E}_i^d = S_{ij}\, B_{jk}\, [\widehat{E}_k^0 + \widehat{E}_k^n]\,. \tag{5.2.38}$$

The rotation tensor Q_{ij} defined as $a_i = Q_{ij}\, \widehat{a}_j$ links the local coordinate system of the particle and the global coordinate system in the matrix. This 2nd-order tensor can be written in a matrix form as

$$[Q_{ij}] = \begin{bmatrix} \cos\psi\, \cos\theta & -\sin\psi & \cos\psi\, \sin\theta \\ \cos\theta\, \sin\psi & \cos\psi & \sin\psi\, \sin\theta \\ -\sin\theta & 0 & \cos\theta \end{bmatrix}. \tag{5.2.39}$$

Using this tensor, one can transform the conductivity tensor into the global coordinate system. So, by transforming equations (5.2.37) and (5.2.38) one obtains

$$E_i^* = Q_{ij}\, B_{jk}\, Q_{kl}^{-1}\, [E_l^0 + E_l^n], \tag{5.2.40a}$$

$$E_i^d = Q_{ij}\, S_{jk}\, B_{kl}\, Q_{lo}^{-1}\, [E_o^0 + E_o^n]. \tag{5.2.40b}$$

Now, consider a unit sphere where the orientation of inclusion is indicated by Euler angles θ and ψ. The integration of quantity of E_i^* over particle domain Ω^p is stated as

$$\int_{\Omega^p} E_i^* \, \mathrm{d}V = \int \int E_i^* \, \xi(\theta, \psi) \, \mathrm{d}s = \int_{\psi=0}^{2\pi} \int_{\theta=0}^{\alpha} E_i^* \, \xi(\theta, \psi) \sin\theta \, \mathrm{d}\theta \, \mathrm{d}\psi, \tag{5.2.41}$$

where α is the limit of the inclusion orientation angle θ as defined in Section 4.4.1.1. The probability density function $\xi(\theta, \psi)$ is defined as the number of particles (ρ) intersecting a unit area of the unit sphere multiplied by the volume of a single particle V_{sp}, that is, $\xi(\theta, \psi) = \rho V_{\mathrm{sp}}$. The function ξ is identity for a uniform random distribution but can take more general forms as shown in further sections. This function was introduced earlier in Section 4.4.1.3.

Similarly, the integration of the quantity of disturbed electric field over the particle domain is computed as

$$\int_{\Omega^p} E_i^d \, \mathrm{d}V = \int_0^{2\pi} \int_0^{\alpha} E_i^d \, \xi(\theta, \psi) \, \sin\theta \, \mathrm{d}\theta \, \mathrm{d}\psi \, . \tag{5.2.42}$$

The volume fraction of inclusions, ϕ, is evaluated as

$$\phi = \frac{1}{V} \int_{\Omega^p} \xi(\theta, \psi) \, \mathrm{d}s = \frac{1}{V} \int_0^{2\pi} \int_0^{\alpha} \xi(\theta, \psi) \, \sin\theta \, \mathrm{d}\theta \, \mathrm{d}\psi \, . \tag{5.2.43}$$

Inserting E_i^* in Equation (5.2.40a) into Equation (5.2.41), and inserting the expression for E_i^d from Equation (5.2.40b) into Equation (5.2.42), derives

$$\int_{\Omega^p} E_i^* \, \mathrm{d}V = \left[\int_0^{2\pi} \int_0^{\alpha} \xi \left[Q_{ik} \, B_{kl} \, Q_{lj}^{-1} \right] \sin\theta \, \mathrm{d}\theta \, \mathrm{d}\psi \right] \left[E_j^0 + E_j^n \right], \tag{5.2.44a}$$

$$\int_{\Omega^p} E_i^d \, \mathrm{d}V = \left[\int_0^{2\pi} \int_0^{\alpha} \xi \left[Q_{ik} \, S_{kl} \, B_{lm} \, Q_{mj}^{-1} \right] \sin\theta \, \mathrm{d}\theta \, \mathrm{d}\psi \right] \left[E_j^0 + E_j^n \right]. \tag{5.2.44b}$$

Substituting V from Equation (5.2.43) into Equation (5.2.27) and introducing tensors C_{ij} and D_{ij} as

$$C_{ij} = \frac{\int_0^{2\pi} \int_0^{\alpha} \xi \left[Q_{ik} \, B_{kl} \, Q_{lj}^{-1} \right] \sin\theta \, \mathrm{d}\theta \, \mathrm{d}\psi}{\int_0^{2\pi} \int_0^{\alpha} \xi \, \sin\theta \, \mathrm{d}\theta \, \mathrm{d}\psi}, \tag{5.2.45a}$$

$$D_{ij} = \frac{\int_0^{2\pi} \int_0^{\alpha} \xi \left[Q_{ik} \, S_{kl} \, B_{lm} \, Q_{mj}^{-1} \right] \sin\theta \, \mathrm{d}\theta \, \mathrm{d}\psi}{\int_0^{2\pi} \int_0^{\alpha} \xi \, \sin\theta \, \mathrm{d}\theta \, \mathrm{d}\psi}, \tag{5.2.45b}$$

to compact the formulation further, Equation (5.2.27) yields

$$E_i^n = \phi \left[C_{ij} - D_{ij} \right] \left[E_j^0 + E_j^n \right]. \tag{5.2.46}$$

Considering the fact that C_{ij} and D_{ij} are diagonal matrices due to K_{ij}^p, $K^m \, \delta_{ij}$ and S_{ij} being diagonal, the components of E_i^n can be explicitly expressed in terms of the components

of vector E_i^0 as

$$E_1^n = E_2^n = \frac{\phi\,[C_{11} - D_{11}]\,E_1^0}{1 - \phi\,[C_{11} - D_{11}]}\,, \tag{5.2.47a}$$

$$E_3^n = \frac{\phi\,[C_{33} - D_{33}]\,E_3^0}{1 - \phi\,[C_{33} - D_{33}]}\,, \tag{5.2.47b}$$

so that the components of $\int_{\Omega^p} E_i^*\,\mathrm{d}V$ in Equation (5.2.44a) are written as

$$\int_{\Omega^p} E_1^*\,\mathrm{d}V = \int_{\Omega^p} E_2^*\,\mathrm{d}V = \frac{\phi\,V\,C_{11}\,E_1^0}{1 - \phi\,[C_{11} - D_{11}]}\,, \tag{5.2.48a}$$

$$\int_{\Omega^p} E_3^*\,\mathrm{d}V = \frac{\phi\,V\,C_{33}\,E_3^0}{1 - \phi\,[C_{33} - D_{33}]}\,. \tag{5.2.48b}$$

Finally, the non-zero components of the overall electrical conductivity K_{ij} of the composite in (5.2.32) can be estimated as

$$K_{11} = K_{22} = K^m \left[1 - \frac{\phi\,C_{11}}{1 + \phi\,D_{11}}\right], \tag{5.2.49a}$$

$$K_{33} = K^m \left[1 - \frac{\phi\,C_{33}}{1 + \phi\,D_{33}}\right]. \tag{5.2.49b}$$

The established EIM for estimating the overall electrical conductivity of randomly distributed inclusions inside a matrix in Equations (5.2.49) is only valid when there is no electron hopping between particles and thus no conductive networks of particles are formed in the composite.

5.2.5 Particles with interphase coatings

To take into account the effects of electron tunnelling and conductive networks, the EIM expressed in Section 5.2.4 for randomly distributed particles is extended for particles with interphase layers by replacing every regular particle with an equivalent particle. For this purpose, it is assumed that every particle is surrounded by an interphase layer of thickness t and isotropic electrical conductivity of K^{int} as shown in Figure 5.3. Here the particles are chosen to be *cylinders*. The effective conductivity of an equivalent cylinder with a length of l and diameter

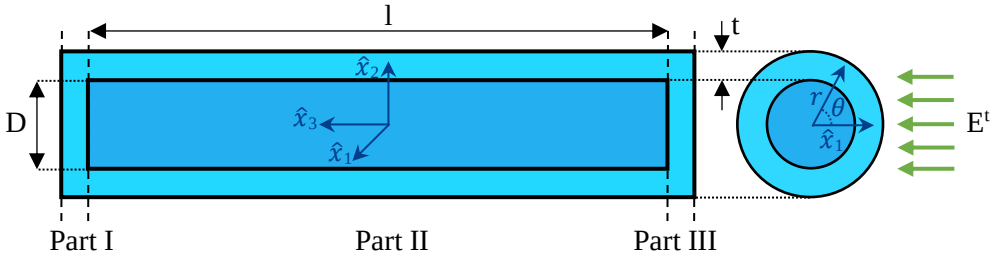

Figure 5.3: An equivalent cylinder particle with its interphase layer surrounding it.

of D along $\widehat{x}_1, \widehat{x}_2$ and $\widehat{x}_3$ is derived by

$$\acute{K}^p_{11} = \acute{K}^p_{22} = \frac{K^{\text{int}}}{l+2t}\left[2t + \frac{l\,K^p_{11}\,D^2/2 + l\left[K^p_{11}+K^{\text{int}}\right]\left[t^2+Dt\right]}{D^2\,K^{\text{int}}/2 + \left[K^p_{11}+K^{\text{int}}\right]\left[t^2+Dt\right]}\right], \tag{5.2.50a}$$

$$\acute{K}^p_{33} = \frac{K^{\text{int}}\left[l+2t\right]\left[K^p_{33}\,D^2/4 + K^{\text{int}}\left[Dt+t^2\right]\right]}{t\,K^p_{33}\,D^2/2 + 2\,tK^{\text{int}}\left[Dt+t^2\right] + l\,K^{\text{int}}\left[D/2+t\right]^2}, \tag{5.2.50b}$$

where the electrical conductivity tensor in the local coordinate system of the equivalent cylinder is given as $\text{diag}(\acute{K}^p_{11}, \acute{K}^p_{11}, \acute{K}^p_{33})$. The detailed derivation of these formulas is provided in Appendix D. Based on these effective cylinders, the effective volume fraction $\acute{\phi}$ can be calculated from the ratio of the volume of one equivalent particle V^{ep} to the volume of one particle V^p multiplied by the volume fraction of original particles as

$$\acute{\phi} = \frac{V^{\text{ep}}}{V^p}\,\phi = \frac{\pi[D/2+t]^2\left[l+2t\right]}{\pi[D/2]^2\,l}\,\phi = \frac{4\phi\left[D/2+t\right]^2\left[l+2t\right]}{l\,D^2}. \tag{5.2.51}$$

Therefore, the EIM described in Section 5.2.4 to estimate the overall electrical conductivity of randomly distributed inclusion composites can be extended for composites with interphase layer by replacing the inclusions with equivalent particles. That is replacing ϕ in (5.2.49) by $\acute{\phi}$ in (5.2.51) and replacing K^p_{ij} in (5.2.36) by $\acute{K}^p_{ij}$ in (5.2.50).

Remark. The established EIM in Section 5.2 for estimating the overall electrical conductivity of randomly distributed inclusions inside a matrix with or without the interphase layer is equivalent to EIM for estimating the thermal conductivity of composite with or without the interphase layer. In the thermal context, electrical conductivity coefficients K_{ij} are substituted with thermal conductivity coefficients κ_{ij}, the electric field E_i with the temperature gradient $\partial_i T$, and the electric current density J_i with heat flux q_i. This analogy extends similarly to elastic properties. □

5.3 Electron tunnelling and conductive networks

From this section onwards, the focus is on CNT/polymer nanocomposites, and the inclusions are chosen to be CNTs. When the distance between two CNTs is less than a threshold value, electrons can transport from one CNT to another as shown in Figure 5.4. This phenomenon is called electron tunnelling or electron hopping (Ounaies et al., 2003; Du et al., 2004; Zhang et al., 2007; Hu et al., 2008). In this section, the EIM developed for composites with interphase layers around inclusions in Section 5.2 is specialised by considering the interphase layer around CNTs as a model for electron hopping (Seidel and Lagoudas, 2009). For this purpose, the extended EIM for randomly distributed inclusions composites with interphase layers around inclusions in Section 5.2.5 is used by assuming the conductive interphase layer around CNTs letting the electrons hop.

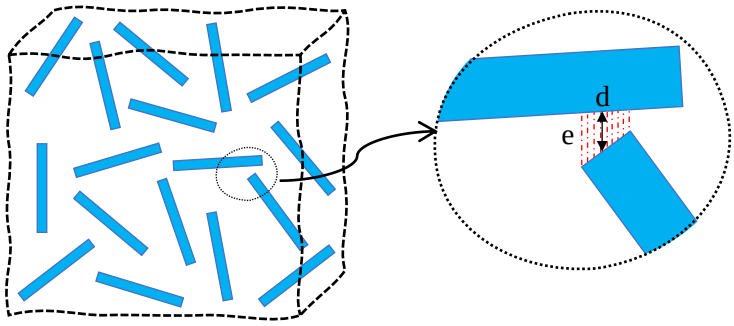

Figure 5.4: Electron tunnelling between two close CNTs.

5.3.1 Electron tunnelling

Simmons (1963) derived a generalized method to calculate the tunnelling current between electrodes when there is an insulating film separating them. By assuming a uniform thickness of the insulating film in the conduction region and neglecting any variations in barrier height along its thickness, one can apply the formula designed for a rectangular potential barrier. Relying on that, one can adopt a generalized framework where the fillers are treated as three-dimensional continuum objects. This approach is widely used in the literature to model the conductivity due to electron tunnelling for CNT-based composites (Mora et al., 2020; Feng and Jiang, 2013; Garcia-Macias et al., 2017; Quinteros et al., 2023; Wang et al., 2021; Chanda et al., 2021; Buroni and García-Macías, 2021).

Based on the Simmons model, these research studies used the following formula to estimate the tunnelling resistance R_t at a junction between two CNTs:

$$R_t = \frac{h^2 d}{A_t\, e^2 \sqrt{2m\,\Delta E}} \exp\left(\frac{4\pi d}{h}\sqrt{2m\,\Delta E}\right), \tag{5.3.1}$$

where h is Planck's constant, d is the distance between two adjacent CNTs, A_t is the area available for tunnelling, e is the charge of an electron, m is the mass of an electron, and ΔE is the energy barrier which is equal to the work required for an electron to tunnel. The universal constants h, e and m have their values listed in Table 5.1.

The above model assumes that the contact surfaces of the CNTs are large, flat, and highly conductive. Bao et al. (2012) argued that this assumption does not hold for CNTs at the nanoscale, where the contact region is composed of only a few atoms. Hence, an alternative approach was proposed based on the assumption that electrons are in a ballistic transport state and confined to one-dimensional channels (Bao et al., 2012; Gong et al., 2013; Li et al., 2005; Bao et al., 2011). This approach is detailed and compared with the Simmons model in Appendix E. Upon comparison, the Simmons model is preferred for this study due to its widespread use and reasonable accuracy.

The distance d between CNTs is chosen to be different for the electron hopping mechanism in comparison to the mechanism based on conductive networks. In order to capture the effect

Table 5.1: Model parameters with constant values

Parameter	Value	Units
h	6.62607×10^{-34}	m^2 kg/s
e	-1.60218×10^{-19}	C
m	9.10938×10^{-31}	kg

of electron tunnelling, the thickness of the interphase layer is considered as $t = d_c/2$, where d_c represents the cut-off tunnelling junction gap. The conductivity of the layer is described as $K^{\text{int}} = d_c/(A_t R_t)$. In the next section, the value of the gap distance between CNTs d, is determined for conductive networks of CNTs.

5.3.2 Conductive networks

In order to consider the effect of the conductive networks of CNTs, the average junction distance between CNTs d_a is introduced so that the thickness of the interphase layer is assumed as $t = d_a/2$, while the conductivity of the layer is given by $K^{\text{int}} = d_a/(A_t R_t)$. The distance d_a is estimated by a power-law as (Feng and Jiang, 2013; Allaoui et al., 2008)

$$d_a = \left[\frac{\phi_c}{\phi}\right]^{1/3} d_c, \tag{5.3.2}$$

where ϕ_c is the percolation threshold, the critical volume fraction at which continuous conductive networks begin to form. At this point, the composite shifts from an insulating to a conductive state as filler particles establish pathways for electron transport.

Eventually, the overall electrical conductivity of CNT-reinforced polymer nanocomposite can be estimated based on a simple rule of mixture considering the effect of electron hopping and conductive networks of CNTs. Estimating the fraction of CNTs taking part in forming conductive networks after percolation threshold as (Deng and Zheng, 2008)

$$\zeta = \frac{\phi^{1/3} - \phi_c^{1/3}}{1 - \phi_c^{1/3}}; (\phi_c \leq \phi < 1)\,, \tag{5.3.3}$$

while the rest contribute to the electron tunnelling mechanism, the overall electrical conductivity of the composite is

$$K = (1 - \zeta)K_{\text{T}} + \zeta K_{\text{N}}. \tag{5.3.4}$$

Here K_T is the contribution to the electrical conductivity from the tunnelling effect which is evaluated by the extended EIM derived in Section 5.2 by substituting the thickness $t = d_c/2$ and conductivity $K^{\text{int}} = d_c/(A_t R_t)$ of interphase in Equation (5.2.50). K_N is the contribution to the electrical conductivity from conductive networks and is evaluated by the extended EIM derived in Section 5.2 by substituting the thickness $t = d_a/2$ and conductivity $K^{\text{int}} = d_a/(A_t R_t)$ of interphase in Equation (5.2.50) under the assumption $L \to \infty$ in Equation (5.2.12).

The primary assumptions of the presented mathematical model are:

(i) CNTs are modelled as straight, ignoring their natural curvatures which influence their properties.

(ii) A uniform size for all CNTs is assumed, contrary to their actual varied dimensions.

(iii) The impact of CNT agglomeration and segregation is overlooked.

(iv) The EIM is based on ellipsoidal particles, while in electron hopping it is assumed that inclusions are cylinders.

For discussions on the impacts of CNT waviness, agglomeration, segregation, and variability in dimensions, refer to studies such as (Chanda et al., 2021; Garcia-Macias et al., 2017; Mora et al., 2020; Wang et al., 2021).

5.4 Numerical results

In this section, the accuracy of the model developed in Section 5.3 is verified using experimental data. Then, the validated model is used to study the influence of CNT dimensions, volume fraction, orientation, and distribution on the overall conductivity of the nanocomposite. The Mathematica file used to perform these calculations is made open source, refer to Ahmadi and Saxena (2023).

Due to their high aspect ratio ($l/D \gg 1$), CNTs in this study are assumed to be isotropic $K^p_{11} = K^p_{33}$(Seidel and Lagoudas, 2009; Garcia-Macias et al., 2017). A value of $d_c = 1.8$ nm is used for the cut-off distance between CNTs to allow for electron-hopping as has been reported in several papers (Feng and Jiang, 2013; Li et al., 2007; Mora et al., 2018). However, choosing other parameters needs more care since different types of CNTs and polymer matrices with various manufacturing processes for a wide range of applications have been reported. Accordingly, in Section 5.4.1 some experimental studies on different CNT/polymer composites are chosen to investigate the analytical model and estimate the parameters based on. The length l, diameter D, and the percolation threshold ϕ_c of CNTs are directly chosen from the measured or reported values in those works.

Remark. In some research papers, an expression is introduced to predict the value of ϕ_c. One of the most common ones is (Gao and Li, 2003; Deng and Zheng, 2008)

$$\phi_c(H) = \frac{9H[1-H]}{2+15H-9H^2}\,, \tag{5.4.1}$$

where $H(\gamma) = \frac{1}{\gamma^2-1}[\frac{\gamma}{\sqrt{\gamma^2-1}}\ln(\gamma+\sqrt{\gamma^2-1})-1]$ and γ is the aspect ratio of the CNTs defined as $\gamma = l/D$. However, investigating further indicates that the above expression does not give an accurate estimation for every case study and as denoted in some papers in the literature, the value of ϕ_c depends on the characteristics of polymer and CNTs and is hard to predict by an analytical expression for all types of polymer composites. □

Table 5.2: Parameters used for comparison with experimental data in Section 5.4.1.

Parameter	Units	PS/CNT	TPU/CNT	Epoxy/CNT	UHMWPE/CNT
l	µm	3	30	30	10
D	nm	15	10	15	16
ϕ_c	%	0.46	0.0723	0.02	0.05
K^m	S/m	10^{-11}	10^{-11}	10^{-11}	10^{-13}
Reference		Wang et al. (2021)	Mora et al. (2020)	Kim et al. (2005)	Lisunova et al. (2007)

Nevertheless, the values of electrical conductivity of CNT nanoparticles K_{11}^p and the energy barrier ΔE of various polymers are reported in a very wide range and the effective conductivity is very sensitive to these values. These parameters are determined separately for each experiment in Section 5.4.1 by a least squares minimisation technique. It is worth noting that this issue has been rather avoided to be discussed in-deep in the literature and the sensitivity of analytical models to these parameters is neglected in most cases except for a few articles. After model validation, the study case from Wang et al. (2021), i.e., polystyrene reinforced by multi-walled CNT (MWCNT) is chosen for the parametric study in Section 5.4.2.

5.4.1 Comparison with experimental data

To verify the accuracy of the presented model, the analytical results are compared with some experimental studies herein. The case studies are chosen from four different nanocomposites: CNT/Polystyrene (PS) from Wang et al. (2021), CNT/Thermoplastic polyurethane (TPU) from Mora et al. (2020), CNT/Epoxy from Kim et al. (2005), and CNT/Thermoplastic ultrahigh molecular weight polyethylene (UHMWPE) from Lisunova et al. (2007). The values of length and diameter of CNTs, percolation volume fraction, and intrinsic electrical conductivity of matrices for all four examples are listed in Table 5.2.

The unspecified parameters are the intrinsic electrical conductivity of CNTs K_{11}^p and the energy barrier ΔE. These parameter are determined based on the given ranges of $K_{11}^p = [10 - 10^6]$ S/m (Ebbesen et al., 1996; Ando et al., 1999; Feng and Jiang, 2013), and $\Delta E = [0.1{-}5.0]$ eV (Shiraishi and Ata, 2001; Garcia-Macias et al., 2017; Allaoui et al., 2008), in comparison to the experimental results. Thus, the following function, which expresses the least square logarithmic difference between the analytical value and the experimental data, is introduced

$$f(K_{11}^p, \Delta E) = \sum_{n=1}^{m} \left[\log_{10}(K_{11}(K_{11}^p, \Delta E, \phi_i)) - \log_{10}(K_{11}^{\exp}(\phi_i))\right]^2 . \tag{5.4.2}$$

In Equation (5.4.2), m is the number of points in the experimental data for different volume fractions ϕ_i and $K_{11}^{\exp}$ is the electrical conductivity measured in the experiments. The goal is to minimize this function to reduce the difference between the analytical model and experiments and thereby determine optimized values of K_{11}^p and ΔE. Optimization using Equation (5.4.2) results in a value of $K_{11}^p = 1000$ S/m $\pm 10\%$ for all the four cases. To illustrate the procedure in a simplified manner, $K_{11}^p = 1000$ S/m is fixed, which is the most commonly used value in

the literature for all the cases, and only analyse the influence of the value of ΔE.

The computation results in the value of ΔE as $0.7, 1.2, 2.7$ and 1.1 eV for CNT/PS, CNT/TPU, CNT/Epoxy, and CNT/UHMWPE, respectively. In comparison, Wang et al. (2021) used $K_{11}^p = 10^4$ S/m and $\Delta E = 2.5$ eV to model the experiments on CNT/PS polymer. These parameter values differ significantly from the optimized range and were not experimentally measured but taken from prior modelling data on CNT nanocomposites. On the other hand, Mora et al. (2020) calculated K_{11}^p as 987 S/m and used a prior published value of $\Delta E = 1.5$ eV for modelling the experiments on CNT/TPU. These parameter values are very close to the optimized range obtained herein.

Figure 5.5 illustrates the electrical conductivity of PS/CNT, TPU/CNT, Epoxy/CNT and UHMWPE/CNT nanocomposites predicted by the current model versus those given by experiments for different volume fractions of CNT. The graphs are plotted for 0.1, 2.5, and 5.0 eV, and the optimized value of ΔE for each case study. All graphs demonstrate a good agreement between the model and experimental results, with the predictions closely matching the observed data across various CNT-reinforced polymer composites. This suggests that the model accurately captures the key trends and behaviour of the system under study, although some deviations may exist due to the inherent assumptions made in the modelling process or limitations in the experimental setup. In Figure 5.5 (a), it can be observed that for energy barriers higher or lower than 0.7, the results are far from the experimentally obtained values. The same trend can be observed for other cases which indicates that determining the energy barrier plays an important role in predicting the electrical conductivity by the present model. Besides, as expected, increasing the value of the energy barrier drastically decreases the electrical conductivity after percolation. This effect is more pronounced for lower volume fractions of CNTs. Moreover, graphs with a higher energy barrier have a softer jump after percolation, while graphs with a lower energy barrier show a sharp change after percolation. It should be noted again that since the distribution of CNTs is uniform in all the cases considered here, the composites are isotropic, that is, $K_{11} = K_{22} = K_{33}$.

5.4.2 Effect of orientation and dimensions

Now that the results of the present model are compared to the experimental data, the effect of different aspects of the reinforcements, i.e., CNT alignment, distribution, and dimensions, on the transverse and longitudinal effective electrical conductivity of the nanocomposites are investigated. For this parametric study, PS/CNT composite material from Wang et al. (2021) is selected. The values of the parameters for PS/CNT composite are listed in Table 5.2. Furthermore, the value of the energy barrier for this composite is obtained as $\Delta E = 0.7$ eV in the previous section. These values are used for all calculations in this section unless otherwise stated.

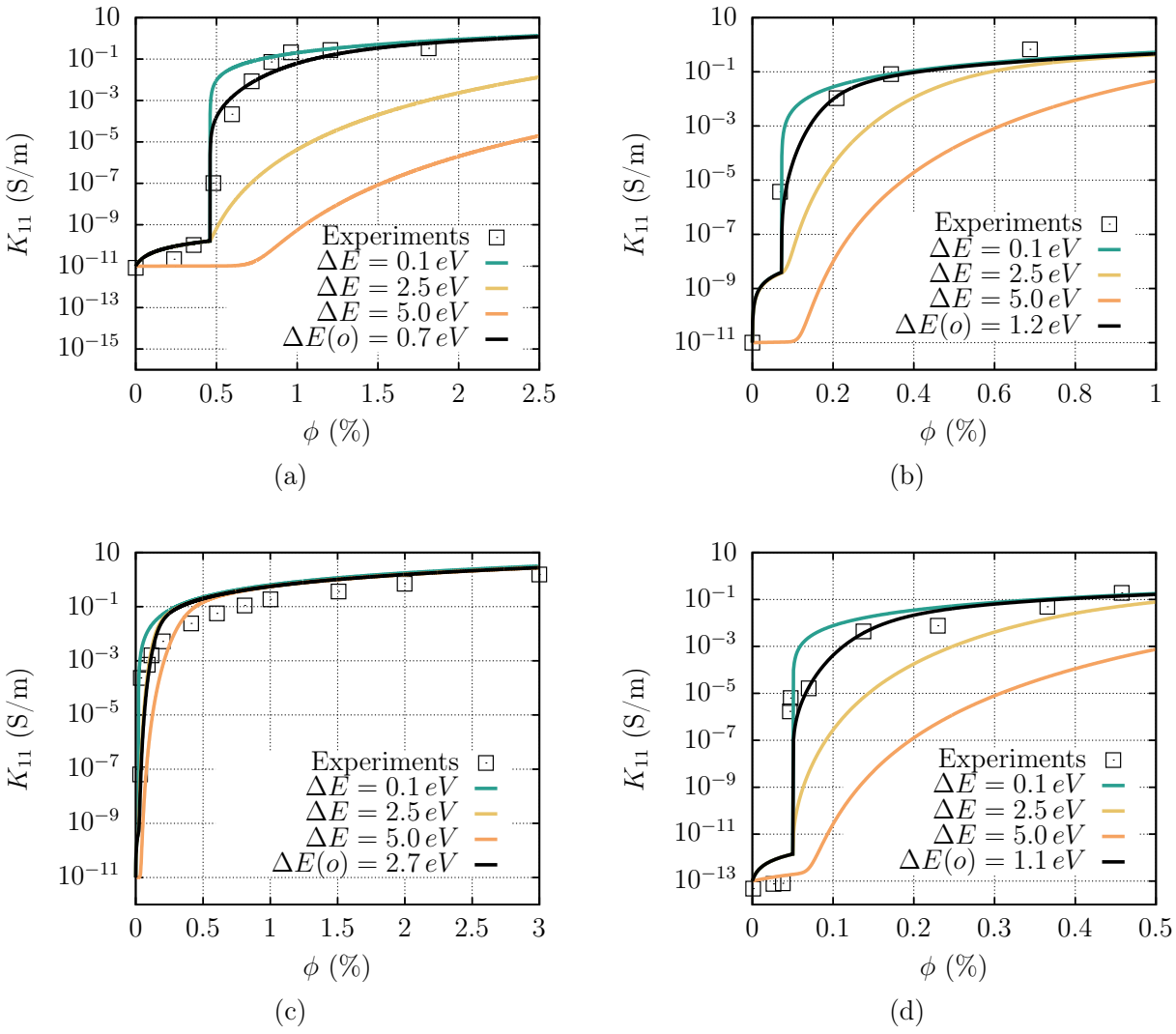

Figure 5.5: Comparing present model to experiments for (a) PS/CNT by Wang et al. (2021), (b) TPU/CNT by Mora et al. (2020), (c) Epoxy/CNT by Kim et al. (2005) and (d) UHMWPE/CNT by Lisunova et al. (2007). The black curves with the label $\Delta E(o)$ show the conductivity for optimized values of the energy barrier.

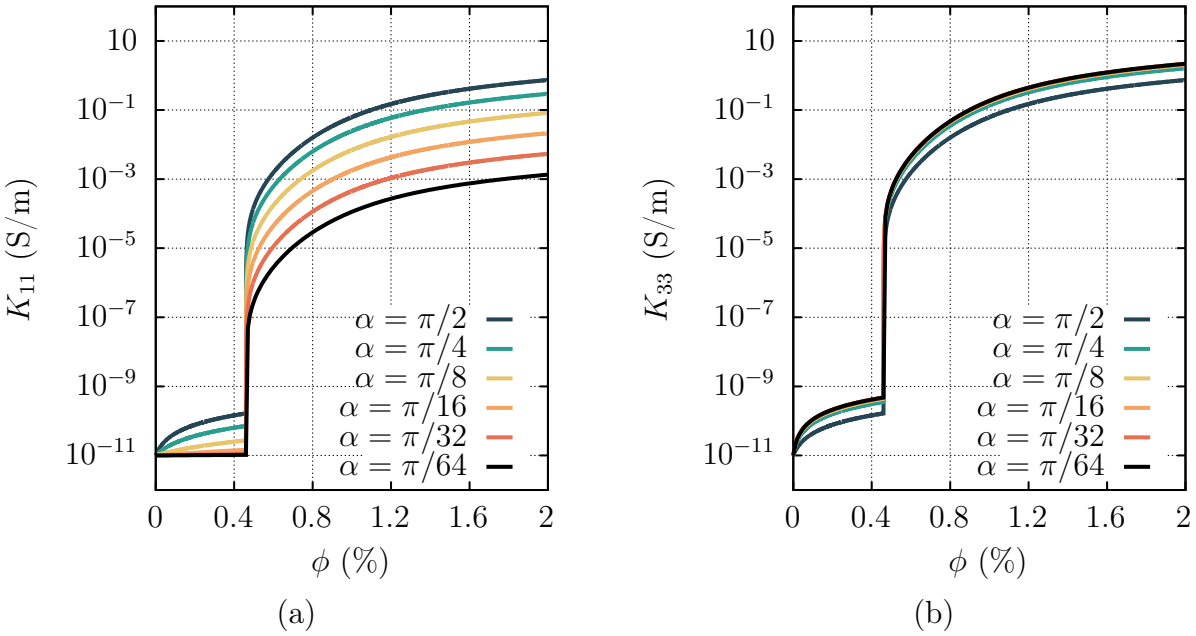

Figure 5.6: The effect of different α angles on the (a) transverse and (b) longitudinal electrical conductivity of the composite.

5.4.2.1 Limit angle

One of the parameters that control the alignment of CNT particles is the limit angle α. Figure 5.6 shows the influence of volume percentage of CNT ϕ on the transverse and longitudinal electrical conductivity of composites with limit angles $\alpha = \{\pi/64, \pi/32, \pi/16, \pi/8, \pi/4, \pi/2\}$. It is reminded that α is the limit angle of θ which is the angle made between a CNT and x_3 direction as it was shown in Figure 5.2. Decreasing the limit angle highly affects the transverse electrical conductivity, while it has less effect on the longitudinal electrical conductivity on a logarithmic scale. The effect is still significant and is easily demonstrated on a linear scale as shown in Figure 5.7. This graph depicts the limit angle α versus the transverse and longitudinal conductivity for $\phi = \{1\%, 1.5\%, 2\%\}$ volume fraction of CNTs. Figure 5.7 confirms that decreasing the angle from 90° which represents the full random distribution states to near 0° which is for the fully aligned CNTs along x_3 axis, results in a drastic decrease in K_{11} so that in $\alpha \to 0$ limit it goes to the matrix conductivity $K_{11} \to K^m$. However, the increase of K_{33} by a decrease of α is more evident here in the linear scale. For every volume fraction, K_{33} increases about three times by a drop of α from 90° to 0°. This suggests that the effect of the limit angle on the conductivity has a weak correlation with the volume fraction of CNT for small volume fractions. Besides, as expected for fully random distribution $\alpha = \pi/2$, the values of transverse and longitudinal conductivity are equal $K_{11} = K_{33}$.

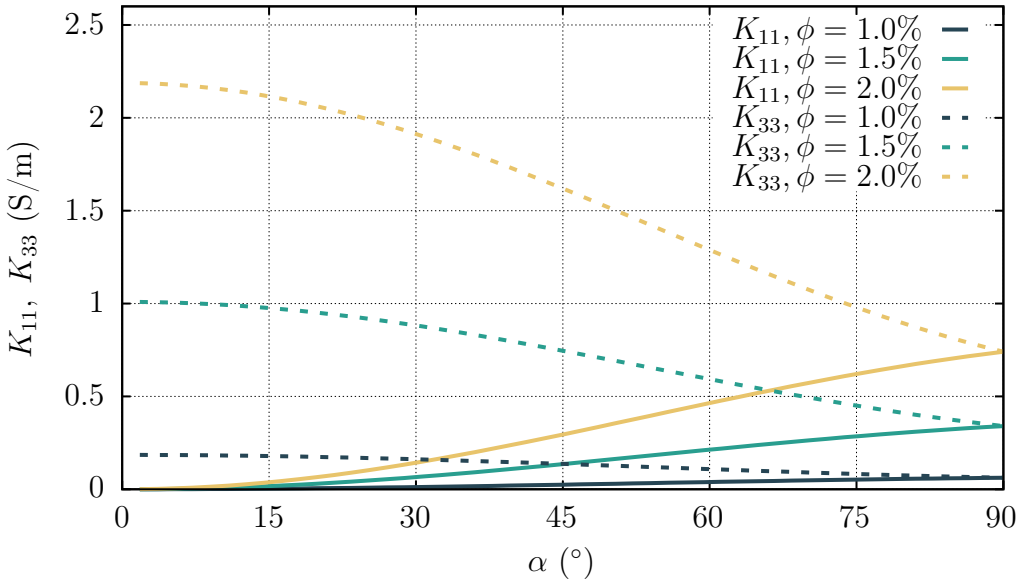

Figure 5.7: The effect of different α angles on the transverse (solid lines) and longitudinal (dashed lines) electrical conductivity of the composite.

5.4.2.2 Distribution function

Unlike the angle α that acts as a sharp cut-off threshold and is hard to measure experimentally, the distribution function provides a smooth transition for the probability of the presence of CNTs along a particular direction and is, therefore, more amenable to modelling approaches. Using a distribution function, on the other hand, is more feasible to account for the variability in inclusion alignment, thereby providing a more realistic and flexible framework for controlling the alignment of inclusions.

In the preceding analysis, a uniform distribution ($\xi = 1$), was used. In this section, the effect of using different distribution functions including a linear function, $\xi = 2 - 4\theta/\pi$, a cosine function, $\xi = \pi/2\cos(\theta)$, and an exponential function, $\xi = \pi/1.25\exp(-2\theta^2)$ is studied. The probability distribution function is normalised as

$$\int_0^{\pi/2} \xi(\theta)\,\mathrm{d}\theta = \frac{\pi}{2}\,, \tag{5.4.3}$$

and is demonstrated in Figure 5.8 for the uniform, linear, cosine, and exponential distributions. As shown, the exponential function gives the most aligned inclusions in one direction while in uniform distribution which is an ideal case, there are no alignments of inclusions.

Remark. Another approach to defining the probability distribution function is that it can be expressed somehow so that it smoothly reaches zero at α degree. For example the cosine distribution function $\xi = \pi/2\cos(\theta)$ can be expressed as $\xi = \cos(\theta\pi/2\alpha)$. □

Figure 5.9 shows the effect of the four different distribution functions on the transverse and longitudinal electrical conductivity of composite for different volume fractions. As expected, a notable trend is observed; transitioning from a uniform distribution function to a non-uniform

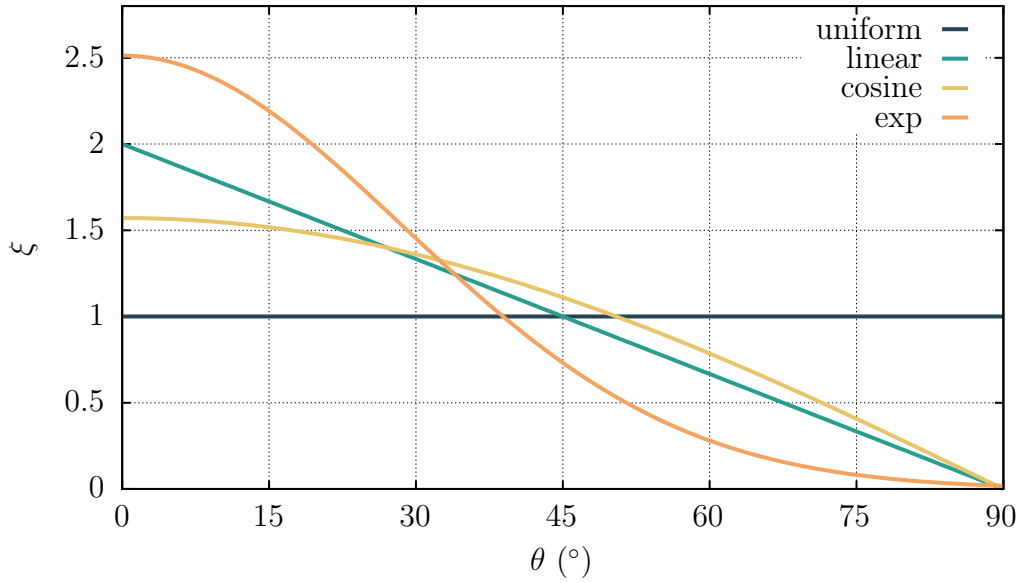

Figure 5.8: The uniform, linear, cosine and exponential distribution functions if α is marked as 60° degree (solid lines) or $\alpha = 90°$ degree (solid and dashed lines).

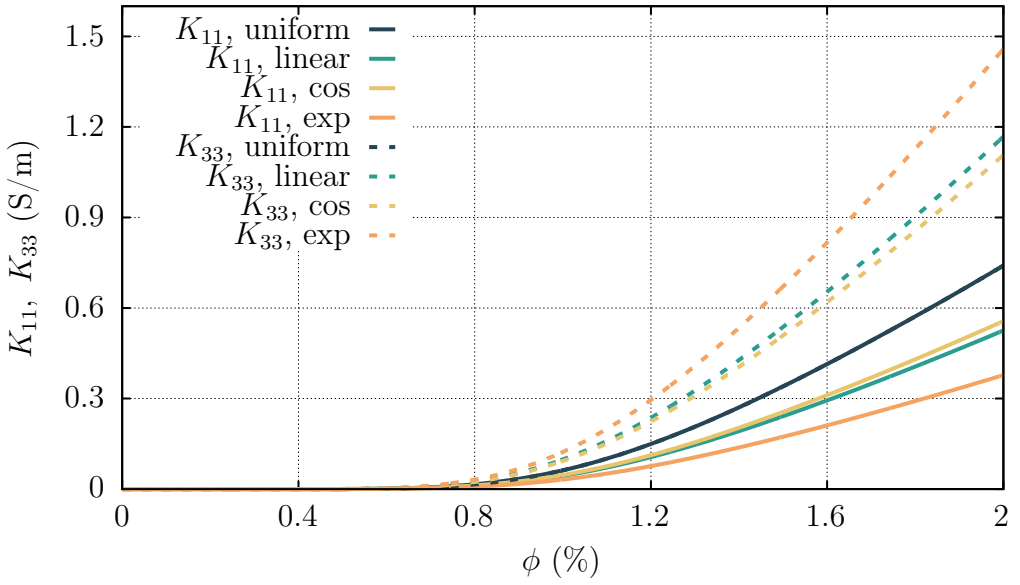

Figure 5.9: The effect of different distribution functions on the transverse (solid lines) and longitudinal (dashed lines) electrical conductivity of the composite.

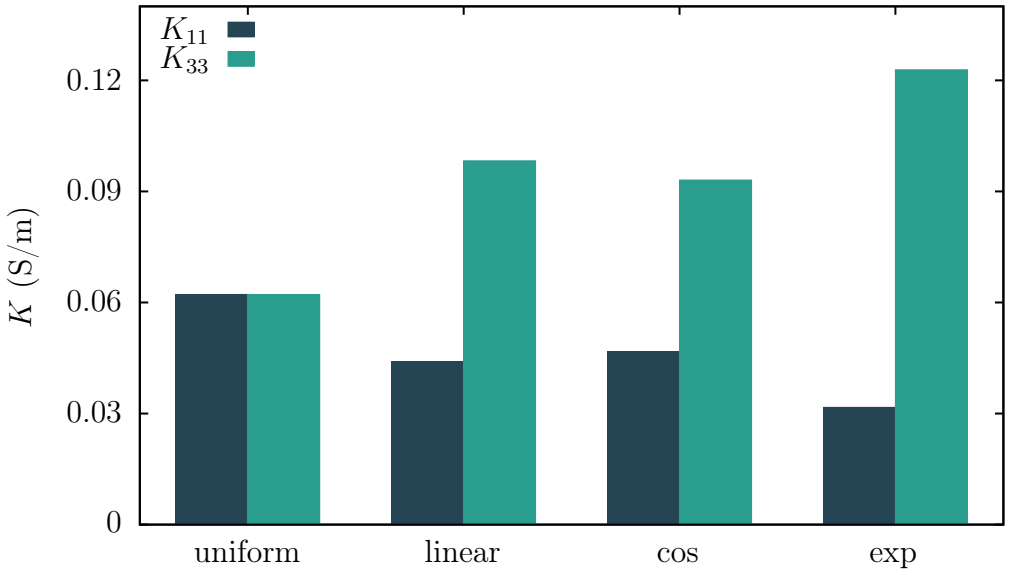

Figure 5.10: The transverse and longitudinal electrical conductivity of composite with $\phi = 1\%$ for different distribution functions.

function exerts a pronounced effect on electrical conductivity. Specifically, such a shift results in higher longitudinal conductivity and lower transverse conductivity. This disparity becomes particularly evident and significant as the volume fraction of CNTs is increased. This finding underscores the critical role played by the distribution function in shaping the electrical properties of CNT-based composites, highlighting its significance as a key parameter in the design and optimization of such materials.

For a clearer comparison, Figure 5.10 presents the values of transverse and longitudinal electrical conductivity of the composite with $\phi = 1\%$ for different distribution functions. The figure highlights the variations observed across different distribution functions, enabling a clearer understanding of the distinct conductivity characteristics associated with each distribution. As shown, the non-uniform distribution functions promote better alignment of CNTs in the x_3 direction, thereby creating more efficient pathways for electron transport and resulting in higher longitudinal conductivity and lower transverse conductivity.

5.4.2.3 CNT dimensions

Different single-walled and multi-walled CNTs with various architectures such as armchair, chiral and zigzag can be found in various diameters and lengths, offering a versatile selection of composite fillers (Soni et al., 2020; Kausar et al., 2016). Here, the effect of the size of CNT length and diameter on the electrical conductivity is investigated. The analysis of how varying the size of CNTs impacts electrical conductivity contributes to a deeper understanding of the relationship between CNT dimensions and conductivity, guiding the selection of appropriate CNTs for various applications. Figure 5.11 demonstrates the effect of the size of CNT particles with different volume fractions on the electrical conductivity of the composite with uniform

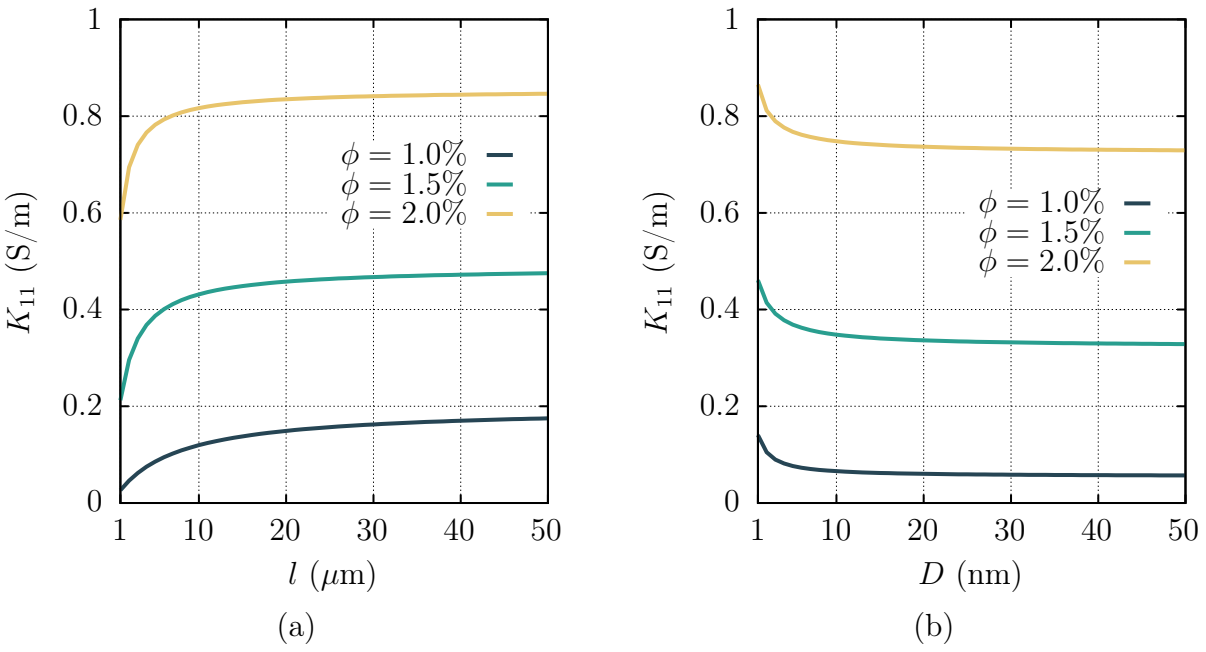

Figure 5.11: The effect of the (a) length and the (b) diameter of CNTs on the electrical conductivity of composite with uniform distribution for $\phi = \{1\%, 1.5\%, 2\%\}$.

distribution. It can be observed that longer CNTs demonstrate higher electrical conductivity compared to shorter ones. This can be attributed to the increased number of conductive pathways formed by longer CNTs, allowing for more electrons to pass through the material. Conversely, shorter CNTs exhibit lower conductivity due to the reduced number of conductive sites available. Moreover, keeping the volume fraction constant, composites made with CNTs of smaller diameters tend to exhibit higher effective electrical conductivity compared to composites made with CNTs of larger diameters. This is because of the higher surface area to volume ratio of CNTs with smaller diameters, which enables a greater number of conductive paths for electrons passing through the composite. Upon increasing the length or decreasing the diameter of the CNT beyond a certain threshold, no significant changes in the conductivity are observed. At this point, the conductivity reaches a plateau as the dominant factors affecting conductivity, such as intrinsic material properties and the distribution of the CNTs, become more influential.

Figure 5.12 shows the impact of the size of CNT particles with different distribution functions on the electrical conductivity behaviour of the composite material. The effect of different distribution functions on the electrical conductivity of the composite with different lengths and diameters of CNTs is notable. In particular, non-uniform distribution functions demonstrate a higher degree of sensitivity of longitudinal electrical conductivity to the changes in the dimension of the CNTs compared to the uniform function.

These results highlight the complex interplay between CNT length, diameter, distribution, and volume fraction in determining electrical conductivity.

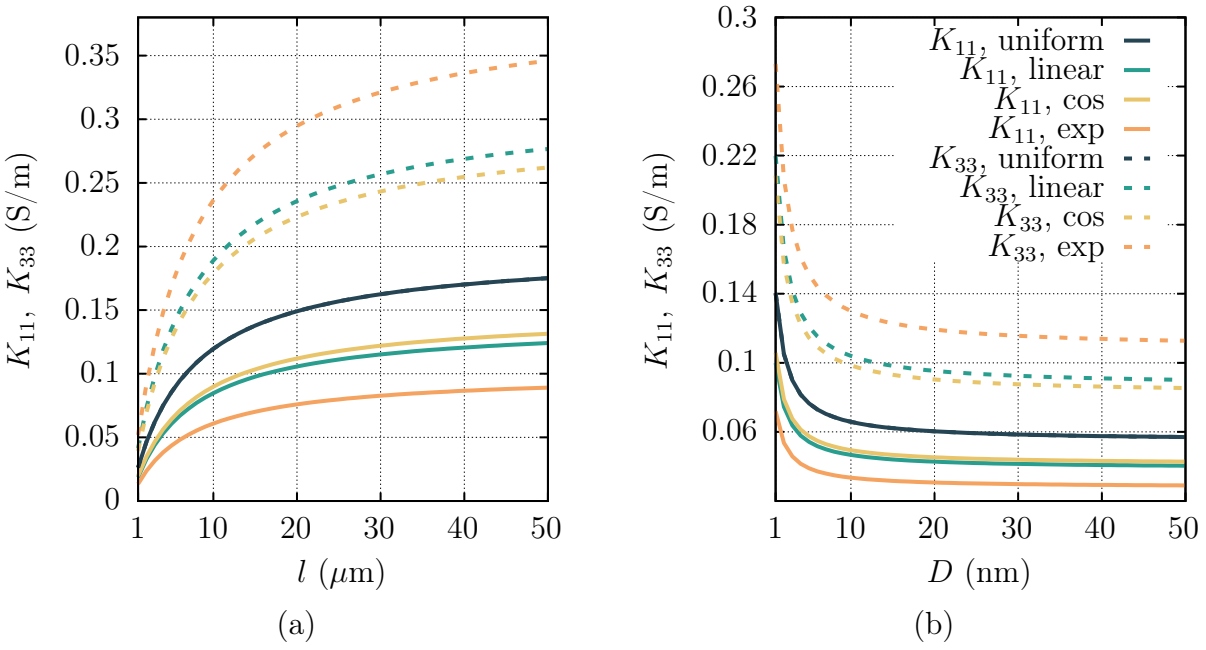

Figure 5.12: The effect of (a) the length and (b) the diameter of CNTs on the transverse (solid lines) and longitudinal (dashed lines) electrical conductivity of composite with different distribution functions. Note that (a) shares the same legends as (b).

5.5 Insights into piezoresistivity

This research study was motivated by the objective of linking changes in the position and alignment of reinforcements to the piezoresistive behaviour of the composite material under deformation. The analytical model developed in this chapter is used in conjunction with the computational model from chapters 2, 3 and 4 to demonstrate how these models can collectively predict piezoresistivity. This integration involves significant assumptions and disregards certain effects. So, while not tailored to specific composites or CNT-reinforced composites, it serves to illustrate the potential of combining the developed models.

To quantify piezoresistivity, the change in resistivity (the inverse of electrical conductivity) is plotted against the applied deformation. The change in electrical resistance is represented as

$$\frac{\Delta R}{R_0} = \frac{R - R_0}{R_0}, \tag{5.5.1}$$

where R represents the resistance under deformation, and R_0 is the initial resistance.

The power-law relationship in (5.3.2) is modified by incorporating the average normalised minimum distance between fibres $\overline{d_m}$ from Chapter 4 as

$$d_a = \overline{d_m}\left[\frac{\phi_c}{\phi}\right]^{1/3} d_c\,. \tag{5.5.2}$$

In Section 4.4.2 of the previous chapter, it was concluded that under the L_I loading condition (where $\lambda_2 = 1/\lambda_1$), the average minimum fibre distance, $\overline{d_m}$, remains unchanged. In this

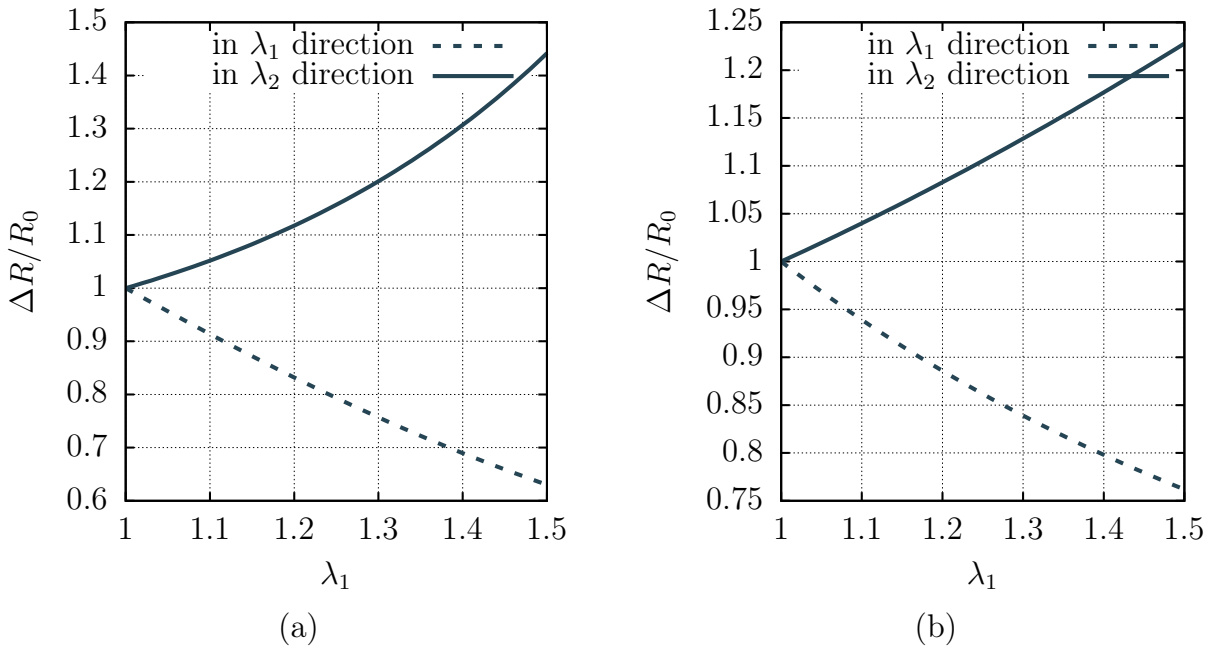

Figure 5.13: Piezoresistive behaviour of polymer with $\phi = 1\%$ reinforcement under loading condition L_I: (a) using α and (b) using exponential ξ.

scenario, the piezoresistive response is predominantly influenced by changes in fibre orientation, as the L_I loading maintains consistent inter-fibre spacing. Consequently, only the orientation changes are considered, represented using either the limit angle α or the exponential distribution function ξ. Figures 5.13(a) and (b) illustrate the piezoresistive response of a polymer reinforced with 1% CNTs under L_I loading condition, using α and ξ respectively.

The piezoresistive behaviour in this scenario is primarily anisotropic, influenced solely by alignment effects. Orientation changes induce systematic fibre realignment, progressively aligning them with the tensile strain direction. As the fibres align more closely along the tensile direction, conductive pathways for electron transport form, enhancing conductivity and lowering resistivity along the x_1 direction. Conversely, resistivity in the x_2 direction rises as fibres become less optimally aligned in that axis. Both α and ξ effectively capture this trend, showing that under L_I loading, fibre rotation primarily dictates the conductive pathways and connectivity within the composite.

Under the L_{II} loading condition, however, both fibre orientation and spacing vary. Figures 5.14(a) and (b) illustrate the piezoresistive response of a polymer reinforced with 1% CNTs under L_{II} loading condition, where orientation effects are captured by α in (a) and by ξ in (b). Here, resistivity increases along both x_1 and x_2 directions, emphasizing that spacing adjustments outweigh reorientation effects under this loading condition. As fibre spacing increases, the conductive networks become more fragmented, resulting in a logarithmic increase in resistivity across both directions. This behaviour highlights the dominant role of spacing between fibres in electrical conductivity.

This analysis demonstrates that the piezoresistive response is highly dependent on the load-

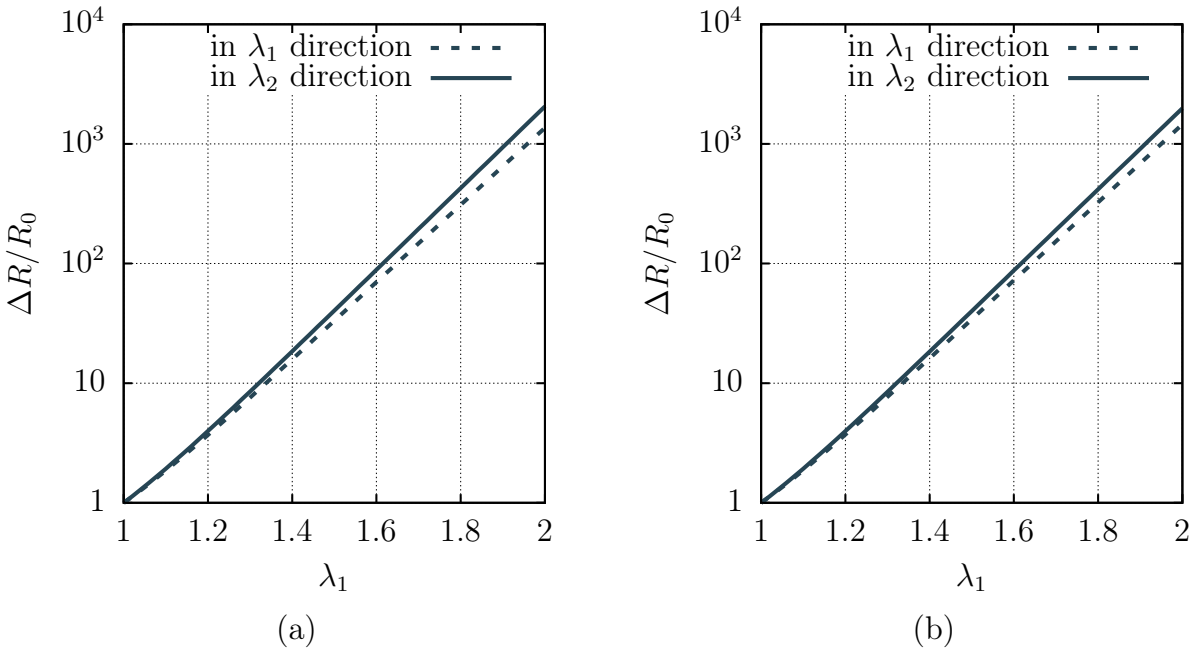

Figure 5.14: Piezoresistive behaviour of polymer with $\phi = 1\%$ reinforcement under loading condition L_{II}: (a) using α and (b) using exponential ξ.

ing type and corresponding changes in fibre orientation and spacing. Under L_I loading, orientation changes are the main drivers of resistivity variation. In contrast, L_{II} loading produces a more complex response due to simultaneous changes in orientation and spacing, with increased fibre spacing diminishing the connectivity of the conductive network, significantly impacting overall resistivity. The significant difference in resistivity levels between Figures 5.13 and 5.14 underscores the critical influence of fibre spacing on the conductive pathways within the composite. This comparison illustrates that while reorientation affects conductivity directionally, spacing has a broader impact on the overall piezoresistive response, establishing it as a more dominant factor in resistivity changes. Moreover, the findings imply that for materials where spacing changes cannot be controlled, resistivity predictions may be less reliable without accounting for spacing effects. In practical applications, such as in stretchable sensors or wearable electronics, understanding these dependencies becomes essential, as they affect the ability of sensors to provide accurate readings under different mechanical loading conditions. These findings underscore the potential of combining analytical and computational models to provide a comprehensive understanding of piezoresistive phenomena in elastomeric composites.

Chapter 6

Conclusions and outlook

This research has developed a modelling framework that uniquely integrates analytical and computational methods to investigate the piezoresistive behaviour of elastomeric composites under finite deformations. This dual approach provides a comprehensive understanding that bridges mechanical and electrical properties, offering insights that facilitate the design of multifunctional materials with integrated sensing capabilities.

6.1 Summary and conclusions

The computational model utilises the FEM to analyse the reorientation of short fibres in elastomeric composites under finite deformations. Key aspects of hyperelastic material formulations and variational principles have been revisited. The derived variational formulation has been cast into the fully-discrete form, using a single-field finite element formulation where the displacement is the only primary variable. The finite element model considers various dimensional configurations, including 3D, plane stress, plane strain, and 2D flatland, with a particular focus on the underexplored plane stress condition in nonlinear elasticity. Modelling the finite deformation of hyperelastic solids under plane stress conditions for compressible materials presents significant challenges. Unlike full incompressibility, where the out-of-plane deformation can be entirely characterised by the in-plane components, enforcing the plane stress condition requires solving an extra nonlinear equation for the out-of-plane deformation component, adding a nested Newton–Raphson scheme.

Computational modelling of nearly incompressible hyperelastic materials poses a significant challenge due to volumetric locking. This concern has been addressed through various solutions, such as mixed formulations. The classical one-field formulation remains effective for modelling under the plane stress condition despite its susceptibility to volumetric locking in other configurations. A three-field mixed formulation incorporating independent pressure and strain variables is introduced to counteract volumetric locking due to incompressibility for 3D, plane strain, and 2D flatland models.

Finite element codes have been developed and are publicly available through the *madeal*

collection (Ahmadi, 2024). These codes have been validated against benchmark problems, and results for different dimensional configurations compared to prior studies. The resulting numerical implementation is robust, demonstrating quadratic convergence for challenging problems. Average stress components and the effective von Mises stress are compared for different cases.

This framework is applied to plane stress representative volume elements (RVEs) of elastomeric composites reinforced with short fibres. A detailed analysis of how fibre orientations change under deformation in elastomeric composites has been conducted. Randomly positioned and oriented fibres within the RVEs are generated via Python scripts, considering both fully enclosed fibres and those crossing boundaries to form periodic patterns. Two admissible boundary conditions are explored, including affine boundary conditions and periodic displacement with antiperiodic tractions. To effectively apply periodic boundary conditions, 2D RVEs must be meshed so that nodes on opposite sides share the same x_2 coordinate on the left and right, and the same x_1 coordinate on the top and bottom. Meshing RVEs with boundary-crossing fibres presents challenges, which have been addressed using the pixel meshing technique facilitated by a hanging nodes strategy. Numerical examples are conducted to explore the effects of various parameters, tracking fibre position and orientation changes. A uniform orientation pattern is suggested for the dispersion of fibres to facilitate tracking of fibre position and alignment. By examining the orientation changes, limit angles, order parameters, and minimum distances, a comprehensive understanding of the microstructural behaviour of these composites has been developed.

The proposed computational model has notable limitations. One significant challenge is that due to the high aspect ratio of CNTs, size effects pose significant challenges for classical continuum formulations, including first-order computational homogenization (Choi et al., 2016; Malagù et al., 2017). Accurately capturing size effects requires extended formulations of continuum mechanics, such as gradient or micromorphic theories, surface elasticity (McBride et al., 2020; Asmanoglo and Menzel, 2017; Javili et al., 2015). Moreover, including fibre bending stiffness necessitates accounting for deformation and fibre direction gradients, requiring non-symmetric stress and couple stress (Spencer and Soldatos, 2007). While the present model considers fibres analogous to CNTs, it is important to recognize the differences stemming from size effects, waviness, and the exceptionally high aspect ratio of CNTs, which require more sophisticated modelling approaches to fully capture their unique behaviour.

Based on Eshelby's EIM, the analytical model that has been presented here evaluates the overall electrical conductivity of composites reinforced with inclusions. The derivation of the classic EIM has been presented, deriving mathematical relationships through a rigorous step-by-step process. The model is extended to account for electron tunnelling and conductive networks, treating the interphase layer around inclusions as a quantum tunnelling region. The validity of the model is confirmed by comparing its results with experimental data from four different CNT-reinforced polymer matrices. The values of the energy barrier are determined for each case study based on a comparison to the experimental data, and it was observed that the energy barrier plays a crucial role in predicting electrical conductivity. Furthermore, a

parametric study was conducted to investigate the influence of volume fraction, orientation, distribution, and dimensions on the transverse and longitudinal electrical properties.

The numerical results demonstrate a high sensitivity of the results on the input parameters such as energy barrier for electron hopping, intrinsic inclusion conductivity, and percolation threshold. Often, the exact values of these parameters are not reported in experiments, and care must be taken to use appropriate values. The effects of fibre orientation and distribution patterns on the electrical conductivity, highlighting how the alignment of fibres influences overall properties, have been investigated. Two measurements, namely, the limit angle of inclusion orientation and probability distribution function, are used to control the orientation. The limit angle of inclusion orientation is varied, and it is found that decreasing the angle from a uniformly random distribution to a fully aligned state results in a drastic decrease in the transverse electrical conductivity. However, the longitudinal electrical conductivity shows less sensitivity to the angle variation. Moreover, it is revealed that distributing CNTs with non-uniform probability distribution functions has a noticeable impact on electrical conductivity. In particular, this shift leads to an increase in longitudinal conductivity and a decrease in transverse conductivity. This difference becomes more prominent when the volume fraction of CNTs is raised.

Additionally, the effects of particle dimensions are examined. It is observed that composites with shorter CNTs demonstrate lower electrical conductivity compared to composites with longer CNTs. This is due to the reduced number of conductive pathways available in shorter CNTs. CNTs with smaller diameters exhibit higher electrical conductivity of composite compared to those with larger diameters of CNTs. However, beyond a certain threshold, further modification of the length or the diameter of CNTs has minimal impact on conductivity, as other factors become more influential. In summary, the presented analytical model provides a valuable framework for predicting the electrical conductivity of CNT-reinforced composites.

To demonstrate the integration between the computational and analytical models, the framework has been used to conduct a preliminary investigation of the piezoresistivity of elastomeric composites. This integration relies on certain assumptions and omits specific material variations and interactions. Two main loading conditions are considered, which affect orientation and space between fibres. The changes in these parameters are input into the analytical model to assess their impact on electrical conductivity. This approach highlights the potential for future research to refine and extend the model for more specific and practical applications in elastomeric composites, aiming for improved accuracy and relevance in real-world scenarios. The waviness, agglomeration, segregation, and variability in dimensions of fillers are not considered in the analytical model (Chanda et al., 2021; Garcia-Macias et al., 2017).

In conclusion, the study provides a novel and original contribution towards advancing the modelling of piezoresistive behaviour in elastomeric composites under finite deformations, laying a robust foundation for further exploration in this field.

6.2 Future directions

Although the current model offers valuable insights, it also has limitations, as acknowledged in the previous section. This research has identified several key areas where further study is crucial for further efforts to explore this field:

- **Multiscale modelling**: Integrating multiscale modelling techniques to bridge microscale and macroscale behaviours. Advancing to the micromechanical scale will enable simulations of nanocomposites, such as CNTs, accounting for size effects.
- **Material models**: Developing more complex material models that incorporate viscoelastic and viscoplastic behaviours to better simulate real-world conditions.
- **Geometry of RVEs**: Generating and analysing 3D RVEs to capture more detailed material behaviours. Better representation of filler geometry, like the waviness of fibres and varying length and diameter.
- **Model expansion**: Extending the model to incorporate additional factors, such as waviness and clustering of fillers, to improve accuracy and applicability.
- **Machine learning integration**: Leveraging machine learning techniques to predict material behaviour and optimise model parameters, thus improving simulation efficiency and accuracy. Explore data-driven simulations in stochastic modelling to further refine predictive capabilities.

Addressing these areas will build on the findings of this thesis, contributing to the development of advanced materials with enhanced functionalities and broader applications. This has the potential to advance the creation of more responsive and versatile strain sensors, improving the real-time detection and monitoring of mechanical stimuli and enhancing the efficiency of robotic systems and wearable technologies.

Appendix A

Isochoric-volumetric decomposition

A.1 Decomposition of the stress

The Piola–Kirchhoff stress, $\mathbf{S}$ can be articulated through its isotropic and volumetric components as

$$\mathbf{S} = 2\,\frac{\partial \psi(\widehat{\mathbf{C}}, J)}{\partial \mathbf{C}} = 2\left[\frac{\partial \psi_{\text{iso}}(\widehat{\mathbf{C}})}{\partial \mathbf{C}} + \frac{\partial \psi_{\text{vol}}\,(J)}{\partial \mathbf{C}}\right] = \mathbf{S}_{\text{iso}} + \mathbf{S}_{\text{vol}}\,. \tag{A.1.1}$$

Using the chain rule on the first term above yields

$$\frac{\partial \psi_{\text{iso}}}{\partial \mathbf{C}} = \frac{\partial \psi_{\text{iso}}}{\partial \widehat{\mathbf{C}}} : \frac{\partial \widehat{\mathbf{C}}}{\partial \mathbf{C}}\,, \tag{A.1.2}$$

where

$$\frac{\partial \widehat{\mathbf{C}}}{\partial \mathbf{C}} = \frac{\partial \left(J^{-2/3}\,\mathbf{C}\right)}{\partial \mathbf{C}} = \frac{\partial J^{-2/3}}{\partial \mathbf{C}} \otimes \mathbf{C} + J^{-2/3}\,\frac{\partial \mathbf{C}}{\partial \mathbf{C}} = J^{-2/3}\,\underbrace{\left[\mathbb{I} - \frac{1}{3}\,\mathbf{C}^{-1} \otimes \mathbf{C}\right]}_{\mathbb{P}}\,. \tag{A.1.3}$$

Applying the chain rule to the second term of Equation (A.1.1), yields

$$\frac{\partial \psi_{\text{vol}}}{\partial \mathbf{C}} = \frac{\partial \psi_{\text{vol}}}{\partial J}\,\frac{\partial J}{\partial \mathbf{C}}\,, \tag{A.1.4}$$

in which $p = \partial \psi_{\text{vol}}(J)/\partial J$ is recognised as the hydrostatic pressure and $\partial J/\partial \mathbf{C} = \frac{1}{2} J \mathbf{C}^{-1}$. Defining $\widehat{\mathbf{S}} = 2\,\partial \psi_{\text{iso}}/\partial \widehat{\mathbf{C}}$, one obtains

$$\mathbf{S} = J^{-2/3}\,\mathbb{P} : \widehat{\mathbf{S}} + pJ\,\mathbf{C}^{-1} = \mathbf{S}_{\text{iso}} + \mathbf{S}_{\text{vol}}\,. \tag{A.1.5}$$

Transforming to the current configuration, the Kirchhoff stress can be written as

$$\boldsymbol{\tau} = \mathbf{F}\,\mathbf{S}\,\mathbf{F}^T = \mathbb{D} : \widehat{\boldsymbol{\tau}} + pJ\,\mathbf{I} = \boldsymbol{\tau}_{\text{iso}} + \boldsymbol{\tau}_{\text{vol}}\,, \tag{A.1.6}$$

where $\mathbb{D}$ represents the deviatoric operator which was defined in Equation (2.1.5), and $\widehat{\boldsymbol{\tau}}$ is stated as follows:

$$\widehat{\boldsymbol{\tau}} = \widehat{\mathbf{F}}\,\widehat{\mathbf{S}}\,\widehat{\mathbf{F}}^{T} = 2\widehat{\mathbf{b}}\,\frac{\partial \psi_{\text{iso}}(\widehat{\mathbf{b}})}{\partial \widehat{\mathbf{b}}}\,. \tag{A.1.7}$$

A.2 Decomposition of incremental constitutive tensor

The 4th-order incremental constitutive tensor in the Lagrangian description can be decomposed as

$$\mathbb{C} = \mathbb{C}_{\text{iso}} + \mathbb{C}_{\text{vol}}\,. \tag{A.2.1}$$

Recalling the definition of the tensor $\mathbb{P}$ in (A.1.3), one obtains

$$\mathbb{C}_{\text{iso}} = 2\,\frac{\partial \mathbf{S}_{\text{iso}}}{\partial \mathbf{C}} = \mathbb{P} : \widehat{\mathbb{C}} : \mathbb{P}^{T} + \frac{2}{3}\,\text{tr}(J^{-2/3}\,\widehat{\mathbf{S}})\,\widetilde{\mathbb{P}} - \frac{2}{3}\,\left[\mathbf{C}^{-1} \otimes \mathbf{S}_{\text{iso}} + \mathbf{S}_{\text{iso}} \otimes \mathbf{C}^{-1}\right], \tag{A.2.2}$$

and

$$\mathbb{C}_{\text{vol}} = 2\,\frac{\partial \mathbf{S}_{\text{vol}}}{\partial \mathbf{C}} = J\left[p + J\,\frac{\mathrm{d}p}{\mathrm{d}J}\right]\mathbf{C}^{-1} \otimes \mathbf{C}^{-1} - 2Jp\,\mathbf{C}^{-1} \odot \mathbf{C}^{-1}, \tag{A.2.3}$$

where $\widetilde{\mathbb{P}}$ and the so-called Lagrangian fictitious elasticity tensor $\widehat{\mathbb{C}}$ are given as

$$\widetilde{\mathbb{P}} = \mathbf{C}^{-1} \odot \mathbf{C}^{-1} - \frac{1}{3}\,\mathbf{C}^{-1} \otimes \mathbf{C}^{-1} \quad \text{and} \quad \widehat{\mathbb{C}} = 2\,J^{-4/3}\,\frac{\partial \widehat{\mathbf{S}}}{\partial \widehat{\mathbf{C}}} = 4\,J^{-4/3}\,\frac{\partial^{2} \Psi_{\text{iso}}(\widehat{\mathbf{C}})}{\partial \widehat{\mathbf{C}}\,\partial \widehat{\mathbf{C}}}\,. \tag{A.2.4}$$

By push-forward, the incremental constitutive tensor in Eulerian description is derived by

$$\mathbb{c} = J^{-1}\chi_{*}\,(\mathbb{C}) = 4\mathbf{b}\,J^{-1}\,\frac{\partial^{2}\psi}{\partial \mathbf{b}\,\partial \mathbf{b}}\,\mathbf{b}\,, \tag{A.2.5}$$

and decomposed into its isochoric and volumetric parts as

$$\mathbb{c} = \mathbb{c}_{\text{iso}} + \mathbb{c}_{\text{vol}}\,, \tag{A.2.6}$$

where

$$\mathbb{c}_{\text{vol}} = 4\mathbf{b}\,J^{-1}\,\frac{\partial^{2}\psi_{\text{vol}}}{\partial \mathbf{b}\,\partial \mathbf{b}}\,\mathbf{b} = \left[p + J\,\frac{\mathrm{d}p}{\mathrm{d}J}\right]\mathbf{I} \otimes \mathbf{I} - 2p\,\mathbb{I}\,, \tag{A.2.7}$$

and

$$J\,\mathbb{c}_{\text{iso}} = 4\mathbf{b}\,\frac{\partial^{2}\psi_{\text{iso}}}{\partial \mathbf{b}\,\partial \mathbf{b}}\,\mathbf{b} = \mathbb{D} : \widehat{\mathbb{c}} : \mathbb{D} + \frac{2}{3}\text{tr}(\widehat{\boldsymbol{\tau}})\,\mathbb{D} - \frac{2}{3}\,\left[\mathbf{I} \otimes \boldsymbol{\tau}_{\text{iso}} + \boldsymbol{\tau}_{\text{iso}} \otimes \mathbf{I}\right]. \tag{A.2.8}$$

The Eulerian fictitious elasticity tensor $\widehat{\mathbb{c}}$ is defined as

$$\widehat{\mathbb{c}} = 4\widehat{\mathbf{b}}\,\frac{\partial^{2}\psi_{\text{iso}}}{\partial \widehat{\mathbf{b}}\,\partial \widehat{\mathbf{b}}}\,\widehat{\mathbf{b}}\,. \tag{A.2.9}$$

Appendix B

Alternative incremental constitutive tensor for plane stress

An alternative formulation for the incremental constitutive tensor under plane stress conditions is derived. From Equation (3.2.15), and considering

$$\frac{\partial J^{-2/3}}{\partial \mathbf{C}} = -\frac{1}{3} J^{-2/3}\, \mathbf{C}^{-1}, \tag{B.1}$$

and recalling the definition in Equation (2.1.3), one derives the 4th-order incremental constitutive tensor $\mathbb{C} \in \mathbb{R}^3 \otimes \mathbb{R}^3 \otimes \mathbb{R}^3 \otimes \mathbb{R}^3$ as

$$\mathbb{C} = 2\,\frac{\partial \mathbf{S}}{\partial \mathbf{C}} = 2\mu J^{-2/3} \left[\frac{1}{3}\, \mathbf{C}^{-1} \otimes \left[C_{33}\, \mathbf{C}^{-1} - \mathbf{I} \right] - \frac{\partial C_{33}}{\partial \mathbf{C}} \otimes \mathbf{C}^{-1} + C_{33}\, \mathbf{C}^{-1} \odot \mathbf{C}^{-1} \right]. \tag{B.2}$$

Using this incremental constitutive tensor, results consistently converge to the correct solution with a descending residual. Although volumetric locking is avoided, it is important to note that the convergence rate is notably affected as the Poisson's ratio $\nu \to 0.5$. While the proposed formulation in Section 3.2.4 exhibits quadratic convergence, convergence for the above formulation, which can be found in the literature, is not quadratic. This discrepancy suggests that the alternative formulation may be less efficient for highly incompressible materials. Figure B.1 illustrates the influence of the Poisson's ratio of material on convergence. Due to the proximity of the values, the horizontal axis is represented as $-\mathrm{Ln}(0.5 - \nu)$ instead of ν. As ν approaches 0.5, the average number of iterations required for convergence increases significantly, indicating slower convergence for highly incompressible materials. Indeed, despite the impact of increasing incompressibility on the rate of convergence, it is reassuring to note that convergence is always achieved.

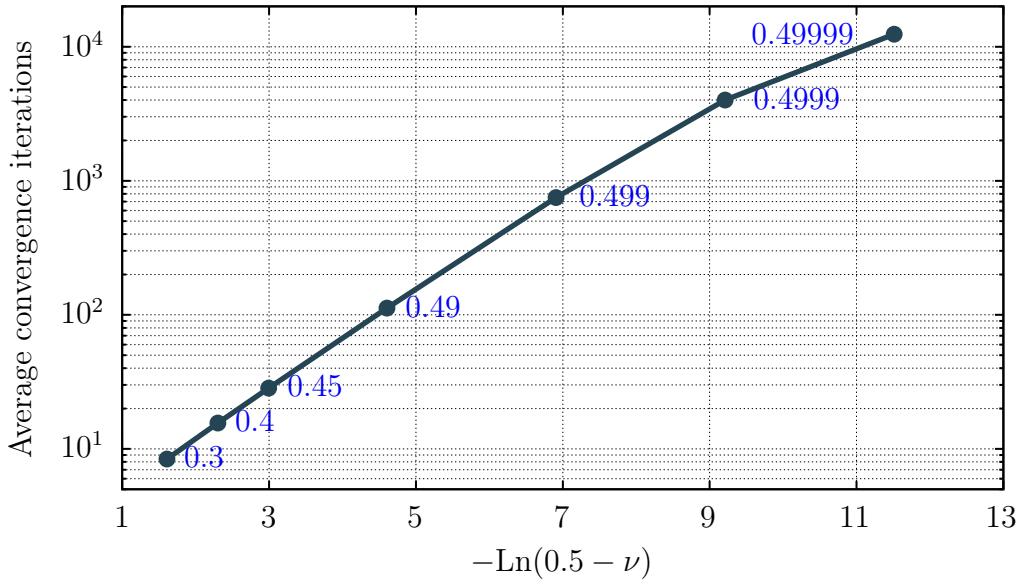

Figure B.1: Effect of material incompressibility on the average Newton–Raphson iterations needed for convergence of the plane stress model using constitutive tensor B.1 (blue labels show the value of ν).

This analysis underscores the importance of having a robust formulation to ensure efficient and accurate simulations, particularly for nearly incompressible materials where convergence rates can be significantly impacted.

Appendix C

Instructions for using *madeal*

Detailed instruction for using the *madeal* package is provided. The guide is based on *madeal* version 1.0, which is the latest version available at the time of writing this thesis.

C.1 Package overview

Installation. First, ensure the system has a C++ compiler (e.g., GCC, Clang) and CMake installed. To install *madeal*, follow these steps:

1. **Install deal.II**: The deal.II library must be pre-installed on the system. Follow the installation guide available at deal.II official website [1].

2. **Clone the repository**: Clone the *madeal* repository into the deal.II directory by running:

   ```
   git clone https://github.com/Masoud16ahm/madeal.git
   ```

Templates. Templates for various problem scenarios are provided. Each template is tailored for specific types of deformation and formulations. For example, to solve an infinitesimal deformation elastic problem, use "template1"; for solving a finite deformation problem in the single-field formulation, use "template2" and in the three-field formulation, use "template3". Modify these templates and input files according to your specific problem requirements. These templates provide a starting point for setting up different types of simulations.

Examples. Navigate to the "examples" folder to view and run examples demonstrating *madeal* capabilities. Various examples are provided for benchmarking and providing practical examples. Each example is designed to highlight different features and applications of the *madeal* package. To compile and run an example, enter:

[1] https://www.dealii.org/

```
cmake .
make run
```

License. *madeal* is distributed under the "*MIT License*", which grants users specific rights to use, modify, and distribute the package both in original and modified form under certain conditions:

- **Usage**: Users are allowed to use the package for any purpose, including commercial and academic.
- **Modification**: Users may modify the source code, ensuring that modifications are documented.
- **Distribution**: Redistribution of the original or modified software is permitted as long as the copies retain the original license terms and a notice of any modifications.
- **Attribution**: Users must credit the original authors in any publications or software distributions that utilise *madeal*.

The license aims to promote the sharing and usage of the software while protecting the intellectual property of the developers. See the *LICENSE* file in the repository for full details.

Testing. Testing is implemented using "*Google Test*". Run the provided test suites to ensure the installation and build function as expected. To run the tests, enter:

```
cmake .
make
./gtest
```

Support and contributions. For support, issues, or contributions, refer to the GitHub repository. Contributions are welcome, and users are encouraged to fork the repository, make modifications, and submit pull requests. For any specific issues or questions, use the GitHub issues section.

C.2 Step-by-step guide

To solve your problem using *madeal*, follow these steps to set up, modify, and run the finite element analysis.

Step 1: modify main file. The "main.cc" file is the main driver for the FE analysis. It sets up the problem, defines the mesh, specifies boundary conditions, and runs the analysis. You can modify this file based on your specific problem by commenting, uncommenting, and modifying the code within the template. Ensure that the necessary headers are included at the beginning of the file. Set the problem dimension and polynomial degree of the finite element in use. Specify the input file and initialise the FEM object. Modify the output name and other parameters manually if needed. You can define the mesh using one of the following methods provided: predefined mesh in deal.II, imported mesh, or using *madeal* RVE generator. Specify the boundary conditions using the "LoadAndBCs" namespace. You can apply different types of loading and boundary conditions, including Dirichlet, Neumann, body force, point force, periodic, or affine. You need to specify the type, the position, and the value of the boundary conditions. For example, to apply a Dirichlet boundary condition on the left boundary of the domain, use the following code:

```
LoadAndBCs::BC bc1;
bc1.type     = LoadAndBCs::dbc;
bc1.position = LoadAndBCs::left;
bc1.value    = {0.0, 0.0, 0.0};
problem1.BCs.push_back(bc1);
```

Listing C.1: Applying a Dirichlet boundary condition on the left boundary of the domain.

Various meshing options and boundary conditions are commented in the templates so that they can be easily used.

Example *main.cc*:

```
/*%-%-%-%-%-%-%-%-%-%-%-%-%-%-%-%-%-%-%-%-%-%-%-%-%-%-%-%-%-%-%-%-
%                    ma deal                    %
%  Template for Compressible Hyperelastic  %
%-%-%-%-%-%-%-%-%-%-%-%-%-%-%-%-%-%-%-%-%-%-%-%-%-%-%-%-%-%-%-%-*/

// Include the "large_classic" header for sibgle-field large deformations
#include <large_classic.h>

// Include madeal RVE generator
#include <rve.h>

// Use madeal name space
using namespace madeal;

// Main function
int main(){

  deallog.depth_console(0);

  // (1) Enter Dimension, Problem dimension and polynomial degree
  const int dim    = 2;
```

```
22  const int p_dim = 3;
23  const int p_deg = 1;
24
25  // (2) Define FEM object and Enter input file
26  Elastic::Large_classic<dim, p_dim> problem1("inputfile.prm", p_deg);
27
28  // (3) Enforce any input manually
29  problem1.output_name = "out"; //The output name
30  problem1.s_typ = 2;  //Solution type (1 plane-stress; 2 plane-strain)
31
32  // (4) Define the mesh
33  // (i) From deal.II
34  problem1.L_m = 1.0;
35  problem1.W_m = 1.0;
36  Point<dim> p1(0, 0), p2(problem1.L_m, problem1.W_m);
37  vector<unsigned int> subd={10,10};
38  GridGenerator::subdivided_hyper_rectangle(problem1.mesh, subd, p1, p2);
39
40  // (ii) Import the mesh
41  // GridIn<dim> grid_in;
42  // grid_in.attach_triangulation(problem1.mesh);
43  // std::ifstream input_mesh("mesh.inp");
44  // grid_in.read_abaqus(input_mesh);
45  // problem1.L_m = 1.0;
46  // problem1.W_m = 1.0;
47
48  // (iii) Generate randomly distributed RVE
49  // const int inputnr = 7; //Number of refinement steps
50  // RVE::fibre<dim> myrve1("inputrve.prm", inputnr);
51  // myrve1.generate_rve(false); //
52  // problem1.mesh.copy_triangulation(myrve1.mesh);
53  // problem1.L_m = myrve1.L_m;
54  // problem1.W_m = myrve1.L_m;
55
56  // (5) Specify Loads and BCs
57  // (i) dbc=Dirichlet
58  LoadAndBCs::BC bc1;
59  bc1.type     = LoadAndBCs::dbc;
60  bc1.position = LoadAndBCs::left;
61  bc1.value    = {0.0, 0.0};
62  problem1.BCs.push_back(bc1);
63  // (ii) nbc=Neumann
64  LoadAndBCs::BC bc2;
65  bc2.type     = LoadAndBCs::nbc;
66  bc2.position = LoadAndBCs::right;
67  bc2.value    = {1.0e4, 1.0e4};
68  problem1.BCs.push_back(bc2);
69  // (iii) ldb=Linear Displacement (Affine)
```

```
  // LoadAndBCs::BC bc3;
  // bc3.type      = LoadAndBCs::ldb;
  // bc3.value     = {1.5, 1.0, 0.0, 0.0}; // F = [F11, F22, F12, F21]
  // problem1.BCs.push_back(bc3);
  // (iv) pbc=Periodic
  // LoadAndBCs::BC bc4;
  // bc4.type      = LoadAndBCs::pbc;
  // bc4.value     = {1.5, 1.0, 0.0, 0.0}; // F = [F11, F22, F12, F21]
  // problem1.BCs.push_back(bc4);

  // (6) Run the FE Analysis
  problem1.run();

  return 0;

}
```

Listing C.2: Example of "main.cc" file used for single-field formulation.

Step 2: modify input file. The "inputfile.prm" file is used to set material properties and solver settings. Specify the shear modulus, Poisson's ratio (or bulk modulus), and other material properties. You can define properties for as many materials as are referenced by the material IDs used in your mesh. Define the number of meshing refine cycles, solution type and plate thickness (if planar), time increment steps, and Newton solver settings.
Example *inputfile.prm*:

```
# List of input variables
# ----------------------

# Number of meshing refine cycle
  set Number of meshing refine cycle = 1

# Shear Modulus
  set Shear Modulus 1 = 80.1938e6
  set Shear Modulus 2 = 200.0e6

# Poisson's Ratio
  set Poisson's Ratio 1 = 0.3
  set Poisson's Ratio 2 = 0.33

# Bulk Modulus
  # set Bulk Modulus 1 = 400890e6
  # set Bulk Modulus 2 = 400890e6

# Solution type (1 plane-stress; 2 plane-strain)
  set Solution type (1 plane-stress; 2 plane-strain) = 2

```

```
# Plate thickness
  set Plate thickness = 1.0e-3

# Time settings
  set Number of time increment steps = 10
  set Save result = 1

# Newton solver
  set Newton iteration tolerance = 1.0e-6
  set Maximum Newton iteration = 25
```

Listing C.3: Example of "inputfile.prm" input file used.

Step 3: modify RVE input file (*if using RVE generator*). The "inputrve.prm" file is used to set parameters for *madeal* RVE generator. Define the number of fibres, aspect ratio, volume fraction, and diameter of fibres. The RVE generator automatically assigns material IDs: "1" for the matrix and "2" for the fibres. Select the distribution pattern: "1" for random, and "2" for uniform.

Example *inputrve.prm*:

```
# Inputs for generating RVE
# ----------------------

# Number of Fibres
  set Number of Fibres = 25

# Aspect Ratio of Fibres
  set Aspect Ratio of Fibres = 10.0

# Volume Fraction of Fibres
  set Volume Fraction of Fibres = 0.10

# Diameter of Fibres
  set Diameter of Fibres = 1.0

# Distribution patterns (rnd=1, unf=2)
  set Distribution pattern = 2
```

Listing C.4: Example of "inputrve.prm" file used.

Step4: output files. The results will be saved with the specified output name (e.g., out). Review the output files to analyse the results of the FE simulation using visualization tools like ParaView [2] or Tecplot [3].

[2] https://www.paraview.org/
[3] https://tecplot.com/

Appendix D

Effective conductivity of an equivalent cylinder

The effective conductivity of the equivalent cylinder can be derived using Maxwell's equations and the rule of mixture (Yan et al., 2007; Feng and Jiang, 2013). To do so, the equivalent cylinder is divided into three parts, including two isotropic interphase-only parts (parts I and III) and one transversely isotropic part of CNT/Interphase (part II) as shown in Figure 5.3. The overall electrical conductivity of part II along $\widehat{x}_3$ is denoted by K_{33}^{II} and can be evaluated from the rule of mixture as

$$K_{33}^{II} = \frac{K_{33}^{p}\, D^2 + K^{\text{int}}[4Dt + 4t^2]}{[D + 2t]^2}\,. \tag{D.1}$$

The overall electrical conductivity of part II along $\widehat{x}_1$ is denoted as K_{11}^{II}. It is evaluated by applying a test electric field E^t on the equivalent cylinder along the radial axis. Maxwell's equations require the electric scalar potential U to satisfy Poisson's equation that is given in the cylindrical coordinate system $\{r, \theta, z\}$ as

$$\nabla^2 U = \frac{1}{r}\frac{\partial}{\partial r}(r\frac{\partial U}{\partial r}) + \frac{1}{r^2}\frac{\partial^2 U}{\partial \theta^2} = 0. \tag{D.2}$$

The boundary conditions are prescribed as

$$U^p\big|_{r=0} = \text{constant}, \qquad E^m\big|_{r\to\infty} = -\frac{\partial U^m}{\partial r}\big|_{r\to\infty} = E^t, \tag{D.3}$$

$$U^p\big|_{r=D/2} = U^{\text{int}}\big|_{r=D/2}, \qquad -K_{11}^{p}\,\frac{\partial U^p}{\partial r}\big|_{r=D/2} = -K^{\text{int}}\,\frac{\partial U^{\text{int}}}{\partial r}\big|_{r=D/2}, \tag{D.4}$$

$$U^{\text{int}}\big|_{r=D/2+t} = U^m\big|_{r=D/2+t}, \qquad -K^{\text{int}}\,\frac{\partial U^{\text{int}}}{\partial r}\big|_{r=D/2+t} = -K^{m}\,\frac{\partial U^{m}}{\partial r}\big|_{r=D/2+t}. \tag{D.5}$$

The above set of equations for U results in

$$U^p = 2\,\gamma\,K^{\text{int}}E^t r\cos\theta, \quad 0 \le r \le D/2, \tag{D.6}$$

$$U^{\text{int}} = \gamma\left[K^{\text{int}} + K^p_{11} + \left[\frac{D}{2r}\right]^2 [K^{\text{int}} - K^p_{11}]\right] E^t r\cos\theta, \quad D/2 < r < D/2 + t, \tag{D.7}$$

$$U^m = \left[\gamma\left[\left[\frac{D+2t}{2r}\right]^2 [K^{\text{int}} + K^p_{11}] + \left[\frac{D}{2r}\right]^2 [K^{\text{int}} - K^p_{11}]\right] + \left[\frac{D+2t}{2r}\right]^2 - 1\right] E^t\, r\cos\theta, \quad D/2 + t < \infty, \tag{D.8}$$

where

$$\gamma = 2K^m\left[[K^{\text{int}} - K^p_{11}][K^{\text{int}} - K^m]\left[\frac{D}{D+2t}\right]^2 - [K^{\text{int}} + K^p_{11}][K^{\text{int}} + K^m]\right]^{-1}. \tag{D.9}$$

The transverse electric field of the interphase and CNT parts of the equivalent cylinder can be evaluated as

$$E^p_1 = -\frac{\partial U^p}{\partial \widehat{x}_1} = -\frac{\partial U^p}{\partial r}\frac{\partial r}{\partial \widehat{x}_1} = -\frac{1}{\cos\theta}\frac{\partial U^p}{\partial r}, \tag{D.10}$$

$$E^{\text{int}}_1 = -\frac{\partial U^{\text{int}}}{\partial \widehat{x}_1} = -\frac{\partial U^{\text{int}}}{\partial r}\frac{\partial r}{\partial \widehat{x}_1} = -\frac{1}{\cos\theta}\frac{\partial U^{\text{int}}}{\partial r}, \tag{D.11}$$

with

$$J^p_1 = K^p_{11}E^p_1, \quad \text{and} \quad J^{\text{int}}_1 = K^{\text{int}}E^{\text{int}}_1. \tag{D.12}$$

Using the volumetric average, we can obtain

$$\frac{1}{V}\int_V J_1\,\mathrm{d}V = K^{II}_{11}\frac{1}{V}\int_V E_1\,\mathrm{d}V. \tag{D.13}$$

Therefore, using equations (D.12) and (D.13), we can write

$$K^{II}_{11} = \frac{D^2K^p_{11}K^{\text{int}} + 2K^{\text{int}}[K^{\text{int}} + K^p_{11}][t^2 + Dt]}{D^2K^{\text{int}} + 2[K^{\text{int}} + K^p_{11}][t^2 + Dt]}. \tag{D.14}$$

Appendix E

Alternative electron tunneling approach

In this approach, the current for the electron tunnelling can be evaluated by *Landauer–Büttiker* formula (Büttiker et al., 1985; Buldum and Lu, 2001) which relates the electrical conductivity of a system to the transmission probability of electrons. Assuming conduction in a 1D system as a transmission problem, the current I is expressed as

$$I = \frac{g_s e}{h} \int_0^{\infty} \tau(E)\, M(E)\, [f(E - eV) - f(E)]\, \mathrm{d}E, \tag{E.1}$$

where E is the total energy of an electron, $\tau(E)$ is the transmission probability of the electron to tunnel through the matrix, $M(E)$ is the total number of conduction channels and f is the *Fermi–Dirac* distribution function given by

$$f(\varepsilon) = \left[\exp\left(\frac{\varepsilon - \mu}{\kappa_B T}\right) + 1\right]^{-1}, \tag{E.2}$$

where μ is the total chemical potential of a CNT, κ_B is *Boltzmann* constant, and T is the temperature. Upon substituting this back to (E.1) one obtains (Bao et al., 2012)

$$I = \frac{g_s e}{h} \int_0^{\infty} \tau(E)\, M(E) \left[\left[\exp\left(\frac{E - eV - \mu}{\kappa_B\, T}\right) + 1\right]^{-1} - \left[\exp\left(\frac{E - \mu}{\kappa_B\, T}\right) + 1\right]^{-1}\right] \mathrm{d}E. \tag{E.3}$$

Furthermore, $g_s = 2$, which indicates spin degeneracy. Using Taylor's series expansion up to the first order for $\tau(E)\, M(E)$, and assuming $\tau(E)\, M(E) = 0$ for $E < 0$, Equation (E.3) is approximated as

$$I \approx \frac{2e}{h} \left[\int_{\mu}^{\mu+eV} \tau(E)\, M(E)\, \mathrm{d}E + \frac{[\pi\, \kappa_B\, T]^2}{6} \frac{\mathrm{d}[\tau(E)\, M(E)]}{\mathrm{d}E}\bigg|_{\mu}^{\mu+eV}\right]. \tag{E.4}$$

Under a low bias voltage, it can be assumed that

$$\int_{\mu}^{\mu+eV} \tau(E)\, M(E)\, \mathrm{d}E \approx eV\tau M, \quad \text{and} \quad \frac{\mathrm{d}[\tau(E)\, M(E)]}{\mathrm{d}E}\Big|_{\mu}^{\mu+eV} \approx eV M \frac{d^2\tau}{dE^2}\Big|_{\mu}. \tag{E.5}$$

Therefore, the tunnelling resistance R_t at a junction between two CNTs can be expressed by Ohm's Law as

$$R_t = \frac{V}{I} = \frac{h}{2Me^2}\left[\tau + \frac{[\pi\,\kappa_B\,T]^2}{6}\,\frac{d^2\tau}{dE^2}\Big|_\mu\right]^{-1}. \tag{E.6}$$

At room temperatures, it is assumed that $\kappa_B T/\Delta E \approx 0$. In this case, Equation (E.6) is simplified to

$$R_t = \frac{h}{2Me^2\,\tau}\,. \tag{E.7}$$

Schrodinger's equation with rectangular potential barrier can be employed to determine the transmission probability of electron hopping τ as (Bao et al., 2012)

$$\tau = \begin{cases} \exp\left(-\frac{d_\mathrm{v}}{d_\mathrm{t}}\right) & 0 \le d_m \le D + d_\mathrm{v}\,; \\ \exp\left(-\frac{d_m - D}{d_\mathrm{t}}\right) & D + d_\mathrm{v} < d_m \le D + d_\mathrm{c}\,, \end{cases} \tag{E.8}$$

where d_v is the van der Waals separation distance, D is the diameter of the CNT, d_m is the minimum distance between two axes of close CNTs, and d_c is the cut-off distance beyond which electron hopping does not occur. The tunnelling characteristic length is given by $d_\mathrm{t} = \hbar/\sqrt{8m\,\Delta E}$ where $\hbar = h/2\pi$ is the reduced Planck's constant. The distance between two CNT is assumed to be no less than the van der Waals separation distance. For a distance d between two CNTs, the probability function in Equation (E.8) is approximated as $\tau = \exp(-d/d_t)$. Upon substituting the probability function in Equation (E.7), one obtains

$$R_t = \frac{h}{2Me^2}\exp\left(\frac{4\pi d}{h}\sqrt{2m\,\Delta E}\right). \tag{E.9}$$

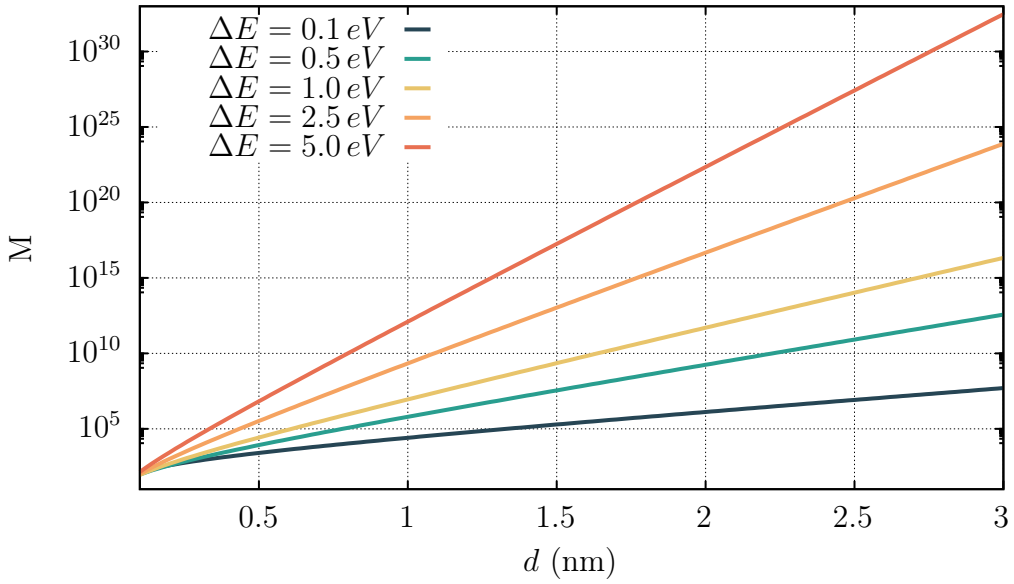

Figure E.1: Variation of parameter M with ΔE and d.

Comparing the two approaches, replacing parameter M in Equation (E.9) by $\frac{1}{2hd} A_t \sqrt{2m\,\Delta E}$ yields Equation (5.3.1). It is noted that while the number of conductive channels M is constant, $\frac{1}{2hd} A_t \sqrt{2m\,\Delta E}$ varies with distance d. Given the conductivity of the interphase layer by $K^{\text{int}} = d/(A_t R_t)$, the parameter A_t cancels out in the Simmons model, while in the alternative model, the value of A_t needs to be determined. Chanda et al. (2021) considered four different possible cases for the area available for electron tunnelling between CNTs. For the most common case, the area available for tunnelling is given by $A_t = D^2$.

To contrast these two methods, $M = \frac{1}{2hd} A_t \sqrt{2m\,\Delta E}$ is plotted for different values of ΔE and d in Figure E.1. The tunnelling area is considered as $A_t = D^2$ with the diameter chosen to be $D = 10\,\text{nm}$. The graph demonstrates the high sensitivity of these parameters, indicating that careful consideration is necessary when using the methods.

Bibliography

Abbott E.A. "Flatland: A romance of many dimensions". *In* "Nineteenth Century Science Fiction", pages 57–68. Routledge (1884)

Affdl J.H. and Kardos J. "The Halpin-Tsai equations: a review". *Polymer Engineering & Science*, 16(5):344–352 (1976)

Ahmadi M. "Madeal FE code collection, doi: 10.5281/zenodo.11636988" (2024)

Ahmadi M., Ansari R., and Hassanzadeh-Aghdam M. "Low velocity impact analysis of beams made of short carbon fiber/carbon nanotube-polymer composite: A hierarchical finite element approach". *Mechanics of Advanced Materials and Structures*, 26(13):1104–1114 (2019a)

Ahmadi M., Ansari R., and Hassanzadeh-Aghdam M. "Micromechanical analysis of elastic modulus of carbon nanotube-aluminum nanocomposites with random microstructures". *Journal of Alloys and Compounds*, 779:433–439 (2019b)

Ahmadi M., Ansari R., and Hassanzadeh-Aghdam M.K. "Finite element analysis of thermal conductivities of unidirectional multiphase composites". *Composite Interfaces*, pages 1–21 (2019c)

Ahmadi M., Ansari R., and Rouhi H. "Multi-scale bending, buckling and vibration analyses of carbon fiber/carbon nanotube-reinforced polymer nanocomposite plates with various shapes". *Physica E: Low-Dimensional Systems and Nanostructures*, 93:17–25 (2017)

Ahmadi M., Ansari R., and Rouhi H. "Free and forced vibration analysis of rectangular/-circular/annular plates made of carbon fiber-carbon nanotube-polymer hybrid composites". *Science and Engineering of Composite Materials*, 26(1):70–76 (2019d)

Ahmadi M. and Saxena P. "Mathematica file for article "Analytical modelling of the electrical conductivity of CNT-filled polymer nanocomposites", doi: 10.5281/zenodo.8114528" (2023)

Ahmadi M. and Saxena P. "Analytical modeling of the electrical conductivity of CNT-filled polymer nanocomposites". *Mathematics and Mechanics of Solids* (2024)

Allaoui A., Hoa S.V., and Pugh M.D. "The electronic transport properties and microstructure of carbon nanofiber/epoxy composites". *Composites Science and Technology*, 68(2):410–416 (2008)

Amjadi M., Kyung K.U., Park I., and Sitti M. "Stretchable, skin-mountable, and wearable strain sensors and their potential applications: a review". *Advanced Functional Materials*, 26(11):1678–1698 (2016)

Ando Y., Zhao X., Shimoyama H., Sakai G., and Kaneto K. "Physical properties of multiwalled carbon nanotubes". *International Journal of Inorganic Materials*, 1(1):77–82 (1999)

Angoshtari A., Shojaei M.F., and Yavari A. "Compatible-strain mixed finite element methods for 2D compressible nonlinear elasticity". *Computer Methods in Applied Mechanics and Engineering*, 313:596–631 (2017)

Ansari R., Ahmadi M., and Rouhi S. "Impact resistance of short carbon fibre-carbon nanotube-polymer matrix hybrid composites: A stochastic multiscale approach". *Proceedings of the Institution of Mechanical Engineers, Part L: Journal of Materials: Design and Applications*, 235(8):1925–1936 (2021a)

Ansari R., Hassani R., Gholami Y., and Rouhi H. "A VDQ-transformed approach to the 3D compressible and incompressible finite hyperelasticity". *The European Physical Journal Plus*, 136(7):1–25 (2021b)

Ariati R., Sales F., Souza A., Lima R.A., and Ribeiro J. "Polydimethylsiloxane composites characterization and its applications: a review". *Polymers*, 13(23):4258 (2021)

Arndt D., Bangerth W., Blais B., Clevenger T.C., Fehling M., Grayver A.V., Heister T., Heltai L., Kronbichler M., Maier M. et al. "The deal. II library, version 9.2". *Journal of Numerical Mathematics*, 28(3):131–146 (2020)

Asmanoglo T. and Menzel A. "A multi-field finite element approach for the modelling of fibre-reinforced composites with fibre-bending stiffness". *Computer Methods in Applied Mechanics and Engineering*, 317:1037–1067 (2017)

Auricchio F., Beirão da Veiga L., Lovadina C., Reali A., Taylor R.L., and Wriggers P. "Approximation of incompressible large deformation elastic problems: some unresolved issues". *Computational Mechanics*, 52:1153–1167 (2013)

Balay S., Abhyankar S., Adams M., Brown J., Brune P., Buschelman K., Dalcin L., Dener A., Eijkhout V., Gropp W. et al. "PETSc users manual" (2019)

Bangerth W., Hartmann R., and Kanschat G. "deal. II—a general-purpose object-oriented finite element library". *ACM Transactions on Mathematical Software (TOMS)*, 33(4):24–es (2007)

Bao W., Meguid S., Zhu Z., and Meguid M. "Modeling electrical conductivities of nanocomposites with aligned carbon nanotubes". *Nanotechnology*, 22(48):485704 (2011)

Bao W., Meguid S., Zhu Z., and Weng G. "Tunneling resistance and its effect on the electrical conductivity of carbon nanotube nanocomposites". *Journal of Applied Physics*, 111(9):093726 (2012)

Bargmann S., Klusemann B., Markmann J., Schnabel J.E., Schneider K., Soyarslan C., and Wilmers J. "Generation of 3D representative volume elements for heterogeneous materials: A review". *Progress in Materials Science*, 96:322–384 (2018)

Bendsøe M.P. and Kikuchi N. "Generating optimal topologies in structural design using a homogenization method". *Computer Methods in Applied Mechanics and Engineering*, 71(2):197–224 (1988)

Bergström J. and Boyce M. "Deformation of elastomeric networks: relation between molecular level deformation and classical statistical mechanics models of rubber elasticity". *Macromolecules*, 34(3):614–626 (2001)

Betsch P., Gruttmann F., and Stein E. "A 4-node finite shell element for the implementation of general hyperelastic 3D-elasticity at finite strains". *Computer Methods in Applied Mechanics and Engineering*, 130(1-2):57–79 (1996)

Bijelonja I., Demirdžić I., and Muzaferija S. "A finite volume method for large strain analysis of incompressible hyperelastic materials". *International Journal for Numerical Methods in Engineering*, 64(12):1594–1609 (2005)

Bokobza L. "Elastomer nanocomposites: Effect of filler–matrix and filler–filler interactions". *Polymers*, 15(13):2900 (2023)

Bonet J. and Wood R.D. *Nonlinear Continuum Mechanics for Finite Element Analysis*. Cambridge university press (1997)

Brink U. and Stein E. "On some mixed finite element methods for incompressible and nearly incompressible finite elasticity". *Computational Mechanics*, 19(1):105–119 (1996)

Buldum A. and Lu J.P. "Contact resistance between carbon nanotubes". *Physical Review B*, 63(16):161403 (2001)

Buroni F.C. and García-Macías E. "Closed-form solutions for the piezoresistivity properties of short-fiber reinforced composites with percolation-type behavior". *Carbon*, 184:923–940 (2021)

Büttiker M., Imry Y., Landauer R., and Pinhas S. "Generalized many-channel conductance formula with application to small rings". *Physical Review B*, 31(10):6207 (1985)

Chagnon G., Rebouah M., and Favier D. "Hyperelastic energy densities for soft biological tissues: a review". *Journal of Elasticity*, 120:129–160 (2015)

Chanda A., Sinha S.K., and Datla N.V. "Electrical conductivity of random and aligned nanocomposites: Theoretical models and experimental validation". *Composites Part A: Applied Science and Manufacturing*, 149:106543 (2021)

Chavan K.S., Lamichhane B.P., and Wohlmuth B.I. "Locking-free finite element methods for linear and nonlinear elasticity in 2D and 3D". *Computer Methods in Applied Mechanics and Engineering*, 196(41-44):4075–4086 (2007)

Chen C.H. and Wang Y.C. "Effective thermal conductivity of misoriented short-fiber reinforced thermoplastics". *Mechanics of Materials*, 23(3):217–228 (1996)

Chen X. and Liu Y. "Square representative volume elements for evaluating the effective material properties of carbon nanotube-based composites". *Computational Materials Science*, 29(1):1–11 (2004)

Chen Y.C. "A tutorial on kernel density estimation and recent advances". *Biostatistics & Epidemiology*, 1(1):161–187 (2017)

Choi J., Shin H., and Cho M. "A multiscale mechanical model for the effective interphase of SWNT/epoxy nanocomposite". *Polymer*, 89:159–171 (2016)

Cook R.D. "Ways to improve the bending response of finite elements". *International Journal for Numerical Methods in Engineering*, 11(6):1029–1039 (1977)

Dai H.H. and Song Z. "On a consistent finite-strain plate theory based on three-dimensional energy principle". *Proceedings of the Royal Society A: Mathematical, Physical and Engineering Sciences*, 470(2171):20140494 (2014)

De S.K. and White J.R. *Rubber Technologist's Handbook*, volume 1. iSmithers Rapra Publishing (2001)

De Gennes P.G. and Prost J. *The Physics of Liquid Crystals*. 83. Oxford university press (1993)

Deng F. and Zheng Q.S. "An analytical model of effective electrical conductivity of carbon nanotube composites". *Applied Physics Letters*, 92(7):071902 (2008)

Dhas B., Roy D., Reddy J. et al. "A mixed variational principle in nonlinear elasticity using cartan's moving frames and implementation with finite element exterior calculus". *Computer Methods in Applied Mechanics and Engineering*, 393:114756 (2022)

Doll S. and Schweizerhof K. "On the development of volumetric strain energy functions". *Journal of Applied Mechanics*, 67(1):17–21 (2000)

Dong C. "A modified rule of mixture for the vacuum-assisted resin transfer moulding process simulation". *Composites Science and Technology*, 68(9):2125–2133 (2008)

Du F., Scogna R.C., Zhou W., Brand S., Fischer J.E., and Winey K.I. "Nanotube networks in polymer nanocomposites: rheology and electrical conductivity". *Macromolecules*, 37(24):9048–9055 (2004)

Dunn M. and Taya M. "Micromechanics predictions of the effective electroelastic moduli of piezoelectric composites". *International Journal of Solids and Structures*, 30(2):161–175 (1993)

Duong H.M., Papavassiliou D.V., Mullen K.J., and Maruyama S. "Computational modeling of the thermal conductivity of single-walled carbon nanotube–polymer composites". *Nanotechnology*, 19(6):065702 (2008)

Ebbesen T., Lezec H., Hiura H., Bennett J., Ghaemi H., and Thio T. "Electrical conductivity of individual carbon nanotubes". *Nature*, 382(6586):54–56 (1996)

Eringen A.C. and Eringen A.C. *Theory of Micropolar Elasticity*. Springer (1999)

Eshelby J.D. "The determination of the elastic field of an ellipsoidal inclusion, and related problems". *Proceedings of the Royal Society of London. Series A. Mathematical and Physical Sciences*, 241(1226):376–396 (1957a)

Eshelby J.D. "The elastic model of lattice defects". *Annalen der Physik*, 456(1-3):116–121 (1957b)

Fakirov S. "On the application of the "rule of mixture" to microhardness of complex polymer systems containing a soft component and/or phase". *Journal of Materials Science*, 42(4):1131–1148 (2007)

Farhat C., Lesoinne M., and Maman N. "Mixed explicit/implicit time integration of coupled aeroelastic problems: three-field formulation, geometric conservation and distributed solution". *International Journal for Numerical Methods in Fluids*, 21(10):807–835 (1995)

Feng C. and Jiang L. "Micromechanics modeling of the electrical conductivity of carbon nanotube (CNT)–polymer nanocomposites". *Composites Part A: Applied Science and Manufacturing*, 47:143–149 (2013)

Ferrari M. "Asymmetry and the high concentration limit of the mori-tanaka effective medium theory". *Mechanics of Materials*, 11(3):251–256 (1991)

Flory P.J. "Molecular theory of rubber elasticity". *Polymer Journal*, 17(1):1–12 (1985)

Franca L.P., Hughes T.J., Loula A.F., and Miranda I. "A new family of stable elements for nearly incompressible elasticity based on a mixed petrov-galerkin finite element formulation". *Numerische Mathematik*, 53:123–141 (1988)

Fung Y.c. *Biomechanics: mechanical properties of living tissues*. Springer Science & Business Media (2013)

Gao J., Yang X., and Huang L. "A numerical model to predict the anisotropy of polymer composites reinforced with high-aspect-ratio short aramid fibers". *Advances in Polymer Technology*, 2019(1) (2019)

Gao L. and Li Z. "Effective medium approximation for two-component nonlinear composites with shape distribution". *Journal of Physics: Condensed Matter*, 15(25):4397 (2003)

Garcia-Macias E., D'Alessandro A., Castro-Triguero R., Pérez-Mira D., and Ubertini F. "Micromechanics modeling of the electrical conductivity of carbon nanotube cement-matrix composites". *Composites Part B: Engineering*, 108:451–469 (2017)

Geers M.G., Kouznetsova V.G., and Brekelmans W. "Multi-scale computational homogenization: Trends and challenges". *Journal of Computational and Applied Mathematics*, 234(7):2175–2182 (2010)

Ginzburg V.V., Bicerano J., Christenson C.P., Schrock A.K., and Patashinski A.Z. "Theoretical modeling of the relationship between young's modulus and formulation variables for segmented polyurethanes". *Journal of Polymer Science Part B: Polymer Physics*, 45(16):2123–2135 (2007)

Girun N., Ahmadun F.R., Rashid S.A., and Ali Atieh M. "Multi-wall carbon nanotubes/styrene butadiene rubber (SBR) nanocomposite". *Fullerenes, Nanotubes, and Carbon Nanostructures*, 15(3):207–214 (2007)

Goh G.L., Agarwala S., and Yeong W.Y. "Directed and on-demand alignment of carbon nanotube: a review toward 3D printing of electronics". *Advanced Materials Interfaces*, 6(4):1801318 (2019)

Gong S., Zhu Z., and Haddad E. "Modeling electrical conductivity of nanocomposites by considering carbon nanotube deformation at nanotube junctions". *Journal of Applied Physics*, 114(7):074303 (2013)

Gong S. and Zhu Z.H. "On the mechanism of piezoresistivity of carbon nanotube polymer composites". *Polymer*, 55(16):4136–4149 (2014)

Goyal R., Tiwari A., and Negi Y. "Microhardness of PEEK/ceramic micro-and nanocomposites: correlation with Halpin–Tsai model". *Materials Science and Engineering: A*, 491(1-2):230–236 (2008)

Gropp W., Lusk E., Doss N., and Skjellum A. "A high-performance, portable implementation of the MPI message passing interface standard". *Parallel Computing*, 22(6):789–828 (1996)

Halpin J. "Stiffness and expansion estimates for oriented short fiber composites". *Journal of Composite Materials*, 3(4):732–734 (1969)

Hartmann S. and Neff P. "Polyconvexity of generalized polynomial-type hyperelastic strain energy functions for near-incompressibility". *International Journal of Solids and Structures*, 40(11):2767–2791 (2003)

Harvard University. "Harvard Microrobotics Laboratory". https://www.micro.seas.harvard.edu/softrobotics (2024)

Hatta H. and Taya M. "Effective thermal conductivity of a misoriented short fiber composite". *Journal of Applied Physics*, 58(7):2478–2486 (1985)

Hatta H. and Taya M. "Thermal conductivity of coated filler composites". *Journal of Applied Physics*, 59(6):1851–1860 (1986)

Heroux M.A., Bartlett R.A., Howle V.E., Hoekstra R.J., Hu J.J., Kolda T.G., Lehoucq R.B., Long K.R., Pawlowski R.P., Phipps E.T. et al. "An overview of the trilinos project". *ACM Transactions on Mathematical Software (TOMS)*, 31(3):397–423 (2005)

Hill R. "Elastic properties of reinforced solids: some theoretical principles". *Journal of the Mechanics and Physics of Solids*, 11(5):357–372 (1963)

Hiroshi H. and Minoru T. "Equivalent inclusion method for steady state heat conduction in composites". *International Journal of Engineering Science*, 24(7):1159–1172 (1986)

Holzapfel G.A. *Nonlinear Solid Mechanics: A Continuum Approach for Engineering Science*. Kluwer Academic Publishers Dordrecht (2000)

Holzapfel G.A. *Nonlinear Solid Mechanics: A Continuum Approach for Engineering Science*. Kluwer Academic Publishers Dordrecht (2002)

Horgan C. and Murphy J. "Plane stress problems for isotropic incompressible hyperelastic materials". *Journal of Elasticity*, pages 1–17 (2024)

Hossain M., Saxena P., and Steinmann P. "Modelling the mechanical aspects of the curing process of magneto-sensitive elastomeric materials". *International Journal of Solids and Structures*, 58:257–269 (2015)

Hu H. *Variational Principles of Theory of Elasticity with Applications*. CRC Press (1984)

Hu N., Karube Y., Yan C., Masuda Z., and Fukunaga H. "Tunneling effect in a polymer/carbon nanotube nanocomposite strain sensor". *Acta materialia*, 56(13):2929–2936 (2008)

Hughes T.J. *The Finite Element Method: linear static and dynamic finite element analysis*. Courier Corporation (2012)

Javid M. and Biglari H. "A multi-scale finite element approach to mechanical performance of polyurethane/CNT nanocomposite foam". *Materials Today Communications*, 24:101081 (2020)

Javili A., Chatzigeorgiou G., McBride A.T., Steinmann P., and Linder C. "Computational homogenization of nano-materials accounting for size effects via surface elasticity". *GAMM-Mitteilungen*, 38(2):285–312 (2015)

Javili A., Saeb S., and Steinmann P. "Aspects of implementing constant traction boundary conditions in computational homogenization via semi-Dirichlet boundary conditions". *Computational Mechanics*, 59:21–35 (2017)

Joo D.H., Kang M.S., Park S.J., Se A.Y., and Park W.T. "Fabrication method of flexible strain sensors with CNTs and solvents". *Sensors and Actuators A: Physical*, 345:113775 (2022)

Joshi U.A., Sharma S.C., and Harsha S. "Effect of carbon nanotube orientation on the mechanical properties of nanocomposites". *Composites Part B: Engineering*, 43(4):2063–2071 (2012)

Kalaitzidou K., Fukushima H., Miyagawa H., and Drzal L.T. "Flexural and tensile moduli of polypropylene nanocomposites and comparison of experimental data to Halpin-Tsai and Tandon-Weng models". *Polymer Engineering & Science*, 47(11):1796–1803 (2007)

Kanit T., Forest S., Galliet I., Mounoury V., and Jeulin D. "Determination of the size of the representative volume element for random composites: statistical and numerical approach". *International Journal of Solids and Structures*, 40(13-14):3647–3679 (2003)

Kashyap K. and Patil R. "On Young's modulus of multi-walled carbon nanotubes". *Bulletin of Materials Science*, 31(2):185–187 (2008)

Kausar A., Rafique I., and Muhammad B. "Review of applications of polymer/carbon nanotubes and epoxy/CNT composites". *Polymer-Plastics Technology and Engineering*, 55(11):1167–1191 (2016)

Kim Y.J., Shin T.S., Do Choi H., Kwon J.H., Chung Y.C., and Yoon H.G. "Electrical conductivity of chemically modified multiwalled carbon nanotube/epoxy composites". *Carbon*, 43(1):23–30 (2005)

Kostagiannakopoulou C., Fiamegkou E., Sotiriadis G., and Kostopoulos V. "Thermal conductivity of carbon nanoreinforced epoxy composites". *Journal of Nanomaterials*, 2016 (2016)

Lai T.K. *Thermal Stress Due to Disturbance of Uniform Heat Flow by An Ellipsoidal Inclusion*. Northwestern University (1977)

Le B., Yvonnet J., and He Q.C. "Computational homogenization of nonlinear elastic materials using neural networks". *International Journal for Numerical Methods in Engineering*, 104(12):1061–1084 (2015)

Lee E.H. "Elastic-plastic deformation at finite strains". *Journal of Applied Mechanics* (1969)

Li C., Thostenson E.T., and Chou T.W. "Dominant role of tunneling resistance in the electrical conductivity of carbon nanotube–based composites". *Applied Physics Letters*, 91(22):223114 (2007)

Li H., Lu W., Li J., Bai X., and Gu C. "Multichannel ballistic transport in multiwall carbon nanotubes". *Physical Review Letters*, 95(8):086601 (2005)

Lisunova M., Mamunya Y.P., Lebovka N., and Melezhyk A. "Percolation behaviour of ultra-high molecular weight polyethylene/multi-walled carbon nanotubes composites". *European Polymer Journal*, 43(3):949–958 (2007)

Liu G. "A step-by-step method of rule-of-mixture of fiber-and particle-reinforced composite materials". *Composite Structures*, 40(3-4):313–322 (1997)

Liu Y.J. and Chen X. "Evaluations of the effective material properties of carbon nanotube-based composites using a nanoscale representative volume element". *Mechanics of Materials*, 35(1-2):69–81 (2003)

Liu Z., McBride A., Ghosh A., Heltai L., Huang W., Yu T., Steinmann P., and Saxena P. "Computational instability analysis of inflated hyperelastic thin shells using subdivision surfaces". *Computational Mechanics*, 73(2):257–276 (2024)

Lötters J.C., Olthuis W., Veltink P.H., and Bergveld P. "The mechanical properties of the rubber elastic polymer polydimethylsiloxane for sensor applications". *Journal of Micromechanics and Microengineering*, 7(3):145 (1997)

Lubliner J. "A model of rubber viscoelasticity". *Mechanics Research Communications*, 12(2):93–99 (1985)

Malagù M., Goudarzi M., Lyulin A., Benvenuti E., and Simone A. "Diameter-dependent elastic properties of carbon nanotube-polymer composites: Emergence of size effects from atomistic-scale simulations". *Composites Part B: Engineering*, 131:260–281 (2017)

Maniatty A.M., Liu Y., Klaas O., and Shephard M.S. "Higher order stabilized finite element method for hyperelastic finite deformation". *Computer Methods in Applied Mechanics and Engineering*, 191(13-14):1491–1503 (2002)

Matos M.A., Pinho S.T., and Tagarielli V.L. "Application of machine learning to predict the multiaxial strain-sensing response of CNT-polymer composites". *Carbon*, 146:265–275 (2019)

McBride A., Davydov D., and Steinmann P. "Modelling the flexoelectric effect in solids: A micromorphic approach". *Computer Methods in Applied Mechanics and Engineering*, 371 (2020)

Merodio J. and Ogden R. "Mechanical response of fiber-reinforced incompressible non-linearly elastic solids". *International Journal of Non-Linear Mechanics*, 40(2-3):213–227 (2005)

Michel J.C., Moulinec H., and Suquet P. "Effective properties of composite materials with periodic microstructure: a computational approach". *Computer Methods in Applied Mechanics and Engineering*, 172(1-4):109–143 (1999)

Miehe C. "Computational micro-to-macro transitions for discretized micro-structures of heterogeneous materials at finite strains based on the minimization of averaged incremental energy". *Computer Methods in Applied Mechanics and Engineering*, 192(5-6):559–591 (2003)

Miyagawa H., Misra M., and Mohanty A.K. "Mechanical properties of carbon nanotubes and their polymer nanocomposites". *Journal of Nanoscience and Nanotechnology*, 5(10):1593–1615 (2005)

Molnár S., Pukanszky B., Hammer C., and Maurer F. "Impact fracture study of multicomponent polypropylene composites". *Polymer*, 41(4):1529–1539 (2000)

Mora A., Han F., and Lubineau G. "Estimating and understanding the efficiency of nanoparticles in enhancing the conductivity of carbon nanotube/polymer composites". *Results in Physics*, 10:81–90 (2018)

Mora A., Verma P., and Kumar S. "Electrical conductivity of CNT/polymer composites: 3D printing, measurements and modeling". *Composites Part B: Engineering*, 183:107600 (2020)

Mori T. and Tanaka K. "Average stress in matrix and average elastic energy of materials with misfitting inclusions". *Acta Metallurgica*, 21(5):571–574 (1973)

Nguyen N.T., Nguyen M.N., Truong T.T., and Bui T.Q. "An improved meshless method for finite deformation problem in compressible hyperelastic media". *Vietnam Journal of Mechanics*, 43(1):27–41 (2021)

Ogden R.W. "Large deformation isotropic elasticity–on the correlation of theory and experiment for incompressible rubberlike solids". *Proceedings of the Royal Society of London. A. Mathematical and Physical Sciences*, 326(1567):565–584 (1972)

Ogden R.W. *Non-linear Elastic Deformations*. Dover Publications (1997)

Ounaies Z., Park C., Wise K., Siochi E., and Harrison J. "Electrical properties of single wall carbon nanotube reinforced polyimide composites". *Composites Science and Technology*, 63(11):1637–1646 (2003)

Pagani A. and Carrera E. "Unified one-dimensional finite element for the analysis of hyperelastic soft materials and structures". *Mechanics of Advanced Materials and Structures*, 30(2):342–355 (2023)

Pal G. and Kumar S. "Multiscale modeling of effective electrical conductivity of short carbon fiber-carbon nanotube-polymer matrix hybrid composites". *Materials & Design*, 89:129–136 (2016)

Papageorgiou D.G., Kinloch I.A., and Young R.J. "Graphene/elastomer nanocomposites". *Carbon*, 95:460–484 (2015)

Paran S.M.R., Das A., Khonakdar H.A., Naderpour N., Heinrich G., and Saeb M.R. "Modeling and interpreting large deformation behavior of rubber nanocomposites containing carbon nanotubes and nanoplatelets". *Polymer Composites*, 40(S2):E1548–E1558 (2019)

Pascon J.P. "Large deformation analysis of plane-stress hyperelastic problems via triangular membrane finite elements". *International Journal of Advanced Structural Engineering*, 11(3):331–350 (2019)

Quinteros L., García-Macías E., and Martínez-Pañeda E. "Electromechanical phase-field fracture modelling of piezoresistive CNT-based composites". *Computer Methods in Applied Mechanics and Engineering*, 407:115941 (2023)

Reese S. "On the equivalent of mixed element formulations and the concept of reduced integration in large deformation problems". *International Journal of Nonlinear Sciences and Numerical Simulation*, 3(1):1–34 (2002)

Rivlin R.S. and Saunders D. "Large elastic deformations of isotropic materials VII. Experiments on the deformation of rubber". *Philosophical Transactions of the Royal Society of London. Series A, Mathematical and Physical Sciences*, 243(865):251–288 (1951)

Saeb S., Steinmann P., and Javili A. "Aspects of computational homogenization at finite deformations: a unifying review from Reuss' to Voigt's bound". *Applied Mechanics Reviews*, 68(5):050801 (2016)

Salvetat J.P., Bonard J.M., Thomson N., Kulik A., Forro L., Benoit W., and Zuppiroli L. "Mechanical properties of carbon nanotubes". *Applied Physics A*, 69:255–260 (1999)

Saxena P., Hossain M., and Steinmann P. "A theory of finite deformation magneto-viscoelasticity". *International Journal of Solids and Structures*, 50(24):3886–3897 (2013)

Saxena P., Pelteret J.P., and Steinmann P. "Modelling of iron-filled magneto-active polymers with a dispersed chain-like microstructure". *European Journal of Mechanics - A/Solids*, 50:132–151 (2015)

Schneider K., Klusemann B., and Bargmann S. "Fully periodic RVEs for technological relevant composites: not worth the effort!" *Journal of Mechanics of Materials and Structures*, 12(4):471–484 (2017)

Scott D.W. "Sturges' rule". *Wiley Interdisciplinary Reviews: Computational Statistics*, 1(3):303–306 (2009)

Seidel G.D. and Lagoudas D.C. "Micromechanical analysis of the effective elastic properties of carbon nanotube reinforced composites". *Mechanics of Materials*, 38(8-10):884–907 (2006)

Seidel G.D. and Lagoudas D.C. "A micromechanics model for the electrical conductivity of nanotube-polymer nanocomposites". *Journal of Composite Materials*, 43(9):917–941 (2009)

Shaw M.T. and MacKnight W.J. *Introduction to polymer viscoelasticity*. John Wiley & Sons (2018)

Shiraishi M. and Ata M. "Work function of carbon nanotubes". *Carbon*, 39(12):1913–1917 (2001)

Shojaei M.F. and Yavari A. "Compatible-strain mixed finite element methods for incompressible nonlinear elasticity". *Journal of Computational Physics*, 361:247–279 (2018)

Shojaei M.F. and Yavari A. "Compatible-strain mixed finite element methods for 3D compressible and incompressible nonlinear elasticity". *Computer Methods in Applied Mechanics and Engineering*, 357:112610 (2019)

Simmons J.G. "Generalized formula for the electric tunnel effect between similar electrodes separated by a thin insulating film". *Journal of Applied Physics*, 34(6):1793–1803 (1963)

Simo J. and Hughes T. "On the variational foundations of assumed strain methods". *Journal of Applied Mechanics* (1986)

Simo J.C. and Armero F. "Geometrically non-linear enhanced strain mixed methods and the method of incompatible modes". *International Journal for Numerical Methods in Engineering*, 33(7):1413–1449 (1992)

Simo J.C. and Rifai M. "A class of mixed assumed strain methods and the method of incompatible modes". *International Journal for Numerical Methods in Engineering*, 29(8):1595–1638 (1990)

Šolín P., Červenỳ J., and Doležel I. "Arbitrary-level hanging nodes and automatic adaptivity in the hp-FEM". *Mathematics and Computers in Simulation*, 77(1):117–132 (2008)

Soni S.K., Thomas B., and Kar V.R. "A comprehensive review on CNTs and CNT-reinforced composites: syntheses, characteristics and applications". *Materials Today Communications*, 25:101546 (2020)

Spencer A. and Soldatos K. "Finite deformations of fibre-reinforced elastic solids with fibre bending stiffness". *International Journal of Non-Linear Mechanics*, 42(2):355–368 (2007)

Steinmann P., Betsch P., and Stein E. "FE plane stress analysis incorporating arbitrary 3D large strain constitutive models". *Engineering Computations*, 14(2):175–201 (1997)

Sukiman M.S., Kanit T., N'Guyen F., Imad A., El Moumen A., and Erchiqui F. "Effective thermal and mechanical properties of randomly oriented short and long fiber composites". *Mechanics of Materials*, 107:56–70 (2017)

Sun W., Chaikof E.L., and Levenston M.E. "Numerical approximation of tangent moduli for finite element implementations of nonlinear hyperelastic material models". *Journal of Biomechanical Engineering* (2008)

Sussman T. and Bathe K.J. "A finite element formulation for nonlinear incompressible elastic and inelastic analysis". *Computers & Structures*, 26(1-2):357–409 (1987)

Sze K., Zheng S.J., and Lo S. "A stabilized eighteen-node solid element for hyperelastic analysis of shells". *Finite Elements in Analysis and Design*, 40(3):319–340 (2004)

Takao Y., Chou T., and Taya M. "Effective longitudinal Young's modulus of misoriented short fiber composites". *Journal of Applied Mechanics* (1982)

Tan H., Huang Y., Liu C., and Geubelle P.H. "The Mori–Tanaka method for composite materials with nonlinear interface debonding". *International Journal of Plasticity*, 21(10):1890–1918 (2005)

Tang Z.H., Li Y.Q., Huang P., Fu Y.Q., Hu N., and Fu S.Y. "A new analytical model for predicting the electrical conductivity of carbon nanotube nanocomposites". *Composites Communications*, 23:100577 (2021)

Taya M. "Micromechanics modeling of smart composites". *Composites Part A: Applied Science and Manufacturing*, 30(4):531–536 (1999)

Taya M. *Electronic Composites: Modeling, Characterization, Processing, and MEMS Applications*. Cambridge University Press (2005)

Taya M., Kim W., and Ono K. "Piezoresistivity of a short fiber/elastomer matrix composite". *Mechanics of Materials*, 28(1-4):53–59 (1998)

Terada K., Hori M., Kyoya T., and Kikuchi N. "Simulation of the multi-scale convergence in computational homogenization approaches". *International Journal of Solids and Structures*, 37(16):2285–2311 (2000)

Truesdell C. "The mechanical foundations of elasticity and fluid dynamics". *Journal of Rational Mechanics and Analysis*, 1:125–300 (1952)

Viebahn N., Steeger K., and Schröder J. "A simple and efficient Hellinger–Reissner type mixed finite element for nearly incompressible elasticity". *Computer Methods in Applied Mechanics and Engineering*, 340:278–295 (2018)

Wang S., Huang Y., Chang E., Zhao C., Ameli A., Naguib H.E., and Park C.B. "Evaluation and modeling of electrical conductivity in conductive polymer nanocomposite foams with multiwalled carbon nanotube networks". *Chemical Engineering Journal*, 411:128382 (2021)

Washizu K. "Variational methos in elasticity and plasticity". *International Series of Monographs in Aeronautics and Astronautics* (1968)

Watanabe I. and Yamanaka A. "Voxel coarsening approach on image-based finite element modeling of representative volume element". *International Journal of Mechanical Sciences*, 150:314–321 (2019)

Watanabe Y. "Evaluation of fiber orientation in ferromagnetic short-fiber reinforced composites by magnetic anisotropy". *Journal of Composite Materials*, 36(8):915–923 (2002)

Wehner M., Truby R.L., Fitzgerald D.J., Mosadegh B., Whitesides G.M., Lewis J.A., and Wood R.J. "An integrated design and fabrication strategy for entirely soft, autonomous robots". *Nature*, 536(7617):451–455 (2016)

Weiss J.A., Maker B.N., and Govindjee S. "Finite element implementation of incompressible, transversely isotropic hyperelasticity". *Computer Methods in Applied Mechanics and Engineering*, 135(1-2):107–128 (1996)

Wisse E., Govaert L., Meijer H., and Meijer E. "Unusual tuning of mechanical properties of thermoplastic elastomers using supramolecular fillers". *Macromolecules*, 39(21):7425–7432 (2006)

Withers P., Stobbs W., and Pedersen O. "The application of the Eshelby method of internal stress determination to short fibre metal matrix composites". *Acta Metallurgica*, 37(11):3061–3084 (1989)

Wriggers P. *Nonlinear Finite Element Methods*. Springer Science & Business Media (2008)

Wriggers P. and Hueck U. "A formulation of the QS6 element for large elastic deformations". *International Journal for Numerical Methods in Engineering*, 39(9):1437–1454 (1996)

Xia Z., Zhang Y., and Ellyin F. "A unified periodical boundary conditions for representative volume elements of composites and applications". *International Journal of Solids and Structures*, 40(8):1907–1921 (2003)

Yan K., Xue Q., Zheng Q., and Hao L. "The interface effect of the effective electrical conductivity of carbon nanotube composites". *Nanotechnology*, 18(25):255705 (2007)

Ye J.Y., Zhang L.W., and Reddy J. "Large strained fracture of nearly incompressible hyperelastic materials: enhanced assumed strain methods and energy decomposition". *Journal of the Mechanics and Physics of Solids*, 139:103939 (2020)

Yosibash Z. and Priel E. "p-FEMs for hyperelastic anisotropic nearly incompressible materials under finite deformations with applications to arteries simulation". *International Journal for Numerical Methods in Engineering*, 88(11):1152–1174 (2011)

Zhang T. and Yi Y. "Monte carlo simulations of effective electrical conductivity in short-fiber composites". *Journal of Applied Physics*, 103(1):014910 (2008)

Zhang W., Dehghani-Sanij A.A., and Blackburn R.S. "Carbon based conductive polymer composites". *Journal of Materials Science*, 42:3408–3418 (2007)